WBS: 1.2.21.2.2.
QA: N/A

Civilian Radioactive Waste Management System
Management & Operating Contractor

Yucca Mountain Site Description

TDR-CRW-GS-000001 REV 01 ICN 01

September 2000

Prepared for:

U.S. Department of Energy
Yucca Mountain Site Characterization Office
P.O. Box 30307
North Las Vegas, Nevada 89036-0307

Prepared by:

TRW Environmental Safety Systems Inc.
1180 Town Center Drive
Las Vegas, Nevada 89144

Under Contract Number
DE-AC08-91RW00134

VOLUME 3

10. FACTORS AFFECTING RADIONUCLIDE TRANSPORT

10.1 INTRODUCTION

Radionuclide migration from the potential repository would be mitigated by several barriers, including the geochemical retardation due to solubility and sorption described in this section. One of the initial retardation factors is the solubility of the radionuclides themselves in any water that infiltrates the potential repository. The solubility of key radionuclides (e.g., Np, Pu, Am, and Tc) has been shown to be controlled by solution speciation and by the solubility-limiting actinide-bearing solid. Kinetic barriers are considered in this analysis and sometimes drive the conceptual choices of the phases to constrain some radionuclide concentrations. As such, this corresponds to metastable equilibrium in some cases and this ensures conservatism. This section summarizes factors affecting radionuclide transport under ambient conditions in the far field. Included are the results of the following investigations: radionuclide solubility and speciation, sorption, the effects of organics on sorption, matrix diffusion, and the conceptual models that describe these phenomena in transport codes. It also summarizes studies of colloid-facilitated radionuclide transport and of field testing of transport in the unsaturated and saturated zones. Section 11.4 considers the interactions of radionuclides with the products of canister corrosion such as iron oxides and cementitious materials that might be generated from concrete tunnel liners.

10.1.1 Radionuclides of Concern

Although the fission products ^{90}Sr and ^{137}Cs will dominate the radioactive inventory at the start of the potential repository's life (Choi and Pigford 1981), the half lives of approximately 30 yr. mean that these radionuclides will be decayed by the time the metal waste packages are projected to fail due to corrosion (a minimum of 1 k.y.) (Langmuir 1997). Therefore, little emphasis is placed on these elements. For spent nuclear fuel, the chief sources of radioactivity from 1 k.y. to 10 k.y. are Am and Pu isotopes (Langmuir 1997, Figure 13.18). From roughly 10 k.y. to 10 m.y., ^{237}Np contributes the most to radioactivity of the waste (Langmuir 1997, Figure 13.18). Therefore, scientific study has concentrated on the geochemical mobility of Am, Pu, and Np as the successively dominant contributors to radioactivity. In addition to these actinides, ^{233}U, ^{234}U, ^{129}I, and ^{99}Tc received attention in total system performance assessment (TSPA) exercises principally because there has been little demonstrated geochemical retardation from solubility or sorption for these radioactive isotopes. The radionuclides of concern singled out here (Tc, U, Np, Pu, and Am) were chosen from the most important species for the first 10 m.y. from the water-dilution figures of Choi and Pigford (1981) and from Langmuir (1997).

The geochemistry and thermodynamic solubility of the long-lived radionuclides are briefly reviewed in this section, followed by more extensive review of Np, Pu, and Am and their relevance to Yucca Mountain in subsequent sections.

Technetium–Technetium is a priority radionuclide due to its high solubility and low sorption. It is also the most important β-emitter in radioactive waste in the greater than 103-yr. time frame (CRWMS M&O 1994 Tables 5-11 and 5-12). Thermodynamic data for solids and solutions are being evaluated critically by scientists collaborating through the Nuclear Energy Agency; this review is scheduled to be published shortly. It is presumed by the TSPA that the waters at Yucca

Mountain are oxidizing waters and that Tc will therefore exist in the Tc (VII) state as TcO_4^-. The tetrahedral arrangement of coordinating oxygens prevents the formation of stable solid precipitates and shields the Tc from mineral sorption sites. Release quantities calculated for solubility considerations would be limited by inventory, not precipitation equilibrium. However, interaction with reduced minerals, or in more reducing waters, may reduce the Tc to lower oxidation states (i.e., Tc [IV]), which would be orders of magnitude less soluble and more sorptive (Lieser and Bauscher 1988). In reducing neutral waters, the predominant aqueous species would be $TcO(OH)_2(aq)$ in equilibrium with $TcO_2 \bullet 2H_2O(c)$ with a solubility of about 10^{-8} M (Rard 1983; Langmuir 1997, Figure 13.21). (Note: In this section, (c) indicates crystalline, (aq) indicates aqueous, and (am) indicates amorphous.)

At higher values of pH (greater than 10), amphoteric behavior starts to increase the solubility to approximately 10^{-7} M at a pH of 11. In the presence of high carbonate concentrations, carbonate complexes can form at pH values greater than 8.5, raising solubility to approximately 10^{-6} M by a pH of 11 for $P_{CO_2} = 10^{-2}$ bar (that is, approximately 33 times standard atmospheric CO_2 pressure). It is not anticipated that these pH and P_{CO_2} conditions will occur together unless alkaline plumes are generated by cement during the thermal pulse. However, cement will not be present in the current design except in small quantities. Little is known about the temperature effects on the Tc (VII)/Tc (IV) equilibrium, so extrapolation to the thermal range of 90° to 95°C in the near field of the repository is not possible. Furthermore, the intervening oxidation states (VI and V) are considered to be unstable with respect to disproportionation, but their stability under very dilute conditions or different temperatures is also not known. These comments on the effect of temperature on speciation, redox barriers, and, ultimately, thermodynamic solubilities can be made almost across the board for all the radionuclides discussed here (although Yucca Mountain water-specific solubility experiments will be described below for Np, Pu, and Am). At this point, the only conservative, nonreproachable course of action is not to use solubility as a limiting factor in Tc release.

Iodine–Iodine occurs as iodate (IO_3^-) in highly oxidizing waters and as iodide (I^-) under less-oxidizing conditions, including most groundwaters (Pourbaix 1966, Figure 1, p. 621; Langmuir 1997, p. 520). Iodide salts are less soluble than iodate salts but are still too soluble to limit maximum possible I concentrations in groundwaters. Therefore, the concentration will be limited by the amount of I available from the inventory.

Uranium–Uranium has been studied extensively for over a century, and the relevant thermodynamics that control U solubility have been critically evaluated by Grenthe et al. (1992) under the auspices of the Nuclear Energy Agency. Spent nuclear fuel from nuclear power plants to be disposed of in the potential repository is largely in the form of UO_2, so the discussion here starts with U (IV) complexes. Note that only U (IV) and U (VI) are considered to be important oxidation states of U, with U (V) quickly disproportionating (Newton 1975). Uranium (IV) is stable only at very reducing potentials, with the principal minerals being uraninite (crystalline UO_2), pitchblende (amorphous UO_2), and coffinite ($USiO_4$) (Langmuir 1997, p. 495). In the absence of carbonates, the principal solution species in equilibrium with uraninite/pitchblende (various degrees of crystallinity found experimentally) at pH values greater than 4 is $U(OH)_4^0(aq)$, with a uranium solubility of less than 10^{-8} M to pH values greater than 12 (Ryan and Rai 1983; Parks and Pohl 1988; Rai et al. 1990, p. 263; Yajima et al. 1995, p. 1142). Given

the formation constant of coffinite, its solubility should also be comparable to these values (Langmuir 1997, pp. 502, 503). Under Yucca Mountain conditions, the most important other ligand for U (besides OH^-) is carbonate. At very reducing conditions, the tetrahydroxide U (IV) complex is more stable in solution than the carbonates (Grenthe et al. 1992, pp. 120 to 122, 306 to 333), so U (IV) carbonates do not need to be considered further.

In the more oxidizing regions of uraninite (but not pitchblende) stability, the solution species in equilibrium over the U (IV) solid can be a U (VI) solution species, either a uranyl aquo/hydroxide species or a carbonate species (Langmuir 1997, Figures 13.8 to 13.9). In fact, several mixed-oxidation-state solids predominate at groundwater-relevant pHs before the U (VI) solid phases (schoepite (β-$UO_3 \cdot 2H_2O$) and [or] secondary uranyl solid phases, such as carbonates) predominate in the higher Eh values of the Eh/pH stability diagram. In ascending order of Eh values, important U solids formed in carbonate-free, near-neutral pH water include UO_2, β-U_4O_9, β-U_3O_7, U_3O_8, and UO_3 (Langmuir 1997, Figure 13.10). Important uranyl solution species under Yucca Mountain waters (e.g., UE-25 J-13, referred to henceforth as J-13) include, with increasing importance with pH, UO_2^{2+}, UO_2OH^+, $UO_2CO_3^0$, $(UO_2)_3(OH)_5^+$, $(UO_2)_2(CO_3)(OH)_3^-$, $UO_2(CO_3)_2^{2-}$, and $UO_2(CO_3)_3^{4-}$ (Grenthe et al. 1992, pp. 98 to 130, 306 to 330; Waite et al. 1994). Langmuir (1997, Figure 13.5) plotted the uranyl solubility as a function of pH with schoepite as the solubility-controlling solid for two P_{CO_2} cases. With no carbonate present, the solubility reached a minimum of just over 10^{-7} M at a pH value of just over 7. By a pH of 8.5 and, on the other side of the minimum, a pH of 5.5, the solubility increased to 10^{-6} M. With $P_{CO_2} = 10^{-2}$ bar (), the minimum shifted to a pH of approximately 6.3 and to a value of about 10^{-6} M. The solubility increased from this value by an order of magnitude by pHs of 5 and 8. Typical Yucca Mountain waters (e.g., J-13) would produce solubilities intermediate between these two P_{CO_2} cases. The presence of other potential solid uranyl phases, such as rutherfordine or $Na_2(UO_2)(CO_3)_2$, was not considered. This fact implies that the present estimate is conservative, as a more stable uranyl carbonate solid would lower the solubility values, and less stable phases would convert to the schoepite.

Although the other actinides also exhibit oxide solubility-limiting solids rather than carbonates in J-13 water conditions (see below), schoepite has been reported to be a nonterminal phase: it dehydrates in dried-out conditions possible in the vadose zone and thereby its crystal structure is compromised, allowing it to be dissolved (Finch et al. 1992, p. 439). Secondary U mineralization subsequently occurs with weathering to form uranyl silicates (uranophane and soddyite), phosphates (autunite), vanadates (carnotite), or carbonates (e.g., rutherfordine), depending on what anions are available. Because many U deposits start out as uraninite and show these weathering/oxidation patterns, they can be used as natural analog systems for a radioactive waste repository to show mobility patterns of U over long periods of time (Curtis et al. 1994). An example of an analog for Yucca Mountain is the Peña Blanca deposit in northern Mexico, which occurs in an unsaturated and oxidized tuff located in an arid region (Pearcy et al. 1994; Section 13 of this report). The formation of some of these secondary phases would limit the solubility of U further from that of schoepite. For instance, the formation of uranophane as the solubility-limiting phase, as is seen at Peña Blanca, should limit the U solubility to approximately 10^{-7} M (Langmuir 1997, pp. 513 to 514). Wilson (1990, p. 425) produced similar Ca-U (VI) silicate solids by leaching spent nuclear fuel with J-13 water.

Neptunium–TSPA results have shown that the inventory of Np from stored radioactive waste under current scenarios would be sufficient to consider Np a potential problem contaminant, with ^{237}Np being the largest contributor to the radioactivity of a radioactive waste repository at times between 10 k.y. to 10 m.y. (CRWMS M&O 1994; Wilson et al. 1994; Rechard 1995; Langmuir 1997). All of the TSPAs for the Yucca Mountain Site have considered neptunium to be the most hazardous radionuclide for repository times beyond 10 k.y. (CRWMS M&O 1994, Wilson et al. 1994, Rechard 1995; CRWMS M&O 1995; DOE 1998). In natural waters, Np (IV) is expected to be the dominant oxidation state under reducing conditions, while Np (V) is the dominant oxidation state in oxidizing waters (Katz et al. 1986; Lieser and Muhlenweg 1988, Section 2; Hobart 1990, p. 407). Although oxidizing conditions are generally expected to prevail in the unsaturated zone within Yucca Mountain, it is possible that reducing conditions may exist in the saturated zone (Sections 5.3.6 and 5.3.7) or locally in the near field (at least temporarily). Theoretical calculations using different thermodynamic data bases predict that the solubility-limiting solid phase would be either a Np (IV) or Np (V) compound, depending upon the redox state of the water (Wilson and Bruton 1990; Hakanen and Lindberg 1991; Janecky et al. 1995, 1997, p. 2). The solubility of solid phases with these different oxidation states is quite different, with the Np (IV) phase having a solubility several orders of magnitude less than that for the Np (V) phase. For Np (IV), solubility-controlling solids include $Np(OH)_4(am)$ and, especially, $NpO_2(c)$. Important solution species include $Np(OH)_4^0$ in low carbonate solutions (for pH greater than 3) and $Np(OH)_3CO_3^-$ in higher carbonate solutions (e.g., total carbonate = 10^{-2} M, similar to UE-25 water, and a pH range from 5 to 11). Under conditions for the Np (IV) oxidation-reduction (redox) state, the solubility in water to at least a total carbonate concentration of up to 10^{-2} M is expected to be lower than 10^{-8} M (Langmuir 1997).

As for uraninite (described above), the stability field for $NpO_2(c)$ extends into the Eh region in which Np (V) solution species may also exist (Langmuir 1997). The degree to which this extension occurs depends critically upon the database used. Neptunium (V) solubility-limiting solids include $Np_2O_5(c)$, $NpO_2OH(am)$, and in high ionic-strength carbonate media, the so-called double carbonate salts $Na_{2x-1}NpO_2(CO_3)_x$ (where x = 1 to 3) (Volkov et al. 1980, 1981; Neck et al. 1994; Neck et al. 1995). In the absence of carbonates, the solution speciation of Np (V) is dominated by the highly soluble NpO_2^+, which does not hydrolyze readily below a pH of 10 (Moskvin 1971; Rosch et al. 1987; Itagaki et al. 1992, Figure 2; Neck et al. 1992, Figure 3, p. 29; Tait et al. 1996, pp. 34 to 49). In J-13 type waters, where the higher carbonate complexes are not strong enough to be predominant even at higher temperatures, the carbonate-complexed Np (V) species of importance includes $NpO_2CO_3^-$ (Tait et al. 1996, p. 41).

Plutonium–Plutonium is a priority radionuclide, because a large quantity of it will exist in the inventory of a radioactive waste repository and, in oxidized form, it can be quite mobile. Unlike most metal cations, Pu can exist in multiple oxidation states simultaneously. The III, IV, V, and VI states of Pu are readily attainable under environmentally relevant conditions, and therefore redox conditions do not necessarily preclude a low release. In general, the solid state is dominated by Pu (IV), specifically $PuO_2(c)$, $Pu(OH)_4(am)$, and radiocolloids (suspended PuO_2 polymer). The aging of Pu solubility-limiting solids might start with the formation of radiocolloids, which gradually dehydrate/polymerize to mixtures of $Pu(OH)_4(am)$ and (or) $PuO_2(am)$, which, in turn, eventually go on to $PuO_2(c)$ (Hobart et al. 1989, pp. 118 to 124; Clark 1994, p. 9). The final aged form should be $10^{6.6}$ times less soluble than $Pu(OH)_4(am)$, but modeling suggests that even aged $PuO_2(c)$ contains $Pu(OH)_4(am)$ units on its surface, lessening

this effect (Efurd et al. 1996, p. 7, Table 2). Mobility of the suspended radiocolloid and Pu-particle sorption (pseudocolloids) form can be significant, especially in highly fractured matrices in which filtration, redox reactions, and so forth are of diminished importance (Penrose et al. 1990; Triay, Simmons et al. 1995). Oxidation states can redistribute through disproportionation (e.g., Pu [V] disproportionates to Pu [IV] and Pu [VI] in acidic conditions at a rate inversely proportional to $[pH]^4$ [Newton 1975]) and from radiolysis effects. These radiolysis effects can cause either reduction (Cleveland 1979a, 1979b) or oxidation (Runde and Kim 1994) to occur, depending on the initial plutonium oxidation state and the chemical composition of the solution. As with Am, radiolysis can also complicate the solubility measurements due to radiation damage of the solubility-limiting solid.

In the solution phase, dilute Pu solutions expected in the environment are likely to have a distribution of oxidation states dominated by the +5 oxidation state, although Langmuir (1997, Figure 13.30) shows a large region of predominance for $Pu(OH)_4^0(aq)$ in the Eh-pH diagram for dilute Pu. As for Np (V), PuO_2^+ does not readily hydrolyze (Bennett et al. 1992, p. 18), in sharp contrast to the other oxidation states (Lemire and Tremaine 1980; Lemire and Garisto 1989; Langmuir 1997). Hydrolysis of the other plutonium oxidation states is high, occurring by a pH of 5 for PuO_2^{2+}, a pH of approximately 1.5 for Pu (IV), and a pH of approximately 8 for Pu (III). Plutonium (IV) undergoes extremely strong hydrolysis, leading to the universally seen formation of radiocolloids at neutral pHs and Pu concentrations greater than approximately 10^{-7} M (Nitsche et al. 1993). All oxidation states have strong complexes with carbonate (Langmuir 1997), cutting into the Pu^{3+} and $Pu(OH)_4^0$ predominance zones even at relatively low total carbonate concentration (10^{-2} M).

Americium–As noted above, in the 1- to 10-k.y. period, Am is, for a while, the largest contributor to radioactivity of the nuclear waste. Unlike other transuranic species, Am exists primarily in one oxidation state, namely as Am (III) (Silva et al. 1995, p. 73). The published Nuclear Energy Agency database for Am (Silva et al. 1995) puts Am and U alone as the actinides whose databases could be agreed upon. At least two complicating factors do exist for interpreting Am data. Like Pu, Am can also exist in colloidal form (Penrose et al. 1990; Bates et al. 1992), so phase separation of truly soluble species is problematic, and there is another route for radionuclide migration. Furthermore, because ^{241}Am is intensely radioactive, it is difficult, if not impossible, to form a good crystalline solid as the solubility-controlling phase.

Americium (III) forms strong hydroxo, carbonato, and, for solids, mixed hydroxo-carbonato species (Silva et al. 1995, pp. 151 to 166). Important solution species at a P_{CO_2} of $10^{-3.5}$ bar (atmospheric CO_2, producing water similar to J-13 at pH values between 7 and 9) include, with pH increasing from a pH of 6, Am^{3+}, $AmOH^{2+}$, $AmCO_3^+$, $Am(OH)_2^+$, $Am(CO_3)^{2-}$, and, beyond a pH of 9, $Am(CO_3)_3^{3-}$ (Silva et al. 1995). The only solid found in Yucca Mountain experiments in J-13 water was $AmOHCO_3$ (Nitsche et al. 1993), consistent with the large stability field of this solid over different values of pH and P_{CO_2} (Silva et al. 1995). Other important solids include $Am(OH)_3(c)$ ($\log P_{CO_2}$ less than –4, pH greater than 7.5) and $Am_2(CO_3)^3$ ($\log P_{CO_2}$ greater than –1, neutral pH) (Runde et al. 1992). Solubilities in Yucca Mountain-specific waters are discussed below. Thermodynamic studies of $AmOHCO_3(c)$ at room temperature and $P_{CO_2} = 10^{-3.5}$ bar by Felmy et al. (1990, p. 196, Figure 2) show a solubility of $10^{-7.5}$ to $10^{-8.5}$ M

for pH values from 6.5 to 9. Above a pH of 9, the solubility increases due to the formation of $Am(CO_3)_3^{3-}$ in solution.

10.1.2 Mineralogy and Strata Characteristics Affecting Radionuclide Transport

The two predominant modes of alteration in Yucca Mountain tuffs are (1) devitrification of the central portions of ash flows to form fine-grained assemblages of feldspars and silica minerals (quartz-tridymite-cristobalite) and (2) zeolitization, principally in the margins of ash flows. The first corresponds with the syngenetic alteration described in Section 5.2.1.1; the second is the principal mode of diagenetic alteration described in Section 5.2.1.2. Those tuffs that have experienced neither syngenetic nor diagenetic alteration retain most of their original glass (vitric tuffs).

Both Na and Ca in clinoptilolite exchange readily with a wide range of potential radionuclides, including Cs, Rb, Sr, and Ba (Ames 1960; Breck 1984, pp. 529 to 588). Potassium, on the other hand, is more difficult to remove from the clinoptilolite structure, exchanging well with Cs and Rb but exchanging poorly with Sr and Ba (Ames 1960). Although the compositional effects are most important for sorption of simple cations in solution, studies for the Yucca Mountain Site Characterization Project have focused on the utility of zeolitic horizons in retarding transport of complex transuranic species, most of which are poorly sorptive. Modeling by Robinson et al. (1995) illustrated the cumulative importance of thick zeolitic horizons in Np sorption; moreover, the data available at present indicate that the compositions of zeolitic rocks may also be an important factor, with Na-K clinoptilolite providing about twice the Np sorption capability of Ca clinoptilolite. The modeling done by Robinson et al. (1995) assumed a Np distribution coefficient (K_d) range of 1.1 to 3.9 for zeolitic rock in the unsaturated zone; in that report, it was concluded that there was no further need for Np sorption studies of vitric and devitrified tuffs, because the impact of the tuffs was negligible. However, a later report (Triay et al. 1997, pp. 85 to 86) assigned the most effective (i.e., larger) Np K_ds to iron-oxides anticipated from corrosion of the multipurpose container (assuming that such a container is actually used and emplaced at the Yucca Mountain site) and assigned the smallest maximum Np K_d for the natural site lithologies in the unsaturated zone to zeolitic tuff (unsaturated zone Np maximum K_ds were assigned as 15, 6, and 3 mL/g for vitric, devitrified, and zeolitic tuff respectively [Triay et al. 1997, pp. 85 to 100]). Despite differences in the assignment of K_ds for these different lithologies in various models, the dependence of model results on lithologic type remains. Furthermore, variations in geochemical properties, such as exchangeable-cation composition in zeolites, remain a factor to be considered.

In the unsaturated zone, exchangeable cations within clinoptilolites on the western side of the exploratory block consist primarily of Na and K (Broxton et al. 1986, p. 22). Clinoptilolites in the unsaturated zone on the eastern side of the exploratory block have mixed Na-K and Ca-K compositions. In the saturated zone, clinoptilolite compositions tend to become more sodic with depth on the western side of Yucca Mountain and more calcic with depth to the east (Broxton et al. 1986, p. 22). If, as Robinson et al. (1995) suggested, the alkali zeolites are more effective in Np sorption than the Ca zeolites, it might be important to add chemical variation as a parameter, along with overall abundance of zeolites, in modeling radionuclide transport. In this case, the initial results for Np suggest that the western part of Yucca Mountain might have more effective zeolite barriers, volume for volume, than the eastern part of Yucca Mountain.

Ultimately, the mineralogy at Yucca Mountain must also be evaluated in four dimensions. The fourth dimension is the possible alteration of mineralogy over time that may affect the way in which waste will or will not interact with the rock. Present rates of alteration at Yucca Mountain are probably low. Geopetal and stable-isotope studies indicate that the major zeolitic intervals near and below the water table formed in the Miocene soon after tuff eruption (Levy 1984, 1991) and have probably altered little since. This situation, however, could be significantly changed in rocks within tens of meters to several hundred meters of the potential repository if high-level radioactive waste is emplaced without prior cooling, and temperatures around the repository are held at or above approximately 100°C for time spans of approximately 1 k.y. (Levy and O'Neil 1989; Bish 1989; Buscheck and Nitao 1992, Figure 18; Bish and Aronson 1993, p. 159).

10.1.3 Fluid and Geochemical Characteristics Affecting Radionuclide Transport

10.1.3.1 Chemical Composition

In general, as described in (Section 5.3.6) unsaturated zone pore waters have higher total dissolved solid concentrations than perched or saturated zone waters, reflecting the low surface infiltration rates. The variability in the dissolved-solids content of the shallowest nonwelded unit, the Paintbrush nonwelded (PTn) unit, directly reflects the spatial variability of surface infiltration rates. This close relationship between infiltration rates and pore-water chemistry is reflected in the fact that infiltration rates calculated on the basis of the chloride-balance method are generally consistent with rates calculated on the basis of physical methods.

Most of the major chemical characteristics of the pore waters appear to be established by soil-zone processes—predominantly evapotranspiration and dissolution or precipitation of pedogenic calcite and amorphous silica—such that pore waters entering the bedrock are nearly always saturated with respect to these two phases. Major ion compositions of deeper pore waters indicate that water-rock reactions are very restricted during percolation through the unsaturated zone. Relative abundances of cations are altered through ion-exchange reactions with clays and zeolites along the flow paths, which results in pore waters in the Calico Hills nonwelded (CHn) unit that become increasingly stronger Na (carbonate+bicarbonate) type waters with increasing depth. Significant lateral movement of water within the CHn unit is implied by the fact that chemical compositions in the CHn are generally similar within a given stratigraphic unit and markedly different between different host lithologies in any given borehole.

10.1.3.2 Isotopic Composition

Isotopic compositional studies are discussed in Section 5 of this report.

If the sampled depth is more than a few meters, the presence of global-fallout nuclides implies a component of fracture flow. Hence, these isotopic data provide a means for estimating the extent to which solute transport is retarded by diffusion from fractures into the adjacent matrix.

Tritium–Detectable levels of tritium have been observed along major structural features in Exploratory Studies Facility (ESF) drill holes and in pore waters extracted from core samples from surface-based boreholes. These detections occur predominantly within the PTn unit, but also in some of the samples from the Topopah Spring Tuff and Calico Hills unit, and as deep as the Prow Pass member of the Crater Flat Tuff.

Chlorine-36–Bomb-pulse concentrations have been reported in the PTn at several locations and in the vicinity of some fault zones in the ESF (Fabryka-Martin, Wolfsberg et al. 1997, p. 78; Fabryka-Martin, Flint et al. 1997, pp. 6-22, 8-18). Bomb-pulse ^{36}Cl does not appear to be present in perched water or groundwater from the site. A validation only of ^{36}C is underway (see Section 5.3.7.3.3 for details).

Carbon-14–Elevated ^{14}C levels, indicating a bomb-pulse component, are present in the Topopah Spring welded unit or the CHn in four of the six surface-based boreholes sampled to this depth. Carbon-14 ages of the gas phase increase with depth in UZ-1, and the measured profile is consistent with gas-transport modeling of downward movement of atmospheric CO_2 by simple Fickian diffusion. In other boreholes, the trends are less clear. Rock gas does not appear to be in isotopic equilibrium with the pore waters with respect to C isotopes.

Carbon-13–Relative to stable C isotope ratios in the atmosphere, most pore-water samples are isotopically light. This signature suggests that these pore waters have been influenced by biogenic processes, probably in the soil zone.

Deuterium and Oxygen-18–Isotopic compositions of H and O in Yucca Mountain groundwaters to the south of the site tend to be isotopically lighter than those farther to the north or east, suggesting that recharge occurred under cooler climatic conditions. Similarly, for unsaturated zone waters, lighter values for CHn pore waters suggest that much of the water at this depth originated either during winter precipitation or during a time of colder climate, as compared to the origin of pore water in the PTn.

10.1.3.3 Flow Paths

Geochemical and isotopic data in waters from the unsaturated zone and saturated zone are consistent with a flow model in which all unsaturated zone waters, including perched waters, originate at the surface of the mountain. Although flow paths appear to be predominantly vertical, there is evidence that suggests lateral flow in some units. The isotopic data further provide evidence of water that has flowed rapidly to at least the depth of the ESF, presumably along pathways that included fractures and/or faults. The available hydrochemical data, on the whole, suggest that the bulk of water in the unsaturated zone moves through the matrix, and the portion moving through fractures is small.

10.1.3.4 Infiltration Rates

Apparent infiltration rates were estimated by the chloride mass-balance method, using chloride concentrations for pore-water samples from surface-based boreholes, ESF drill holes, and Cross Drift drill holes. Apparent infiltration rates in the PTn were generally higher than the rates estimated for alluvium, presumably due to lateral flow and mixing within this unit. Nonetheless, the rates appear to be roughly correlated with surface topography. PTn samples beneath deep alluvium had infiltration rates between 0.6 and 3.3 mm/yr. PTn and Topopah Spring welded unit pore waters beneath sideslopes and ridgetops, which have thin alluvial cover, had average infiltration rates between 5 and 8 mm/yr. in the northern half of the study area (e.g., Cross Drift, North Ramp, Main Drift up to Station 45+00), but only about 1 mm/yr. in the southern half (ESF

South Ramp). The overall average infiltration rate for pore-water samples collected along the Main Drift and Cross Drift (30 samples) is about 6 mm/yr.

10.1.3.5 Perched Water

Based on ^{14}C and ^{36}Cl aging studies, perched water samples appear to be up to 11 ka, which favors the idea that perched water bodies reflect an earlier period of increased infiltration rates. Major ion concentrations and U isotope data suggest that these bodies were formed by water flowing through fractures in the unsaturated zone rather than through the matrix. The fact that these waters do not appear to have equilibrated with water in the matrix of units in which the perched water bodies are found also supports a distinct origin (e.g., fracture flow) and very slow exchange between fracture and matrix reservoirs.

10.1.3.6 Implications for Repository Performance

The chemistry of water is a potentially important factor in radionuclide transport because it influences the solubilities of radionuclide compounds that form and because it influences the sorption behavior of the radionuclides. Because most flow paths that would produce water in the potential repository horizon will likely represent fracture flow paths, the water compositions may be more dilute than those of matrix pore waters. If infiltration rates increased in the site area as a result of a climatic shift, these compositions would likely become even more dilute, presumably more like the perched-water compositions. The pH of these waters should be near neutral.

Pore-water compositions combined with ^{14}C age data indicate that ion exchange processes operate on vertically migrating young pore waters in the CHn. This suggests that ion exchange processes would also operate on any radionuclides released from the potential repository into aqueous solutions that migrate vertically into the zeolitic CHn.

INTENTIONALLY LEFT BLANK

10.2 SOLUBILITY AND SPECIATION STUDIES

10.2.1 Data Sources

Measurements (Efurd et al. 1996) have shown that the bulk solubility of Np in J-13 water ranges from 6×10^{-6} to 1×10^{-3} M. These results are generally an order of magnitude lower than those of earlier reports (Nitsche, Gatti et al. 1993). This difference has been attributed to the artificially higher ionic strength in the earlier studies caused by continual pH control. Some models, depending on the Np database employed, have predicted Np (IV) as the predominant oxidation state in Yucca Mountain waters, which, if true, would lower the ultimate solubility of Np by several orders of magnitude. However, the oxidation state of Np in the later study still points to Np (V) as the predominant species (Efurd et al. 1996), albeit a different solid than reported in the earlier study (Nitsche, Gatti et al. 1993). Whether this Np (V) solid is the equilibrium state or a kinetically controlled state has not been determined. Similarly, the more refined solubility measurements of Efurd et al. (1996, Table V) found lowered variability and lowered Pu solubility in J-13 water, although the difference between the two studies was less pronounced than for Np. The solubility data for Np and Pu from Efurd et al. (1996) are considered more reliable than those of Nitsche, Gatti et al. (1993) because they have an ionic strength closer to that expected for groundwater at Yucca Mountain and because the solids were better characterized.

For Am, the existing solubility and sorption data are difficult to interpret, at least partly because they were performed in Yucca Mountain conditions using Am as a tracer in Nd/Am solutions (Nitsche, Gatti et al. 1993; Nitsche, Roberts, Prussin et al. 1995). Radiation damage of a pure Am solid may preclude the formation of the stable solid indicated in the Yucca Mountain studies. Trivalent actinides are known to be more soluble than the analogous lanthanide (III) compounds (Runde et al. 1992).

10.2.2 Solubility in Yucca Mountain Relevant Waters

The Yucca Mountain Site Characterization Project (YMP) requires "studies to provide the information required on radionuclide retardation by precipitation processes along flow paths to the accessible environment" before licensing and construction of the project (DOE 1988). This study summarizes data for calculating radionuclide transport along potential transport pathways from the repository to the accessible environment. In selecting these experiments, the U.S. Nuclear Regulatory Commission generic technical position entitled "Determination of Radionuclide Solubility in Groundwater for Assessment of High-Level Waste Isolation" was considered (NRC 1984). This technical position served as guidance for experiments to determine radionuclide solubility. It requires that if radionuclide solubility is used as a factor in limiting radionuclide release, experiments must be designed to determine solubility under site-specific conditions. To predict behavior at higher temperatures expected in the near field of a potential repository, databases used for modeling calculations must contain data on thermodynamic functions at elevated temperatures. To date, many of these data are unavailable and are therefore estimated by extrapolation from lower temperature data.

Radionuclide concentrations in water passing through the emplacement area can be limited by two mechanisms: low dissolution rates of the solid waste form, and solubility of individual

radionuclides. If solid waste dissolution rates are low enough, it might not be necessary to depend on the solubility to limit radionuclide concentrations. In other words, the amount of a radionuclide dissolved in solution could be limited by the amount of that radionuclide freed from the solid waste form by the dissolution of the waste form. Alternatively, determination of radionuclide solubility limits provides an upper bound on radionuclide concentrations in solution and a basis for "extrapolation to long-term behavior." The rate of groundwater flow through the waste is expected to be sufficiently slow to permit saturation of water with radionuclides freed from the waste form. Dissolution limited by saturation will provide maximum concentration limits. Therefore, an assessment of radionuclide release rates using a saturation-limited dissolution model represents the most conservative approach possible for solution transport (Dozol and Hageman 1993, Sections 1 to 2).

The range of water conditions at Yucca Mountain (dominating solubility and speciation effects) effects is generally anticipated to be in the pH range from 6 to 8.5, but contact with cement or backfill may push the pH higher (up to 11). This possibility is examined in detail in Section 11.4. Ionic strength of groundwaters in the western United States is generally low, and J-13 and UE-25 p#1 waters are low-ionic-strength waters that are considered to be representative of potential Yucca Mountain waters (Ogard and Kerrisk 1984). Future considerations of repository loading (e.g., thermal loading) might cause groundwaters to be refluxed and, hence, affect the ultimate ionic strength that could contact the waste. This is discussed in Section 11.4. The effects of salts from such waters on canisters of salts combined with humidity as the repository cools are also considered in Section 11.4.

The solubilities of Np and Pu in J-13 groundwater from the Yucca Mountain region at three temperatures and three H-ion concentrations were studied best by Efurd et al. (1996). The actinide solubilities were determined from oversaturation at 25°, 60°, and 90°C and initial pH values at 6.0, 7.0, and 8.5. Tables 10.2-1 and 10.2-2 summarize the results. Sample evaporation was minimized to maintain the ionic strength of the solutions as close to that of J-13 water as practical for the duration of the experiments. The pH of each solution was initially adjusted at the start of the solubility experiments; no pH adjustments were performed during the year that the solubility experiments were conducted. In general, the Np solubilities decreased with increasing pH and temperature. The steady-state solids were greenish brown in color. X-ray diffractometry identified a mixture of Np compounds. Crystalline Np_2O_5 and a salt of Np were identified. Plutonium was less soluble than Np. In general, Pu solubility decreased with pH and decreasing temperature. The solubility-controlling, steady-state solids were dense green crystals that produced X-ray diffraction patterns indicative of a mixture of amorphous and crystalline materials. The relative amount of crystalline solid (PuO_2) increased with temperature.

The solution behavior of the element Pu is the most complicated of all the elements of interest and the least understood, particularly in near-neutral solutions representative of water compositions expected within the Yucca Mountain flow system. Plutonium can have several oxidation states in a given solution, and it can form complexes with a variety of ligands.

According to Nitsche, Gatti et al. (1992, Figures 19, 20, 21, Table 17) and Nitsche, Roberts, Prussin et al. (1995), Pu will be present in the +3, +4, +5, and +6 oxidation states in solutions representative of water compositions expected within Yucca Mountain. The +5 and +6 oxidation states should predominate in solution at redox potentials in the range of 230 to 350 mV. In J-13

and UE-25 p#1 waters, the +5 oxidation states should be dominant (60 to 80 percent) at 25°C. Most of the remaining Pu in solution is in the +6 oxidation state in J-13 water and the +4 oxidation state in UE-25 p#1 water.

Experimentally determined solubilities range from 3.0×10^{-7} to 1.0×10^{-6} M at 25°C. The solubility-controlling solids were found to be mixtures of polymeric Pu (IV) and smaller amounts of plutonium carbonates. The solubilities measured at pH values of 6 and 7 are consistent with the data reported by Rai, Serne et al. (1980). However, the solubilities measured for a pH of 8.5 exceed those reported by Rai, Serne et al. (1980, Table 2) for amorphous $Pu(OH)_4$ in 0.0015 M $CaCl_2$. This result suggests that carbonate complexation of Pu is significant at a pH of 8.5 in Yucca Mountain groundwaters.

At 60°C, the +6 oxidation state was dominant (more than 80 percent) in the UE-25 p#1 water at all three pH values. In J-13 water, the +5 and +6 oxidation states were present in nearly equal amounts (50 percent) at a pH of 7, whereas the +5 state dominated (60 percent) at a pH of 8.5 and the +6 state dominated (70 percent) at a pH of 6.

Experimentally determined solubilities at 60°C in J-13 water ranged from 2.7×10^{-8} M at a pH of 6 to 1.2×10^{-7} M at a pH of 8.5. For UE-25 p#1 water, the solubilities ranged from 4.5×10^{-7} M at a pH of 7 to 1.0×10^{-6} M at a pH of 8.5. The solubility-controlling solids at 60°C were found to be amorphous Pu (IV) polymer and PuO_2.

Finally, there are Am solubility values for Yucca Mountain site-specific conditions as well (Nitsche, Gatti et al. 1993). As noted above, these experiments were done ultimately at high ionic strength and with Am as a tracer in a Nd-Am mixture. Given that the solubility-limiting solid state is $AmOHCO_3$, the effect of the ionic-strength differences should be relatively small, and these numbers (Table 10.2-3) are the best site-specific values available. However, some outliers, especially at 60°C, should be viewed with caution. In general, though, these site-specific numbers are similar to or slightly less than the thermodynamic values measured by Felmy et al. (1990, pp. 196 to 198) for $P_{CO_2} = 10^{-3.5}$ atm.

According to Nitsche, Gatti et al. (1992, pp. 73 to 75) and Nitsche, Roberts, Prussin et al. (1995), the solubilities of Am compounds in solutions representative of groundwater compositions expected within Yucca Mountain are approximately 1×10^{-9} to 2×10^{-9} M in J-13 water and 3×10^{-7} to 30×10^{-7} M in UE-25 p#1 water as a function of pH at 25°C. At 60°C, the solubilities of Am compounds were 1×10^{-8} to 2.5×10^{-6} M in J-13 water and 7×10^{-10} to 3×10^{-9} M in UE-25 p#1 water as a function of pH. The solubility-controlling solids were found to be hexagonal and orthorhombic forms of $AmOHCO_3$. The speciation of Am in these solutions could not be determined due to the low solubilities of Am in these water compositions relative to the detection limits of the available spectroscopic techniques. Preliminary modeling calculations with the speciation code EQ3 suggest that carbonate complexes dominate in both J-13 and UE-25 p#1 waters at 25°C and 60°C (Ogard and Kerrisk 1984).

10.2.3 Solid State and Solution Speciation

The solubility-limiting solid of Yucca Mountain solubility experiments have been characterized with X-ray diffraction, Raman vibrational, and X-ray absorption techniques. For Np, the sodium

neptunyl carbonates found in earlier studies (Nitsche, Gatti et al. 1993) are unlikely to be formed in the low-ionic-strength J-13 water. Other Np (V) solids, such as Np_2O_5 and/or $NpO_2OH(am)$, have been indicated to be the solubility-limiting solid phase in J-13 (Efurd et al. 1996). No evidence for Np (IV) solids, such as NpO_2, has been observed yet, even though thermodynamic modeling suggests that NpO_2 is the most stable solid (see Section 10.2.4). The solution species are dominated by two species, NpO_2^+ and $NpO_2CO_3^-$, at about equal proportions for a pH of 8.5 in J-13 water. For Pu, the solid phase is best described as poorly crystalline PuO_2, with higher crystallinity for the higher-temperature solutions (Efurd et al. 1996, p. 40). The presence of $Pu(OH)_4(am)$ is also possible, especially on the surface of the precipitate (see modeling in Section 10.3), as is the presence of a binary oxide containing Pu (VI) (Stakebake et al. 1993; Haschke and Ricketts 1997, p. 148). The solution phase contains several oxidation states (Nitsche, Gatti et al. 1993), including a Pu colloid with an unknown Pu oxidation state. Much of the colloid was filtered out of the solution before counting and was therefore not included in the soluble Pu concentration figures. Finally, the Am precipitation solid has been reported to be $AmOHCO_3$ (Nitsche, Gatti et al. 1993), although the presence of two different phases (orthorhombic and hexagonal) may require further scrutiny. Also, the trace nature of the Am in these experiments must always be kept in mind: the Np phase was what was determined.

10.2.4 Thermodynamic Modeling

Different databases for Np exist. Using the Lemire-based data accepted into GEMBOCHS (a thermodynamic database used to generate data for EQ3/6 by the YMP), NpO_2 is always the most thermodynamically stable solid in J-13 for pH values from 6 to 9 and temperatures from 20° to 90°C (Janecky, Duffy et al. 1997, p. 2; Janecky, Enter et al. 1995; Efurd et al. 1996, pp. 27 to 30). This stability extends to an ionic strength of 0.1 M, at which point the sodium neptunyl carbonate becomes stabilized. Other solids of calculated importance include (in decreasing importance) $Np(OH)_4$ (the hydrated amorphous form of NpO_2), $NpO_2OH(am)$, and Np_2O_5 (the observed bulk solid). More recent calculations show that Np_2O_5 is a more reasonable choice for the solubilities actually measured and that Np (IV) solids do not have to be invoked to explain the solubility data (Efurd et al. 1996). The predicted solubility of $PuO_2(c)$ is orders of magnitude below what is actually measured (Efurd et al. 1996, Table VII), but the predicted solubility of $Pu(OH)_4(am)$ is about right. It may be that although the bulk of the precipitate is $PuO_2(c)$, the surface is coated to some extent with $Pu(OH)_4$, and this latter solid is the solubility-controlling one. Radiation damage to any real Am solid would introduce an added uncertainty. However, modeling shows that $AmOHCO_3(c)$ is just about at saturation for the experimental conditions reported by Nitsche, Gatti et al. (1993), whereas $Am(OH)_3(c)$ and $Am(OH)_3(am)$ are both significantly undersaturated (Janecky, Duffy et al. 1997, p. 2).

Because the Nuclear Energy Agency has published critically reviewed data for U, Am, and Tc, this tabulation includes only the GEMBOCHS data for Np and Pu, with the Np section modified only slightly in recognition of YMP work on neptunium (V)-carbonate thermodynamic constants.

Selection of Data for Performance Assessment–The values quoted in Tables 10.2-1 to 10.2-3 represent the best available site-specific solubilities for use in the total system performance assessment for Pu and Am. The values chosen were from Nuclear Energy Agency sources (Grenthe et al. 1992; Silva et al. 1995), YMP quality assurance sources tested with specific-ion

interaction theory (e.g., Tait, Clark et al. 1996), and literature sources (e.g., Langmuir 1997, Sections 13.4 to 13.5). Note that the use of Efurd et al. (1996) values for Np and Pu gives more consistent and smaller values than those of Nitsche, Gatti et al. (1993), which have been used in performance assessment calculations to date. For oxidizing waters such as those expected at Yucca Mountain, radionuclide mobility cannot conservatively be limited by solubility for Tc and I. Uranium is an interesting case, and the solubility depends on the secondary phase that will precipitate. Langmuir (1997) favors the view that U solubility will be limited by the formation of uranophane ($Ca(H_3O)_2(UO_2)_2(SiO_4)_2{\cdot}3H_2O(c)$) to be about 10^{-7} M at Yucca Mountain. Other phases could also be suggested as potential controls on U. For example, in the high-silica groundwaters of Yucca Mountain, the solubility-controlling compound for U could be haiweeite ($Ca(UO_2)_2(Si_6O_{15})(H_2O)_5$), according to available thermodynamic data (Bruton 1991, p. 11). Interestingly, leaching experiments on uranium-oxide pellets (Bates, Tani et al. 1990, Table II) at 90°C using J-13 water produced a variety of phases on reacted surfaces that did not include haiweeite.

Ultimately, total system performance assessment requires that radionuclide solubilities be extracted to simple terms that can be dealt with efficiently. Table 10.2-4 indicates the selection of solubility values for radionuclides of concern. The elements listed include relevant radionuclides whose source terms could be solubility limited. The values used are from expert elicitations, primarily as cited by Triay, Meijer, Conca et al. (1997) and Langmuir (1997, Sections 13.4 to 13.5) but also Rechard (1995). These values have been updated with some new experimental data from Efurd et al. (1996).

INTENTIONALLY LEFT BLANK

10.3 SORPTION AND SORPTION MODELING STUDIES

Radionuclide migration from the potential repository would be inhibited by several barriers, including the geochemical retardation due to limited of solubility and sorption. Sorption coefficients for radionuclides of interest were obtained using water and rock samples from the site. Sorption coefficients were obtained in batch experiments performed at several pH levels to evaluate the impact of pH variations on the sorption coefficient. In general, oxidation-reduction (redox) conditions were oxidizing in all the experiments. The potential effects of organics on actinide sorption were evaluated in batch experiments with model organic compounds in water and rock samples from the site. Models were developed to explain the sorption coefficient data and to allow prediction of coefficient values under anticipated conditions.

10.3.1 Important Minerals and Strata in Radionuclide Interactions

Zeolites–The large sorptive capacity of zeolites for certain cations provided part of the initial impetus for considering altered tuffs for the disposal of radioactive waste. Radioactive alkali and alkaline-earth cations (Sr, Cs) in particular are strongly selected in exchange for the Na, Ca, and K loosely held in the zeolites clinoptilolite and mordenite. Work summarized by Thomas (1987, pp. 16 to 21) confirmed the sorptive capacity for Sr and Cs but also indicated a much lower sorptive capability for the longer-lived transuranic elements (especially Pu and Np). Nevertheless, ^{135}Cs is a radioactive isotope that may be abundant in the emplaced waste and has a long half-life (3 m.y.). This half-life is much longer than the expected life of the waste canisters, and ^{135}Cs alone is sufficient to make zeolites an important component of the natural barrier.

Clinoptilolite and mordenite are the most abundant zeolites at Yucca Mountain. Major stratigraphically continuous intervals of clinoptilolite occur in all drill holes, from approximately 100 to 150 m (328 to 492 ft) above to approximately 500 m (1,640 ft) below the water table (Section 4.8.4). Mordenite often occurs along with clinoptilolite but is less abundant in drill holes farther south. The zeolite analcime occurs as a prograde alteration product at greater depth, but the depths of analcime occurrence are so great that little interaction with waste is likely. The zeolitic intervals are strongly controlled by tuff stratigraphy; zeolites have commonly formed from the glasses of nonwelded and bedded intervals, between those portions of the tuffs that devitrified, to form feldspars and silica minerals soon after emplacement.

The zeolite mineral chabazite is generally rare at Yucca Mountain. However, samples from the Calico Hills Formation in USW SD-7 have significant amounts (up to 9 percent) of chabazite in this zeolitized interval, occurring principally in a 45-ft-thick (14-m-thick) clinoptilolite + chabazite zone above a clinoptilolite + mordenite zone. The occurrence of chabazite provides information about geochemical conditions that existed during its formation. Chipera et al. (1995) used representative chemical formulas and estimated thermodynamic data to model the conditions under which the various zeolite species at Yucca Mountain formed. Chemical analyses of modern Yucca Mountain groundwater using present-day silica activities were found to plot within the predicted clinoptilolite stability field. A stability field for chabazite occurred only for groundwater compositions that were significantly more potassic than present Yucca Mountain groundwaters. Decreases in aqueous silica and Na activities and increases in temperature also enhance the stability field for chabazite. Despite the unusual abundance of

chabazite in SD-7, the principal sorptive zeolite mineral at Yucca Mountain remains clinoptilolite, followed by mordenite in abundance.

In addition to clinoptilolite, mordenite, analcime, and minor chabazite, restricted occurrences of a few other zeolites have been found at Yucca Mountain. Heulandite and stellerite are common in fractures of the Topopah Spring Tuff, with stellerite being particularly common in both fractures and matrix of the Topopah Spring Tuff in drill hole UE-25 UZ#16 (Sections 2 and 3). Phillipsite and erionite have a very restricted occurrence in the zone of alteration above the water table at the top of the basal vitrophyre of the Topopah Spring Tuff, as well as in the adjacent unsaturated fractures (Carlos et al. 1991; Bish and Chipera 1991, pp. 433 to 444). Laumontite occurs in very small amounts (less than 4 percent) in deep, altered tuffs of drill hole UE-25 p#1 and perhaps in USW G-1 (Bish and Chipera 1989, p. 1, Abstract).

Temperature can be an important factor affecting radionuclide exchange in zeolites. In dilute solutions, sorption ratios rise with an increase in temperature (Meijer 1990, p. 17). This result is in accord with conclusions concerning cation-exchange behavior based on measurements of zeolite electrical properties at various temperatures and salinities (Olhoeft 1986). However, Olhoeft's (1986) study of clinoptilolite conductivity behavior also indicated that the increase in cation-exchange capacity with temperature is reversed at high salinities. The sorption-enhancing effects of temperature at low water/rock ratios may thus be minimal, and other thermal effects (e.g., zeolite dehydration or rehydration, weakening of heated zeolitic rocks) become more critical in evaluating the consequences of high-level waste emplacement.

Clays–Smectite occurs in virtually all samples, typically in amounts less than 2 percent. However, above the water table, there are two continuously mappable zones of up to 75 percent smectite alteration in the Paintbrush Tuff: one near the top of the vitric nonwelded base of the Tiva Canyon Tuff and one at the top of the basal vitrophyre of the Topopah Spring Tuff. These smectites typically have nonexpandable illite contents of 10 to 20 percent. Well beneath the water table, an ancient (about 10.7 Ma) hydrothermal system at depths greater than 1,000 m contains abundant smectite/illite but with a much higher illite content (about 80 to 90 percent) (Bish 1989). These illitic clays have a higher fixed layer charge, which reduces their effective cation-exchange capacity; however, they occur at such great depths that they are of little importance for transport modeling at Yucca Mountain.

Iron, Manganese-Oxides, and Hydroxides–Hematite is the most ubiquitous oxide mineral at Yucca Mountain. It occurs in several forms and associations, principally within the matrices of glassy, devitrified, and zeolitized tuffs, but also within fractures. The main occurrences are (1) as a product of exsolution-oxidation of magnetite or ilmenite phenocrysts; (2) as an alteration of iron, magnesium-silicate phenocrysts (mostly of biotite); (3) as a vapor-phase mineral; and (4) as a product of later low-temperature alteration (e.g., small grains or splays in zeolitized tuffs). Typical abundances in most tuff samples are about 1 percent by weight in tuff matrices, with locally greater abundance in many fractures (Carlos et al. 1991). Although studies with pure synthetic hematite can result in high sorption of actinides, experiments with iron-oxides from Yucca Mountain show little of this effect, probably because of "passivation" of surface sorption sites by other metals (Triay et al. 1993b). However, in microautoradiography studies of a sample from the upper part of the rhyolitic, devitrified Topopah Spring Tuff, the oxide minerals account for less than 1 percent of the tuff but hold 60 percent of the Pu track

concentrations. The oxide minerals that retain Pu have track clusters that are concentrated around the mineral edges and along internal fractures (distributions of tracks along fractures within these opaque grains can be seen in reflected light, through the film coating). This observation should be considered along with other evidence showing that grain-edge and vein alteration, in part due to manganese oxides that may be largely amorphous, is common around magnetite/maghemite phenocrysts. As with altered orthopyroxenes of the devitrified Prow Pass Tuff (discussed below), it is this peripheral and likely amorphous alteration rather than the original trace minerals that accounts for Pu accumulation.

In contrast with the evidence for general passivation of iron-oxides at Yucca Mountain, microautoradiography studies of manganese oxides from Yucca Mountain indicate a significant role for these minerals. Most manganese oxides have structures that allow only limited cation exchange (Bish and Post 1989, pp. 184 to 185), and these minerals are more likely to interact with radionuclide wastes by surface reaction mechanisms (Means et al. 1978, p. 1764). Although not volumetrically abundant, a large variety of manganese oxides occur in the Yucca Mountain tuffs. They are most widely distributed in fractures (Carlos et al. 1990, Tables 1, 11; 1991), but also occur within the groundmass of devitrified tuffs, mostly encircling and along microcracks radiating from oxidized magnetite and ilmenite phenocrysts. Above the water table, the principal manganese oxides are lithiophorite, rancieite, and todorokite; the principal cations in these minerals include Na, K, Ca, Ba, and Ce. Below the water table, cryptomelane-group minerals (hollandite, cryptomelane, coronadite) and lesser amounts of todorokite and pyrolusite occur. The principal cations in the cryptomelane-group minerals include K, Ba, Pb, Sr, Na, and Ca. The abundance and variety of exchangeable constituents in these minerals beneath the water table is evidence of their effective collection and retention of heavy elements, perhaps by surface complexation with later structural incorporation. This mineral group in particular is a key recorder of past water-rock interaction. Studies by Zielinski (1983, p. 7) and Zielinski et al. (1986) showed a strong correlation of leachable U with leachable Mn at Yucca Mountain; the correlation of leachable U with leachable Fe was much poorer, perhaps suggesting a greater heavy-metal adsorptive capacity for the manganese-oxides than for the iron-oxide minerals. However, it should be noted that some experiments (Milton and Brown 1987, p. 1327) have found that U is strongly retained by amorphous iron-oxyhydroxide, and desorption of U from these phases is limited.

Other Phases and Other Processes–Evidence of recent formation of opal, calcite, and perhaps some other phases (e.g., manganese oxides) suggests that even under ambient conditions, coprecipitation is a possible waste interaction. Precipitation of calcite is the mineralization most likely to be occurring above the water table at Yucca Mountain today. Calcite with U-series ages as young as 26 ka (Szabo and Kyser 1990, Table 2) and ^{14}C ages as young as 21 ka (Whelan et al. 1994, Table 2) has been found in fractures above the water table, making this the youngest directly dated mineral at Yucca Mountain. Szabo and Kyser (1990) also analyzed opals and found that all gave ages of more than 400 ka; however, fracture mineralogy studies (Carlos et al. 1991; Vaniman 1993a; 1993b, p. 1939) show that some opal deposits have formed on top of some calcites. This relationship leaves the possibility of some relatively recent opal deposition. Intergrowths of fracture calcite are also found with sepiolite, kaolinite, Ca-zeolite, and manganese oxides; palygorskite within fractures may also have formed relatively recently. The parageneses of fracture deposition suggest that calcite, opal, and some zeolites, clays, and manganese oxides were deposited under a variety of conditions beginning soon after tuff

emplacement, but that deposition of calcite and some of these other minerals may be continuing under ambient conditions or during Pleistocene episodes of greater flow through the unsaturated zone.

Some radionuclides leached from canisters could be coprecipitated with calcite under ambient conditions at Yucca Mountain. Those elements that substitute readily for Ca in the calcite structure at low temperature are limited to the divalent metals that are smaller than Ca (principally Mg, Fe, Mn, Cd, Zn, Co, and Ni). Larger metals and the larger alkaline earths (Sr, Ba) are incorporated in defects or upon transformation from orthorhombic carbonate structures. (Note: no evidence of orthorhombic carbonates has been found at Yucca Mountain). The abundances of these other elements, which are not defined by stoichiometry, can be sensitive to crystallization rate and to their chemical environment in solution. In aqueous solution, the partitioning of Sr into calcite can shift from distribution coefficients less than 1 to coefficients greater than 1 as the crystallization rate increases (Lorens 1981, p. 557). Cations that form carbonate complexes may also be readily incorporated and carbonate-complexed transuranic radionuclides can be precipitated along with calcite (Penrose et al. 1990). Meece and Benninger (1993, pp. 1455 to 1457) found that Pu sorbs readily onto calcite with little sensitivity to Pu oxidation state; their experiments also indicated that Am can be similarly incorporated into calcite. In experiments specific to Yucca Mountain samples and water compositions, calcite was found to be an important factor in retarding the transport of radioactive nuclides of lanthanides, Am, Pu, and, to a lesser extent, Np (GCX 1994, pp. 4 to 6). However, at present, the interactions of calcite with these elements are not readily predictable; "situational" distribution coefficients for these elements, dependent for various elements on speciation in solution, Eh, pH, and kinetics, are not yet reduced to routine calculation. Nevertheless, at a site like Yucca Mountain, where calcite deposits record a long history of water-rock interaction, it is possible to examine the incorporation of those elements that exist both in nature and in radionuclide wastes (e.g., Sr) and those like the lanthanides that are analogous to transuranic elements that do not provide a comparable geologic record. Results of such studies are summarized in Section 5.2.2.

The situation at Yucca Mountain during the period of interest (ranging about 100 k.y.) may not always be as it is now or has been in the recent past. One of the effects of any of the currently conceived potential repository designs at Yucca Mountain will be some form of thermal aureole caused by radioactive decay heating. The consequences of such heating on calcite saturation can be considerable, for even a small heat rise. With heating at constant pH, the rise in αSiO_2 is maintained by progressive dissolution of the least stable SiO_2 phases (opal, cristobalite/tridymite, then quartz). Conversely, αCa^{2+} is reduced by heating, through the precipitation of carbonates (or Ca-zeolites, if Al activity is sufficient) as temperature rises. At higher temperature, the calcite that forms is likely also to be more defect-rich, leading to increased incorporation of nonstoichiometric heavy metals, including lanthanides and the radioactive actinides that are likely to behave analogously to lanthanides. Under conditions of active calcite precipitation, entrapment of transuranics may become a significant process (Meece and Benninger 1993, pp. 1447 to 1458).

Opals in fractures of the unsaturated zone at Yucca Mountain are U-rich (Szabo and Kyser 1990, p. 1715). Coprecipitation of waste elements with silica might be a consequence, not of ongoing natural processes, but of silica dissolution and reprecipitation that are expected in the thermal aureole surrounding a repository. Dissolution of silica polymorphs or feldspar, the principal

constituents of devitrified tuff, or dissolution of vitrophyre glass might be a consequence of the migration of a condensation front through the host rock under a repository-induced thermal load (Section 11 of this report). This process may provide large amounts of silica for transport and deposition. Incorporation of U and other waste species into opaline precipitates may occur if waste releases occur while silica precipitation is occurring, particularly as part of the cooling process beneath the repository. Rimstidt et al. (1989, p. 587) tested a boiling water-vapor system in which silica and Fe were leached from the condensation zone and transported with the condensed liquid. Opal and iron-oxyhydroxide were precipitated near the condensation zone, but thicker deposits of these minerals with small amounts of stilbite and perhaps clay occurred adjacent to the underlying heat source. In a repository where boiling occurs, such phenomena may lead to extensive silica precipitation near the waste containers. If the silica remains opaline through the thermal pulse, then a relatively high silica activity of water may later transport waste from breached canisters and could lead to waste coprecipitation with opal.

Amorphous materials occur in the tuffs of Yucca Mountain and might have significant sorptive capabilities. Amorphous materials in altered orthopyroxene microphenocrysts account for less than 1 percent of the devitrified Prow Pass Tuff but hold 11 percent of the Pu track concentrations in this sample as determined by microautoradiography (Section 10.3.1.2). It is evident that it is the alteration features specific to the orthopyroxenes, rather than the unaltered pyroxene, that retain Pu; microautoradiography data from unaltered orthopyroxenes of the vitric Calico Hills Formation show no accumulation of Pu. Analysis of the chemical composition of the altered orthopyroxenes shows that amorphous Fe-rich vein in veins within the orthopyroxenes is particularly active in Pu retention.

Stratigraphic Factors–The descriptions of samples used in sorption studies include information on stratigraphic horizon as well as lithology. Table 10.3-1 shows the lithologic stratigraphy and 10.3-1 the number of different samples from each unit that have been used in sorption studies. In addition, the geochemically distinct units that are quartz-latitic in composition are shaded. The quartz-latitic units stand out in comparison with the generally rhyolitic compositions of the other units (Figure 5.2-1). The importance of distinctions between rhyolitic and quartz-latitic units is discussed in Section 10.3.1.1.

10.3.1.1 Mineralogy of Sorption Experiments

Quantitative X-ray diffraction analyses and chemical data show that the Yucca Mountain rock samples used in sorption studies can be categorized into three principal rock types, although subdivisions of these three types should be considered in evaluating the results of sorption experiments. The first rock type is devitrified tuff, characterized by prominent feldspar associated with tridymite, cristobalite, and/or quartz, often with minor amounts of hematite and smectite. For reasons discussed in this section, the composition of the devitrified tuffs (rhyolitic or quartz latitic) should also be distinguished. The second major rock type is zeolitic tuff, generally characterized by abundant clinoptilolite, less often associated with abundant mordenite, and rarely by chabazite and/or one of several lesser zeolites (Section 10.3.1). Zeolitic tuff may be partially vitric in the basal Topopah Spring Tuff, Calico Hills Formation, and upper Prow Pass Tuff and typically contains opal-CT with lesser amounts of feldspar, quartz, and smectite. The third major rock type is vitric tuff, which is distinguished by its glass component and lesser amounts of smectite, zeolites, silica polymorphs, and hematite. There is a fourth type of sample

used in sorption experiments, obtained from surface soils and distinguished by the presence of variable amounts of opaline material, calcite, sepiolite, smectite, quartz, and feldspar.

In addition to these rock samples, pure mineral phases were used in batch-sorption and column-sorption experiments. These studies were pursued because natural materials are multicomponent mixtures of minerals, and it is often difficult to determine which mineral or minerals were responsible for the observed sorption. The minerals studied represent many of the phases that have either significant sorption coefficients or are present in significant abundance at Yucca Mountain. Some of the minerals analyzed were clinoptilolite, smectite, quartz, opal, hematite, magnetite, feldspar, calcite, and the manganese-oxides hollandite/cryptomelane and romanechite. Sorption studies were conducted on the manganese-oxides because they are important as fracture-lining minerals, even though they are not common in the bulk rock at Yucca Mountain.

Assessment of Potential Processing Effects on Sample Composition–Tests of processed and unprocessed samples show that sieving of sorption samples into several size fractions for sorption studies does not have a significant effect on the relative amounts of individual minerals, although smectite and zeolite abundances were often slightly greater in the finer-size fractions. Likewise, samples pretreated and washed in the J-13 and synthetic Paleozoic carbonate waters do not show significant variation in mineral abundances, although, once again, the smectite and zeolite abundance are often slightly greater in the nonwashed samples. This result is to be expected, because clays are very fine grained and zeolites are soft minerals susceptible to mechanical disintegration and would be expected to be preferentially removed with the fine material sieved or washed from a sample.

During one flow-through experiment, some fine material was washed out the end of the column. A portion of this sample was examined by X-ray diffraction to determine whether the fine materials being washed out represented a close approximation of the bulk sample or a preferential loss of mineral components. Comparing the results from this fraction with those obtained for the original bulk sample showed that the fine materials are very representative of the bulk sample used in the experiment. Thus, preferential loss of mineral components should not affect the results of column experiments. It should be noted, however, that calcite may be forming in the column and washing out in the fines, as evidenced by the presence of 2 percent calcite in the fine material.

10.3.1.1.1 Mineralogy and Petrology of Samples Used in Batch-Sorption Experiments

The results of batch-sorption experiments have provided abundant information on the relative extent of interaction between radionuclides of greatest concern and the rocks and minerals that constitute natural barriers at Yucca Mountain (Triay et al. 1997, pp. 55 to 108). In particular, Np was found to present a problem in its particularly low degree of interaction with most rocks and minerals representative of Yucca Mountain. Because of this poor performance, a more extensive sample suite was tested. The list of batch-sorption samples used is therefore more extensive for Np than for most other radionuclides.

The samples used in the batch-sorption experiments are the most comprehensive of any sample suite used in sorption studies. In general, the batch-sorption results show that the lithologies at

Yucca Mountain can be broadly considered as the three major types described above: devitrified, zeolitic, and vitric. However, the distinctions between these lithologies are blurred in the sorption affinities of some radionuclides (e.g., Am, which sorbs readily regardless of lithology) and require finer subdivision to explain the sorption behavior of other radionuclides. As an example of the latter case, Np exhibits particularly complex behavior. If the Np sorption data are considered only in light of the tripartite "zeolitic-devitrified-vitric" distinction, it appears that the only K_d values consistently greater than 1 are in the zeolitic samples. The devitrified and vitric samples may have K_d values greater than 1, but there are some devitrified or vitric samples with lower K_d values. However, by splitting out the quartz-latitic from the rhyolitic devitrified and vitric samples, it can be seen that the lowest K_d values (less than 0.5) are associated only with quartz-latitic compositions, whether vitric or devitrified. The reassessment of Np sorption along these lines, based on geochemistry as well as lithology, allows interpretation of the data as follows:

- Neptunium K_d values for zeolitic samples: approximately 1 to 5 mL/g
- Neptunium K_d values for devitrified rhyolitic samples: approximately 1 to 2 mL/g
- Neptunium K_d values for vitric rhyolitic samples: approximately 0.5 to 2.2 mL/g
- Any Np K_d values less than 0.5 mL/g are in quartz-latitic devitrified or vitric samples.

This analysis of the Np data provides an approach to assessments of Np transport that can be linked to the site stratigraphy as well as to lithology, because the quartz-latitic tuffs are all above the potential repository horizon (Section 5.2 contains a discussion of the nature and distribution of rhyolitic and quartz-latitic rock types). The exceptionally low Np K_d values determined for quartz-latitic compositions in batch-sorption experiments thus supply information on the nature of Np-rock interactions but are not a factor in calculating Np migration rates. This is because unsaturated zone and saturated zone transport beneath the potential repository will occur in tuffs that are rhyolitic and not quartz-latitic.

10.3.1.1.2 Mineralogy and Petrology of Dynamic Transport Column Experiments

It is important to note that, in these dynamic transport column experiments, the devitrified lithologies tested are quartz-latitic, and the sorption results for Np can be expected to be poor in this rock type, as discussed above. This is, in fact, the result observed, with highest K_d values in the zeolitic samples (1.7 to 2.1) and K_d values of less than 0.1 in the devitrified quartz-latitic samples. The vitric rhyolitic samples also had relatively low K_d values in the column experiments (0.1 to 0.2), but these values were still higher than those recorded for the quartz-latitic samples. Results for Pu at different flow rates indicate significant sorption by vitric and zeolitic tuffs but with distinct kinetic effects. Plutonium breakthrough in the columns of devitrified quartz-latitic tuffs was rapid, but it is not known whether the breakthrough would have been any slower in columns of devitrified rhyolitic tuff.

10.3.1.1.3 Mineralogy and Petrology of Fracture Transport Experiments

For fracture-flow experiments, only fractures of devitrified tuff were used. In these samples, natural fractures were identified by their mineral coatings (stellerite, iron-oxides, hollandite, romanechite), although some apparently drilling-induced fractures were tested as well. The results of the fracture transport experiments showed high Np affinity for the manganese-oxide

minerals hollandite and romanechite; these results were confirmed in batch-sorption studies using pure mineral samples.

The fracture-transport experiments show very rapid breakthrough of Tc (principally due to anion exclusion from matrix diffusion), relatively rapid breakthrough of ^{3}H with somewhat more matrix retention across the hollandite + romanechite fracture lining, and markedly strong retention of Np by hollandite + romanechite relative to stellerite + iron-oxides. The Np results are backed by batch-sorption results indicating very high Np K_d values (600 to 700) with pure mineral experiments using hollandite and romanechite. These batch-sorption results are much higher than obtained with bulk-rock experiments (K_d values less than 5 in J-13 water). The combined data make it evident that manganese-oxides provide an important component of the natural barrier against Np movement. These laboratory results should be considered in conjunction with the field evidence of significant interaction between groundwater and manganese-oxides in Yucca Mountain fractures (Section 5.2.2.2). The latter data provide a strong indication that the interactions observed in the laboratory will indeed occur on the field scale at Yucca Mountain, even with manganese-oxide minerals that are only thin and intermittent linings along fractures.

10.3.1.1.4 Mineralogy and Petrology of Diffusion Experiments

Diffusion studies were pursued to test the movement of radionuclides through matrix diffusion. These experiments were conducted in two forms. In the first experiment, rock beakers were prepared with drilled-out cavities of 2.8-cm diameter and 2.5-cm depth. The beakers were surrounded with J-13 water and radionuclide-containing solutions of J-13 water were introduced into the drilled-out cavities. In the beaker experiments, the solution introduced into the drilled-out cavity was sampled over time to determine the progressive loss of radionuclides by diffusion through the rock beaker. Radionuclides used in the beaker experiments included ^{3}H, Tc, Np, Am, Sr, Cs, and Ba. In these beaker experiments, only devitrified tuffs were tested.

The second type of diffusion experiment used diffusion cells with a simpler geometry, measuring the diffusion across a planar slab of tuff. In these experiments, two chambers were separated by a slab of tuff approximately 1 cm thick. The radionuclide tracer solution was emplaced on one side and groundwater without radionuclides was introduced on the other side. Both J-13 and synthetic carbonate aquifer waters were used. Aliquots were periodically sampled from the untraced solution, and the radionuclide activity was measured. As aliquots were removed, the untraced side of the cell was replenished with groundwater to maintain volume. Radionuclides used in the diffusion-cell experiments included ^{3}H, Tc, U, Pu, and Np for devitrified and zeolitic tuffs, using both groundwaters. Mixed solutions of ^{3}H-U-Pu and Tc-Np were studied with devitrified and vitric tuffs. Results of these experiments show that diffusion is slower in devitrified than in zeolitic tuff, but Pu was not observed in the sampled side of the cell for either lithology over time spans of more than 2,000 hr.

Results of the diffusion experiments agree well with batch-sorption data. For sorbing tracers such as Cs, the diffusion out of the rock beakers was faster than predicted from assumptions of reversible, instantaneous, and linear sorption (Triay et al. 1997, pp. 189 to 203). The dispersal of sorbing species into the matrix thus appears to be more effective than these simplified assumptions would suggest. In the diffusion cell experiments, results indicated that diffusion of

nonsorbing tracers (^3H) is more rapid in zeolitic than in devitrified tuff. Sorbing species (such as U) with K_d values of the order of 10 mL/g or less also diffused more rapidly through the zeolitic tuff, but more highly sorbing species (Pu) were effectively blocked from diffusion into either rock type (Triay et al. 1997, p. 196, Figure 133).

10.3.1.2 Microautoradiography

Microautoradiography studies of Yucca Mountain samples focused on the three principal rock types—devitrified, vitric, and zeolitic—that underlie the site. In a round of experiments with Pu (Vaniman et al. 1996), optical analysis of the distributions of ^{239}Pu α-decay tracks in these three types of samples showed only four definitive mineral types that are associated with enhanced affinity for Pu. All of these associations are with trace minerals. Two of these associations are very restricted in stratigraphic occurrence: the altered orthopyroxenes of the devitrified Prow Pass Tuff and the altered opaque oxides of the upper Topopah Spring Tuff (Section 10.3.1). The two other associations, however, are with smectites and manganese-oxyhydroxides that are much more widely distributed across virtually all stratigraphic levels, albeit generally in trace amounts.

Figure 10.3-1 shows a microprobe linescan collected across a clay-rich fracture lining in a sample of zeolitized tuff. The raw counts for Ag are represented for each point along the linescan, with each point representing a step where the electron beam was allowed to rest for 15 seconds while Ag counts were accumulated. The Ag in the photoemulsion is an effective and sensitive measure of underlying Pu activity. The walls of the fracture, lined by clays, are clearly marked by high Ag concentrations corresponding to exceptionally high Pu retention. The zeolitic tuff that forms the matrix away from the fracture walls has Ag counts per 15 seconds that are only marginally higher than background (average 360 ± 90 counts per 15 seconds, determined from 25 analytical points on zeolitic tuff; in comparison, the instrumental background in the emulsion is 210 counts per 15 seconds).

These results provide a valuable comparison to the more quantitative data obtained in sorption studies. However, certain caveats must be considered when using the electron microprobe technique in microautoradiography. First, the use of planar thin sections provides a two-dimensional view of what is essentially a three-dimensional process. Factors in sorption studies such as crushing and grinding can provide surfaces not seen in the polished cuts of thin sections. Second, Ag contents in emulsions are variable and the emulsion itself can be somewhat irregular in thickness, surface texture, and distribution of α-track "noise." The variability in emulsion and in random α-track occurrences is nevertheless a minor problem if Ag abundances are compared between immediately adjacent mineral grains, on a scale where the emulsion coverage and properties are uniform. Third, the size of the electron beam (in this study, 10 μm) might be larger than the individual minerals of interest. The clays analyzed in thin section 1244 are aggregates of micrometer-scale crystals, often interspersed with either zeolites or epoxy. The maximum count rates for Ag obtained over smectite (about 12,600 background-corrected counts per 15 seconds) (Figure 10.3-1) are probably less than would be obtained from an absolutely pure smectite, without epoxy impregnation, exposed to the same Pu solution. For the data obtained in this study by electron microprobe, the clay/zeolite radionuclide distribution factor can be calculated as maximum background-corrected counts for smectite divided by background-corrected counts for zeolite = 12,600/150 = 84.

The accuracy of clay/zeolite radionuclide distribution factors determined by electron microbeam methods may be affected by (1) the large (10 μm) electron beam size relative to the size of the clay bodies being analyzed and (2) the incorporation of epoxy into parts of the thin section that had originally been occupied by clay. Together, these effects probably lead to underestimates of clay/zeolite radionuclide distribution factors. Nevertheless, in zeolitic rocks such as those in the Calico Hills Formation, smectites that account for less than 10 percent of the rock mass can provide approximately 90 percent of Pu retardation, particularly where the smectites are concentrated along microfractures.

Further microautoradiography experiments exposed the three major lithologies from Yucca Mountain (devitrified, vitric, and zeolitic) to three actinide elements (Am, Pu, U) in two different waters (tuffaceous and carbonate aquifers), providing some insight into the mechanisms that account for variability in batch-sorption results. Batch-sorption analysis of the three lithologies used shows a general ranking of effective retardation for all three actinides in all rock types and both waters with retention of Am >> Pu ≥ U. The use of microautoradiography to measure differential retention of these actinides by specific minerals shows that Pu is particularly strongly concentrated over smectite + manganese-oxide associations in zeolitic rocks (regardless of water composition). However, Pu is concentrated over smectite in vitric samples only when synthetic UE-25 p#1 water is used (J-13 water does not lead to any notable smectite preference in the vitric tuff). Phase preferences with Am and U were also tested in the zeolitic lithology. For both of these actinides, a significantly higher preference for smectite + manganese-oxide bodies was observed in synthetic UE-25 p#1 water, but there was little or no discrimination of mineral sites with J-13 water. The implications of enhanced phase preference in p#1 water for explaining shifts in retardation factors may be best illustrated by the behavior of Am in p#1 versus J-13 water. All lithologies exposed to Am in p#1 water have batch-sorption values ranging from 5 to 7 times (in devitrified and vitric rocks) to 55 times (in zeolitic rocks) the batch-sorption values in J-13 water. The strong phase preference for trace but widely dispersed smectite and manganese-oxides in zeolitic rocks with UE-25 p#1 water might account for much of this shift, with the much larger shift in zeolitic rock attributable principally to the presence of the manganese-oxide mineral rancieite (Figure 10.3-2). Figure 10.3-2 also shows, however, that not all manganese-oxide minerals can be treated similarly in terms of sorptive potential; in this example, a sample with fracture-lining cryptomelane shows no effective Pu retention. The microautoradiography data provide a sensitivity test of how retardation operates with insights into phase preferences that may drive the sensitivity of particular lithologies to changes in water composition.

10.3.2 Data Sources

The primary input data used for sorption and sorption modeling studies (CRWMS M&O 2000, Table la) include laboratory results of radionuclide experiments using waters collected from Yucca Mountain or synthesized to reflect Yucca Mountain waters, and materials either collected from the field or synthesized in the laboratory. Parameters used in this section are the radionuclide concentration and percent sorbed onto various substrates.

10.3.3 Description of Batch-Sorption Data

10.3.3.1 Introduction

The solubility limits of radionuclides may act as an initial barrier to radionuclide migration from the potential repository at Yucca Mountain for some radionuclides. However, once radionuclides have dissolved in water infiltrating the site, sorption of these radionuclides onto the surrounding tuffs becomes a potentially important second barrier. Thus, the study of the retardation of actinides and other key radionuclides is of major importance in assessing the performance of the potential repository.

Sorption actually is composed of several physicochemical processes, including ion exchange, adsorption, and chemisorption. Determining whether sorption will occur requires knowledge of the likely flow paths of the groundwater and the spatial and temporal distribution of sorbing minerals along these paths. Evaluating the retardation effectiveness of sorption for repository design and licensing requires theoretical and quantitative understanding of sorption. Thus, experimental measurements of sorption were combined with modeling of the data in an attempt to identify key sorption mechanisms.

The use of batch-sorption experiments to obtain sorption distribution coefficients and to identify sorption mechanisms is fast, easy, and inexpensive compared to other sorption experiments. A disadvantage is that such experiments are static in nature, whereas transport of radionuclides through the site is dynamic. However, batch-sorption experiments are useful for bounding more detailed and mechanistic sorption studies, and a major part of the experimental effort was devoted to such measurements.

In the experiments, batch-sorption distribution coefficients were determined as a function of variables representing conditions expected outside of the region disturbed by waste emplacement. The variables included mineralogy, groundwater chemistry, sorbing element concentration, atmospheric conditions, and temperature. The sorption behavior of individual pure minerals found in Yucca Mountain tuffs, such as zeolites and Mn or iron oxyhydroxides, was also examined. This approach is designed to allow estimation of sorption coefficients along flow paths of known mineral content. Sorption data are presented in Tables 10.3-2 to 10.3-16.

The Distribution Coefficient–The batch-sorption distribution coefficient, K_d, was calculated using

$$K_d = \frac{F}{C} = \frac{\text{moles of radionuclide per gram of solid phase}}{\text{moles of radionuclide per milliliter of solution}} \quad \text{(Eq. 10.3-1)}$$

K_d values thus have units of mL/g.

The determination of very small or very large batch-sorption distribution coefficients results in large uncertainties in the K_d values calculated. When very little sorption occurs, calculations can yield negative K_d values; the error results from subtracting two large numbers (the initial radionuclide concentration in solution and the radionuclide concentration after sorption) to obtain a small number (the amount of radionuclide left in the solid phase). Therefore, very small

K_d values are not very significant. On the other hand, when a great deal of sorption occurs, there can be large uncertainties associated with measuring the small amount of radioactivity left in solution after sorption. This also results in large uncertainties in the calculated K_d. Because of these uncertainties, most K_d values are only reported to one significant figure.

Linear Versus Nonlinear Sorption–The sorption distribution coefficient, K_d, for the species being sorbed is the ratio of its concentration in the solid phase, F, to its concentration in the solution phase, C, which implies a linear relationship between the concentrations:

$$F = K_d C \qquad \text{(Eq. 10.3-2)}$$

Besides linearity, the valid use of sorption distribution coefficients in transport calculations also requires the sorption to be instantaneous and reversible, conditions that may not be met for the sorption of radionuclides onto Yucca Mountain tuffs.

Nonlinear adsorption isotherms were reviewed by de Marsily (1986, p. 258). A useful nonlinear relationship, Freundlich's isotherm, is given by the equation

$$F = KC^{1/n} \qquad \text{(Eq. 10.3-3)}$$

where K and n are positive constants (with $n \geq 1$).

Another nonlinear relationship is Langmuir's isotherm, given by

$$F = \frac{K_1 C}{1 + K_2 C} \qquad \text{(Eq. 10.3-4)}$$

where K_1 and K_2 are positive constants. Part of the research discussed in this section was an attempt to assess the validity of using the linear distribution coefficients as opposed to other isotherm functional forms to describe retardation by sorption in transport calculations.

Experimental Procedures–All batch-sorption experiments were performed at room temperature and under atmospheric conditions or inside glove boxes with a carbon-dioxide overpressure. The pHs of the UE-25 J-13 and p#1 waters under atmospheric conditions were approximately 8.5 and 9, respectively; inside the glove boxes, the pH was 7.

10.3.3.2 Plutonium

Data from Sorption Experiments Reported in the Literature–The data discussed in this section are provided to show trends for the sorption of Pu. Allard (1982, Sections 4 to 5) reported results on experiments involving Pu sorption on quartz, apatite, attapulgite, montmorillonite, and various minerals rich in ferrous Fe in a dilute groundwater containing Pu at 1.8×10^{-11} M. For all the minerals, the sorption coefficients were greater than 10^3 mL/g over a pH range of 4 to 9. Apatite, attapulgite, biotite, and montmorillonite showed sorption coefficients greater than 10^4 mL/g over this pH range. Torstenfelt et al. (1988, Tables 17 to 25) presented data for Pu sorption on feldspars, clays, and granite in contact with J-13 water. The sorption coefficients reported by Torstenfelt et al. (1988, Tables 17 to 25) are generally between 100 to 200 mL/g in neutral to alkaline solutions. These authors emphasized the importance of

proper experimental technique in the determination of sorption coefficient values for Pu and noted the potential for colloid formation in these types of experiments. Data indicating high affinity of Pu for ferric oxyhydroxide, manganese oxide, and carbonate mineral surfaces were presented by Means et al. (1978), Keeney-Kennicutt and Morse (1985), and Sanchez et al. (1985). Means et al. (1978, pp. 1771 to 1772) noted that manganese oxides sorb Pu more strongly than ferric oxyhydroxides in natural environments (presumably as a result of redox reactions on the manganese-oxide surface).

Data from Laboratory Sorption Experiments with Yucca Mountain Rock and Water Samples–Measurements of Pu sorption coefficients involving Yucca Mountain rock samples and J-13 groundwater were summarized by Thomas (1987, p. 20). The values measured for the Pu sorption coefficient range from 20 to greater than 4,500 mL/g, with most values lying between 100 to 2,000 mL/g within a pH range of 8.2 to 8.8. The coefficients determined during the desorption experiments were occasionally in the range of the sorption coefficient values, but, more typically, they were 10 to 20 times larger, reflecting the irreversibility of the sorption reactions. Zeolitic samples typically had lower sorption-coefficient values than vitric or devitrified samples. It appears that rocks that have essentially no reduction capacity remaining (i.e., samples lacking ferrous Fe or sulfide) show the lowest sorption coefficients for Pu. Samples with calcite or clay showed the largest sorption coefficients (greater than 4,500 mL/g for samples with 30 percent calcite).

Based on the eight experiments for which data are available, there was up to a factor of 12 variation in sorption coefficients as a function of groundwater composition. Water from well UE-25 p#1 was associated with the largest values (240 to 540 mL/g, sorption-desorption) with waters from wells H-3 and J-13 showing the lowest values (20 to 230 mL/g). The higher values obtained with UE-25 p#1 water might reflect calcite precipitation. There did not appear to be a dependence of the sorption coefficient on pH over the range from 7 to 9, although the available data are limited on this issue. Finally, there was less than a factor of four dependence of the sorption coefficient on radionuclide concentration over the range from 10^{-9} to 10^{-12} M.

Plutonium sorption coefficients have been measured on a variety of solid samples in contact with Yucca Mountain groundwaters UE-25 J-13 and p#1 under atmospheric conditions (i.e., oxidizing conditions and pH equal to 8.2 to 8.6). The data (summarized in Table 10.3-2) show that Pu sorption coefficients will be greater than 100 mL/g for vitric and zeolitic tuffs under these conditions. For devitrified tuffs, sorption coefficients will be less than 100 mL/g in both water compositions. These data were reported in CRWMS M&O (2000, Section 6.4.4.1.4.1).

The sorption of Pu onto the three main types of tuff in J-13 water at a pH of 7 was studied using a carbon-dioxide overpressure to maintain a pH of 7. These experiments were also conducted under oxidizing conditions (i.e., atmospheric O concentrations). The affinity of tuffs for Pu at pH = 7 is, in decreasing order, zeolitic > vitric > devitrified (Triay et al. 1997, Figure 37). Compared to the data presented in Table 10.3-2, Pu appears to sorb somewhat less at a pH of 7.0 than at pH values from 8.2 to 8.6 (atmospheric conditions), particularly on devitrified tuff (K_d less than 10 mL/g).

To investigate which minerals in tuffs were responsible for most Pu sorption, sorption experiments were carried out with pure mineral separates. The minerals investigated included

hematite, clinoptilolite, albite, and quartz. The results of the batch-sorption experiments for Pu on these minerals are shown in Table 10.3-2. The relative affinities of these minerals for Pu are, in decreasing order, hematite > montmorillonite > clinoptilolite > calcite >> gibbsite > albite ≥ quartz. These data suggest that montmorillonite and zeolite minerals are likely responsible for most of the Pu sorption onto the bulk tuffs. The trace amounts of hematite found in the tuffs do not appear to have a significant impact based on other data (Triay et al. 1997, pp. 65 to 73). However, the presence of calcite in the tuffs can have a significant impact depending on the amounts present and on the surface area of the calcite present.

As stated above, sorption coefficients are not necessarily constant with increasing concentration of the sorbing element. That is, sorption isotherms can be linear or nonlinear. To investigate the shape of the Pu sorption isotherm with increasing Pu concentration, experiments were conducted over a range of solution concentrations with various rock and water combinations. The data obtained indicate that the Pu sorption isotherm is generally nonlinear on tuffs from Yucca Mountain (Triay et al. 1997, pp. 69 to 73). The cause of the nonlinearity is not known. The solution concentrations in these experiments range from 3×10^{-10} to 2×10^{-7} M. Because the upper limit of this range is close to the solubility of Pu in Yucca Mountain groundwaters, the concentration of aqueous Pu transported in the flow system will likely not exceed this value. Experiments conducted with concentrations at the low end of the range produce sorption coefficients that are higher than experiments conducted with solution concentrations at the high end of the range. Therefore, the use of sorption coefficients in performance assessment calculations obtained with the more concentrated solutions will result in conservative predictions of Pu transport rates.

The sorption of Pu onto tuffs and minerals in UE-25 J-13 and synthetic p#1 water under atmospheric conditions was studied as a function of time and initial Pu solution concentration. The resulting data (Triay et al. 1997, p. 69) indicate that it takes a long time for the Pu sorption reactions to reach a steady state. Even after 32 days, a steady-state concentration in solution was not achieved in these experiments. This slowness in reaching a steady state may be due to redox reactions at solid surfaces in the samples.

Nitsche et al. (1993) reported that even when a Pu solution in UE-25 J-13 or p#1 water is prepared starting in the +4 oxidation state, the predominant final oxidation state is +5, or Pu (V). The solution used for Pu sorption experiments was prepared from a well-characterized Pu (V) acidic stock in J-13 well water. It was assumed that, during the short time of the sorption experiment (e.g., 30 days), the Pu would have remained predominantly in the +5 oxidation state. Although over the long term, it may not have remained in that state.

Comparing data for Pu sorption coefficients to similar data for Np and U indicates that significant Pu sorption occurred in tuffs and minerals that exhibit very small sorption coefficients for Np (V) and U (VI). This result is puzzling; if Pu in J-13 well water is predominantly Pu (V) and Pu (VI) (Nitsche et al. 1993), it is expected that its sorption behavior would have been similar to that observed for Np (V) and U (VI). There are several possible explanations for this apparent discrepancy:

- The Nitsche et al. (1993) data for the oxidation states are incorrect, and the predominant plutonium oxidation state in J-13 well water at a pH of 7 is Pu (IV), not Pu (V) and Pu (VI).

- The Pu (IV) species is what sorbs from J-13 water, but a reequilibration in the solution phase produces more Pu (IV) to maintain equilibrium (which implies that the kinetics of Pu speciation in solution are fast, but are slow on the solid).

- Pu (V) and Pu (VI) reduce to Pu (IV) at solid surfaces (as a result of changes in the solution redox potential in the presence of the solid phases).

The impact of the slow sorption kinetics on predictions of transport rates of Pu in Yucca Mountain is that the sorption coefficients from the batch tests should generally result in conservative predictions.

Conclusions Regarding Sorption Behavior of Plutonium in the Yucca Mountain Flow System–Based on information in the previous sections, it appears the most important factors controlling the sorption of Pu from oxidizing groundwater onto Yucca Mountain tuffs are the abundances of montmorillonitic clays and zeolite minerals. Calcite, if present, may also result in high Pu sorption coefficients. The affinity of Yucca Mountain tuffs for Pu is highest in zeolitic tuffs, slightly lower in vitric tuffs, and lowest in devitrified tuffs. Groundwater compositional parameters that appear to have the most impact on Pu sorption behavior are redox potential (i.e., Eh) and pH. Under less-oxidizing redox potentials than those maintained in the batch experiments, Pu sorption coefficients would be larger. Therefore, the sorption coefficients reported here will result in conservative predictions of Pu transport rates. The change in sorption coefficients that may result from variations in groundwater pH are accounted for in the distributions reported in Tables 10.3-3 and 10.3-4 (Section 10.3.6). Similarly, the impact of potential variations in Pu concentration are incorporated in the distributions by assuming that the high end of the range of potential Pu concentrations in groundwater pertain to the Yucca Mountain flow system. Although the kinetics of the Pu sorption reactions appear to be relatively slow compared to elements with simpler solution chemistry (e.g., Cs), the sorption coefficients reported here should result in conservative predictions of Pu transport rates.

10.3.3.3 Cesium, Radium, and Strontium

Behavior in Solutions Representative of Yucca Mountain Groundwaters–These elements (Cs, Ra, and Sr) show relatively simple solution behavior in typical groundwaters and are not subject to changes in oxidation state in the groundwater compositions expected in Yucca Mountain. Radium and Cs are invariably present as the simple Ra^{2+} and Cs^{+} cations in the expected groundwater compositions (Ogard and Kerrisk 1984). Strontium exists primarily as the Sr^{2+} ion in these waters, but may also be present as the neutral aqueous species $SrSO_4$, at concentrations of a few percent of the total Sr solution concentration (Ogard and Kerrisk 1984). The data of Langmuir and Riese (1985) indicated that $RaSO_4$ (aq)/Ra^{2+} will be greater than or equal to 0.6 when the sulfate ion concentration is greater than 10^{-3} M. These numbers suggest that $RaSO_4$ (aq) will be a significant species ($RaCO_3$ (aq) and $SrCO_3$ (aq) may also be significant).

Literature Data–The literature on the behavior of Cs, Ra, and Sr in the surficial environment is voluminous and will not be reviewed here. Their sorption behavior is fairly well understood and is largely controlled by ion-exchange reactions (Bolt and Bruggenwert 1978), although surface-complexation reactions involving these elements have also been discussed (e.g., Balistrieri and Murray 1982). The dominant controls on the ion-exchange reactions are the cation-exchange capacities of the minerals in the system, the abundances of these ion-exchanging minerals, their selectivity coefficients for the various cations in the solution phase, and the concentrations of the competing cations in the solution phase. The selectivity of most clays and zeolites for Cs, Ra, and Sr is greater than the selectivities for the major cations in solution. Further, pH does not have a significant effect on the sorption behavior of these elements over the pH range of interest. Because their sorption behavior is fairly well understood, and because this behavior depends strongly on local conditions, data from sites other than Yucca Mountain will not be reviewed here.

Data from Laboratory Sorption Experiments with Yucca Mountain Rock and Water Samples–Sorption coefficients for Cs, Ra, and Sr were reviewed by Daniels et al. (1983, Table 14, pp. 39 to 40), Thomas (1987, p. 4), and Meijer (1990, p. 20). For Cs at low concentrations (10^{-8} M), sorption coefficients are greater than 100 mL/g for all water-rock combinations tested except UE-25 p#1 water in contact with vitric tuff (Knight and Thomas 1987, Table 4, pp. 4 to 7). Cesium sorption coefficients for the devitrified-tuff/J-13-water system show a clear concentration dependence that has been modeled with a Freundlich isotherm (Polzer and Fuentes 1988). The coefficients for this particular rock-water system are greater than 100 mL/g for Cs solution concentrations below 5×10^{-5} M. For UE-25 p#1 water in contact with this rock type, the coefficient would be 100 mL/g at somewhat lower solution concentrations. In any case, in the higher ionic-strength waters (0.02 eq/L), including unsaturated zone waters, the sorption coefficients for Cs on devitrified and vitric samples may be less than 100 mL/g if solution concentrations of Cs exceed 10^{-6} M. For zeolitic tuffs, Cs sorption coefficients are greater than 100 mL/g for all water compositions and Cs concentrations anticipated in the potential repository environment.

Radium appears to have a somewhat higher affinity for sorption onto Yucca Mountain tuffs than Cs. In addition, the solubility of $RaSO_4$ limits the concentrations in solution to trace levels (10^{-7} to 10^{-8} M) (Ogard and Kerrisk 1984). At concentrations below the solubility limit for $RaSO_4$, sorption coefficients for Ra are greater than 100 mL/g in essentially all rock-water combinations tested, using Ba as an analog for Ra (Knight and Thomas 1987, Table 4, pp. 4 to 7). This fact suggests that a minimum sorption coefficient of 100 mL/g can be used for Ra in all rock-water systems. For zeolitic samples, a minimum value of 1,000 mL/g can be used.

Strontium sorption behavior is more sensitive to mineral and water compositions than the other two elements discussed in this section. For devitrified and vitric tuffs, sorption coefficients for the higher ionic-strength waters (e.g., UE-25 p#1) are in the range of 10 to 30 mL/g (Knight and Thomas 1987, Table 4, pp. 4 to 7). These sorption coefficients will decrease as the solution concentration of Sr increases above approximately 10^{-5} M (Thomas 1987, Appendix). However, this concentration is close to the solubility limit for $SrCO_3$ in these waters so that the 10 to 30 mL/g range is likely appropriate for use in performance assessment calculations in the devitrified or vitric tuffs. For zeolitic tuffs, a minimum value of 1,000 mL/g would be appropriate (Knight and Thomas 1987, Table 4, pp. 4 to 7).

Conclusions Regarding Sorption Behavior with Respect to Expected Variations in Groundwaters–The existing sorption-coefficient database for Cs, Ra, and Sr should be adequate for performance assessment calculations. The main concern would be the concentration of Cs in the solution phase in contact with devitrified and vitric tuffs. If this concentration is over 10^{-5} M, the appropriate value for the sorption coefficient might be less than the minimum recommended value of 100 mL/g. The sorption coefficients for Sr in devitrified and vitric tuffs will be as low as 10 to 30 mL/g in higher ionic-strength waters. If additional experiments were to be carried out for this group of elements, they should focus on Sr in contact with devitrified and vitric tuffs in the higher ionic-strength waters.

10.3.3.4 Nickel and Lead

Behavior in Solutions Representative of Yucca Mountain Groundwaters–The aqueous solution behavior of Ni and Pb is relatively simple. Within the range of groundwater compositions expected in the Yucca Mountain flow system, these elements are present in solution primarily as simple divalent cations. Several percent of the total Ni concentration will be present as the $NiSO^{o}_{4}$ (aq) and possibly $NiCO^{o}_{3}$ (aq). Similarly, several percent of the total Pb concentration will be present as the $PbCl^{+}$ complex.

Literature Data–The behavior of Ni and Pb in the surficial environment has been studied in some detail (e.g., Snodgrass 1980). These elements are generally quite particle-reactive. The dominant mechanisms that control their sorption behavior are ion exchange on clay minerals (e.g., Bowman and O'Connor 1982, p. 933) and adsorption onto various oxides (e.g., Theis and Richter 1980). The selectivities of clay minerals for Ni and Pb are large relative to the major cations (e.g., Mg^{2+}) in typical groundwaters (Decarreau 1985 p. 1540). Solution compositional parameters that can influence this adsorption behavior include pH, ionic strength, concentrations of competing ions, and concentrations of complexing agents (Rai and Zachara 1984, pp. 143-145 and 18-3 to 18-4).

Data on sorption of transition metals on synthetic zeolites suggest that Pb^{2+} has a high affinity for ion exchange compared with Sr^{2+}, whereas Ni^{2+} has a lower affinity relative to Sr^{2+} (Barrer and Townsend 1976; Obeng et al. 1981; Blanchard et al. 1984, p. 1501, Figure 1). This result suggests the zeolitic zones within Yucca Mountain could be significant barriers to Pb migration.

Data from Laboratory Sorption Experiments with Yucca Mountain Rock and Water Samples–Data on the sorption behavior of Ni in Yucca Mountain rock-water systems were reported by Knight and Lawrence (1988). Sorption and desorption ratios were determined in several water compositions in the pH range from 8.3 to 9.0 with Ni concentrations in solution of approximately 10^{-8} M. For devitrified and zeolitic samples, sorption coefficients were in the range of 200 to 400 mL/g. Sorption coefficients obtained in the desorption step were generally a factor of two larger than the sorption coefficients. In the only vitric sample analyzed, sorption coefficients ranged from approximately 30 to 70 mL/g. For the desorption step, the coefficients were in the range of 33 to 72 mL/g for this rock type. References to the adsorption behavior of Pb on tuffaceous or even granitic rock samples were not found.

Conclusions Regarding Sorption Behavior with Respect to Expected Variations in Groundwaters–Based on information in the literature, the sorption behavior of these elements

will be determined largely by the free-ion activities in solution and the cation-exchange capacity of the host rock (e.g., Bowman and O'Connor 1982, p. 934; Rai and Zachara 1984, pp. 143 to 145, and 18-3 to 18-4). Solution pH and oxide-mineral abundances may be a factor in rocks in which Ni and Pb sorb primarily by surface-complexation mechanisms. In any case, Pb appears to sorb more strongly than Ni in most surficial environments, and both elements appear to sorb more strongly than Sr (Bowman and O'Connor 1982, p. 935, Figure 3). The Ni sorption coefficients discussed in the previous section could reasonably be used as default values for Pb in performance assessment calculations. For Ni, a minimum sorption coefficient of 100 mL/g could be used in the devitrified and zeolitic zones. For the vitric zones, the performance assessment calculations could be done using random sampling and a normal distribution ranging from 0 to 50 mL/g.

10.3.3.5 Neptunium

Neptunium, Pa, Se, and U share a common characteristic in that they all tend to show small values for sorption coefficients in the rock-water systems expected within Yucca Mountain under oxidizing conditions (Tables 10.3-5, 10.3-6). Under more reducing conditions, they would all have much lower solubilities and higher sorption affinities in Yucca Mountain groundwaters. As the solution and sorption behavior is somewhat different for each of these elements, they will be discussed separately, starting here with Np. In solutions representative of oxidized water compositions expected within the Yucca Mountain flow system, Np will be predominantly in a +5 oxidation state. In this oxidation state, Np is quite soluble when compared to lower oxidation states. If reducing conditions are encountered along the flow path between the potential repository and the accessible environment, Np could be reduced to the +4 oxidation state.

Data from Sorption Experiments Reported in the Literature–The results of Np sorption experiments with pure mineral separates were reported by Allard (1982, Sections 4 to 5), Meijer et al. (1990), and others. On the basis of these results, it is evident that in oxidizing solutions, Np has a high affinity for ferric oxides and oxyhydroxides, apatite, and attapulgite (a Mg-rich clay). It has a somewhat lower affinity for carbonates (e.g., calcite), sulfates (e.g., anhydrite), and Mn minerals (e.g., cryptomelane). It has a low affinity for most silicate minerals. Neptunium also shows high affinities for minerals that contain ferrous Fe (e.g., pyrite, olivine, augite, magnetite, hornblende, epidote, biotite, and chlorite). This affinity is likely due to the reduction of Np^{5+} to Np^{4+} by Fe^{2+} on the surfaces of these minerals. Although ferrous Fe-bearing minerals are, at best, minor species in Yucca Mountain tuffs (Bish and Chipera 1989), they could be of considerable significance to Np sorption where present in the flow system.

In addition to the nature of the available mineral surfaces, it is evident that pH is also a critical parameter in Np sorption. In general, Np sorption increases with increasing pH. This effect is particularly evident in the experiments with ferric-oxyhydroxides (e.g., Combes et al. 1992). However, similar behavior is evident in the sorption experiments with silicate minerals (Allard 1982, Section 4.1, Figure 9). In the latter case, the sorption edge (as a function of pH) is located at a higher pH (8 to 9) than the edge associated with the ferric-oxyhydroxides (a pH of 6 to 7). Neptunium does not appear to have a high affinity for ion-exchange reactions on clays and zeolites (Allard 1982, Figure 16; Triay et al. 1993a, p. 1505). This phenomenon might be due to the small charge-to-radius ratio and the large size of the neptunyl ion.

Data from Laboratory Sorption Experiments with Yucca Mountain Rock and Water Samples–The results of Np sorption experiments involving Yucca Mountain rock and water samples were reported by Daniels et al. (1982), Thomas (1987, p. 20 Appendix; 1988), and Triay et al. (1993a, p. 1505). These experiments indicated that Np has K_d values of 0 to 5 mL/g for the surfaces in Yucca Mountain tuffs over most of the pH range and water compositions expected in the Yucca Mountain flow system. The sorption mechanisms are apparently not entirely reversible, as coefficients obtained from desorption experiments are commonly larger than those obtained from sorption experiments, even though the isotherms are linear in the concentration range covered by these experiments. There is some indication of increased sorption coefficients (5 to 40 mL/g) at the highest pH values (8.5 to 9.0). Torstenfelt et al. (1988, p. 115) suggested that this result reflects increased hydrolysis of the neptunyl ion, resulting in an increase in surface-adsorption reactions. However, in Yucca Mountain rock-water systems, it could also reflect increased potential for calcite precipitation at high pH.

In the pH range from 6.5 to 8.5, the small but consistent affinity of Np for the tuffs most likely reflects the existence of a limited number of favorable adsorption sites for Np. This number apparently does not involve ion-exchange sites because zeolitic rock samples also show low sorption coefficients. For example, Thomas (1988) described a case in which a zeolitic tuff sample (G4-1608) with a cation-exchange capacity of approximately 1.5 meq/g appears to have essentially the same affinity for Np as a devitrified tuff sample (GU3-433) with an exchange capacity of approximately 0.02 meq/g. These sites are apparently not present in the same abundance on all tuff samples. That is, some zeolitic, vitric, and devitrified tuff samples have almost no affinity for Np over the pH range from 6.5 to 8.5, whereas other samples with similar proportions of major minerals show sorption coefficients in the range of 5 to 10 mL/g. This result suggests, but does not prove, that the favorable sites are associated with some minor primary or secondary phase that has variable abundance. Hematite and calcite are candidates for this phase based on pure mineral studies. Because ferric oxides are present at trace levels in most of the rock units within Yucca Mountain, they could be the source of the consistent values (0.5 to 2 mL/g) observed in experiments on devitrified and zeolitic tuffs. Alternatively, Np may be sorbed (through reduction to Np^{4+}) by the small amounts of ferrous Fe-bearing minerals present in the rock samples used in the sorption experiments.

The increased sorption of Np on tuffaceous samples known to contain calcite suggests this mineral is of considerable potential significance to Np sorption on Yucca Mountain tuffs. If so, prediction of the adsorption behavior of Np will depend on knowledge of the surface areas of calcite in the various hydrologic units or on the saturation state of calcite in groundwaters present in these units. Because even small amounts of calcite appear to significantly increase Np sorption coefficients, current mineral identification techniques may not be adequate for prediction of Np sorption behavior involving calcite. For vitric units lacking iron oxides and calcite, Np may not be sorbed at all.

Additional YMP data were reported in CRWMS M&O (2000, Section 6.4.4.1.4.2).

Sorption coefficients for Np (V) on samples of the three main types of tuff under atmospheric conditions (pH = 8.2 to 8.6; oxidizing) are shown in Figure 10.3-3. Note that the sorption coefficients for all samples are less than 5.0 mL/g. The values less than 1.0 are generally for vitric and devitrified samples, and those greater than 1.0 are for zeolitic samples.

Zeolitic tuffs show substantial variation in the Np sorption coefficient in different samples and under different pH conditions. Some zeolitic samples show very little affinity for Np, although more at a pH value of 8.5 than at 7.0 (Figure 10.3-4). Other zeolitic samples (e.g., G4-1510 and GU3-1992) show a higher affinity (i.e., higher K_d), particularly at a pH value of 7.0. Why some zeolitic samples show substantially higher Np sorption coefficients is not entirely clear. The explanation likely revolves around the type of zeolite structure and the chemistry of the zeolite.

The impact of pH variations on Np sorption behavior was also investigated with experiments on devitrified and vitric tuff and albite and quartz in J-13 water (under oxidizing conditions) at two pH values (7 and 8.5). It was found that in J-13 water, Np sorbs only sparingly onto devitrified and vitric tuffs under both pH conditions.

Experiments with pure clinoptilolite indicate that sorption increases with decreasing pH for Np (V). Because the major constituent of tuff G4-1510 is clinoptilolite, predictions of the K_a (K_d divided by the solid-phase surface area) were made for Np sorption onto this tuff by assuming that clinoptilolite is the only sorbing phase. Table 10.3-5 shows measured and predicted values of K_a for the clinoptilolite-rich tuff G4-1510 at two different pH values. Because sorption is correlated with surface area, similar calculations (Table 10.3-6) were made for a series of tuff samples containing various amounts of clinoptilolite for which the surface area had been measured. The values in these two tables indicate that reasonable predictions can be made based on Np sorption data for pure clinoptilolite (assuming clinoptilolite is the only sorptive mineral).

The dependence of Np sorption on Np concentrations for zeolitic tuffs and pure zeolites was tested in two samples. The sorption of Np onto zeolitic tuffs and clinoptilolite appears to be linear in the concentration range from 1×10^{-7} to 3×10^{-5} M, and can be fitted using a constant K_d. In a zeolite-rich tuff at a pH of 7.0, the K_d was 3.0 mL/g, whereas at a pH of 8.5, the K_d was 1.5 mL/g (Figure 10.3-5). Similar results were obtained with a pure zeolite sample (Figure 10.3-6). The higher sorption of Np onto zeolites at a pH of 7 might be explained by the larger amount of NpO_2^+ relative to $NpO_2CO_3^-$ in J-13 well water at a pH value of 7 compared to that at a pH of 8.5.

The relatively small amount of sorption observed in the zeolitic tuffs, given the large cation-exchange capacity of zeolites, suggests that the mechanism for Np sorption onto clinoptilolite is a surface reaction involving only the cation sites accessible on the zeolite surface. One possible explanation for this behavior is that the shape and large size of the neptunyl cation prevents it from entering the pores in the zeolite structure, thereby gaining access to most of the exchange sites. This ion likely has a trans-dioxol configuration normal to a puckered equatorial ring containing six bound water molecules.

Because Np was thought to sorb with a surface mechanism even in zeolitic tuffs and because the batch experiments are conducted with crushed tuff samples (i.e., increased surface area), the sorption coefficient for Np was investigated as a function of sieving procedure for devitrified (G4-270) and zeolitic (G4-1506) tuffs and calcite in UE-25 J-13 and p#1 well waters. The data obtained in these experiments indicate that dry-sieving probably produces artificially high K_d values because of the increased surface area contributed by the small particles. As previously determined by Rogers, Meijer, and Kung (1994), the optimal batch-sorption procedure involves wet-sieving the tuff samples to a size of 75 to 500 μm.

The sorption of Np onto pure iron oxides (hematite) in J-13 water was also measured. The measured values of K_d for hematite range from 100 to 2,000 mL/g. Although the sorption onto the pure iron oxide hematite is very large, Np sorption onto devitrified tuffs, which appear to have traces of hematite (1 percent ± 1), is close to zero. This result could be due to differences in the surface chemistry of pure hematite compared to hematite in tuff. For example, it could be due to passivation of the hematite surfaces in the tuff by elements (e.g., the rare earths) that have a higher affinity for hematite than Np and, thus, occupy the sorption sites. Alternatively, there could be too little hematite present in the tuffs (concentrations are within experimental error).

The kinetics of Np sorption onto tuffs and pure minerals were investigated, and it was found that the sorption of Np onto tuffs and clinoptilolite appears to be fast (steady state in 5 to 7 days). Although the data are scant, they can be used as guidelines. No significant differences are observed in Np sorption as a function of time for the tuffs studied and for clinoptilolite. This is not the case for pure minerals that tend to sorb by means of a co-precipitation mechanism (e.g., calcite) or by surface complexation (e.g., hematite). The dissolution/precipitation reactions that may accompany the co-precipitation of Np with calcite appear to be slow compared with other sorption mechanisms. Why the Np sorption reaction on hematite is slow is not clear. Future experiments will address this issue by monitoring the chemistry of the groundwater as it is being equilibrated with these minerals.

Experiments with UE-25 p#1 water indicate that Np sorption onto tuffs and zeolites is very limited (K_d less than 1 mL/g) in this water regardless of conditions (pH and Np concentration). If clinoptilolite is the only mineral affecting Np sorption, and if ion exchange at the surface is the dominating mechanism, it could be that the reason for the lack of Np sorption on clinoptilolite is the formation of the neptunium carbonado complex ($NpO_2CO_3^-$) in UE-25 p#1 water to the exclusion of the neptunyl cation. However, the data reported by Nitsche, Roberts, Prussin et al. (1995) do not support this conclusion; the relative amount of neptunyl in UE-25 p#1 water is larger than that in J-13 water at a pH of 7. If the data of Nitsche, Roberts, Prussin et al. (1995) are correct, another possible reason for the lack of Np sorption on clinoptilolite is required. One possibility is that in UE-25 p#1 water there is strong competition for sorption sites due to the higher ionic strength of this water compared with J-13 water.

Figures 10.3-7 and 10.3-8 summarize the sorption of Np under atmospheric conditions for tuffs and minerals as a function of water type. Sorption onto zeolitic tuffs decreases considerably with increasing carbonate content and ionic strength of the water (Figure 10.3-7). Figure 10.3-8 shows that calcite and hematite have high affinities for Np, particularly in UE-25 p#1 water. The calcite-rich tuff G2-723 (34 percent calcite) exhibits considerable sorptive capacity for Np. Assuming that the calcite in the tuff sample has the same surface area as the natural calcite used for the experiments (and that calcite is the only sorptive mineral in the tuff), a log K_d for tuff G2-723 of 1.5 could be predicted from Np sorption on pure calcite. This prediction agrees well with the measured K_d (Figure 10.3-8).

Conclusions Regarding Sorption Behavior with Respect to Expected Variations in Groundwaters–The mechanisms by which Np appears to sorb onto mineral surfaces in the Yucca Mountain flow system appear to be ion exchange or surface complexation on zeolitic phases and co-precipitation and surface adsorption involving carbonate minerals. The ion exchange/surface-complexation mechanism appears to be responsible for the 0.5 to 5.0 mL/g

range in sorption-coefficient values consistently measured in zeolitic rock samples. The high end of this range may reflect other mechanisms, such as the presence of trace minerals with high affinities for Np. Regardless of the details of the mechanisms, performance assessment calculations could use a probability distribution for sorption-coefficient values as shown in Table 10.3-3. This distribution is based on the opinion of experts who are familiar with the data set discussed in this section.

For hydrologic units in which calcite is known to be present or in which groundwaters are oversaturated in calcite, higher Np sorption coefficients could be used in the performance assessment calculations if it could be established through laboratory experiments that such coefficients are appropriate.

10.3.3.6 Protactinium

Behavior in Solutions Representative of Yucca Mountain Groundwaters–In aqueous systems, Pa appears to exist dominantly in the +5 oxidation state, although the +4 state may occur in reducing environments (Brookins 1988). In both oxidation states, Pa is strongly hydrolyzed and forms highly insoluble compounds (Cotton and Wilkinson 1988, pp. 1062, 1003). This result implies that the +5 solution chemistry of Pa is more akin to that of Nb (V) than to other actinides in +5 oxidation states, such as PuO_2^+ or NpO_2^+. If this interpretation is correct, the solution parameter of greatest importance to Pa sorption behavior would be pH.

Qualitative Evidence for Behavior in the Surficial Environment–Information on behavior of Pa in the surficial environment is sparse. Because Pa forms such insoluble compounds, it is generally assumed to be immobile in the surficial environment.

Data from the Literature–Batch-sorption experiments with Pa have yielded some interesting results. In dilute to intermediate ionic-strength solutions, Allard (1982) reports large values (10^4 mL/g) for the Pa sorption coefficient on alumina and silica at pH values greater than 6 to 7 but much lower values (90 to 500 mL/g) at pH values less than 7.

Data from Laboratory Sorption Experiments With Yucca Mountain Rock and Water Samples–Rundberg et al. (1985, p. 63, Table 17) report Pa sorption coefficients in the range from 3.7 to 8.2 mL/g for a zeolitic tuff in contact with J-13 water spiked with 10^{-11} to 10^{-14} M Pa at pH values of 6.3 to 6.7. Combined with the data reported by Allard (1982), these data suggest that Pa sorbs by a surface-complexation mechanism, and that there is a rather steep sorption edge for Pa as a function of pH at a pH value of approximately 7.

Conclusions Regarding Sorption Behavior with Respect to Expected Variations in Groundwaters–Batch-sorption data for Pa suggest that sorption coefficients for this element will be small (less than 10 mL/g) at lower pH values (Tables 10.3-3, 10.3-4). Because Pa sorption experiments on rock samples from Yucca Mountain have only been carried out in the low pH range, it would be prudent to carry out several experiments using a Yucca Mountain groundwater at several pH values from 7 to 9.

10.3.3.7 Selenium

Behavior in Solutions Representative of Yucca Mountain Groundwaters–Selenium will occur as anionic species in all water compositions expected at Yucca Mountain. Although the two oxidation states of +4 and +6 (Howard 1977, p. 1665) are found for Se in surficial waters in contact with atmospheric O, the +4 state predominates under the conditions expected for groundwaters at Yucca Mountain (Howard 1977, Figure 1; White et al. 1991, Figure 9). In that state, Se is found as the SeO_3^{2-} and $HSeO_3^-$ selenite ions. In the +6 oxidation state, Se occurs as the SeO_4^{2-} and $HSeO_4^-$ selenate ions.

Qualitative Evidence for Behavior in the Surficial Environment–Selenium behavior in the surficial environment is very closely tied to the redox potential of different parts of the near-surface environment. Under reducing conditions, Se is immobilized as $FeSe_2$ at low pH (less than 5) and as native Se at higher pH (Howard 1977, Figure 3). The stability range for native Se extends nearly to surface redox conditions. When in contact with atmospheric O levels, Se is apparently stabilized as the selenite ion (SeO_3^{2-}). At higher redox potentials, Se is oxidized to the selenate ion (SeO_4^{2-}), which appears to be more mobile in the surficial environment than the selenite ion (Howard 1977, Figure 7, p. 167).

Data from the Literature–Because Se occurs as anionic species in the surficial environment, its adsorption behavior is controlled primarily by surface-complexation reactions on oxide minerals, including iron oxides and oxyhydroxides (Balistrieri and Chao 1987), manganese oxides and oxyhydroxides, clays (Bar-Yosef and Meek 1987) (Tables 10.3-3, 10.3-4), and other minerals with affinities for anionic species. These surface-complexation reactions are quite sensitive to pH. For example, adsorption on iron oxyhydroxides decreases for both selenite and selenate ions with increasing pH (Balistrieri and Chao 1987, Figure 2). Selenate ions appear to sorb dominantly in the outer layer of the electrical double layer present on oxide surfaces, whereas selenite tends to sorb in the inner layer (Hayes et al. 1987, p. 785). Selenate ions are subject to ionic-strength effects, as well as competitive effects with sulfate and other anions in solution, presumably because they sorb in the outer layer. Selenite ions are not subject to ionic-strength effects but may be subject to competition from other anions sorbing on inner-layer sites (Hingston et al. 1971).

Studies of selenite adsorption on soils in the pH range expected for Yucca Mountain groundwaters indicate relatively limited adsorption (less than 30 percent) from 0.05 nitrogen chloride solutions containing 0.16 to 0.63 mg/L Se (Neal et al. 1987, Figure 3, p. 1104). This limited sorption potential will likely be further decreased in natural waters containing high concentrations of competing anions.

Data from Laboratory Sorption Experiments with Yucca Mountain Rock and Water Samples–Data for Se sorption coefficients on Yucca Mountain rock samples in contact with J-13 water were summarized by Thomas (1987, p. 20, Appendix). Most measured values were less than 5 mL/g, and they do not appear to correlate with rock type. A puzzling feature of the data is that, for a given rock sample, sorption coefficients were larger in the higher pH experiments (pH of 8.8) compared to the lower pH experiments (pH of 6.0). This result is contrary to the pH dependence predicted on the basis of double-layer theories. Neal et al. (1987) noted a similar effect for Se sorption on soils for a solution phase enriched in Ca. They suggested the effect may

be due to the formation of a Ca-rich surface precipitate or, alternatively, a change in surface charge due to the adsorption of divalent Ca cations. Benjamin (1983) made similar observations involving other divalent cations. These data suggest that in groundwaters relatively enriched in Ca, and perhaps other divalent cations, Se adsorption may be somewhat enhanced in the alkaline pH range.

Conclusions Regarding Sorption Behavior with Respect to Expected Variations in Groundwaters–Sorption coefficients for Se on Yucca Mountain rock samples have only been measured in J-13 water. These experiments do not show the expected decrease in sorption coefficient with pH. Therefore, variations in pH over the range expected in Yucca Mountain groundwaters do not appear to be the most important groundwater compositional parameter in the sorption behavior of this element. Based on the data obtained in other studies, divalent cations may have a significant impact on the sorption behavior of this element in Yucca Mountain rock-water systems. Additional experiments with waters enriched in divalent cations (e.g., UE-25 p#1 water) may be productive and may enlarge the range of Se sorption-coefficient values appropriate for use in performance assessment calculations.

10.3.3.8 Uranium

Behavior in Solutions Representative of Yucca Mountain Groundwaters–Under the redox potentials expected in Yucca Mountain groundwaters, particularly in the unsaturated zone, U should be in the +6 oxidation state. In this oxidation state, U will be present in solution in a variety of complexes, including $(UO_2)_2CO_3(OH)_3^-$, $UO_2(CO_3)_2^{2-}$, $UO_2(CO_3)_3^{4-}$, $UO_2(OH)_2(aq)$, $UO_2(CO_3)(aq)$, and other minor species. Phosphate, fluoride, or sulfate species will not be significant within the concentration ranges for these anions and the pH range expected in Yucca Mountain groundwaters.

Qualitative Evidence for Behavior in the Surficial Environment–Data on the behavior of U in the surficial environment are available from various sources. Several types of U ore deposits were studied as natural analogs to repository settings. Other data include studies of U mill-tailings piles, waste-stream outfalls, and other U ore deposits. Only the natural analog studies are discussed in this section.

The deposits that were studied as natural analogs include the deposits at Oklo, Gabon, the Alligator Rivers region in Australia, Cigar Lake in Canada, Poças de Caldas in Brazil, and Peña Blanca in Mexico. Each deposit was studied in considerable detail to define the geochemical behavior of U and its daughter products in the environments in which the ore deposits are found. Although none of the environments is completely analogous to the Yucca Mountain site, the Peña Blanca deposit is at least situated in Tertiary volcanic tuffs similar to those present at Yucca Mountain. These natural analogs are discussed in detail in Section 13.

A critical aspect of any analog for potential U migration at the Yucca Mountain site is that the U source must be subject to redox potentials similar to those expected at Yucca Mountain, particularly in the unsaturated zone. This fact eliminates data from the Cigar Lake and probably the Oklo deposits (Goodwin et al. 1989, Appendix B.3.4; Cramer and Sargent 1994, p. 2238; Brookins 1983, pp. 206 to 207) from detailed consideration.

The Alligator Rivers deposits are exposed to oxidizing conditions in a surficial environment (Giblin and Snelling 1983, p. 37). Uranium isotope-disequilibrium studies at this site indicate that U migration has occurred relatively recently (Snelling and Dickson 1979). However, evidence for recent transport does not by itself provide an estimate of the transport rate and, more importantly, of the chemical controls on this rate. The latter information could be very useful to the YMP.

At the Koongarra deposit, U migration is significantly retarded by the precipitation of uranyl phosphate minerals (Snelling 1980). Although phosphate concentrations in local groundwaters are not high (0.01 to 0.1 mg/L), significant phosphate concentrations are found in the country rocks in minerals such as apatite. The phosphate in the rocks is apparently redistributed locally by groundwater, resulting in the precipitation of uranyl phosphate minerals within the zone of weathering (Snelling 1980). This retardation mechanism is not expected to be important at Yucca Mountain, given the low phosphate concentrations found in Yucca Mountain rock units (Broxton et al. 1986).

Uranium in the zone of weathering at Alligator Rivers also appears to be associated with, and is probably retarded by, ferric-Fe compounds (Payne et al. 1990). Sorption experiments were carried out involving U sorption on whole-rock samples and on pure mineral samples (Payne et al. 1990). These experiments suggest that ferric hydroxides are strong sorbers of U in this system over a pH range of 5 to 9. This result is not particularly new, as similar results on ferric oxyhydroxides were reported by others (e.g., Hsi and Langmuir 1985, p. 1931). A potentially important result of these studies would be the derivation of some defensible estimate of the rate of transport of U in this system using the experimentally derived chemical constraints on U adsorption behavior and a valid groundwater flow model. Unfortunately, hydrologists knowledgeable about the site suggest the complicated nature of the flow system may preclude the development of defensible flow models (S.N. Davis cited in Curtis and Fabryka-Martin 1988, 13.1).

The Peña Blanca U deposits in Mexico provide a potentially more appropriate analog site in relation to Yucca Mountain. The primary U deposits at this site are hydrothermal in origin and were emplaced in structural features associated with Tertiary silicic volcanic tuffs that overlie Mesozoic carbonate strata (George-Aniel et al. 1991, pp. 234 to 236). In addition to the hydrothermal deposits, which contain sulfide minerals as well as uranium oxides, supergene deposits have formed locally through the leaching of U from the volcanic rocks and subsequent precipitation as uranyl silicate minerals, including uranophane (Murphy 1992, p. 20). The supergene deposits are hosted by kaolinitized and silicified rhyolite and do not appear to contain sulfide minerals. The absence of sulfide minerals is important because sulfides, such as pyrite, oxidize readily in the surficial environment to produce acidic conditions unlike those expected within Yucca Mountain. The supergene deposits are thought to have formed in a near-surficial environment (George-Aniel et al. 1991, p. 246), and their study may offer useful insight into the potential for migration of U from the potential repository within Yucca Mountain.

A qualitative study by Rosholt et al. (1971) established that U was leached from devitrified tuff samples, but not from hydrated glassy samples obtained from a given geologic unit. These and other data presented suggest devitrification makes the U in tuffs more mobile in the surficial environment. Zielinski et al. (1986) and Flexser and Wollenberg (1992, Abstract, pp. 1593 to

1598) observed that U in Yucca Mountain devitrified tuffs was commonly associated with manganese oxides. This fact suggests that, although U may be mobile in the unsaturated devitrified tuffs in Yucca Mountain, it could be retarded to the extent that there are manganese oxides present along the flow path with sufficient capacity to sorb the potential flux of U from the potential repository horizon. Given the amount of U to be emplaced in the potential repository, it would seem the sorption capacity of the manganese oxides present in the mountain (Bish and Chipera 1989) would be rapidly saturated. Nonetheless, manganese oxides may significantly retard the movement of U in some of the fracture-flow scenarios.

Data from the Literature–Data have been presented in the literature on the adsorption of U as U (VI) onto a variety of pure mineral phases in simple electrolytes. Among the solid phases investigated are goethite (e.g., Hsi and Langmuir 1985), hematite (Ho and Miller 1986), silica gel (Zielinski 1980), clays (Tsunashima et al. 1981), and zeolites (Ames et al. 1983, Table 2). The results reported are sometimes difficult to reconcile. For example, Hsi and Langmuir (1985, Figure 2) reported that hematite sorbs very little of the U in solutions with 5×10^{-5} M U and 1×10^{-3} M total carbonate, whereas Ho and Miller (1986, Figure 1) reported that hematite sorbs up to 100 percent of the U in their experiments with similar U and bicarbonate solution concentrations. Both sets of experiments had similar hematite surface areas. The main difference was that the solution phase in the Hsi and Langmuir (1985) experiments also contained 0.1 M $NaNO_3$. However, $NaNO_3$ is generally considered to be a nonreactive electrolyte, and nitrate does not form complexes with U in the pH range addressed in these experiments. Why there is a difference in these results is unclear. One possibility is that the surface characteristics of the solid phases used were not the same in the two sets of experiments.

Silica gel appears to have a clear affinity for U as established by the results of laboratory experiments and by observations on the association of U with opals in nature (Zielinski 1980). According to Maya (1982), the U is adsorbed to silica gel as the uranyl ion, free of carbonate ligands. Zielinski (1980) has shown that sorption of U onto silica gel is sensitive to the total carbonate concentration of the solution phase when this concentration is above 0.01 M. Interestingly, experiments carried out at elevated temperatures (65° to 80°C) resulted in somewhat higher sorption coefficients. Data regarding competitive effects on silica gel between U and other constituents in groundwaters at near-neutral pH were not found in the literature.

Sorption of U by clays was investigated in some detail. Borovec (1981, Figure 2, Table 111) presented data that indicate montmorillonite has a high selectivity for uranyl ions relative to divalent ions of zinc, Mn, Ca, Mg, cobalt, cadmium, and Ni at a pH value of 6 in chloride solutions. However, Tsunashima et al. (1981) found montmorillonite has a greater selectivity for Ca, Mg, and Ba ions than for uranyl ions in nitrate solutions over the pH range from 4.0 to 4.5. Montmorillonite was found to have a greater selectivity for the uranyl ion than for Na and K ions in the same solutions. Ames et al. (1983, Tables 5 to 7) found that U was strongly sorbed to montmorillonite from 0.01 M NaCl solutions but weakly sorbed from 0.01 M $NaHCO_3$ solutions in the pH range from 8 to 9.

Because groundwaters in Yucca Mountain contain significant concentrations of bicarbonate, Ca, and Mg ions, these data suggest overall that uranyl ions may not compete favorably for exchange sites on clay minerals in Yucca Mountain, although quantitative prediction of the extent of exchange would require more detailed analysis.

Data available on U sorption on zeolitic minerals are very limited. Ames et al. (1983, pp. 329 to 331) report that clinoptilolite has a low affinity for trace levels of U in the pH range from 8 to 9 in 0.01 M $NaHCO_3$. Doi et al. (1975, p. 637) found that U at concentrations of 10^{-6} g per gram of solution was strongly sorbed onto clinoptilolite from perchlorate solutions in the pH range from 4 to 8.5.

Data from Laboratory Sorption Experiments with Yucca Mountain Rock and Water Samples–Data on U sorption coefficients for Yucca Mountain rock-water systems were reported by Thomas (1987, p. 20, Appendix) and discussed by Meijer (1990, 1992). The affinity of the devitrified and vitric tuffs for trace levels of U is generally small (K_d less than 5 mL/g) over the pH range from 6 to 9 in J-13 water. For zeolitic tuffs, the K_d is near zero at a pH value of 9 but increases with decreasing pH to values of approximately 25 mL/g at a pH of 6 in J-13 water. This behavior suggests the uranyl cations can exchange with the major cations in zeolites.

In p#1 water, U batch-sorption experiments were only carried out in the pH range from 8.3 to 9.3 with the result that measured sorption coefficients were small (0 to 2.7 mL/g) (Thomas 1988, Table 4, p. 26). A devitrified sample showed the largest sorption coefficient. In the pH range from 6 to 8, it is expected that the sorption coefficients for U in UE-25 p#1 water will increase with decreasing pH (because of predominance by $UO_2CO_3^0$ at higher pH values), but they will likely be smaller than the coefficients obtained for the same rock samples in J-13 water over this pH range. In H-3 groundwater, sorption coefficients were also low for zeolitic and devitrified rock types over the pH range from 9.2 to 9.3, presumably reflecting the elevated carbonate content of this water. However, data for a vitric sample showed a value of 6.2 mL/g for the U sorption coefficient at a pH value of 9. This relatively high value was not explained.

The sorption of U (VI) onto samples of the three types of tuff in J-13 water (under oxidizing conditions) at the two pH values (7 and 8.5) was studied. However, to identify the sorbing minerals in the tuffs, sorption onto the pure minerals hematite, clinoptilolite, albite, and quartz was also studied. It was found that U in J-13 water does not sorb onto devitrified and vitric tuffs, albite, and quartz (Table 10.3-7).

Wet-sieved tuffs, albite, and quartz samples with particle sizes ranging from 75 to 500 μm were used. Initial U concentrations ranged from 8×10^{-8} to 1×10^{-4} M. The pretreatment period was 2 to 4 days, and the sorption period was 3 to 4 days. The negative values reported in Table 10.3-7 are the result of analytical error for the case of very little sorption (i.e., a small number obtained as the difference of two large numbers). For the experimental conditions cited, U sorption onto zeolitic tuffs and clinoptilolite is nonlinear and can be fitted with Freundlich and Langmuir isotherms (Figures 10.3-9 and 10.3-10).

For the clinoptilolite-rich zeolitic tuff sample G4-1510, the scatter in the data makes it impossible to conclude whether there is a significant difference between the experiments performed under a carbon-dioxide overpressure and a pH of 7 or at atmospheric conditions and a pH of 8.5 (Figure 10.3-10). However, the experiments with pure clinoptilolite indicate that sorption increases with decreasing pH for U (VI) (Figure 10.3-10), as is the case for Np (V). Because the major constituent of tuff sample G4-1510 is clinoptilolite, predictions of the K_a (K_d divided by the solid-phase surface area) were made for U sorption onto this tuff by assuming that clinoptilolite is the only sorbing phase. Inspection of Table 10.3-8 indicates that reasonable

predictions are obtained with this assumption for a pH of 7 but not for a pH of 8.5. In all cases, predictions based on clinoptilolite sorption are conservative.

The sorption of U onto pure iron oxides (e.g., hematite) is very large (and large uncertainties in the K_d values result from measuring the small amounts of radionuclide left in solution after sorption). Although the measured sorption of U onto pure hematite is very large, sorption onto devitrified tuffs, which appear to have traces of hematite (1 percent ± 1), is essentially zero. As with Np, this result could be due to differences in the surface of pure hematite compared to hematite in tuff, or it could be due to passivation of the hematite surfaces in the tuff by elements (e.g., the rare earths) that have a higher affinity for hematite than U and, thus, occupy the sorption sites.

Conclusions Regarding Sorption Behavior with Respect to Expected Variations in Groundwaters–The dominant groundwater compositional controls on the sorption behavior of U on Yucca Mountain rock samples will likely be pH, carbonate content, and the concentrations of Ca and Mg ions in solution. The pH and carbonate contents influence the sorption largely as a result of the decrease in carbonate complexation of U with decreasing pH. These two parameters are therefore not entirely independent. However, different water compositions can have different carbonate contents at a given pH. The expectation is that waters with higher carbonate contents will be associated with lower sorption coefficients. This trend would apply to both ion-exchange and surface-complexation sorption mechanisms. However, decreasing pH will have different effects on U sorption behavior in zeolitic and clay-rich samples versus devitrified and vitric samples. In the former samples, the U sorption coefficient will likely increase with decreasing pH due to the increase in uranyl ion concentrations with decreasing pH. For a given rock-water system, the magnitude of this increase will depend on the concentrations of competing ions, such as Ca and Mg. For high Ca and Mg waters, the competition effects will be substantial. Because unsaturated zone waters are relatively enriched in Ca and Mg, U sorption coefficients in the unsaturated zone might be on the low end of the range reported to date (Thomas 1987, p. 29; 1988, Table 4, p. 28), unless the low total carbonate concentrations in these waters balance the effect of the elevated Ca and Mg concentrations.

It will be important to carry out experiments on representative rock samples using a high-Ca-and-Mg, low-carbonate, unsaturated zone water composition with pH controlled over a range from 6 to 9. Similar experiments should be carried out with a high total-carbonate and high Ca-and-Mg water composition, such as UE-25 p#1 water, over the pH range from 6 to 8.

10.3.3.9 Carbon, Chlorine, Iodine, and Technetium

Because C, Cl, and I are unlikely to have significant sorption affinity in the rock-water systems expected at Yucca Mountain, their sorption behavior is not discussed in detail. For C, the most robust retardation mechanism will be isotopic exchange with stable C isotopes in groundwater and on carbonate mineral surfaces (Meijer 1993, Abstract, p. 110).

Chloride and iodide ions will have no significant retardation in Yucca Mountain rock-water systems and may even have slightly enhanced migration rates due to anion-exclusion effects (Ogard and Vaniman 1985, p. 7). If conditions were to become sufficiently oxidizing to convert iodide to iodate, some retardation of I might occur in the flow system. Although such conditions

might occur locally, for example, due to radiolysis, it is considered unlikely that such conditions would be present over a significant volume of the flow system for an extended time.

Technetium appears to show nonzero, although minimal, retardation in Yucca Mountain rock-water systems (Ogard and Vaniman 1985, p. 44; Table 10; Rundberg et al. 1985, pp. 65 to 69; Thomas 1988, p. 31). However, the cause of this retardation was not identified, and it may simply be an experimental artifact. Because the minimal values obtained for Tc sorption coefficients to date will not result in significant retardation of Tc, it does not seem prudent to expend funds on the detailed investigation of potential sorption mechanisms for this element. More significantly, if sufficiently reducing conditions could be shown to exist in portions of the flow system downgradient of the potential repository, retardation of Tc by the precipitation and sorption of Tc^{4+} species might occur.

10.3.4 Effects of Organics on Actinide Sorption

Naturally occurring organic compounds generated during the transformation of plant and animal debris over time and as a result of the synthetic activities of microorganisms are ubiquitous in surface and subsurface environments. For example, pore water from a well-developed soil environment usually contains dissolved organic C in quantities greater than 20 mg/L in top soils and in quantities of about 5 mg/L in subsoils. Dissolved organic C concentrations in groundwaters typically depend on the environment and are usually below 2 mg/L (Drever 1988, p. 46). The decrease in concentrations of organic materials with increasing depth is attributed to chemical and biological degradation as well as to sorption on mineral surfaces. Sorption of organic materials onto mineral surfaces is considered the dominant contributing factor to the removal of organics from solution during percolation through the subsurface.

The interaction between organic materials and mineral surfaces in the natural environment is important to mineral surface geochemistry. Sorption of organic material onto mineral surfaces affects not only the solubility and charge of the organic materials in solution but also the properties of the mineral surfaces, such as their charge and hydrophobicity, thereby altering the reactivity of the mineral toward metal ions. A clear understanding of the effects of the organic materials that frequently coat mineral surfaces in natural environments will lead to improvements in the sorption models used to predict the mobility of radionuclides in natural aquatic environments (Choppin 1992).

The objective of this section is to summarize the laboratory results for the effect of organic materials on the sorption of Pu and Np on selected mineral oxides and tuff material.

10.3.4.1 Experimental Conditions

Under the experimental conditions used in this work, the Pu and Np are expected to exist as the chemical species PuO_2^+ and NpO_2^+, respectively. Synthetic boehmite, goethite, hematite, ferrihydrite, and a crushed natural tuff material from Yucca Mountain served as model sorbents (boehmite served as an end member in relation to Yucca Mountain tuffs). Details of the methods for preparing the oxides are described in the literature (Kung and McBride 1989a, 1989b, 1991, pp. 702 to 703).

The surface area of the oxides, calculated from N_2 adsorption by the three-point Brunauer-Emmett-Teller method (Gregg and Sing 1967, Chapter 2), was 89.5 m^2/g for goethite, 91.5 m^2/g for ferrihydrite, 39.4 m^2/g for hematite, and 324 m^2/g for boehmite. X-ray powder diffraction analysis of the crushed tuff material (USW G-4 270) indicated that it was about 30 percent quartz and 69 percent feldspar, the remainder consisting of trace amounts of layer silicates and iron oxide.

Catechol, alanine, dihydroxyphenylalanine (DOPA), and Nordic aquatic fulvic acid (NAFA) were used as model organic materials. Alanine is an amino acid that will complex with the hard acid type of metal ions in solution. Catechol is a phenolic compound that may chelate with metal ions and undergo redox reaction with the metal. DOPA, a naturally occurring amino acid commonly found in plant seedlings, pods, and broad beans, was chosen because it contains well-defined organic functional groups, such as carboxylic acid, amine, and phenols.

10.3.4.2 Results and Discussion

10.3.4.2.1 Neptunium

Sorption as a Function of Tuff and Oxide Minerals–The isotherms for Np sorption on different iron oxides are shown in Figure 10.3-11. In this experiment, hematite, goethite, and ferrihydrite were used as sorbents. Results show that, on a weight basis, hematite was the most adsorptive, whereas goethite was the least adsorptive. The sorption of Np on model iron oxides follows the order hematite > ferrihydrite > goethite.

Two things should be noted in this study. First, the surface areas of these iron oxides were different. The sorptivity of Np on these iron oxides was not compared on a unit surface area basis. For ferrihydrite and goethite, the surface areas are around 90 m^2/g. The surface area of hematite is about 40 m^2/g. Higher surface areas are expected to have higher sorptions. Second, the sorption experiments were not conducted at the same pH. Sorption on ferrihydrite was conducted at pH 6.2. Sorption on hematite and goethite was conducted at pH 6.9. The pH may affect the sorptivity of Np on iron oxides, and this effect will be presented in the next section.

Effect of pH on Sorption–To quantify organic sorption, it is required that the effect of organics on radionuclide sorption must be understood. Experiments were conducted to study organic sorption, and the results are presented in this section. The isotherms for DOPA adsorption on goethite and boehmite at different pH levels are shown in Figure 10.3-12. By weight, boehmite was more adsorptive than goethite. The linear sorption curves for these materials suggest low coverage of the surface reactive sites by the organic material in the presence of excess potassium chloride. This finding is consistent with the theoretical calculation of coverage, which suggests that the amount of DOPA sorption is much less than a monolayer, based on the Brunauer-Emmet-Teller surface area measurement method (Gregg and Sing 1967, Chapter 2).

Increasing the solution pH resulted in a higher organic sorptivity for all oxides. Under neutral and slightly acidic conditions (pH 5.5 to 7), iron and aluminum oxides were expected to have positive surface charges (Sposito 1989). However, the sorption of DOPA on all sorbents was found to increase as solution pH increased despite the fact that the surface charge of silicon oxide is opposite that of iron and aluminum oxides. Although the sorption of DOPA apparently does

not depend on surface-charge effects such as electrostatic attraction, it may be controlled by the deprotonation process of the organic material. DOPA is expected to be dominated by neutral species under neutral and slightly acidic conditions, but raising the pH level will increase the concentration of deprotonated DOPA species, which are expected to have a stronger affinity for oxide surfaces in direct surface complexation. Therefore, it is reasonable to assume that DOPA forms direct surface bidentate complexes on the oxide surfaces. The isotherms for Np sorption on goethite at different pH levels are shown in Figure 10.3-13. Increasing the solution pH from 6.2 to 6.9 resulted in a higher Np sorptivity.

Effect of Model Organics on Sorptive Behavior–The study examined the effect of natural organics on radionuclide sorption onto natural tuff material that may have been precoated with natural organic material. The standard method for removing the natural organic material from mineral samples is to use hydrogen peroxide to oxidize the organic matter (Kunze and Dixon 1986, pp. 95 to 97). In these experiments, a 15 percent hydrogen peroxide solution was used to remove the possibly presorbed natural organic from the crushed tuff material collected from Yucca Mountain. In sorption experiments conducted to study the effect of the naturally presorbed organics on Np sorption on tuff materials, half of the samples were treated with hydrogen peroxide, half were not.

Figure 10.3-14 shows the sorption isotherms of Np on both types of tuff samples. The results suggest that treatment with hydrogen peroxide had little or no effect on the sorption of Np onto the tuff material.

The lack of effect of hydrogen peroxide treatment on Np sorption on tuff materials is attributable to three factors. First, untreated tuff may contain very little or no organic material on its surface. Low organic content on the untreated tuff surface could be expected because crushed tuff material is generated from bedrock that may have little exposure to natural organic materials. New surfaces generated during the crushing process would not contain organic materials, in which case untreated tuff would be expected to behave essentially the same as tuff treated with hydrogen peroxide. Second, Np has intrinsically low sorptivity on tuff material. No observable difference in sorption on both treated and untreated tuff is attributed to the low sorption of Np on both sorbents. Any minute differences in sorption are likely to occur below the level of detection. Third, the sorption of Np may be unaffected by organic material, assuming that organic materials such as DOPA do not influence Np sorption on tuff, goethite, or boehmite.

To explore the possibility that the untreated tuff contained little organic material, 4 to 50 μM of DOPA were purposely added to both treated and untreated crushed tuff materials, and the sorption isotherms of Np on these systems were compared. As Figures 10.3-15 and 10.3-16 illustrate, the addition of DOPA had no effect on Np sorption on either treated or untreated crushed tuff materials. These data thus support the premise that the presence of organic material does not affect Np sorption on tuff materials.

Because this experiment did not rule out the possibility that the lack of an observable effect was a result of the intrinsically low sorptivity of tuff materials, the sorption of Np on iron and aluminum oxides in the absence and presence of DOPA was examined. The sorption of Np is expected to be much higher on iron and aluminum oxides than on tuff material. Thus, any effect of DOPA on Np sorption ought to appear in the oxide systems. To verify this assumption,

sorption isotherms were measured for Np on iron and aluminum oxides and tuff material in the absence of organic materials with 0.1 M KCl at pH 6.2. The results presented in Figure 10.3-17 indicate that the sorptivity of boehmite and goethite is approximately one and two orders of magnitude higher, respectively, than the sorptivity of tuff material. Thus, any effect of DOPA on Np sorption should be easily detectable in these oxide systems.

Neptunium sorption isotherms on iron and aluminum oxides in the presence of DOPA are shown in Figures 10.3-18 and 10.3-19. In these experiments, 0.1 M KCl was used to maintain an essentially constant ionic strength, and the final pH of the suspensions was adjusted to 6.2. The initial Np concentration ranged from 0.2 to 2 μM, and the initial DOPA concentration ranged from 4 to 50 μM. The sorption isotherms of Np on aluminum and iron oxides suggest that DOPA does not significantly affect the sorption of Np. The relatively weak complexation of the pentavalent Np ion is a result of its relatively low effective charge on the cation (Choppin and Rao 1984, p. 146). These results imply that there is no significant influence of DOPA on Np sorption on aluminum and iron oxides.

The occurrence of surface complexation between DOPA and oxide surfaces is supported by the observed sorption of catechol on metal oxide, which indicates that catechol chemisorbs on metal oxide by forming a bidentate complex with surface metal. DOPA is an organic with functional groups like catechol (phenols) and alanine (amino acids). Thus, the effect of simple organics such as catechol and alanine on the sorption of Np was studied. Both catechol and alanine are expected to complex with metal ions in solution. Besides the formation of metal-organic complexation, catechol readily undergoes redox reactions with some metal and metal oxides (McBride and Wesselink 1988). For example, catechol at high concentrations may undergo electron transfer reactions with manganese and iron oxides. The effect of catechol and alanine on Np sorption was quantified by sorption isotherms.

Neptunium sorption isotherms on hematite, ferrihydrite, and goethite in the presence and absence of catechol and alanine are shown in Figures 10.3-20 to 10.3-22, respectively. In these experiments, 0.1 M KCl was used to maintain an essentially constant ionic strength. The final pH of the suspensions was adjusted to 6.2 for ferrihydrite and to 6.9 for goethite and hematite. The initial Np concentration ranged from 0.2 to 2 μM, and the initial catechol and alanine concentrations were 1 μM. The sorption isotherms of Np on iron oxides suggest that catechol and alanine do not significantly affect the sorption of Np. These results imply that there is no significant influence of catechol and alanine on Np sorption on different iron oxides (CRWMS M&O 2000, Section 6.4.4.2).

Although both catechol and alanine may complex with Np in solution, the organic-metal complexes are apparently not strong enough to affect the Np sorption. These results are consistent with the data obtained from Figure 10.3-18, which indicate that DOPA has no effect on Np sorption.

In another set of experiments to study the effect of naturally occurring organic material on Np sorption, NAFA served as the model fulvic material. The sorption isotherms of Np on boehmite in the presence and the absence of NAFA are shown in Figure 10.3-23. The sorption isotherms of Np on goethite in the presence and the absence of NAFA are shown in Figure 10.3-24. Sorption isotherms of Np on treated tuff materials are shown in Figure 10.3-25. Sorption

isotherms of Np on untreated tuff materials are shown in Figure 10.3-26. In these experiments, 0.1 M KCl was used as the background electrolyte, and the final pH was adjusted to 6.2. Initial Np concentrations ranged from 0.2 to 3 μM, and NAFA concentrations ranged from 0.1 to 0.4 ppm. As shown in Figures 10.3-23 to 10.3-26, NAFA had little effect on Np sorption in all systems. Thus, it is concluded that organics do not affect the sorption of Np in both simple, low-molecular-weight organics and naturally occurring fulvic organic material. The lack of detectable effects of organics on Np sorption is possibly attributed to the stable redox state of Np (V) in solution and to low complexation between Np ions and organic chemicals.

10.3.4.2.2 Plutonium

Sorption as a Function of Tuff and Oxide Minerals–Plutonium sorption on different materials is shown in Figure 10.3-27. By weight, hematite was the most adsorptive, whereas goethite was the least adsorptive. The sorption of Pu follows the order hematite > ferrihydrite > goethite. Two things should be noted in this result. First, the surface areas of these iron oxides were not the same. For ferrihydrite and goethite, the surface areas are around 90 m^2/g; for hematite, the surface area is about 40 m^2/g. Second, the sorption experiments were not conducted at the same pH. The sorption on ferrihydrite was conducted at pH 6.1, the sorption on goethite was conducted at pH 6.6, and the sorption on hematite was conducted at pH 6.9. The effect of oxide surface areas on Pu sorption was replotted in Figure 10.3-28, with the amount of Pu sorption normalized to unit surface area (m^2). Results again showed that the sorption of Np follows the order hematite > ferrihydrite > goethite (Triay et al. 1997, p. 157). The effect of pH on Pu sorption is presented in the next section.

Effect of pH on Sorption–The isotherms for Pu sorption on goethite at two different pH levels are shown in Figure 10.3-29. Increasing the solution pH from 6.6 to 6.9 resulted in a higher Pu sorptivity. It should be noted that the initial Pu concentration was the same for both isotherms; however, the amount of goethite was different. The linear sorption curves suggest a low degree of coverage of the surface reactive sites by Pu ions in the presence of excess potassium chloride. This finding is consistent with the theoretical calculation of coverage, which suggests, based on Brunauer-Emmet-Teller surface areas, that the amount of Pu sorption is much less than a monolayer.

Increasing the solution pH resulted in a higher Pu sorptivity. Under neutral conditions (pH 7), goethite is expected to have positive surface charges. However, the sorption of Pu on goethite was found to increase as solution pH increased. The sorption is believed to be controlled by a surface-complexation process because Pu is expected to be dominated by the cationic species PuO_2^+ under neutral and slightly acidic conditions.

Effect of Model Organics on Sorptive Behavior–The isotherms for Pu sorption on ferrihydrite in the presence of catechol and alanine are shown in Figure 10.3-30, and the isotherms for Pu sorption on goethite and hematite in the presence of catechol and alanine are shown in Figure 10.3-31. These sorption isotherms clearly demonstrate that the sorption of Pu onto goethite and ferrihydrite was affected by the presence of the organic materials. The amount of Pu sorption on goethite and ferrihydrite was lower in systems that contained alanine than in systems that contained no alanine. Apparently, the presence of alanine suppressed the Pu sorption on goethite and ferrihydrite. The inhibition of Pu sorption on the iron-oxide surface in

the presence of alanine is probably caused by the lowering of the free Pu ion activity in solution by formation of an alanine-Pu complex. Conversely, the amount of Pu sorption on goethite and ferrihydrite was higher in the presence of catechol than it was in the absence of catechol. Evidently, catechol enhanced the sorption of Pu on goethite and ferrihydrite.

However, the effect of catechol and alanine on Pu sorption was not found in the hematite system. The presence of catechol and alanine had little effect on the sorption of Pu on hematite (Figure 10.3-31). The lack of an observable effect from the presence or absence of catechol and alanine on Pu sorption on hematite is probably a result of the intrinsically high sorptivity of Pu on hematite. Any small enhancement or suppression of sorption that might be attributed to catechol and alanine under such a high sorptivity would not be detected. Results of this study suggest that the model organic materials catechol and alanine do affect the sorption of Pu on iron oxides.

The isotherms for sorption of Pu on ferrihydrite and goethite in the absence of DOPA and in its presence at three concentration levels (1×10^{-6}, 1×10^{-7}, and 1×10^{-8} M) clearly demonstrate (Figures 10.3-32, 10.3-33) that such sorption was affected by the presence of the organic material DOPA. Plutonium sorption was higher in systems that contained DOPA than in systems that did not contain DOPA. Furthermore, sorptivity increased as initial DOPA concentration increased from 1×10^{-8} to 1×10^{-6} M. Evidently, the presence of DOPA enhanced Pu sorption on goethite and ferrihydrite. This result is likely attributed to the formation of stable surface DOPA-Pu ternary complexes and a redox reaction between DOPA and Pu. Reduction of Pu (V) to lower oxidation states will enhance the sorption/precipitation of Pu. However, the effect of DOPA on Np sorption was not found in goethite (Figure 10.3-18), boehmite (Figure 10.3-19), and tuff material (Figure 10.3-16). The presence of DOPA had little effect. It is possible that DOPA does not complex with Np in solution and/or that DOPA cannot reduce Np (V) to lower oxidation states. Such relatively weak complexation is possibly a result of the relatively low effective charge on the cation (Choppin and Rao 1984, p. 146), consistent with the fact that Np complexed weakly with a natural humic material extracted from a groundwater (Kim and Sekine 1991).

10.3.4.2.3 Effect of Humic and Fulvic Acids on Sorptive Behavior on Tuff Material in Groundwater

The sorption of Pu (V) on three tuff materials, vitric tuff (Gu3-1496), devitric tuff (G4-275), and zeolitic tuff (G4-1529), collected from Yucca Mountain in natural J-13 and synthetic UE-25 p#1 groundwater, is shown in Figures 10.3-34 to 10.3-39. The results indicate that no conclusive effects of aquatic humic and fulvic acids on Pu (V) sorption could be identified on all tuff materials.

The Pu (V) species was not stable in the presence of fulvic and humic acids in natural J-13 and synthetic UE-25 p#1 groundwaters. This fact is especially obvious for Pu (V) in natural J-13 groundwater with humic acid. As shown in Table 10.3-9, about 11 percent of Pu (V), on average, disappeared from natural J-13 water in the presence of fulvic acid during the sorption experimental processes (Triay et al. 1997, pp. 158 to 159). For humic acid, about 19 percent of Pu (V), on average, disappeared from natural J-13 water during the sorption experimental processes (Table 10.3-10). However, Pu (V) is relatively more stable in the presence of organic

materials in synthetic p#1 groundwater than in natural J-13 water. For example, about 4.7 percent of Pu (V), on average, was lost in fulvic acid environments and 7.3 percent of Pu (V) disappeared from solution in the presence of humic acid (Tables 10.3-11, 10.3-12). Because the reason that Pu (V) disappears from solution phase in these groundwater environments is unknown, control concentrations for each organic and water condition were used to obtain the sorption data presented in Figures 10.3-34 to 10.3-39. It should be noted that no Pu (V) disappearance was observed in the sorption experiments conducted in 0.1 M KCl solution.

10.3.4.3 Summary of Effects of Organics on Actinide Sorption

From the sorption data, the following conclusions can be drawn concerning the effect of natural organic materials on Np and Pu sorption by iron and aluminum oxides and crushed tuff material:

- The sorption of model organic material DOPA on oxide surfaces follows the order aluminum oxide > iron oxide. For a given sorbent, the higher the pH, the more DOPA is sorbed. Surface complexation is the most likely sorption mechanism.

- The sorption of Pu generally follows the order hematite > ferrihydrite > goethite. The sorption of Np on iron oxide is higher than that on aluminum oxide. The sorption of Np on crushed tuff material was much lower than that on oxide surfaces.

- The sorption of Pu and Np on iron oxides increases as the solution pH is raised. The sorption of Pu is much higher than that of Np on hematite, goethite, and ferrihydrite.

- The amount of Np sorption was not affected by any organic materials that were studied. The presence of the model organic materials alanine, catechol, DOPA, and NAFA did not influence the sorption of Np on tuff or on iron and aluminum oxides. This lack of an observable effect is presumably a result of the weak complexation between Np and the model organics.

- The sorption of Pu was influenced by the presence of DOPA on goethite and ferrihydrite. Increasing the amount of DOPA resulted in higher sorption of Pu on goethite and ferrihydrite. Alanine decreased the sorption of Pu. However, in the system containing catechol, Pu sorption was increased. The enhancement of Pu sorption in the presence of catechol is probably due to the reduction of Pu (V) to Pu (IV) by the organic. The inhibition of Pu sorption in the presence of alanine is probably caused by the lowering of the free Pu -ion activity in solution by formation of an alanine- Pu complex. No observable effect of organics on Pu sorption was found in the hematite system, which is probably due to a relatively high sorptivity of Pu on the hematite surface.

10.3.5 Cation Exchange and Surface Complexation

10.3.5.1 Cation Exchange

Description of Cation Exchange Sites in Yucca Mountain Tuff–Detailed adsorption isotherms adequate for the analysis described above have not been done for the YMP. Measurements of the mineralogy of Yucca Mountain tuffs have shown an abundance of minerals known to have

both pH-independent cation exchange sites (that is, tetrahedral Al sites) and surface complexation sites (e.g., clay edge sites) for outer-sphere surface-complex formation. The most abundant minerals found in Yucca Mountain tuffs (Bish et al. 1983, Figure 2; Daniels et al. 1982) with a high cation exchange capacity are listed in Table 10.3-13.

In addition to the minerals listed in Table 10.3-13, feldspars may be important cation exchangers in the devitrified tuffs. Cation exchange capacity for a feldspar is not an intrinsic property because only the external surfaces are available for exchange. Thus, the number of sites depends on the crystal size and morphology.

State of Knowledge of Cation Exchange with Respect to Yucca Mountain Tuffs–As early as 1983 (Daniels et al. 1982), it was shown that the sorption distribution coefficient, K_d, for the adsorption of Cs onto Yucca Mountain tuffs could be predicted to within a factor of three using literature data for the cation exchange on the minerals in Table 10.3-13 with the addition of analcime. These predictions only considered competition with Na. This simplification was made because there were no data for the cation exchange of the other alkali metals and alkaline earths present in J-13 well water. Some of the observed scatter could possibly be reduced with these additional data. Unfortunately, since 1983, the situation has not changed. Thus, there is no predictive model based on mineralogy for cation exchange for radionuclides other than Cs.

The relative contribution of cation exchange to the adsorption of neptunyl onto the zeolitic tuff sample G4-1506 from a sodium-bicarbonate solution was determined. The experiment was based partly on the method of Baeyens and Bradbury (1995a, 1995b). Crushed tuff G4-1506 was equilibrated with 1 M sodium perchlorate to remove alkali metals and alkaline earths by mass action. Solutions containing 0.0022 M sodium bicarbonate (as a pH buffer) were prepared with sodium perchlorate added to provide Na concentrations that varied from 0.0022 to 0.22 M. Distribution coefficients for Np were determined using the standard procedure (Figure 10.3-40).

The surface complexation of neptunyl was shown to be inner sphere and noncharging. Therefore, the surface complexation of Np is expected to be largely independent of Na-ion concentration. The results show a linear decrease in K_d with Na concentration at low Na concentrations, which is consistent with cation exchange. At high Na concentrations, the K_d asymptotically approaches 2.5 mL/g, consistent with surface complexation. The ion-exchange component is larger than the surface-complexation component, which corresponds to a K_d of about 10 in 0.0022 M sodium bicarbonate. The relatively low K_d for neptunyl in a zeolitic tuff is likely due to the large ion size and high hydration number. The K_d in pure sodium bicarbonate solution is larger than that observed in J-13 water; this effect is due to competition with the additional cations in J-13 water of Ca, Mg, and K. A model that describes these data and predicts Np sorption in the zeolitic tuff of Calico Hills will be described in the next section.

10.3.5.2 Surface Complexation

Modeling of Yucca Mountain Tuff–A surface-complexation model for Np adsorption onto the zeolitic tuff sample G4-1506 was developed to fit the Na-concentration dependence. The model considered a simple ion-exchange mechanism:

$$AlO^{-}Na^{+} + NpO_2^{+} \leftrightarrow AlO^{-}NpO_2^{+} + Na^{+} \qquad \text{(Eq. 10.3-5)}$$

and the formation of an inner-sphere surface complex with octahedral alumina (edge sites) or hematite:

$$AlOH + NpO_2^+ \leftrightarrow AlONpO_2 + H^+ \qquad \text{(Eq. 10.3-6)}$$

The number of cation exchange sites available to Np (tetrahedral aluminum site density of 2×10^{-4} eq/kg [Triay et al. 1997, Table 55]) was based on the apparent saturation of sites observed in a Np adsorption isotherm measured for tuff sample G4-1608 in a carbon-dioxide atmosphere (Thomas 1987, pp. 57 to 58). The Np exchange capacity is four orders of magnitude smaller than the cation exchange capacity of clinoptilolite (Table 10.3-13). This difference can be explained by the large size of the hydrated neptunyl ion. If no sorption occurs in the intracrystalline channels of the clinoptilolite, the maximum exchange capacity will be on the order of a micromole per gram, assuming a 3-μm crystal diameter. The selectivity for Np was used as an adjustable parameter, and the model was fit to the results of the Na-ion dependence of Np adsorption onto tuff sample G4-1506.

The inner-sphere surface complexation of Np was modeled, assuming that surface complexation occurs primarily on clay-edge sites or iron-oxide surfaces. The constant for inner-surface complexation of Np onto iron oxide was used because the analogous constant for alumina is expected to be nearly equal on the basis of the hard-soft, acid-base theory shown above. Thus, the second adjustable parameter was the edge-site density.

To extend this model to the empirical measurements done under the YMP's geochemistry program, additional assumptions were made. The competition of cations in groundwater for cation exchange sites was based on the selectivities derived from measurements on the mineral tobermorite (Tsuji and Komarneni 1993). This approach was the result of the argument explaining the reduced cation exchange capacity for Np. If exchange occurs only on the exterior of the zeolite crystal, then steric effects must be avoided. Tobermorite offers an open structure that could be expected to have less steric effects than a zeolite. Furthermore, that work showed little difference between Mg and Ca so that both Mg and Ca were treated as one competitor. There were no data for K, so competition with K was not considered.

The surface-complexation constant for Ca was taken from the hard-soft, acid-base theory. Thus, there were no additional adjustable constants. The concentrations used for UE-25 J-13 and p#1 well water are shown in Table 10.3-15. The calculations were made using the FITEQL equilibrium code in the forward mode only, that is, no fitting. The results of the modeling are shown in Figures 10.3-41 and 10.3-42. The correct pH dependence was predicted for the dry-sieved samples; the wet-sieved samples agreed better with a calculation that had no surface complexation sites. The implications of these results are not yet fully understood. Two possibilities are that either the clay particles are washed out, reducing the available edge sites, or that a trace component of J-13 water is forming a strong surface complex that competes with Np. The model also predicted the observed reduction in the sorption distribution coefficient, K_d, due to the components of UE-25 p#1 water. In this water, the higher carbonate concentration eliminates the contribution of surface complexation observed in J-13 water at pH values above 7.

A model was also developed for pH dependence of U adsorption onto crushed devitrified tuff. This treatment was similar to that used to model Np adsorption, except that the cation exchange

capacity for U was not known (i.e., there was no adsorption isotherm) and a cation exchange with the monohydroxy-uranyl complex was included. The parameters used are listed in Table 10.3-16. The number of sites used to model these data was much greater than for the zeolitic tuff. The possible reason for this is the exposure of fresh surfaces of feldspar and quartz combined with the lack of exposure to a complex groundwater.

The results of this exercise are shown in Figure 10.3-43 and are in excellent agreement with the results of Leckie and his students (Davis et al. 1978, pp. 492 to 497). The equilibrium concentration of U at pH values of 9 and higher are above the solubility limit for uranium hydroxide. The effect of precipitation was evident in the experimental data. The solubility product was not included in this model.

State of Knowledge of Surface Complexation with Respect to Yucca Mountain– Surface-complexation reactions with Yucca Mountain tuffs have just begun to be studied. The pH dependence of actinide adsorption can be readily explained with a combined surface-complexation and ion-exchange model. The effect of changing groundwater composition on Np adsorption has also been successfully modeled using a surface-complexation model. There are significant gaps in the knowledge base, however. From a fundamental standpoint, a hard-soft, acid-base model for bidentate inner-sphere complexes needs to be developed. The consequences of a bidentate attachment mechanism, as was included in the U adsorption model, is an increased sensitivity to competition with metal ions favoring monodentate attachment (e.g., Ca). From an experimental standpoint, the effects of wet-sieving need to be better understood. If wet-sieving removes all of the clay minerals, the resulting distribution coefficients may be too low (overly conservative). On the other hand, if a trace component of groundwater is responsible for the decrease in surface complexation, it must be identified and measured in groundwaters and in pore waters.

The modeling of actinide sorption shows that high carbonate concentrations will severely reduce the ability to form surface complexes on tuff. The ion exchange of actinides appears to dominate under normal conditions over surface complexation. Furthermore, divalent cations are found to be strong competitors for cation exchange sites found in Yucca Mountain tuffs.

10.3.6 Sorption Results Recommended for Performance Assessment

Sorption is a function of water chemistry and the type of tuff at Yucca Mountain (CRWMS M&O 2000). The concentration of the major cations and anions in unsaturated zone groundwaters at Yucca Mountain appears to be intermediate between the saturated zone tuffaceous waters (e.g., from well J-13) and waters from the Paleozoic carbonate aquifer (from well UE-25 p#1). Consequently, the first assumption made for the performance assessment recommendations was that the waters from wells UE-25 J-13 and p#1 bound the chemistry of the groundwaters at Yucca Mountain.

The second assumption dealt with grouping all strata on the basis of rock type. This assumption reduced the number of sorption-coefficient distributions elicited to about four per radionuclide: iron oxides, devitrified tuff, vitric tuff, and zeolitic tuff (Wilson et al. 1994) and occasionally the alluvium material. The basis for this grouping is the fact that sorption of radionuclides is the result of a chemical reaction between the radionuclide in the groundwater and the minerals in the

tuff. The mineralogy of the different strata of the same rock group is very similar, and the sorption coefficients can be grouped in terms of these rock types (Thomas 1987).

The containers to be used in the potential repository were added to the list after consideration of whether the corrosion byproducts of the container could become a substrate for sorption. Actinides are sorbed strongly by iron oxides. However, although hematite is found in the tuffs at Yucca Mountain, the iron-oxide minerals in the tuffs appear to be "passivated"—that is, all of the sorption sites could be occupied by other metals (Triay et al. 1993b)—and the sorption of the radionuclides onto tuff (containing iron oxides as trace minerals) is not as large as predicted on the basis of the sorption of radionuclides onto synthetic pure iron oxides. (It should be noted that passivation is only a hypothesis to explain the observation that Np does not sorb significantly with respect to Yucca Mountain tuffs.) Because the sorption sites on the degraded container material would not necessarily be occupied by other metals, the experts agreed to add iron oxides to the list of "rock" types.

Table 10.3-3 shows the parameters for the sorption-coefficient probability models recommended for performance assessment for the unsaturated zone units, and Table 10.3-4 shows the same parameters for saturated zone units. The source of these values for each of the elements is discussed separately in the following paragraphs. However, the values given in Tables 10.3-3 and 10.3-4 are general and cannot account for the many variations in rock properties and mineralogy, and water chemistries that can and will occur throughout the flow paths to the accessible environment. Therefore, the tables are conservative and should be considered as expert elicitation. They are consistent but more conservative when compared to specific data, such as those from Busted Butte, which occasionally shows greater adsorption for specific rocks and specific radionuclides.

Americium–Americium sorbs strongly to most materials (Triay et al. 1991a). The potential mechanisms for actinide sorption onto mineral surfaces were reviewed by Meijer (1992). The sorption-coefficient distributions for Am in Yucca Mountain tuffs and iron oxides given in Tables 10.3-3 and 10.3-4 were inferred from the data presented by Thomas (1987, pp. 20 to 21), Triay et al. (1991a, Table 4), and Meijer (1992).

Plutonium–One of the problems of interpreting sorption data for Pu is that this element can exist in multiple oxidation states under oxidizing conditions at near-neutral pH values (Nitsche et al. 1993). Plutonium can also exist as a polymer (Triay et al. 1991b). The lack of information on the speciation of Pu in the groundwaters at Yucca Mountain makes it difficult to assess the sorption mechanism for this element. However, the empirical data obtained in Yucca Mountain tuffs indicate that Pu sorbs strongly. The sorption-coefficient distributions for Pu in Yucca Mountain tuffs given in Tables 10.3-3 and 10.3-4 were inferred from the data presented by Thomas (1987, pp. 20, 21) and Meijer (1992).

Uranium–No additional data for U were collected for Yucca Mountain tuffs since the 1991 TSPA effort (Barnard et al. 1992, p. 3-45, Table 3-25, Figures 3-11, 3-12, 3-13, 3-19). Consequently, no change was made for the sorption-coefficient distributions used for this element. As previously discussed (Meijer 1992), U sorbs strongly to synthetic iron oxides.

Thorium–The information elicited for Am was also used for Th. This approach is due both to the lack of sorption information available for Th and to the similarities exhibited by the sorption behavior of these two elements (Thomas 1987, pp. 20 to 21).

Radium–Barium was used as an analog for Ra in the experiments performed at Los Alamos National Laboratory (Thomas 1987, pp. 4, 16). These elements sorb to Yucca Mountain tuffs via an ion-exchange mechanism and surface-adsorption reactions (Meijer 1992). The sorption-coefficient distributions for Ra in Yucca Mountain tuffs and iron oxides given in Tables 10.3-3 and 10.3-4 were inferred from the data presented by Thomas (1987, p. 16), Meijer (1992), and Triay et al. (1991a).

Lead–The sorption-coefficient distributions for Pb in Yucca Mountain tuffs and iron oxides given in Tables 10.3-3 and 10.3-4 were inferred from the data presented by Meijer (1990).

Neptunium–Sorption-coefficient distributions for Np in tuff are the same as those used in the 1991 TSPA. Studies carried out since 1991 have focused on details of Np sorption (e.g., effects of pH, types of substrates, differences in water chemistry) and corroborate the values used in 1991). For example, data reported by Triay et al. (1993b, Table 2) agree with previous observations. Neptunium is a poorly sorbing radionuclide in tuff even when the tuffs are known to have iron oxides because the iron oxides in the tuff appear to be passivated. The Np sorption-coefficient distribution for sorption onto iron oxides given in Tables 10.3-3 and 10.3-4 was inferred from data presented by Meijer (1992) and Triay et al. (1993b) for sorption onto synthetic iron oxides.

Protactinium–Very little information exists for Pa sorption onto tuffs (Thomas 1987, p. 20), so, for this element, the experts decided to use the same sorption coefficients elicited for Np.

Tin–There is very little information for the sorption of tin onto tuffs (Thomas 1987). Based on the data available, Meijer (1992) suggested that tin exhibited large values of K_d in the devitrified tuffs (larger than 1,000 mL/g). The sorption-coefficient distributions given in Tables 10.3-3 and 10.3-4 were inferred from the work by Andersson (1988); the uniform distributions chosen were the result of the experts' uncertainty about the sorption of tin.

Nickel–For devitrified, vitric, and zeolitic tuffs, the Ni sorption-coefficient distributions given in Tables 10.3-3 and 10.3-4 were inferred from data presented by Meijer (1992). For iron oxides, the Ni sorption-coefficient distribution was inferred from the data presented by Siegel et al. (1992, 1993, pp. 353 to 356).

Cesium–Cesium sorption-coefficient distributions for tuff and iron oxides were inferred from the data presented by Thomas (1987, p. 16), Meijer (1992), and Triay et al. (1991a). Cesium has one of the highest selectivity coefficients for zeolites among all chemical elements (Meijer 1992). Cesium sorption onto devitrified and vitric samples could be the result of ion exchange onto clays or feldspars in the tuff samples or surface-adsorption reactions (Meijer 1992).

Strontium–Strontium sorption-coefficient distributions for tuff and iron oxides were inferred from the data presented by Thomas (1987, p. 16) and Triay et al. (1991a). Strontium sorbs strongly onto zeolites by ion exchange. This element's sorption onto other types of tuff may be

dominated by the amount of clay in the tuff units. The values given in Tables 10.3-3 and 10.3-4 are generally conservative.

Selenium–There are limited data on tuff for Se sorption (Thomas 1987, p. 20), so the experts decided to use the same sorption-coefficient distributions for Se as the ones elicited for U. This decision is a conservative one because U can be oxidized much more readily than Se in Yucca Mountain groundwaters.

Carbon–Carbon is a special case because transport is expected to occur primarily in the gaseous phase as carbon dioxide. The major retardation mechanism is exchange of ^{14}C with the C in the carbon dioxide dissolved in the groundwater.

Actinium, Samarium, Niobium, and Zirconium–All these elements are strongly sorbing (Meijer 1992). The experts advised using the same sorption-coefficient distributions for these elements as those elicited for Am.

Iodine, Technetium, and Chlorine–Iodine and Cl have anions that do not sorb onto tuffs. Technetium exists as pertechnetate under oxidizing conditions and does not sorb either (Triay et al. 1993b).

10.3.7 Adsorption of Radionuclides by Alluvium

Alluvium is the generic name for clay silt, sand gravel, or similar detritus material deposited by running water. It provides a natural barrier to migration of waste elements from high-level radioactive waste in geologic repositories. It is therefore necessary to enumerate the retardation processes and predict the release behavior of radionuclides in alluvial deposits.

The principal purpose of the adsorption measurements and models is to predict the retardation potential of alluvium to the radionuclides. Specifically, there is a substantial need to know the apparent distribution coefficient, K_d (mL/g), of these three radionuclides in alluvium under different environmental conditions. In addition, the chemical adsorption mechanism between alluvium and these nuclides needs to be explored.

At the time the *Yucca Mountain Site Description* was being prepared, batch-adsorption experiments were in progress to determine the element distribution between groundwater and alluvium for ^{237}Np, ^{99}Tc, and ^{129}I (CRWMS M&O 2000, Section 6.4.5).

The alluvium used in the experiments come from three Nye County boreholes located south of the potential repository (Table 10.3-17). Also shown are the density values for the samples used in the sorption experiments. The particle size used for the adsorption experiments was the standard 75-to 500-μm fraction.

Transport column experiments are also underway for ^{237}Np, ^{99}Tc, and ^{129}I using alluvial material from the same three boreholes that supplied samples for the batch sorption tests (NC-EWDP-02D, NC-EWDP-095x, and NC-EWDP-035). Final data from these column experiments are not yet available.

10.3.7.1 Results and Discussion

Table 10.3-18 lists the quantitative X-ray diffraction results for the three samples used for the first adsorption kinetic experiments, which are the deepest samples tested from each borehole suite. The quantitative X-ray diffraction results show that the major phase in the Yucca Mountain alluvium is feldspar, and the amount of feldspar in the three samples is about the same. The amount of the poorly sorbing minerals, tridymite, cristobalite, and quartz, is also about the same in these three samples. The important differences among these are the presence of smectite, clinoptilolite, calcite, and hematite.

10.3.7.2 Adsorption of Neptunium-237

Figure 10.3-44 presents the results of adsorption of Np as a function of stratigraphic position performed on three types of alluvium, respectively. The results indicate that the retardation capacity with respect to Np varies depending on the depths and types of the testing alluvium. In general, the alluvia from borehole-02D and borehole-03S have relatively high retardation capacity. Of special note, the K_d value from borehole-02D, 400 to 405 ft, is 77 and the one from borehole-03S, 60 to 65 ft, is almost 45. These are significant values. If the three samples are compared with quantitative X-ray diffraction analyses, the highest Np K_d value is for the sample with the highest amount of the sorptive phases calcite, smectite, clinoptilolite and hematite. Calcite has a high affinity for Np at this pH. Further quantitative X-ray diffraction analyses should be performed to determine the role of mineralogy on the sorptive behavior of the alluvium.

The deepest sample from each borehole was chosen to carry out the adsorption kinetic experiments. The results, depicted in Figure 10.3-45, show that adsorption of Np on alluvium is fast, nearing the maximum after a few days.

10.3.7.3 Adsorption of Technetium-99

The results of adsorption of Tc as a function of stratigraphic position are presented in Figure 10.3-46. Although the degree of retardation of Tc on alluvium is low, it is positive and could be significant for long-term performance.

Figure 10.3-47 indicates that adsorption of Tc slowly increases in the first 10 days, then increases rapidly with time. Because the experiments are still ongoing, the final results and discussions will wait until they are completed. However, the results suggest a mechanism other than simple adsorption, such as redox reactions. Although no sulfides or other reduced minerals were found in the quantitative X-ray diffraction analyses, only a trace amount needs to be present to greatly affect the reactivity of the surfaces. The accuracy of quantitative X-ray diffraction is poor below a few percent and, also, if the phases are poorly crystalline. Scanning electron microscope-energy dispersive X-rays should be used to determine the presence of any trace sulfides that could be present. Similarly, total organic carbon should be determined to see if trace amounts could be responsible for the sorption observed.

10.3.7.4 Adsorption of Iodine-129

Experiments to determine the overall K_d values for ^{129}I are not yet complete, but the kinetic experiments have yielded some preliminary K_d values.

Similar to Tc, retardation of ^{129}I on alluvium is small but positive, as indicated in Figure 10.3-48. The K_d value from the sample from borehole-03S, however, is still increasing. Analyses for total organic C may suggest the sorption mechanism for ^{129}I.

10.3.7.5 Conclusions of Alluvium Sorption

Sorptive properties of alluvial material were investigated by the YMP as part of the far-field natural geologic barrier to radionuclide transport. The tested samples were collected from various depths from three of the Nye County Early Warning Detection Program (NC-EWDP) boreholes located about 10 to 15 km south and southwest of Yucca Mountain. These samples showed significant sorption potential for Np and low but positive sorption potential for Tc and I. Distribution coefficients (K_d values) varied as a function of depth and borehole. K_d values for Np ranged from about 5 to 77 mL/g; K_d values for Tc ranged from about 0.35 to 0.8 mL/g; and preliminary K_d values for ^{129}I ranged from about 0.41 to 0.75 mL/g. Sorption was much faster for Np than for Tc or ^{129}I. The differences in sorptive properties among samples probably result from differences in the amount of the sorptive phase—smectite, clinoptilolite, calcite, and hematite—and perhaps from the presence of organic C and trace amounts of sulfides, which may explain the slow sorption response for Tc and ^{129}I. Biological activity could also be important and account for the slow sorption response for Tc and ^{129}I. Ongoing experiments may resolve this issue. During these tests, significant amounts of colloids were also found, but their transport properties were not investigated. Waters were in equilibrium with atmospheric O, which probably resulted in lower K_d values for Tc and ^{129}I. Additional experiments should use ambient pε conditions.

10.3.8 Effects of Temperature Perturbations on Adsorption of Radionuclides

Little work has been done on the effects of potential repository perturbations on the transport of radionuclides. Some of the obvious effects involve increased temperatures as the potential repository heats up. These effects will be important for the drift and near-field environments. Increased temperature will affect the solubilities of existing phases, the precipitation of new phases, the generation and stability of colloids, and the overall aqueous geochemistry of the drift and near-field environments. This section will discuss the effect of temperature on the adsorption (K_d values) of the radionuclides.

Temperature will affect adsorption by shifting equilibria among solution species, by changing the zero point of charge of the substrate surfaces, and by changing the ratio of adsorbed to solution-phase species. The magnitude can be modeled with standard thermodynamic relationships if solution and adsorption enthalpy data are available (Machesky 1990). Relationships such as the van't Hoff equation and Boltzmann functions can be used to predict the effect of temperature. This should be done for all radionuclides of concern for Yucca Mountain. There is general agreement that increasing temperature increases the sorption of cations and decreases the sorption of anions (Machesky 1990; Beckman et al. 1988). The few data that exist

support this assertion. Machesky used the van't Hoff equation to predict a doubling of K_d values with every increase of 20°C.

Beckman et al. (1988, Figure 2, pp. 11 to 12) presented data that showed that Ba adsorption onto tuff was increased by an order of magnitude, from 25° to 70°C, and describes similar effects for Ce, Eu, Cs, and Sr. They also concluded that temperature effects are overwhelmingly more important than effects of concentration or particle size.

The effect of temperature on sorption coefficients was also reviewed by Meijer (1990, p. 17). Again, measured sorption coefficients onto tuffs were higher at elevated temperatures for all elements studied: Am, Ba, Ce, Cs, Eu, Pu, Sr, and U. Consequently, an assumption can be made that sorption coefficients measured at ambient temperatures should be applicable and generally conservative when applied to describing aqueous transport from a hot repository. This assumption must be weighed against the possibility that high temperatures, sustained for long time periods due to potential high thermal loads, could result in changes in the mineralogy and water chemistry at Yucca Mountain that are not predictable by short-term laboratory and field experiments.

As a preliminary evaluation, the effect of temperature in a perturbed repository will increase adsorption of cationic species and decrease adsorption of anionic species. Since anions do not adsorb very well at ambient temperatures, a conservative estimate is their K_d values at higher temperatures will be zero. However, the K_d values of cationic species at higher temperatures will increase significantly over those listed in Table 10.3-3, by as much as 10 times at repository temperatures above 70°C, and the exact number should be determined by modeling efforts.

10.4 DYNAMIC TRANSPORT STUDIES IN THE LABORATORY

10.4.1 Data Sources

The primary input data used for dynamic transport studies are described in (CRWMS M&O 2000, Table 16) and include laboratory results of radionuclide experiments using waters collected from Yucca Mountain or synthesized to reflect Yucca Mountain waters and materials either collected from the field or synthesized in the laboratory. Parameters used in this section are the radionuclide concentration and either percent sorbed onto various substrates or percent eluted through a column as a function of time.

10.4.2 Crushed-Rock Columns

10.4.2.1 Approach

Generally, batch-sorption experiments are used to identify sorption mechanisms and to obtain sorption distribution coefficients (Triay et al. 1996a, 1996b). This section describes attempts to verify the results of earlier batch-sorption measurements by performing crushed-tuff column studies under flowing conditions without significantly changing the surface properties of the tuff. By comparing differences with the batch-sorption measurements, such studies would be most sensitive to multiple-species formation, colloid formation, and any other geochemical reactions (e.g., changes in surface reactivity due to agitation) not adequately described by batch-sorption distribution coefficients. In these crushed-tuff column experiments, mass-transfer kinetics were investigated by studying radionuclide migration as a function of water velocity.

Column elution curves can be characterized by two parameters: the time of arrival of the radionuclide eluted through the column and the broadness (dispersion) of the curve. The arrival time depends on the retardation factor, R_f, which for soluble radionuclides depends in turn on the sorption distribution coefficient, K_d together with the water content and bulk density of the solid phase. Significant deviations (those larger than expected based on sampling variability) in arrival time from that predicted on the basis of the batch-sorption distribution coefficients indicate one of the following problems:

- The presence of more than one chemical species that are not readily exchanged and that have different selectivities in tuff minerals
- The presence of the radionuclide as a colloid
- Extremely slow sorption kinetics
- Irreversibility of the sorption process
- Solubility effects due to the presence of solids
- Hydrologic parameters (conductivity and porosity)
- Experimental artifacts.

The broadness, or apparent dispersion, of the curve depends on:

- The kinetics and reversibility of sorption
- The linearity of the isotherm that describes the dependence of sorption on radionuclide concentration.

The main goal of the study was to test the necessary assumptions made in using values of the sorption distribution coefficient, K_d (determined by batch-sorption measurements) to describe hydrologic transport (see Equation 10.4-1 that follows for the relationship between the retardation coefficient and the sorption distribution coefficient). These assumptions are:

- Microscopic equilibrium is attained between the solution species and the adsorbate.
- Only one soluble chemical species is present (or if more than one is present, they interchange rapidly).
- The radionuclides in the solid phase are adsorbed on mineral surfaces (i.e., they are not precipitated).
- The dependence of sorption on concentration is described by a linear isotherm.

The importance of verifying these assumptions can be demonstrated by the following hypothetical cases. If equilibrium were not attained in the batch experiments (violation of assumption 1), the retardation of radionuclides could be dependent on groundwater velocity. If a radionuclide were present in solution as an anionic and a cationic species and solution equilibrium were not maintained (violation of assumption 2), the batch measurement would predict a single retardation factor, whereas in a flowing system, the anion could move unimpeded (its size and charge excluding it from the pores of the Yucca Mountain tuffs) compared to movement of the cation. If the radionuclide had precipitated in the batch experiments (violation of assumption 3), the value of the K_d thus determined would be meaningless, and depending on the precipitation mechanism, colloid transport could be important. If the isotherm was nonlinear (violation of assumption 4), the migration front of the radionuclides in a column study would usually broaden, appearing as increased dispersion over that observed for nonsorbing tracers.

10.4.2.2 Experimental Conditions

Because the UE-25 J-13 and p#1 well waters that bound the Yucca Mountain groundwaters are both oxidizing (Ogard and Kerrisk 1984), all the batch-sorption and column experiments were performed under oxidizing conditions. In the batch-sorption experiments, both groundwaters (filtered by a 0.05-μm filter) were used, but in the column experiments, J-13 water (filtered) and a sodium-bicarbonate buffer that simulated UE-25 p#1 groundwater (because of the unavailability of water from this well) were used.

As in the batch-sorption experiments, all tuff samples were crushed and wet-sieved (with the groundwater being used in the experiment) to obtain particle sizes ranging from 75 to 500 μm.

Relationship Between Column and Batch Experiments–The batch-sorption distribution coefficients were measured under static conditions by equilibrating a solution containing the radionuclides with a sample of crushed tuff. If it is assumed that equilibrium is achieved between a single aqueous chemical species and the species adsorbed on the solid phase, the rate at which a radionuclide moves through a column can simply be related to the sorption distribution coefficient, K_d. The relationship between the retardation factor, R_f, obtained from column-transport experiments, and the values of K_d, obtained from batch-sorption experiments, is generally given by

$$R_f = 1 + \frac{\rho_b}{\varepsilon} K_d \qquad \text{(Eq. 10.4-1)}$$

where ρ_b is the dry bulk density (including pores) and ε is the porosity of the column. Hiester and Vermeulen (1952, p. 514) derived this equation and carefully described its underlying assumptions. To test these assumptions, the radionuclide solution used in the batch-sorption measurements was eluted through columns containing tuff samples that came from the same drill hole and depth interval and that had been crushed and sieved to the same size fraction as samples used in the batch-sorption studies.

10.4.2.3 Results and Discussion

10.4.2.3.1 Neptunium Results

Elution of Np (V) was measured as a function of water velocity through zeolitic, devitrified, and vitric crushed tuff in columns with J-13 well water and with synthetic UE-25 p#1 water. The elution curves were published by Triay et al. (1996c, Appendix A). Porosity was calculated as the free column volume divided by the total column volume (free volume was defined as the volume of ^3H solution that had to be eluted to recover 50 percent of the injected tritium). Values of R_f were then calculated for the column experiments by dividing the free column volume into the volume of Np solution that had to be eluted to recover 50 percent of the injected ^{237}Np. From these values of R_f, Equation 10.4-1 was used to calculate the column sorption-distribution coefficients listed in Table 10.4-1.

How do the earlier results of batch-sorption experiments (Triay et al. 1996a, 1996b) compare with the results of the crushed-tuff column experiments? Inspection of Table 10.4-1 indicates good agreement between the values of K_d obtained by the two approaches, which means that the arrival time of ^{237}Np can be predicted from a value for K_d. On the other hand, the broad, dispersive shape of the elution curves indicates that sorption of Np onto zeolitic and vitric tuffs appears to be nonlinear, nonreversible, or noninstantaneous. Previous work has found that sorption of Np onto clinoptilolite-rich tuffs is rapid (Triay et al. 1996a, p. 18) and can be fit with a linear isotherm (Triay et al. 1996b, Figure 4.5). Consequently, the degree of reversibility of Np sorption onto zeolitic and vitric tuffs might be the most likely reason for the apparent dispersivity in the tuff-column elution curves.

The elution curves also reveal that, regardless of the water being studied, the elution of ^{237}Np does not precede the elution of tritium for any of the tuffs. This observation is extremely important because if charge-exclusion effects were to cause the neptunyl-carbonato complex (an

anion) to elute faster than neutral tritiated water molecules, significant Np releases could occur at Yucca Mountain. Another important observation that can be drawn from these experiments is that values of K_d can be used to obtain accurate or conservative estimates for the performance assessment calculations of Np transport through Yucca Mountain tuffs. This conclusion assumes that transport of radionuclides through the unsaturated zone from the potential repository would occur homogeneously through tuff.

A Np summary follows:

- Using crushed-rock columns, the retardation of ^{237}Np by zeolitic, devitrified, and vitric tuffs in sodium-bicarbonate waters under oxidizing conditions (at room temperature, under atmospheric conditions, and using different water velocities) was studied.

- The sorption distribution coefficients obtained from the column experiments under flowing conditions were compared to those obtained from batch-sorption experiments under static conditions.

- The column and batch distribution coefficients agreed well for all tuffs regardless of the groundwater studied and the water velocity used for the column experiments.

- It was found that batch-sorption distribution coefficients predict well the arrival time for Np eluted through a crushed-rock column.

- The apparent dispersivity of the Np elution curves through the zeolitic and vitric tuffs indicates that the sorption is either nonlinear, irreversible, or noninstantaneous, which means the transport cannot be completely described using a sorption distribution coefficient. The reversibility of Np sorption onto tuff will be studied as the most likely reason for the apparent dispersivity of the elution curves.

- The use of a batch-sorption distribution coefficient to calculate Np transport through Yucca Mountain tuffs would result in conservative values for Np release.

- Neptunium never eluted prior to the nonsorbing radionuclide (tritiated water) used in the column experiments. Thus, charge exclusion does not appear to exclude Np from the tuff pores.

- Corroborated by these column experiments were the general trends previously observed for Np sorption using batch-sorption experiments: Np sorption onto devitrified and vitric tuffs is minimal, and Np sorption onto zeolitic tuffs decreases as the amount of Na and bicarbonate/carbonate in the groundwaters increases.

10.4.2.3.2 Plutonium and Technetium Results

The elution of Pu (V) through zeolitic, devitrified, and vitric crushed tuff was measured in columns with J-13 well water and with synthetic UE-25 p#1 water. The elution curves for these experiments (Figures 10.4-1 to 10.4-3) indicate that vitric and zeolitic tuffs sorb Pu significantly, which is probably due to their clay content. The shape of the elution curves for Pu indicates that use of K_d values to predict Pu transport through Yucca Mountain tuffs will predict Pu releases

conservatively. Results by Triay et al. (1995, pp. 12 to 13) indicate that Pu sorption onto tuffs is a slow process and probably due to a redox reaction occurring at the tuff surfaces. To verify these batch-sorption results, which suggest that Pu sorption, even to the lowest sorbing tuff type (devitrified), could be significant, the migration of Pu as a function of flow velocity was measured in devitrified tuff using J-13 and UE-25 p#1 waters. Inspection of these elution curves (Figures 10.4-4 and 10.4-5) confirms the trends observed using batch-sorption techniques; the elution curves observed for these columns are consistent with slow sorption kinetics.

The elution of pertechnetate was also studied in devitrified, vitric, and zeolitic tuffs in J-13 and synthetic UE-25 p#1 waters as a function of flow velocity. Inspection of the elution curves (Figures 10.4-6 to 10.4-8) indicate that anion-exclusion effects for pertechnetate in crushed tuff are essentially negligible except in the case of Tc transport through zeolitic tuff in J-13 well water (Figure 10.4-8). In this case, the anion-exclusion effect is small but measurable.

10.4.3 Solid-Rock Columns

Direct measurements of transport parameters in actual subsurface materials under subsurface conditions are necessary for defensible modeling of contaminant transport in host rocks and engineered barriers surrounding radioactive and hazardous waste repositories. The hydraulic conductivity, K, and the retardation factor, R_f, along with the associated distribution coefficient, K_d, are poorly known transport parameters for real systems, but are key input parameters to existing and developing contaminant release models. Unsaturated R_f and K were experimentally determined for core samples of Yucca Mountain vitric-member tuff, and zeolitic nonwelded tuff from G-Tunnel, Bed 5, with respect to J-13 well water with a Se concentration (as selenite) of 1.31 mg/L (ppm) at 23°C. The intent was to demonstrate that a method in which flow is induced with an ultracentrifuge could rapidly and directly measure R_f and K in whole-rock tuff cores, and then to compare these directly measured unsaturated R_f values with those calculated from K_d values obtained through traditional batch tests on the same materials.

10.4.3.1 Experimental Approach

10.4.3.1.1 Retardation

Retardation factors can be determined in flow experiments where R_f for a particular species is the ratio of the solution velocity to the species velocity. The retardation factor for that species is given by:

$$R_f = \frac{V_{gw}}{V_{sp}} = 1 + \rho_d \frac{K_d}{\varepsilon} \qquad \text{(Eq. 10.4-2)}$$

where V_{gw} is the velocity of carrier fluid, V_{sp} is the velocity of the species, ρ_d is the dry bulk density, ε is the porosity, and K_d is defined as the moles of the species per gram of solid divided by the moles of the species per milliliter of solution. If none of a particular species is lost to the solid phase, then $K_d = 0$ and $R_f = 1$ for that species. In column experiments, a breakthrough curve is obtained for the particular species and R_f is determined as the pore volume at which the concentration of the species in the solution that has passed through the column is 50 percent of the initial concentration ($C/C_0 = 0.5$). It is now generally assumed that, for unsaturated systems,

$\varepsilon = \theta$, where θ is the volumetric water content (Bouwer 1991, p. 42; Conca and Wright 1992a, pp. 1553 to 1554). The study described in this section experimentally addresses this concern under unsaturated conditions in whole rock, and evaluates the use of data from batch experiments in determining R_f in whole rock.

10.4.3.1.2 Hydraulic Conductivity

One way to drive fluid through rock is to use centripetal acceleration as the driving force. This approach was used with a new technology (unsaturated flow apparatus) to produce hydraulic steady state, to control temperature, degree of saturation, and flow rates in all retardation experiments, and to measure the hydraulic conductivity. A specific advantage of this approach is that centripetal acceleration is a whole-body force similar to gravity that acts simultaneously over the entire system and independently of other driving forces, such as gravity or matrix suction. It has been shown that capillary bundle theory holds in the unsaturated flow apparatus method (Conca and Wright 1992a, p. 1546).

The unsaturated flow apparatus instrument consists of an ultracentrifuge with a constant, ultralow flow-rate pump that provides fluid to the sample surface through a rotating seal assembly and microdispersal system. Accelerations up to 20,000 g are attainable at temperatures from 150° to 220°C and flow rates as low as 0.001 mL/hr. The effluent is collected in a transparent, volumetrically calibrated container at the bottom of the sample assembly. The effluent collection chamber can be observed during centrifugation using a strobe light.

The current instrument has two different rotor sizes that hold up to 50 and 100 cm^3 of sample, respectively. Three different rotating-seal assemblies facilitate various applications and contaminant compatibilities: a face seal, a mechanical seal, and a paramagnetic seal. The large sample option with the paramagnetic seal is a configuration that is optimal for adsorption and retardation studies.

Numerous studies have compared use of the unsaturated flow apparatus approach with traditional methods of analysis in soils and clays, and the agreement is excellent (Conca and Wright 1992b, Figure 14; Nimmo et al. 1987). Good agreement is expected because the choice of driving force does not matter provided the system is Darcian (see next paragraph) and the sample is not adversely affected by a moderately high driving force (≤1,000 g for all samples run in these experiments); both of these provisions hold for most geologic systems. Additionally, all techniques for estimating hydraulic conductivity, $K(\theta)$, are extremely sensitive to the choice of the rock or soil residual water content, θ_r, and to the saturated hydraulic conductivity, K_s; minor variations in θ_r or K_s produce order-of-magnitude changes in $K(\theta)$ (Stephens and Rehfeldt 1985).

The unsaturated flow apparatus technology is effective because it allows the operator to set the variables in Darcy's Law, which can then be used to determine hydraulic conductivity. Under a centripetal acceleration in which water is driven by both the potential gradient, $d\psi/dr$, and the centrifugal force per unit volume, $\rho\omega^2 r$, Darcy's Law is

$$q = -K(\psi)\left[\frac{d\psi}{dr} - \rho\omega^2 r\right] \qquad \text{(Eq. 10.4-3)}$$

where q is the flux density into the sample; K, the hydraulic conductivity, is a function of the matric suction, ψ, and, therefore, of water content, θ; r is the radius from the axis of rotation; ρ is the fluid density; and ω is the rotation speed. When multicomponent and multiphase systems are present in the unsaturated flow apparatus instrument, each component reaches its own steady state with respect to each phase, as occurs in the field. Appropriate values of rotation speed and flow rate into the sample are chosen to obtain desired values of flux density, water content, and hydraulic conductivity in the sample. Above speeds of about 300 rpm, depending upon the material and providing that sufficient flux density exists, $d\psi/dr << \rho\omega^2 r$. Under these conditions, Darcy's Law is given by $q = -K(\psi)\ [-\rho\omega^2 r]$. Rearranging the equation and expressing hydraulic conductivity as a function of water content, Darcy's Law becomes

$$K(\theta) = \frac{q}{\rho\omega^2 r} \qquad \text{(Eq. 10.4-4)}$$

As an example, a whole-rock core of Topopah Spring member tuff accelerated to 7,500 rpm, with a flow rate into the core of 2 mL/hr, and achieved hydraulic steady state in 30 hr. with a hydraulic conductivity of 8.3×10^{-9} cm/s at a volumetric water content of 7.0 percent. Previous studies verified the linear dependence of K on flux and the second-order dependence on rotation speed (Conca and Wright 1992a, p. 1546; Nimmo et al. 1987, Figure 11), and several comparisons between the unsaturated flow apparatus method and other techniques have shown excellent agreement (Conca and Wright 1992a, Figure 2; 1992b, Figure 14). Because the unsaturated flow apparatus method can directly and rapidly control the hydraulic conductivity, fluid content, temperature, and flow rates, other transport properties can then be measured as a function of fluid content, by associated methods, either inside or outside the unsaturated flow apparatus instrument during the overall run.

Fundamental physics issues involving flow in an acceleration field have been raised and successfully addressed by previous research and in numerous forums (Conca and Wright 1992a, p. 1547; 1992b, p. 8; Nimmo et al. 1987; Nimmo and Akstin 1988; Nimmo and Mello 1991). These studies have shown, first, that compaction from acceleration is negligible for subsurface soils at or near their field densities. Bulk density in all samples remains constant because a whole-body acceleration does not produce high point pressures. A notable exception is surface soils, which can have unusually low bulk densities; special arrangements must be made to preserve their densities. Whole rock cores are completely unaffected.

The studies have also shown that three-dimensional deviations of the driving force with position in the sample are less than a factor of two, but moisture distribution is uniform to within 1 percent in homogeneous systems because water content depends only upon ψ, and unit gradient conditions are achieved in the unsaturated flow apparatus instrument in which $d\psi/dr = 0$. Hydraulic steady state is not as sensitive to changes in rotation speed as to flux density. In heterogeneous samples or multicomponent systems such as rock, each component reaches its own hydraulic steady state and water content, as occurs for such materials under natural conditions in the field. This last effect cannot be reproduced with pressure-driven techniques, but only under a whole-body force field, such as with gravity columns or centrifugal methods. The ratio of flux to rotation speed is always kept high enough to maintain the condition of $d\psi/dr = 0$.

10.4.3.2 Results and Discussion for Vitric and Zeolitic Tuff

10.4.3.2.1 Column Breakthrough Test Results

For these experiments, the rotation speed was set at 2,000 rpm with a flow rate into each sample of 0.2 mL/hr. The experiment was run for 9 days with an initial selenium concentration of 1.31 mg/L. Figure 10.4-9 shows the breakthrough curves for selenite (C/C_o is given for selenium as selenite) in the Yucca Mountain vitric member at 62.6 percent saturation and in the zeolitic nonwelded tuff at 52.8 percent saturation. Pore volume is given as water-filled, or effective pore volume, the same as the volumetric water content and is dimensionless. The experiment was stopped before full breakthrough in the zeolitic nonwelded tuff, but the C/C_o = 0.5 point was reached. The retardation factor for each tuff sample is 2.5. The K_d for each tuff sample can be calculated by rearranging Equation 10.4-2 into $K_d = (R_f - 1)$(water content)/(bulk density). The water content is the total porosity multiplied by the degree of saturation. For the Yucca Mountain vitric-member tuff $K_d = (0.25 - 1)(0.626)(0.23)/1.54 = 0.14$ mL/g, and for the zeolitic nonwelded tuff, $K_d = (2.5 - 1)(0.528)(0.4)/1.21 = 0.26$ mL/g.

During these experiments, the unsaturated hydraulic conductivity K for each sample at these water contents was 2.5×10^{-8} cm/s for the Yucca Mountain vitric-member tuff and 1.2×10^{-8} cm/s for the zeolitic nonwelded tuff. Figure 10.4-10 gives the characteristic curves $K(\ )$ for these tuffs determined in separate experiments, as well as measurements for other tuffs and materials for comparison.

10.4.3.2.2 Batch-Sorption Test Results

Batch-sorption tests were conducted using the same J-13 well water with the slightly lower Se concentration of 1.1 ppm and the same zeolitic nonwelded tuff from G-Tunnel, Bed 5, as in the unsaturated flow apparatus column breakthrough test. The sorption distribution coefficients obtained are given in Table 10.4-2. The Eh of all solutions, measured after the sorption experiments, varied from 140 to 150 mV.

The data presented in Table 10.4-2 and Figure 10.4-9 indicate agreement between the column and the batch-sorption experiments. At a Se concentration of about 1 ppm, no sorption of the Se by the tuff is observed for the zeolitic tuff used in batch experiments, and minimal sorption (K_d of 0.8 mL/g) is observed for the zeolitic tuff used in the unsaturated column experiments (Triay et al. 1997, p. 190). The method used for the batch-sorption experiments to determine K_d values (by difference) involves subtracting the Se concentration in solution after equilibration with the solid phase from the initial Se concentration in solution. This method yields large scatter in the data when the batch-sorption distribution coefficient is small because two large numbers are subtracted to get a small number. Inspection of Table 10.4-2 also suggests that the kinetics of Se sorption onto tuff are fast.

10.4.3.2.3 Conclusions

This study demonstrated the feasibility of using the unsaturated flow apparatus technology to rapidly and directly measure retardation factors and hydraulic conductivities in whole-rock cores of tuff under the unsaturated conditions that exist in the field. The batch sorption technique is inadequate for measuring K_d in weakly sorbing solutes, demonstrating the necessity for using

new techniques, including the unsaturated flow apparatus approach. In unsaturated flow apparatus column breakthrough tests, the retardation factor for the selenite species was only 2.5 in both Yucca Mountain vitric member tuff at 62.6 percent saturation and zeolitic nonwelded tuff from G-tunnel at 52.8 percent saturation for a Se concentration in J-13 water of 1.31 ppm. In batch tests on the same material with an initial Se concentration of 1.1 ppm, the average K_d was 0.08 ± 0.2 mL/g, which gives retardation factors that are slightly lower than those from the unsaturated flow apparatus column breakthrough experiments. This finding suggests that using batch-sorption coefficients to predict radionuclide transport through unsaturated tuff will yield conservative results.

Future experiments will use initial Se concentrations smaller than the ones used in these experiments to further assess the validity of batch-sorption distribution coefficients to predict transport under unsaturated conditions. The unsaturated hydraulic conductivities during the experiments were 2.5×10^{-8} cm/s for the Yucca Mountain vitric-member tuff and 1.2×10^{-8} cm/s for the zeolitic nonwelded tuff.

10.4.4 Radionuclide Transport Through Fractures

10.4.4.1 Overview

One reason that Yucca Mountain was chosen as a potential site for a high-level radioactive waste repository because its geochemistry is believed to form both a physical as well as a chemical barrier to radionuclide migration. However, the Yucca Mountain region has undergone significant deformation, with the most recent tectonic activity occurring during the development of the basin and range geologic province and silicic volcanic activity. As a result of the tectonics and volcanism, many faults and fractures were produced within the tuffaceous units, as well as the entire region. In addition, volcanic tuffs are often fractured as a result of cooling. The numerous fractures present at Yucca Mountain potentially represent a breach in the natural barrier, providing a fast pathway for contaminant migration.

Radionuclide transport calculations often assume that radionuclides can travel through fractures unimpeded; this assumption is too simplistic and leads to overconservative predictions of radionuclide releases to the accessible environment. The assumption ignores two main mechanisms by which retardation of radionuclides migrating through fractures can occur: diffusion of the radionuclides from the fractures into the rock matrix and sorption of radionuclides onto the minerals coating the fractures.

Minerals coating the fracture walls are generally different from the host-rock mineralogy due to a variety of factors ranging from precipitation of hydrothermal waters or meteoric waters to alteration of the preexisting minerals. A review of the literature (Carlos 1985, 1987, 1989, Tables I and II, 1994, Table I; Carlos et al. 1993; Carlos et al. 1990) has provided a list of the minerals lining the fractures found at Yucca Mountain (Table 10.4-3).

The transport of radionuclides through fractures from Yucca Mountain was examined to assess the retardation that can be provided by radionuclide diffusion into the matrix and sorption onto the minerals coating the Yucca Mountain fractures.

10.4.4.2 Experimental Conditions

The groundwaters used for the experiments presented in this section were waters from well J-13 (filtered through a 0.05-μm filter) and two sodium bicarbonate buffers that simulated the water chemistry of the groundwaters from wells UE-25 J-13 and p#1.

Tuff samples with natural fractures from drill holes at Yucca Mountain were chosen from the Yucca Mountain Site Characterization Project Sample Management Facility in Mercury, Nevada. The tuff matrix of all samples consisted of devitrified tuff, and the minerals lining the fractures were stellerite, magnetite, hollandite, and romanechite. The sampling criteria were confined to cores with natural fractures, determined by the presence of secondary mineral coatings, and fractures with removable fracture walls that could be repositioned to their original orientation. Based on these criteria, it was concluded that of the fractured-tuff cores selected (USW G1-1941, UE-25 UZ-16 919, USW G4-2981, and USW G4-2954) all consisted of natural fractures except G1-1941, the only core sample that did not have secondary minerals coating its fracture. The fracture in sample G1-1941 is apparently induced.

Table 10.4-4 gives the characteristics of the four columns used in the experiments.

Batch-Sorption Experiments–For comparison with the fractured-column experiments, batch-sorption tests of Np onto the fracture minerals stellerite, hollandite, romanechite, and magnetite were conducted. These tests were performed under atmospheric conditions using J-13 well water with a Np (V) concentration of 6.7×10^{-7} M. The pH of the water in these experiments was approximately 8.5.

10.4.4.3 Results and Discussion

As discussed earlier, Np does not sorb onto devitrified tuff (Triay et al. 1996b, p. 12), which constitutes the matrix of all the fractures studied. Retardation during fracture flow occurs by diffusion of the radionuclides into the tuff matrix or by sorption of the radionuclides onto the minerals coating the fractures. Table 10.4-5 lists the results of batch-sorption experiments describing the sorption of Np onto natural minerals.

Although the extrapolation from these experiments to Yucca Mountain tuffs containing the same minerals is not immediate, the data of Table 10.4-5 show some important trends. Neptunium has a high affinity for hollandite and romanechite, whereas sorption onto the zeolite stellerite is not significant. If ion exchange is the main mechanism for Np sorption onto stellerite, changing the water from J-13 to p#1 will only result in less sorption (due to the formation of a larger amount of the neptunyl carbonado complex and competitive effects as a result of the higher ionic strength in the UE-25 p#1 water). The sorption of Np onto magnetite does not appear to be significant either. As shown in Table 10.4-5, the magnetite sample studied contains hematite and goethite, which could account for the entire observed sorption.

Because no secondary minerals coating the fractures were observed for the G1-1941 fractured sample (Table 10.4-4, column 1, and Figure 10.4-11), it can be concluded that the retardation of Np observed for that column is due to diffusion into the matrix.

The total Np recovery of 70 percent in the UE-25 UZ-16 919 fractured sample (Table 10.4-4, column 2, and Figure 10.4-12) could be due to minimal sorption onto the stellerite and magnetite coating that fracture or due to diffusion into the matrix. It is important to note that in changing the water for this column from synthetic J-13 to synthetic UE-25 p#1, the speciation of Np changes from a mixture of neptunyl and carbonado complex to almost 100 percent carbonado complex (which can be excluded from tuff pores due to size and charge).

Neptunium seems to be significantly retarded even during fracture flow in the G4-2981 fractured sample (Figure 10.4-13) that is coated with hollandite and romanechite. The recovery of Np in this fracture is less than 10 percent, and its first appearance is delayed with respect to tritium and Tc.

Inspection of Figures 10.4-13 and 10.4-14 (columns 3 and 4 of Table 10.4-4) indicates that diffusion from the fracture into the matrix has taken place because recovery of tritium was only 80 percent compared to 90 percent for Tc. This trend agrees with diffusion data that were previously obtained for ^{3}H and ^{95m}Tc in devitrified tuff and water from well J-13. These data were fitted to the diffusion equation using the transport code TRACRN (Triay et al. 1993b), which yielded diffusion coefficients for saturated devitrified tuffs that were of the order of 10^{-6} cm^2/s for tritiated water and 10^{-7} cm^2/s for Tc. Thus, anion exclusion, in which the large pertechnetate anion is excluded from tuff pores due to its size and charge, was previously observed.

According to de Marsily (1986, Chapter 10), the equation for a sorbing, nonreactive solute can be expanded to account for a solute that also undergoes radioactive decay

$$\nabla \cdot (\mathbf{D} \nabla C - C\mathbf{U}) = \varepsilon \left(\frac{\partial Q}{\partial t} + \lambda C \right) + \rho_b \left(\frac{\partial F}{\partial t} + \lambda F \right) \qquad \text{(Eq. 10.4-5)}$$

where λ is related to the half-life, $t_{1/2}$, of the decaying radionuclide by the relationship $\lambda = 0.693/t_{1/2}$.

As was pointed out earlier, the mechanism of sorption determines the relationship between F and C. If the linear, reversible, and instantaneous relationship for sorption is substituted, that is $F = K_d C$, Equation 10.4-5 becomes

$$\nabla \cdot (\mathbf{D} \nabla C - C\mathbf{U}) = \varepsilon \left(1 + \frac{\rho_b}{\varepsilon} K_d \right) \left(\frac{\partial C}{\partial t} + \lambda C \right) \qquad \text{(Eq. 10.4-6)}$$

The expression inside the first set of parentheses in Equation 10.4-6 is the retardation factor, R_f, which, of course, is only valid if sorption is linear, reversible, and instantaneous.

For radionuclide elution through fractures, two transport equations (like Equation 10.4-5) are considered: one for the porous medium and one for the fractured medium, each with its own Darcy's velocity and porosity (de Marsily 1986). The two transport equations for the porous and the fractured media can be coupled by a convection and a dispersion-exchange term.

The radionuclide elution data through fractured media was reduced and analyzed using the transport code FEHM and reported on by Robinson et al. (1995). Their analyses of ^{237}Np elution through fractured rock made it clear that the data are consistent with very large values of K_d, at least compared to the typical value of 2.5 for ^{237}Np on zeolitic tuff. They also felt it possible that minerals present in trace quantities in the bulk rock that appear to contribute insignificantly to sorption may be quite effective at retarding ^{237}Np transport when concentrated on fracture surfaces.

The most significant conclusion of the work presented here is that, contrary to previous assumptions about the role of fractures in radionuclide retardation, preliminary results from these experiments indicate that fracture flow does not necessarily result in a fast pathway for actinide migration through fractures. As can be seen in the experiments described above, the migration of actinides through fractures could be significantly retarded by sorption onto minerals coating the fractures and by diffusion into the tuff matrix.

10.5 DIFFUSION TRANSPORT STUDIES IN THE LABORATORY

A model for matrix and fracture flow regimes in unsaturated, fractured porous media at Yucca Mountain was developed by Nitao (1991). This model provides a framework for assessing the importance of matrix diffusion at Yucca Mountain. Solute transport in fractured rock in a potential radioactive waste repository was discussed by Neretnieks (1990, Section 6), who concluded that most rocks (even dense rocks, such as granites) have small fissures between the crystals that interconnect the pore system containing water. Small molecules of radioactive materials can diffuse in and out of this pore system. The inner surfaces in the rock matrix are much larger than the surfaces in the fractures through which the water flows. The volume of water in the microfissures is much larger than the volume in fractures. Therefore, over a long time, diffusion can play an important role in radionuclide retardation.

The objective of diffusion experiments was to provide diffusion information for nonsorbing neutral molecules, anions, and sorbing radionuclides. Because the uptake of radionuclides by tuff is measured as a function of time, the experiments also yield information on the kinetics of sorption.

10.5.1 Data Sources and Quality Status

The primary input data used for diffusion transport studies described in CRWMS M&O (2000, Table 1c) include laboratory results of radionuclide experiments using waters collected from Yucca Mountain or synthesized to reflect Yucca Mountain waters and materials either collected from the field or synthesized in the laboratory. Parameters used in this section are the radionuclide concentration and either percent sorbed onto various substrates or percent diffusing through tuff as a function of time.

10.5.2 Rock-Beaker Experiments

10.5.2.1 Experimental Conditions

The radionuclides used in these experiments were ^{3}H, ^{95}Tc, ^{237}Np, ^{241}Am, ^{85}Sr, ^{137}Cs, and ^{133}Ba. A solution (prepared with groundwater from well J-13) containing the radionuclide of interest was placed in the cavity of a rock beaker and then aliquots of the solution from the beaker for the remaining radionuclide concentration were analyzed as a function of time. Batch-sorption experiments were also performed with J-13 water and the tuffs under study.

10.5.2.2 Data Analysis

The results of the rock/beaker experiments were corroboratively modeled using the TRACRN, a three-dimensional geochemical/geophysical-model transport code (Travis and Birdsell 1991). Because the geometry of the rock beaker is complex, an analytical solution is not available for this system. The concentration profiles of the diffusing tracer are fitted to the transport equation (de Marsily 1986, Chapter 10):

$$\nabla \cdot (\varepsilon d \nabla C) = \varepsilon \frac{\partial C}{\partial t} + Q \qquad \text{(Eq. 10.5-1)}$$

where ε is the total porosity of the tuff, *d* is the diffusion coefficient through the tuff, *C* is the concentration of the diffusing tracer in solution, and the source term, *Q*, is zero for a nonreactive tracer, but for a sorbing solute

$$Q = \rho_b \frac{\partial F}{\partial t} \qquad \text{(Eq. 10.5-2)}$$

where *F* is the amount of tracer sorbed per unit mass of solid and ρ_b is the bulk tuff density ($\rho_b = (1 - \varepsilon)\rho_s$, where ρ_s is the density of the solid particles).

As discussed in previous sections, the mechanism of sorption determines the relationship between *F* and *C*. When sorption is linear, reversible, and instantaneous, the relationship between *F* and *C* is given by the sorption distribution coefficient

$$K_d = \frac{F}{C} \qquad \text{(Eq. 10.5-3)}$$

Substitution of this equation and Equation 10.5-2 into Equation 10.5-1 yields

$$\nabla \cdot (\varepsilon d \nabla C) = \varepsilon R_f \frac{\partial C}{\partial t} \qquad \text{(Eq. 10.5-4)}$$

where, once again, the retardation factor, R_f, is given by

$$R_f = 1 + \frac{\rho_b}{\varepsilon} K_d \qquad \text{(Eq. 10.5-5)}$$

Equation 10.5-5 provides a means of comparing results for sorption coefficients obtained under diffusive conditions with sorption coefficients obtained from batch-sorption experiments and is valid only if sorption is linear, reversible, and instantaneous (the Langmuir and Freundlich isotherms are examples of nonlinear relationships between *F* and *C*).

Consequently, the diffusion coefficient can be determined by fitting concentration profiles for the nonsorbing tracers, and sorption parameters, such as K_d, can be determined by fitting concentration profiles for the sorbing tracers.

10.5.2.3 Results and Discussion

Figure 10.5-1 shows an example of a set of diffusion data for a rock-beaker experiment in which the feldspar-rich tuff G4-737 and solutions of tracers in J-13 water were used. The concentration of tracer, *C*, remaining in the solution inside the cavity of the rock beaker divided by the initial concentration, C_o, is plotted as a function of elapsed time.

The solid lines in Figure 10.5-2 are a fit of these same data to the diffusion equation (Equation 10.5-1) using the TRACRN transport code for the two nonsorbing radionuclides, tritium, and ^{95}Tc. The diffusion coefficients obtained in this manner for these radionuclides for all the tuff samples studied (Table 10.5-1) agree well with previous results (Rundberg et al.

1987). These two tracers diffuse essentially as tritiated water and the pertechnetate anion, TcO_4^-. Large anions are excluded from tuff pores because of their size and charge, which can account for the lower diffusivity of TcO_4^-.

If sorption is linear, reversible, and instantaneous, then *F/C* is equal to a sorption coefficient, K_d. To test this assumption, values of K_d in batch-sorption experiments using the tuffs under study (Table 10.5-2) were determined. An expected diffusion curve was calculated using, for each tuff, the diffusion coefficient measured for tritiated water and the batch-sorption coefficient measured for each sorbing radionuclide. Figure 10.5-3 shows these calculated diffusion curves for devitrified tuff G4-737. Comparing of the calculated curves with the actual measured data (see the example in Figure 10.5-4) shows that concentration of the sorbing radionuclides remaining in the rock beaker drops faster than predicted on the basis of a linear K_d. This result indicates that the diffusion of the sorbing radionuclides could not be fitted by assuming reversible, instantaneous, and linear sorption. These results also indicate that transport calculations using a batch-sorption K_d value and the diffusion coefficient measured for tritiated water will result in conservative predictions for the transport of sorbing radionuclides. Note that Cs appears to diffuse much faster than the ^3H in tritiated water, mostly HTO because of the combined effects of diffusion and sorption of Cs, giving a conservative prediction (less apparent diffusion than observed) when using HTO diffusion and batch values of K_d for Cs.

The results obtained from rock-beaker experiments agree with previous results (Rundberg 1987, Tables VI, VII). Experiments were performed on the uptake of sorbing radionuclides by tuff, and it was found that rate constants for uptake of the sorbing cations from solution onto tuff were consistent with a diffusion-limited model in which diffusion occurs in two stages. In the first stage, the cations diffuse into rock through water-filled pores; in the second stage, they diffuse into narrower intracrystalline channels. This diffusion model yielded sorption coefficients for Cs, Sr, and Ba that agree well with the sorption coefficients determined by batch techniques.

10.5.3 Diffusion-Cell Experiments

10.5.3.1 Experimental Conditions and Data Analysis

Diffusion cells were constructed with two chambers containing groundwater separated by a slab of tuff. After radioactive tracers were added to one of the chambers, the untraced chamber was periodically monitored for the presence of radioactivity by taking an aliquot of the solution in the chamber and then replenishing that chamber with groundwater. The dimensions of the diffusion cells used are given in Table 10.5-3.

The only driving force in this experimental setup is the chemical concentration gradient; thus, the solute flux is purely diffusive. The apparent time of arrival depends on the porosity, the heterogeneity of the pore structure, the retardation factor for a given radionuclide, and the sensitivity of radionuclide measurements. The rate of concentration increase in the untraced chamber depends on the ionic diffusivity, the tuff porosity, and the tuff tortuosity/constrictivity factor. Thus, by measuring the movement of sorbing and nonsorbing tracers through tuff slabs as a function of time, the rock-dependent diffusion parameters can be measured.

The two major rock types used for the diffusion-cell experiments were zeolitic (UE-25 1362) and devitrified (G4-287). The zeolitic tuff has a porosity of 0.4 and a bulk density of 1.5 g/mL. The devitrified tuff has a porosity of 0.2 and a bulk density of 2.3 g/mL. The major component of the zeolitic tuff is clinoptilolite; the major component of the devitrified tuff is alkali feldspar.

The actinide concentration of the solutions used for the diffusion experiments was very close to the solubility limit of the actinides in the groundwaters. The experimentally determined solubilities (Nitsche et al. 1993; Nitsche, Roberts, Prussin et al. 1995) of Pu range from 2×10^{-7} (J-13 water at a pH of 7) to 1×10^{-6} M (UE-25 p#1 water at a pH of 8.5) and of Np range from 7×10^{-6} (UE-25 p#1 water at a pH of 8.5) to 5×10^{-3} M (J-13 water at a pH of 6).

The experimental setup for the diffusion cells can be described by a one-dimensional diffusion model. Thus, Equation 10.5-4 (on rock-beaker experiments) can be rewritten as

$$D_e \frac{\partial^2 C}{\partial x^2} = \alpha \frac{\partial C}{\partial t} \qquad \text{(Eq. 10.5-6)}$$

where x is the axis along the direction of tracer diffusion, D_e is the effective diffusivity ($= \varepsilon d$), and α is the rock-capacity factor ($= \varepsilon R_f$). This equation yields an analytic solution to diffusion through a slab.

Bradbury et al. (1986) solved Equation 10.5-6 for a porous rock. For the experimental setup, the boundary conditions can be taken to be:

1. At $x = 0$, a constant source concentration, C_o, is maintained
2. At $x = L$, where L is the tuff-slab thickness, the concentration measured at the initially untraced cell, C_t, is much smaller than the source concentration ($C_t << C_o$).

For these conditions, the total quantity, Q_t, diffused through a tuff slab of area A after a time t is given by the equation

$$\frac{Q_t}{ALC_o} = \frac{D_e t}{L^2} - \frac{\alpha}{6} - \frac{2\alpha}{\pi^2} \sum_{n=1}^{\infty} \frac{(-1)^n}{n^2} e^{-\left(\frac{D_e n^2 \pi^2 t}{L^2 \alpha}\right)} \qquad \text{(Eq. 10.5-7)}$$

As $t \rightarrow \infty$, the asymptotic solution becomes

$$Q_t = \frac{AC_o D_e}{L} t - \frac{AC_o L\alpha}{6} \qquad \text{(Eq. 10.5-8)}$$

Consequently, a plot of Q_t versus t yields the effective diffusivity, D_e, from the slope and the rock-capacity factor, α, from the intercept on the time axis of the extrapolated linear region. For a nonsorbing species, $K_d = 0$, $R_f = 1$, and $\alpha = \varepsilon$; for a sorbing species, K_d may be calculated from the value of α.

The diffusion coefficient, d, can be calculated from the effective diffusivity ($D_e = \varepsilon d$). The difference between the diffusion coefficient, d_s, for a tracer diffusing in the solution phase and the diffusion coefficient, d, for a tracer passing through tuff pores is given by

$$d = \frac{\delta}{\tau^2} d_s \qquad \text{(Eq. 10.5-9)}$$

where δ is the constrictivity and τ is the tortuosity of the tuff pore structure.

10.5.3.2 Results and Discussion

The diffusion of ^{3}H, ^{95m}Tc, natural U (VI), ^{237}Np (V), and ^{239}Pu (V) through devitrified and zeolitic tuffs was studied using water from well J-13 and synthetic UE-25 p#1 water. (Note that ^{95m}Tc refers to the metastable version of ^{95}Tc.) For example, data reported byThe radionuclides ^{3}H, natural U (VI), and ^{239}Pu (V) were studied together in four diffusion cells (devitrified and vitric tuff cells, each with both types of water). Likewise, the radionuclides ^{95m}Tc and ^{237}Np (V) were studied together in another four diffusion cells. Typical results for these experiments are shown in Figures 10.5-5 to 10.5-7.

The results indicate that the diffusion of nonsorbing radionuclides into saturated tuff (illustrated by the diffusion of tritiated water in Figures 10.5-5 to 10.5-7) is slower in devitrified tuffs than in zeolitic tuffs. Large anions such as pertechnetate (which are excluded from the tuff pores by size and charge) diffuse slower through the pores than ^{3}H regardless of the groundwater or tuff type (as also observed in the rock-beaker experiments). The migration of Pu through tuff under diffusive conditions is dominated by sorption (as shown by Figures 10.5-5 and 10.5-7). The migration of Np (V) and U (VI) through tuff depends on tuff type and water chemistry. In cases, such as tuff G4-287, for which the reported sorption of Np is essentially zero (Triay et al. 1996b; Triay et al. 1996a), the diffusion of Np through the tuff is slower than the diffusion of ^{3}H but comparable to the diffusion of a nonsorbing, large anion, such as pertechnetate (Figure 10.5-6).

The analysis of data described above has some problems with respect to the assumptions required to find an analytical solution. The assumptions do not allow for a changing concentration in the traced chamber, for a concentration in the untraced chamber that is not much smaller than the initial concentration in the traced chamber, and for the addition of groundwater to the untraced chamber each time an aliquot was taken.

Therefore, future analysis of these data will involve fitting the diffusion profiles using a transport code (such as the TRACRN code used in the rock-beaker diffusion experiments) to obtain diffusion coefficients. The concentration profiles of the diffusing radionuclides would be fitted to the same equation as Equation 10.5-6 but using the algebraic form given in the section on rock-beaker experiments (Equations 10.5-1 to 10.5-3).

10.5.3.3 Matrix Diffusion Recommendations for Performance Assessment

Matrix diffusion coefficients need to be recommended for use in performance assessment. These are gleaned from reviews of the literature and the results described above. These values will also be treated as expert elicitation. For anions, the average matrix diffusion coefficient is

3.2×10^{-11} m^2/s (3.2×10^{-7} cm^2/s) with a standard deviation of 1×10^{-11} m^2/s, a minimum value of zero and a maximum value of 10^{-9} m^2/s (10^{-5} cm^2/s) with a beta distribution. For cations, the average matrix diffusion coefficient is 1.6×10^{-10} m^2/s (1.6×10^{-6} cm^2/s) with a standard deviation of 0.5×10^{-10} m^2/s, a minimum value of zero and a maximum value of 10^{-9} m^2/s (10^{-5} cm^2/s) with a beta distribution.

10.6 COLLOID-FACILITATED RADIONUCLIDE TRANSPORT

Recently, generation and mobilization of colloids have become important issues for contaminant transport (Kersting et al. 1999), particularly facilitated transport of radionuclides as intrinsic colloids (e.g., colloidal Pu (V)), or as radionuclide-bearing pseudocolloids (e.g., ^{239}Pu, ^{237}Np, ^{243}Am, and ^{247}Cm from high-level radioactive wastes, or ^{137}Cs, ^{90}Sr, and ^{60}Co from low-level radioactive wastes) (Triay et al. 1996d, p. 16; Buddemeier and Hunt 1988; Kaplan et al. 1994; McCarthy and Degueldre 1993, pp. 250 to 260). Radionuclide-bearing pseudocolloids consist of radionuclides adsorbed onto nonradioactive colloids, such as clays or oxides. New colloids can be generated or activated by perturbations in the hydrogeochemistry of the aquifer system, particularly by waste disposal activities (McCarthy and Degueldre 1993, p. 304). Colloids exist naturally in groundwater in almost all subsurface environments, with the composition and concentration of colloids being site specific and determined by the geologic nature of the subsurface. According to McCarthy and Degueldre (1993, Table 6), the size of natural colloids ranges from 0.01 to 1.0 μm, and concentrations range from 0.1 to 100 ppm. The large surface area of colloids (10^4 to 5×10^5 m^2/kg) can significantly sorb radionuclides, even for relatively low mass concentrations of colloidal particles in the aquifer (Vilks and Degueldre 1991; Penrose et al. 1990). Triay et al. (1996d) studied the generation and stability of colloids in Yucca Mountain groundwater and found that colloids of clays, Si, and iron oxides were generated in the groundwater, and strong sorption of radionuclides onto these colloids occurred. The stability of clay and silica colloids was a function of the ionic strength. Triay et al. (1997) found that hematite and goethite colloids rapidly sorbed soluble Pu (V) as well as colloidal Pu (IV) in groundwater. However, the desorption of ^{239}Pu from these two iron oxide colloids is much slower than the sorption process (CRWMS M&O 2000, Section 6.7.3), suggesting that once sorbed onto mobile colloids, radionuclides could be transported great distances before they desorb. It is the details of these processes and their relevance to YMP that need to be addressed adequately prior to final determination of the suitability of the Yucca Mountain site for long-term radioactive waste disposal.

Under most geologic conditions, transport of radionuclides via iron oxide or clay colloids dominates over transport of radionuclides by true polymerized radiocolloids (McCarthy and Zachara 1989). Champ et al. (1982, pp. 749 to 751) reported that almost 75 percent of the Pu was associated with colloidal particles and rapidly transported when groundwater was pumped through otherwise undisturbed aquifer cores. In porous media, where the sizes of colloids are smaller than the pores, colloids can migrate over long distances. O'Melia (1990, pp. 447 to 457) reported in one study that colloidal particles with sizes ranging from 0.1 to 1.0 μm were the most mobile during natural gradient flow through a sandy porous medium (unconsolidated), with larger and smaller colloids being preferentially removed. Therefore, these mobile colloids may enhance the transport of the strongly sorbing radionuclides along flow paths. At the Nevada Test Site, transition metals and lanthanide radionuclides associated with inorganic colloids were recovered from groundwater 300 m from a nuclear detonation cavity (Buddemeier and Hunt 1988). Americium and Pb were transported in the vadose zone with organic and inorganic colloids. Penrose et al. (1990) reported that Pu and Am were associated with siliceous colloids in a near-surface alluvial aquifer at Los Alamos National Laboratory. The actual Pu transport velocity was nearly 1,200 times greater than the predicted transport velocity based solely on partitioning between dissolved and stationary solid phases. Kersting et al. (1999) showed that Pu

associated with colloids had migrated 1.3 km from the Benham underground nuclear test site of 1968, a significant finding for Yucca Mountain.

Experimental studies on colloid transport through soil or rock under partially saturated or highly unsaturated conditions are few, but do indicate that colloids can migrate even under relatively dry conditions, although migration rates exhibit strong dependence upon colloid size as the system desaturates (McGraw 1996; Wan and Tokunaga 1997). To examine the influence of colloid size on transport, McGraw (1996, pp. 61 to 68) used five different colloid sizes between 20 and 1,900 nm, under both saturated and unsaturated conditions in a quartz sand. The results indicated that under saturated conditions, the breakthrough of each colloid at C/C_o = 50 percent was the same as that of the breakthrough of KBr, the nonreactive tracer, indicating no relationship of colloid size to migration under saturated conditions. However, the breakthrough of the colloids under highly unsaturated conditions exhibited a strong relationship between the colloid breakthrough and the colloid size, with a fairly complete breakthrough of the 20-nm colloid and little or no breakthrough of the 1,900-nm colloid.

In another set of experiments, McGraw (1996, pp. 68 to 101) compared four sets of hydrophobic and hydrophilic colloids. Results indicated that transport of hydrophobic colloids depends on colloid size, water film thickness, and colloid charge density. In contrast, hydrophilic colloids were not affected by these variables and were rapidly transported through the system, even under very low moisture contents. McGraw concluded that the unsaturated zone is not an effective barrier to colloid migration, even for large colloids, although it will somewhat retard larger colloids.

In light of these studies, colloid migration must be adequately bounded for the Site Recommendation and License Application. Information from the recent advances in this field is presented chronologically, ending with the most recent results for attachment or detachment of Pu and Am on colloids of hematite, goethite, montmorillonite, and silica in natural and synthetic groundwater.

10.6.1 Data Sources

The primary input data used for colloid-facilitated radionuclide transport studies are described in (CRWMS M&O 2000, Sections 6.7) include laboratory results of colloid experiments using waters collected from Yucca Mountain or synthesized to reflect Yucca Mountain waters and colloidal materials either collected from the field or synthesized in the laboratory. Data from previous studies are reviewed but are not used as input into the conclusions or recommendations. Parameters used in this section are colloid type and concentration, percent sorbed onto various substrates, and attachment/detachment rates for radionuclides onto, and off of, various substrates.

10.6.2 Global Approach to Colloid Stability

This section presents groundwater colloid results from various geological formations around the world, ranging from crystalline to sedimentary, saturated to unsaturated, and organic rich to organic depleted. Colloid presence and potential mobility are estimated on the basis of stability properties in the investigated groundwater. The colloid concentration is a function of pH, potential oxidation-reduction (redox), the concentrations of Na, K, Ca, Mg, and organic C, as

well as the status of the chemical and physical steady state of the hydrogeochemical system. The colloid properties are discussed with a non-site-specific approach.

In natural groundwaters, there is a continuum between inorganic colloids (clay, oxide), inorganic colloids coated with organic material, organic colloids associated with inorganic phases, and organic colloids. A first list of colloid data (e.g., concentration) for shallow as well as deep groundwater systems was published by McCarthy and Degueldre (1993). Key factors affecting colloid stability were identified as pH, redox potential, salt (Na, Ca) concentrations (Degueldre et al. 1996a, p. 692), the presence of dissolved organics (O'Melia and Tiller 1993, pp. 374, 380, 383), and the status of the system at steady state.

Conceptual models describing the colloid occurrence take into account their generation and disappearance, aggregation and desegregation, and attachment and detachment on the rock or substrate. In the aquifer, the balance between generation and disappearance may be postulated for the undisturbed saturated zone. However, it is considered that the stability of the colloid phase is a function of the disappearance rate by attachment, which determines the colloid concentration in the aquifer. Because attachment parameters are defined in stationary conditions, this concept must be extended for perturbed aquifers. This extension might justify larger colloid concentrations during hydrogeochemical transients in the aquifer.

The general consensus about contaminant transport by colloid-facilitated processes is the need to understand the colloid generation mechanisms to evaluate a contamination hazard or to design remediation when required. It is necessary to discuss and define rules for evaluating colloid properties in natural systems or systems modified by the presence of contaminants and to sketch a conclusion on a non-site-specific basis. This type of general study, based on recent results obtained from selected hydrogeochemical systems, allows the development of a global approach. Addition of Yucca Mountain-specific data can then result in a more robust model.

Data were collected for systems ranging from various crystalline to sedimentary geological formations. Table 10.6-1 summarizes the minerals composing the rocks of the considered formations. The crystalline systems comprise recent granitic systems (e.g., the Central European Basement with studies in the Black Forest, South Germany, and the northern part of Switzerland, as well as in the Alpine area, Grimsel, Switzerland) and older granitic systems (e.g., the Scandinavian or Canadian shield). The rock in these systems is mainly composed of quartz, feldspar, and mica. Minerals currently found in the granitic fractures are illite, muscovite, quartz, chlorite, calcite, iron oxyhydroxides, and some pyrite. Their organic content is quite low.

The Swiss crystalline studies (Degueldre et al. 1996a; Degueldre et al. 1996b) selected systems ranging from shallow to deep aquifers. The sites are the Menschenchwand U prospect, the Bad Säckingen spring, the Zurzach thermal well, the Leuggern borehole, and, in the Alps, both the Grimsel Test Site and the Transitgas tunnel. The depth ranges from about 100 to 1,680 m in 600-Ma granite. In Sweden, two systems were considered in the 2,000-Ma granite: Äspö, the Experimental Underground Laboratory at a depth of 70 m below the surface (Laaksoharju et al. 1995), and the Laxemar deep borehole, with a 1,420- to 1,705-m depth. Both sites are located on the Baltic coast about 350 km south of Stockholm. In Canada, Vilks et al. (1991) investigated waters at the Whiteshell Research Area, underlain by the Lac du Bonnet granite batholith, located in the southeastern part of Manitoba Zones, at depths down to 1,150 m.

Yucca Mountain consists of a 1,500-m-thick accumulation of Miocene silicic ash-flow tuffs. The rocks can be generally characterized as alternating layers of highly porous nonwelded tuff and low-porosity, densely welded tuff. The original rock constituent was predominantly volcanic glass, but high-temperature devitrification and lower-temperature alteration have produced mineral assemblages dominated by feldspar, zeolites, and various silica polymorphs with low organic content. Crystallized accumulations of former colloidal material, produced during rock alteration, are present in the pores of some rock layers (Levy 1992, p. 79).

Morro do Ferro, Brazil, is an altered (weathered) formation, with some organic content that issued from volcanic activities in a subtropical area. Morro do Ferro is located in the caldera of Poços de Caldas, Minerais Generai. The rocks are predominantly carbonitites deeply weathered to laterites (rich in gibbsite, illite, and kaolinite-rich). Morro do Ferro is characterized by magnetite dikes and breccia, which are believed to comprise the most hydraulically conductive zones (Miekeley et al. 1992).

Partially and nonmetamorphosed sedimentary systems were also considered. They generally contain more organic compounds than the previously mentioned formations.

The Wellenberg system (Degueldre et al. 1994) is located in central Switzerland and comprises a marl formation slightly metamorphosed. The investigated aquifer lies in this marl formation at a 360-m depth, but another system of interest lies at a depth of 1,600 m below the marl formation in a chalk (limestone) layer. Longworth et al. (1989) investigated colloids from the Triassic Sandstone aquifer (120-m depth) at the Markham, United Kingdom, site 50 km north of Nottingham. At Gorleben, central Germany, Kim et al. (1992) investigated a system composed of porous sediments with lignite intercalations. The aquifers there are located at a depth between 50 and 300 m and are composed of glacial sand, silt, marl, and clay. Uplift has caused rupturing and folding of the overlying and surrounding Miocene brown-coal sand and clay.

The Cigar Lake U deposit is a sandstone-hosted ore body located in the Athabasca Basin of northern Saskatchewan, Canada (Vilks et al. 1993). The ore is located at the contact between sandstone and altered basement rock and is separated from the sandstone host by zones of clay-rich, diagenetically altered sandstone. The sandstone formation lies at a depth of 432 m below the surface. Finally, the Bangombé fossil reactor zone, Gabon, discovered in 1980, is located some 30 km south of the Oklo deposit. The sandstones are overlain by a thick series of marine-derived, organic-rich pelites and limestones. These formations were also slightly metamorphosed (Pedersen 1996).

Before a comparison can be made of colloid properties, the hydrochemical properties of the studied groundwaters must be well considered. Table 10.6-2 shows the most important hydrogeochemical parameters. The individual water properties may be summarized as follows:

- In the Transitgas tunnel, zone 1, nine springs were investigated with mixed Na-Ca-SO_4-HCO_3 waters at pH values from 7.8 to 9.4 that were mostly oxic with temperatures between 5° to 9°C. Locally, in zone 2 (springs 10 to 14), hydrothermal (18° to 28°C) Na-SO_4 waters with pH values of 8.8 to 9.2 were sampled that were reducing. Finally, in zone 3 (springs 15 to 16), shallow groundwaters of the Ca-HCO_3 type with oxic character, pH values of 9.2 to 9.6, and temperature around 4° to 6°C were sampled. At

the Grimsel Test Site, a deep Na-Ca-HCO_3-F groundwater was collected at a depth of 450 m below the surface. From the boreholes in Leuggern and Zurzach, crystalline waters of a Na-SO_4-HCO_3-Cl type were sampled at depths of 1,860 and 450 m, respectively.

- At Whiteshell, Na-Ca-HCO_3 waters were studied in the upper zones down to 400 m, and Ca-Na-Cl waters were collected at depths down to 1,100 m below the surface. At Äspö, mixed waters of Na-Ca-Cl-HCO_3 type were studied at a depth of 70 m below the surface, and at Laxemar, deep Na-Ca-Cl water was pumped from a depth of 1,400 m.

- At Yucca Mountain, the J-13 oxic water of a Na-HCO_3-SiO_2 type is pumped from a depth 300 m below the surface. At Morro do Ferro, the K-SO_4-F water was also pumped but only from a depth of 30 m.

In the sedimentary aquifers, the water properties may be summarized as follows:

- At Gorleben, Na-HCO_3-OC ("OC" represents organic-carbon rich) waters are sampled at depths of 60 and 80 m below the surface.

- At Wellenberg, deep Na-HCO_3 waters flow under artesian pressure at depths of 350 and 1,350 m below the surface.

- In Markham, the oxic municipal water of a Mg-Ca-Na-HCO_3 type is pumped at a depth 100 m below the surface.

- At Cigar Lake, the Ca-Na-HCO_3 groundwaters were sampled at depths down to 435 m.

- In Bangombé, complex Ca-Mg-Na-HCO_3 (relatively demineralized) waters were pumped at depths of about 20 m below the surface. The considered anaerobic aquifers are rather shallow but not oxidized.

These groundwaters range from oxic to anoxic, Na (Bad Säckingen) or Na-Ca-rich (Äspö), to K-rich (Poços de Caldas) or with a large Mg contribution (Markham, Wellenberg), and organic depleted (Zurzach) to organic rich (Gorleben). Their types go from shallow Ca-HCO_3 (Transitgas tunnel, zone 3) to more complex Na-SO_4-HCO_3-Cl (Zurzach) or K-SO_4-F (Poços de Caldas). For the water considered, the salt concentrations range over four orders of magnitude, the total hardness of the water over two orders of magnitude, and the pH from 6 to 10. Total organic C is low in most of the groundwater and is less than 10^{-5} M in the Swiss crystalline and of the order of 6 x 10^{-5} M in the sedimentary (e.g., Wellenberg). Its concentration in the Gorleben system may reach the 10^{-2} M level, because the waters originate from the brown coal formation (nonmetamorphosed system).

Steady-state conditions in the aquifers do not exist in some cases. For example, mixing of Na-Ca-HCO_3-Cl and Na-Ca-(Mg)-Cl-HCO_3 waters is observed at Äspö. A similar situation is also locally observed at Bad Säckingen. An important assessment of the status of the aquifer is comparison of water temperature with the temperature estimated by the geothermometer ($T\&T_{geo}$ in Table 10.6-2), which may give information about the status of the thermal steady state of the water. For example, large differences between temperature at the source and temperature

evaluated from the geothermometer are noted in the hydrothermal waters collected in zone 2 of the Transitgas tunnel.

10.6.2.1 Results and Discussion of Global Studies

Colloid occurrences in aquifers are postulated to be a consequence of the colloid stability in the hydrogeochemical system. The systems are first supposed to be at steady state (no hydrogeochemical changes). Colloid phases range from clay (Grimsel Test Site, Wellenberg), to SiO_2 (Yucca Mountain), Fe-organic-rich phases (Morro do Ferro), clay-coated with organics (Äspö), and clay associated with organic phases (Gorleben).

Comparisons of all results were performed at the 100-nm size for accuracy and consistency. Factors decreasing the colloid stability are an increase of salt (Na^+, K^+) concentration and of water total hardness (Ca^{2+}, Mg^{2+}). The trend of colloid concentrations as a function of salt concentration and water hardness is shown in Figure 10.6-1. Strong coagulants (e.g., Fe^{3+}, Al^{3+}) are quasi-insoluble in the groundwater, limiting their action in the aquifer. The effect of Ca may be diminished (Seaman et al. 1995) in weakly acidic oxic water loaded with positively charged iron-oxyhydroxy colloids for which cations are not able to act as a coagulant. This effect was observed in the Poços de Caldas mine where iron-oxyhydroxide colloids are stabilized at pH values from 3 to 5 in the surface water in which pyrite oxidation decreases the pH, locally increasing the stability of these positively charged Fe colloids. The Ca does not act as a coagulant for Fe-rich colloids in these waters. It must be noted that water sampling itself generates artifacts such as calcite, a particular problem in Ca-rich water. Therefore, data from Laxemar, Whiteshell, and Äspö are absent from Figure 10.6-1.

The apparent trend observed in Figure 10.6-1 must be justified on the basis of the physicochemical properties of alkali and alkaline-earth elements with respect to the stability of model colloids. This basis was tested for montmorillonite colloids, selected as an example of clay colloids. The attachment factor (a) of these colloids increases toward a=1 with increasing alkali and alkaline-earth element concentrations (Figure 10.6-2). This test clearly demonstrates that the salinity and hardness of the water play an important role in colloid stability and that the attachment factor of these clay colloids reaches about a=1 for salt concentrations around $10^{-1.5}$ M and alkaline-earth element concentrations around $10^{-3.5}$ M.

Factors increasing colloid stability and, therefore, their transport include the presence of organics or changes in the hydrogeochemical state in the aquifer. The effect of organics on the colloid phase stability was studied in detail by O'Melia and Tiller (1993). They confirmed that the specific increase of dissolved organic concentration and of pH enhances colloid stability. This result contributes to the large colloid concentration observed in Gorleben. The next cases studied were systems subject to chemical or dynamic changes that are not at steady state with respect to the hydrothermal signature (e.g., zone 2 in the Transitgas tunnel, Bad Säckingen, and Yucca Mountain) or with colloid populations consisting of amorphous components (vitrified tuff from Yucca Mountain) or in which the chemistry is variable (e.g., the mixing waters at Äspö). In zone 2 from the Transitgas tunnel, the colloid concentration remains large, because the hardness of these waters is low.

A model of contaminant transport by colloids should consider these properties. Colloid stability is more a function of the water chemistry and less of the rock itself, because groundwater chemistry is already driven by rock properties on the basis of rock-water interactions. The stability of colloid in a particular water limits mobile concentration.

10.6.2.2 Conclusions from Global Studies

Colloid concentration in a given aquifer is a function of the colloid phase stability in the hydrochemical system. Stability is a function of the chemical composition of the water as well as of the hydrogeochemical steady state of the aquifer. For an aquifer in a steady-state situation, decreases of the concentration of alkali elements below 10^{-2} M and of alkali-earth elements below 10^{-4} M contribute to an increase in the colloid stability and concentration. Water mixing and large concentrations of colloidal or dissolved forms of organic C also contribute to an increase in the colloid stability and concentration. Additionally, the presence of transient situations, such as changes of *T*, flow rate, or chemistry (pH, salt, or redox potential) in the aquifer, induces larger colloid concentrations.

10.6.3 Recent Experimental Studies

In a study by Noell et al. (1998), an idealized laboratory setup was used to examine the influence of amorphous silica colloids on the transport of Cs. Synthetic groundwater and saturated glass-bead columns were used to minimize the presence of natural colloidal material.

The retardation factor for Cs in the two types of glass-bead columns was determined both in the absence of the silica colloids and in the presence of a constant flux of colloids. Also, the influence of anthropogenic colloids was tested by injecting pore-volume slugs of an equilibrated suspension of Cs and colloids into the colloid-free columns.

The intent of these experiments was to establish data, under ideal circumstances, that show the influence of silica colloids on the migration of radionuclides through porous media. This goal was accomplished by using synthetic groundwater and saturated glass-bead columns so that the amount of natural colloidal material in the columns was minimized. Cesium-137 was used as a model radionuclide because of its detectability and simple chemistry. Colloidal silica was examined because of its abundance in many groundwaters, including those expected in the repository situation.

The sorption of Cs to the amorphous silica colloids was found to be significant and fully reversible. In independent batch-sorption experiments, it was determined that a Freundlich isotherm, with the partitioning coefficient K equal to 0.111 $\times/\div$ 1.17 mL/mg, and with the empirical order m equal to 0.882 ± 0.013, adequately described the partitioning of Cs to the amorphous silica colloids at equilibrium. Nonlinear Freundlich isotherms also best described the sorption of Cs to the glass beads. The nonlinear least-squares approximations of Freundlich parameters for the sorption of Cs to the 150- to 210-μm glass beads gave $K = 1.58 \times 10^{-4}$ $\times/\div$ 3.18 mL/mg and $m = 0.828 \pm 0.007$, whereas for the sorption of Cs to the 355- to 420-μm glass beads, the parameters were $K = 9.86 \times 10^{-5}$ $\times/\div$ 9.23 mL/mg and $m = 0.821 \pm 0.014$ (Noell et al. 1998).

The impact of amorphous silica colloids on the transport of Cs was assessed in saturated glass-bead columns. Independently calculated column parameters were verified using tritiated water as a groundwater tracer. The retardation of Cs in colloid-free water was initially examined. The migration of Cs through the columns with the smaller glass beads was more retarded than it was in the larger glass-bead columns. Linear Freundlich partitioning coefficients determined from these column experiments agreed with the sorption data determined in batch experiments. The flow of colloids was also examined independently. Because the surface charges of the silica colloids and the glass beads were similar, the colloids were repelled from the surface of the media and were able to migrate easily through the glass-bead columns. The slight retardation of the colloids was mainly due to physical interactions between the silica colloids and glass beads. To simulate the effect of anthropogenic colloids, an equilibrated suspension of Cs and silica colloids was injected into colloid-free columns as a 0.09 pore-volume pulse. In the smaller glass-bead columns, the colloid front traveled eight times faster than the Cs front. Because the sorption of Cs to the colloids is reversible, this effect resulted in little noticeable, colloid-facilitated transport of Cs. In the larger glass-bead columns, however, there was a slight reduction in the retardation of Cs. This reduction was probably due to the fact that the colloid front only traveled 3.6 times as fast as the Cs front. When silica colloids had a continuous presence and a constant flux through the columns, silica colloids significantly enhanced the migration of Cs. In the smaller glass-bead columns, the silica colloids reduced the retardation of Cs by 14 to 32 percent, whereas in the larger glass-bead columns, they reduced the retardation of Cs by 38 to 51 percent.

A sorption rate equation was developed for the reaction. Because the moles of sorption sites overwhelmed the moles of sorbents, this rate equation was able to be expressed with first-order adsorption and desorption rates. The ordinary differential equation was solved, which allowed calculation of the forward adsorption and reverse desorption first-order sorption rates. It was also found that a Freundlich isotherm adequately described the sorption of Cs to these amorphous silica colloids in the given synthetic water.

The sorption of Cs to amorphous silica colloids occurred very rapidly and was completely reversible. This fact allowed the reaction to be approximated with sorption isotherms. The sorption of Cs to amorphous silica colloids in a synthetic water resembling UE-25 p#1 groundwater under atmospheric conditions was best approximated using a Freundlich isotherm. Although the sorption of Cs to amorphous silica colloids was slightly underestimated at lower Cs concentrations, a K_d equal to 0.0219 ± 0.0022 mL/mg adequately described sorption of Cs to the amorphous silica colloids for most of the regions examined.

Although the sorption of Cs to amorphous silica colloids appeared to be rapid and completely reversible, a methodology was established to determine first-order, kinetic sorption rate coefficients from batch experiments. To find these coefficients uniquely, batch-sorption experiments must be performed at multiple time intervals, both before and after sorption equilibrium occurs. The first-order sorption of Cs to silica colloids is described by (Noell et al. 1998):

$$\frac{d[Cs \cdot OSi(OH)]}{dt} = k_f[Cs^+] - k_r[CsOSi(OH)] \qquad \text{(Eq. 10.6-1)}$$

where k_f and k_r are the first-order forward and reverse reaction rates, respectively, and brackets denote concentrations in moles. Ordinarily, the forward reaction should be described as second order, but when the sorbed contaminant does not influence the sorption of additional contaminants (as is the case when the moles of sorption sites overwhelms the moles of sorbents), it is valid to use a first-order adsorption rate coefficient.

The analytical solution of Equation 10.6-1, in terms of the ratio of moles of colloidally sorbed Cs to moles of dissolved Cs ions, is

$$\frac{[Cs \cdot OSi(OH)]}{[Cs^+]} = \frac{k_f - k_f \exp[-(k_f + k_r)t)]}{k_r + k_f \exp[-(k_f + k_r)t)]} \qquad \text{(Eq. 10.6-2)}$$

It was determined that the first-order desorption rate coefficient for Cs on silica colloids was approximately eight times greater than the first-order adsorption rate coefficient. Because equilibrium was achieved in all of the samples, only minimum values of the sorption rate coefficients were determined. These values were

$$k_f > 0.005 \text{ s and } k_r > 0.04 \text{ s} \qquad \text{(Eq. 10.6-3)}$$

By finding batch kinetic sorption rates between various radionuclides and naturally occurring colloidal material, it is possible to determine which radionuclides have the lowest desorption rates from natural colloids. This information could aid in predicting their migration, because radionuclides that are irreversibly sorbed to colloids are most likely to be transport-facilitated.

10.6.3.1 Reversibility of Radionuclide Sorption onto Colloids: Plutonium onto Iron Oxides

Triay et al. (1997, pp. 65 to 72) applied the methodology described in Section 10.6.3, developed for an idealized system, to colloids expected at Yucca Mountain, namely Pu sorbed onto iron-oxide colloids. A natural groundwater and a filtered carbonate-rich synthetic groundwater (0.05-μm membrane) were used as media in this study. Laboratory batch-sorption experiments were performed to evaluate sorption of Pu as a function of different iron-oxide colloid mineralogy and different oxidation states of Pu and to examine the sorption kinetics of Pu (IV) colloids (hydrous plutonium oxide) and soluble Pu (V) onto these iron-oxide colloids.

The preliminary results showed that adsorption of Pu exhibits different patterns between Pu (IV) colloid and soluble Pu (V), hematite and goethite, and natural and synthetic J-13 groundwaters. Adsorption of both the Pu (IV) colloid and soluble Pu (V) onto the hematite and goethite colloids occurs as a function of time. Iron-oxide colloids sorbed more soluble Pu (V) than Pu (IV) and also sorbed more Pu from synthetic J-13 groundwater than from natural J-13 groundwater. The results also showed that the hematite colloids sorbed more Pu than the goethite colloids. This result was due to differences in surface characteristics. Results indicate that Pu (IV) colloids, as well as soluble Pu (V), can be rapidly adsorbed by hematite or goethite colloids in natural or synthetic groundwater, whereas desorption of Pu (IV) colloids as well as soluble Pu (V) was slower than the sorption processes.

Thermodynamic calculations show that Pu (V) is a stable oxidation state in the pH range of 5 to 7 at a pε of 12 and that Pu (VI) is the most stable oxidation state at higher pH values (Sanchez et al. 1985, p. 2297). It was assumed that adsorption of Pu (IV) onto suspended colloids is due to the interaction of the strongly hydrolyzable Pu (IV) oxidation state with the surfaces of natural particulate matter (Sanchez et al. 1985, p. 2305). Keeney-Kennicutt and Morse (1985) found that Pu $(V)O_2^+$ can be adsorbed from diluted solution and seawater on goethite, aragonite, calcite, and δ-MnO_2. The sorption behavior of Pu $(V)O_2^+$ is influenced by redox reactions occurring on the mineral surface. Adsorption of Pu $(V)O_2^+$ on goethite results in a reaction in which Pu (IV) and Pu (VI) are formed on the mineral surface. The Pu (VI) is slowly reduced to Pu (IV), leaving Pu (IV) as the dominant surface Pu species (Keeney-Kennicutt and Morse 1985). Sanchez et al. (1985) studied adsorption of soluble Pu (IV) and Pu (V) on goethite from a sodium-nitrate solution and found that redox transformations are an important aspect of Pu adsorption chemistry. The adsorption behavior of Pu on goethite is related to the different hydrolytic character of these two oxidation states in the solution. The adsorption edge of the more strongly hydrolyzable Pu (IV) occurred in the pH range of 3 to 5, whereas that for Pu (V) is at pH 5 to 7 (Sanchez et al. 1985).

However, information on affinity, kinetics, and reversibility critical to the evaluation of the significance of colloids to Pu transport is largely unavailable for groundwater particles. Studies, performed in three phases, focus on the adsorption affinity, kinetics, and reversibility of the sorption of soluble Pu (V) and Pu (IV) colloids onto iron-oxide, silica, and clay colloids and on the effect of different plutonium oxidation states with different forms (e.g., colloidal or soluble form) on their behavior in natural and synthetic groundwater. In this phase of the study, laboratory batch-sorption experiments were performed using a natural groundwater and a carbonate-rich synthetic groundwater as media, to evaluate the following:

- The sorption of Pu as a function of two different iron-oxide colloids (hematite and goethite)
- Sorption of Pu as a function of two different oxidation states with different forms [Pu (IV) colloid and soluble Pu (V)]
- Sorption kinetics of Pu (IV) colloid and soluble Pu (V) onto these iron-oxide colloids
- Desorption of Pu from Pu -loaded iron-oxide colloids as a function of time over a long period (approximately 1 year).

10.6.3.2 Adsorption of Plutonium (IV) and Plutonium (V) onto Hematite Colloids

Adsorption of Pu onto the hematite and goethite colloids was investigated as a function of time. The amounts of Pu adsorbed varied among the two iron oxides and two solutions. The adsorption of Pu also exhibited different patterns between the Pu (IV) colloid and the soluble Pu (V). The ionic strength of deionized water was brought to 0.005 M using sodium nitrate ($NaNO_3$) (same ionic strength as the natural and the synthetic groundwater). The alkalinity of the natural and synthetic groundwater used in the study ranged from 22.5 to 25 meq/L. At these values, it was predicted that the adsorption of both Pu (IV) and Pu (V) should not be affected. Sanchez et al. (1985, p. 2301) reported that adsorption of soluble Pu (IV) and Pu (V) was not

affected by alkalinity values less than about 100 meq/L, where the amount of adsorbed Pu on goethite was similar to that obtained at the same pH in 0.1 M sodium-nitrate solution.

Hematite sorbed more soluble Pu (V) than Pu (IV) colloids (Table 10.6-3). Adsorption of Pu also shows different patterns for the two solutions (natural J-13 groundwater and synthetic J-13 groundwater). In the synthetic groundwater, the adsorption of Pu (IV) colloids shows a one-step mechanism. After a 10-min. contact period, about 66 percent of Pu (IV) colloids were adsorbed onto hematite colloids, and, from then on, the percentage of adsorbed Pu (IV) remained constant over time. Additional contact time between Pu (IV) colloids and hematite colloidal particles did not affect the amount of Pu (IV) colloids adsorbed onto the hematite colloidal particles. The adsorption rate is 11.4 pCi/mg/min. during the first 10 min.

In the natural groundwater, although the amounts of adsorbed Pu (IV) colloids increased slightly as the contact time extended from 10 to 60 min., the adsorption of Pu (IV) colloids also shows a one-step mechanism. The percentage of adsorbed Pu (IV) colloids remained constant with additional time. After 10 min. of contact period, about 60 percent of the Pu (IV) colloids was adsorbed by hematite colloids. The adsorption rate is 10 pCi/mg/min. in the natural groundwater (Table 10.6-3). At the end of the experiments (5,760 min.), about 60 to 66 percent of the Pu (IV) colloids were adsorbed by hematite colloids in both natural and synthetic groundwater. These results indicate that Pu (IV) colloids can be rapidly adsorbed by hematite colloid in natural or synthetic groundwater.

With soluble Pu (V), adsorption patterns of Pu (V) onto hematite colloids varied between the two solutions. Generally, hematite colloids sorbed more Pu (V) in the synthetic groundwater than in the natural groundwater.

In the synthetic groundwater, the adsorption of soluble Pu (V) shows a two-step mechanism. The first step is a fast process that occurred in the 10-min. contact period. About 82 percent of the Pu (V) was sorbed during this short period (Table 10.6-3). The adsorption rate is 14.18 pCi/mg/min. in the natural groundwater during this period (Table 10.6-3). The second step is a slow process that continued for 5,750 min. Only an additional 5 percent of Pu (V) was adsorbed during this period.

Soluble Pu (V) and Pu (IV) colloids can be rapidly adsorbed by hematite colloids in natural or synthetic groundwater. In natural groundwater, the adsorption of Pu (V) shows a positive correlation with time. The amounts of Pu (V) adsorbed gradually increased from 44 to 76 percent as the sorption time increased from 10 to 5,760 min. (Table 10.6-3). However, these data were not adequate to determine if the adsorption of Pu (V) in natural water is a one-step or a two-step mechanism. The adsorption of Pu (V) may be a one-step mechanism.

Desorption of Pu from Pu-loaded hematite colloids did not occur during the first 3 days of the desorption process. After 30 days of desorption, Pu (V) was not desorbed from hematite, and less than 0.01 percent of Pu (IV) colloid was desorbed from hematite. Desorption of Pu is much slower than sorption.

10.6.3.3 Adsorption of Plutonium (IV) and Plutonium (V) Onto Goethite Colloids

Generally, goethite sorbed less Pu (IV) and Pu (V) than hematite did in both natural and synthetic groundwater. Adsorption of Pu onto goethite colloids also exhibits different patterns between Pu (IV) colloids and soluble Pu (V). Adsorption of Pu also shows different patterns between the two solutions (natural and synthetic groundwaters).

In the synthetic groundwater, adsorption of Pu (IV) onto goethite colloids is slower than onto hematite colloids. After a 10-min. contact period, only 34 percent of the Pu (IV) was adsorbed. The adsorption rate is 5.6 pCi/mg/min. (Table 10.6-4). Although the amounts of Pu (IV) adsorbed increased with increasing contact time, only 52 percent of Pu (IV) was adsorbed after 5,760 min. of sorption (Table 10.6-4).

In the natural groundwater, about 29 percent of the Pu (IV) colloids was adsorbed during the first 10-min. period; after 10 min., the amount of Pu (IV) colloids adsorbed reached a maximum (45 percent) at 60 min., then decreased with additional time. The adsorption rate is 4.5 pCi/mg/min. during the first 10-min. contact period (Table 10.6-4).

With Pu (V), goethite also sorbed more of the Pu (V) in the synthetic groundwater than in the natural groundwater. In the synthetic groundwater, about 63 percent of the soluble Pu (V) was sorbed during the first 10-min. period. The adsorption rate is 10.6 pCi/mg/min. during this period (Table 10.6-4). Thereafter, there is a small but significant increase in the adsorption of soluble Pu (V) with time.

In the natural groundwater, the adsorption of soluble Pu (V) onto goethite also shows a positive correlation with time. Amounts of Pu (V) adsorbed gradually increased from 19 to 62 percent as the sorption time increased from 10 to 5,760 min. (Table 10.6-4).

These results indicate that Pu (IV) colloids and soluble Pu (V) can be rapidly adsorbed by goethite colloids in natural or synthetic groundwaters. However, desorption of Pu (V) and Pu (IV) from Pu-loaded goethite colloids did not occur during the first three days of the desorption process. After 30 days of desorption, less than 0.01 percent of Pu (V) and less than 0.1 percent of Pu (IV) desorbed from the goethite. Desorption of Pu is much slower than sorption.

The results show that hematite colloids sorbed more Pu than goethite (Tables 10.6-3 and 10.6-4). This result is due to differences in their surface characteristics and the purification of the mineral materials. The hematite material contained 99.6 percent Fe_2O_3; the goethite material contained 86 percent Fe_2O_3 (in terms of oxides, not mineralogy). Because the usual crystal morphology of synthetic hematite particles is hexagonal plates and the crystal morphology of synthetic goethite particles is an acicular, hematite colloids may have larger surface areas than goethite when the particle sizes of both iron-oxide colloids are the same.

Both iron-oxide colloids sorbed more Pu in the synthetic groundwater than in the natural groundwater. The zero point of charge of synthetic hematite and goethite ranged in pH value from 7.95 to 8.01 in both groundwaters, indicating a similar surface activity with regard to the Fe-OH groups for the two iron-oxides. However, the surface electrical potential of iron-oxide colloids in the synthetic groundwater was higher than in the natural groundwater.

Adsorption of soluble Pu (V) may be a chemisorption process in which the soluble Pu (V) or its hydrolysis species bind to hydroxyl (OH^-) groups on the hematite or goethite surface. Assuming that Pu (V) binds to hematite or goethite surface (OH^-) groups analogous to aqueous coordination reactions, the adsorption of Pu (V) to both iron-oxide colloids can be chemically described by the following equation (Liang and McCarthy 1995, p. 88).

$$\equiv SOH^{o} + \tilde{N}u(V)O_2^{+} \Leftrightarrow \equiv SO - \tilde{N}u(V)O_2^{\delta} + H^{+} \qquad K_{1,\,app} \qquad \text{(Eq. 10.6-4)}$$

where ≡SOH denotes a surface site of hematite or goethite, and ≡SO-Pu^{4+} is the concentration of Pu (V) adsorbed on the surface sites of the colloids. The apparent surface equilibrium constant is $K_{1,app}$ and is defined as:

$$K_{1,app} = \{\equiv SO\text{-}Pu^{4+}\}[H^{+}]/\,[\equiv SOH]\;[Pu^{5+}] \qquad \text{(Eq. 10.6-5)}$$

Because of the charge characteristics of the surface of iron-oxide colloidal particles, the activity of ions at the surface needs to be corrected to obtain the intrinsic equilibrium constant, which can be calculated by the following equation:

$$K_{1,\,int} = K_{1,\,app} \exp\,[(z-1)F\Psi/RT] \qquad \text{(Eq. 10.6-6)}$$

where Ψ is the potential difference between the binding site and the bulk solution, F is the Faraday constant, R is the gas constant, T is temperature in absolute degrees, and z is the ionic charge of the sorbing metal ion. The exponential term accounts for the coulombic contribution to the intrinsic equilibrium constants.

Theoretically, from the reaction equation, after soluble Pu (V) adsorbs onto iron oxide, Pu (V) is reduced to Pu (IV) on the surface of colloidal particles. The hydrolysis constants for adsorption of Pu (V) onto iron-oxides are not well known (Sanchez et al. 1985, p. 2301).

However, sorption of Pu (IV) colloids onto iron-oxide colloids may have different mechanisms, although the adsorption mechanism of Pu (IV) colloids onto hematite or goethite colloids is not well understood. During the experiments of Triay et al. (1997), precipitation of Pu (IV) colloids did not occur. The sorption of Pu (IV) colloids onto iron-oxide colloids may have happened by an electrostatic force. In the natural or the synthetic groundwater with pH ranges of 8.4 to 8.6, the surface electrical potential of hematite and goethite colloids ranged from 27.1 to 35.4 mV. Therefore, the negatively charged surfaces of iron-oxide colloids may electrostatically bind positively charged Pu (IV) colloids.

Sanchez et al. (1985, p. 2301) studied the sorption of soluble Pu (IV) species onto goethite. They found that soluble Pu (IV) species were chemically described by three reactions involving the adsorption of Pu (IV) hydrolysis species:

$$\equiv SOH + Pu^{4+} + 2H_2O \Leftrightarrow \equiv SO^{-}Pu\,(OH)_2^{2+} + 3H^{+} \qquad {}^{*}K_{1,\,int} \qquad \text{(Eq. 10.6-7)}$$

$$\equiv SOH + Pu^{4+} + 3H_2O \Leftrightarrow \equiv SO^{-}Pu\,(OH)_3^{+} + 4H^{+} \qquad {}^{*}K_{3,\,int} \qquad \text{(Eq. 10.6-8)}$$

$$\equiv SOH + Pu^{4+} + 4H_2O \Leftrightarrow \equiv SO^{-}Pu\,(OH)_4^{0} + 5H^{+} \qquad {}^{*}K_{3,\,int} \qquad \text{(Eq. 10.6-9)}$$

It is not known whether the sorption of Pu (IV) colloids onto hematite or the goethite used by Triay et al. (1997, pp. 65 to 72) follows the same reactions described by Sanchez et al. (1985).

Because of the presence of carbonate and bicarbonate ions in both natural and synthetic groundwaters, the formation of plutonium (V)-carbonate complexes may occur, which may influence the adsorption of Pu (V).

10.6.4 Reversibility of Sorption onto Colloids

The mechanism that dominates the sorption of actinide contaminants onto oxides or hydroxides in a solid/aqueous interface system is surface complexation (Fuger 1992). This results in the formation of actinide-hydroxide complexes on the surface of silica, clay, or iron-oxide colloids. According to Fuger (1992), hydrolysis reactions of tetravalent and pentavalent actinides can be described as follows:

$$q\,M^{4+} + n\,H_2O = M_q\,(OH)_n^{(4q-n)+} + n\,H^+ \qquad \text{Log } \beta^*_{n.q.} \qquad \text{(Eq. 10.6-10)}$$

$$q\,MO_2^{+} + n\,H_2O = (MO_2)_q\,(OH)_n^{(q-n)+} + n\,H^+ \qquad \text{Log } \beta^*_{n.q.} \qquad \text{(Eq. 10.6-11)}$$

The surface complexation of a soluble metal is correlated to the aqueous metal-ion hydrolysis (Fuger 1992; Sanchez et al. 1985). Therefore, adsorption of actinide onto colloids can be generally described as follows (Liang and McCarthy 1995):

$$\equiv SOH + M^{z+} + n\,H_2O = \equiv SO\text{-}M(OH)_n^{(z-n)+} + n\,H^+ \qquad K_{1,\,app} \qquad \text{(Eq. 10.6-12)}$$

where ≡SOH denotes a surface site and $\equiv SO\text{-}M(OH)_n^{(z-n)+}$ is the complex on the surface of colloids. The apparent surface equilibrium constant is $K_{1,\,app}$ and is defined as:

$$K_{1,\,app} = [\equiv SO\text{-}M(OH)_n^{(z-n)+}][H^+]^n / [\equiv SOH][\,M^{z+}] \qquad \text{(Eq. 10.6-13)}$$

However, iron-oxide colloids have different types of surface hydroxyl groups than do clay colloids or silica colloids. The predominant mechanism of surface complexation reactions of actinide with surface hydroxyl may be different among iron oxide, clay, and silica.

Keeney-Kennicutt and Morse (1985) found that $Pu(V)O_2^+$ could be adsorbed from diluted solution and seawater on goethite, aragonite, calcite, and δ-MnO_2. The sorption behavior of PuO_2^+ is influenced by redox reactions occurring on the mineral surface. Adsorption of PuO_2^+ on goethite resulted in a reaction in which Pu (IV) and Pu (VI) are formed on the mineral surface. The Pu (VI) is slowly reduced to Pu (IV), leaving Pu (IV) as the dominant Pu surface species (Keeney-Kennicutt and Morse 1985). Sanchez et al. (1985) found that adsorption behavior of Pu onto goethite is related to the different hydrolytic character of these two oxidation states in the solution. The adsorption of the more strongly hydrolyzable Pu (IV) occurred in the pH range of 3 to 5, whereas for Pu (V), it occurred in the pH range of 5 to 7.

Information on affinity, kinetics, and reversibility, which is critical to evaluate the colloid-facilitated transport of radionuclides, is largely unavailable for groundwater particles. There is no information on the adsorption of true polymerized radiocolloids (e.g., Pu (IV) colloids) onto colloids of iron-oxide, clays, and silica in groundwater. Laboratory batch-sorption experiments

were conducted to evaluate: (1) sorption of ^{239}Pu and ^{243}Am onto different colloids (e.g., hematite, goethite, montmorillonite, and silica), (2) sorption kinetics of ^{239}Pu and ^{243}Am onto these colloids, (3) the effect of colloidal concentrations on the sorption of soluble Pu (V) and ^{243}Am, (4) the stability of colloidal Pu (IV) in groundwater, and (5) desorption of ^{239}Pu or ^{243}Am from ^{239}Pu -loaded or ^{243}Am-loaded colloids as a function of time.

10.6.4.1 Water, Colloidal Solution, and Tracer

Water from well J-13 and a simulated water were used in these studies. The J-13 water had a pH of 8.2 and an ionic strength of 0.005 M. It contained 1.0 ppm of total organic C, 30.7 ppm of Si, 43.2 ppm of Na, 11.9 ppm of Ca, 1.9 ppm of Mg, and 3.4 ppm of K. It also contained 136 ppm of HCO_3^-, 9.4 ppm of NO_3^-, 6.9 ppm of Cl^-, and 17.8 ppm of SO_4^{2-}. The simulated water, referred to as SYN.J.13, was prepared by dissolving sodium carbonate (Na_2CO_3) and sodium bicarbonate ($NaHCO_3$) in nanopure deionized water. The water had a pH of 8.47, an alkalinity of 25 meq/L, and an ionic strength of 0.005 M.

The man-made colloidal solutions include pairs of solutions in J-13 and in simulated water for hematite (Fe_2O_3-J.13 and Fe_2O_3-SYN.J.13), goethite (FeO^oOH-J.13 and FeO^oOH-SYN.J.13), montmorillonite (M-J.13 and M-SYN.J.13), silica-ST-ZL (silica-ST-ZL-J.13 and silica-ST-ZL-SYN.J.13), and silica-PST-1 (silica-PST-1-J.13 and silica-PST-1-SYN.J.13). The average particle size of colloids in the solutions was 416 nm for hematite, 334 nm for montmorillonite, and 139 nm for ST-ZL and PST-1. Approximately 97 percent of goethite colloidal particles were in the size range of 100 to 200 nm. The zeta potential of colloidal particles ranges from –14 to –35.3 mV for hematite, from –11.6 to –29.0 mV for montmorillonite, from –21.5 to –35.7 mV for silica ST-ZL, and from –31.0 to –32.5 mV for silica PST-1. The surface electrical potential for goethite ranges from –27.1 to –32.6 mV. The cation exchange capacity of montmorillonite was 152.4 mol/kg, which was determined using a method described by Sumner and Miller (1996).

Two Pu (V) work solutions (plutonium (V)-J.13 and plutonium (V)-SYN.J.13) each contained 2.74×10^{-7} M of Pu. The pH values of the two work solutions were 8.0 and 8.22, respectively. Two Pu (IV) colloidal work solutions (colloidal plutonium (IV)-J.13 and colloidal plutonium (IV)-SYN.J.13) contained 2.40×10^{-7} M and 2.35×10^{-7} M of Pu (IV), respectively. The particle size of Pu (IV) colloids was $\leq$ 10 nm. The pH values of the two work solutions were 8.18 and 8.33, respectively.

Two ^{243}Am work solutions (Am-J.13 and Am-SYN.J.13) each contained 1.26×10^{-8} M of Am. The pH values of the two work solutions were 8.18 and 8.53, respectively.

10.6.4.2 Sorption Procedure

Three sorption experiments, referred to as sorption #1, sorption #2, and sorption #3, were performed in duplicate at room temperature. Sorption #1 examined the sorption kinetics of soluble Pu (V) and colloidal Pu (IV) onto colloids of hematite, goethite, montmorillonite, silica ST-ZL, and silica PST-1. Sorption #2 was performed to evaluate the sorption kinetics of ^{243}Am onto colloids of hematite, montmorillonite, silica ST-ZL, and silica PST-1. Sorption #3 was

conducted to examine the effect of colloidal concentration on the sorption of Pu (V) and ^{243}Am onto colloids of hematite, montmorillonite, silica ST-ZL, and silica PST-1.

The sorption distribution coefficient (K_d value) of Pu or Am on iron oxide, montmorillonite, or silica colloids is calculated using the following equation:

$$K_d \text{ (mL/g)} = [(A_o V_o - A_f V_f)/M] / A_f \qquad \text{(Eq. 10.6-14)}$$

where

A_o = the initial α activity of Pu (V) or Pu (IV) per milliliter solution
V_o = the initial volume (milliliter) of Pu work-solution in contact with colloidal particles
A_f = the final α activity of Pu (V) or Pu (IV) per milliliter solution after sorption
V_f = the final volume (milliliter) of the solution after sorption
M = the mass in grams of colloids used in the sorption process

10.6.4.3 Desorption Procedure

Plutonium-239-loaded colloidal particles were collected from a 96-hour sorption process. After the wet weights of the colloids were obtained, the colloids were extracted successively with plutonium-free J-13 or simulated water. Desorption was allowed to proceed from 2 to 150 days.

10.6.4.4 Results

10.6.4.4.1 Sorption Kinetics of Plutonium-239 onto Colloids

Sorption of Plutonium-239 onto Hematite Colloids–Sorption of colloidal Pu (IV) onto hematite was rapid in both natural and simulated groundwaters. Hematite colloids sorbed approximately 94 percent of colloidal Pu (IV) in natural groundwater during the first 10 min. (Figure 10.6-3). The initial sorption rate was 12.7 pCi/mg/min. In simulated water, the sorption of colloidal Pu (IV) was higher than in natural groundwater. During the first 10 min., approximately 95 percent of Pu (IV) was adsorbed. The initial rate was 16.4 pCi/mg/min. Thereafter, the amount of sorbed Pu (IV) increased gradually with time. By the end of the sorption process, the value of the sorption distribution coefficient, K_d, reached 2×10^6 mL/g in natural groundwater and 7×10^5 mL/g in simulated groundwater. Sorption of soluble Pu (V) by hematite colloids involved two phases in both waters: a fast phase, which occurred in the first 10 min., followed by a slow phase that lasted 95.83 hr. In the fast phase, about 46 percent of Pu (V) was adsorbed in natural groundwater during the first 10 min. (Figure 10.6-3). The initial sorption rate was 7.3 pCi/mg/min. In the simulated water, approximately 75 percent of Pu (V) was adsorbed during the first 10 min. The initial rate was 12.5 pCi/mg/min. In the slow phase, an additional 41 percent of soluble Pu (V) in natural groundwater and 23 percent additional Pu (V) were adsorbed during the remaining 95.83 hr. At the end of the sorption process, the K_d value of Pu (V) on hematite colloids was 10^5 mL/g in both natural and simulated groundwaters.

Sorption of Plutonium-239 onto Goethite Colloids–Goethite colloids sorbed approximately 75 percent of Pu (IV) in natural groundwater during the first 10 min. (Figure 10.6-4). The initial sorption rate was 8.7 pCi/mg/min. After 10 minutes, the amounts of sorbed colloidal Pu (IV) reached a maximum (approximately 92 percent) at 1 hr., then it decreased gradually during the

remaining 95 hr. This result indicates that partial desorption of Pu (IV) from goethite colloids occurs after 1 hr. By the end of the sorption process, the K_d value was 7×10^4 mL/g. In the simulated water, approximately 76 percent of Pu (IV) was sorbed during the first 10 min. (Figure 10.6-4). The initial sorption rate was 12.0 pCi/mg/min. Thereafter, the amount of sorbed Pu (IV) increased, reaching a maximum (approximately 96 percent) at 6 hr., and then remained at this level during the remaining 90 hr. At the end of the sorption process, the K_d value was 2×10^5 mL/g, which was the same K_d value as on hematite colloids.

Goethite colloids sorbed 56 percent soluble Pu (V) in natural groundwater during the first 10 min. (Figure 10.6-4). The initial sorption rate was 7.7 pCi/mg/min. In the simulated water, approximately 89 percent of Pu (V) was sorbed during the first 10 minutes. The initial sorption rate was 13.4 pCi/mg/min. After 10 min., the amount of sorbed Pu (V) increased with time, and an additional 39 percent of Pu (V) in natural groundwater and 10 percent additional Pu (V) in the simulated water were adsorbed during the remaining 95.83 hr. By the end of the sorption process, the K_d value was 6×10^4 mL/g in natural groundwater and 2×10^5 mL/g in the simulated water.

Sorption of Plutonium-239 Onto Montmorillonite Colloids–Montmorillonite colloids sorbed 69 percent of Pu (IV) in natural groundwater during the first 10 min. (Figure 10.6-5). The initial rate was 8.5 pCi/mg/min. After 10 min., the amount of sorbed Pu (IV) increased and reached a maximum (approximately 86 percent) at 4 hr., and then it decreased slowly throughout the remaining 236 hr. This result indicates that release of Pu (IV) occurs after 4 hr. in natural groundwater. At the end of the sorption process, the K_d value of Pu (IV) was 3×10^3 mL/g, which was an order of 10^2 lower than the K_d value on hematite colloid. In simulated water, montmorillonite colloids sorbed 98 percent of Pu (IV) during the first 10 minutes (Figure 10.6-5). The initial rate was 18.1 pCi/mg/min. At the end of the sorption process, the K_d value was 2×10^5 mL/g, which was almost 10^2 times higher than the K_d value in natural groundwater, and was the same value on hematite colloids.

Montmorillonite colloids sorbed 54 percent of Pu (V) in both natural and simulated groundwater during the first 10 min. (Figure 10.6-5). The initial rate was 8.3 pCi/mg/min. in natural groundwater and 10.1 pCi/mg/min. in the simulated water. After 10 min., the amount of sorbed Pu (V) increased with time in both waters. At the end of the sorption process, approximately 90 percent of Pu (V) in natural groundwater and 97 percent in the simulated water was adsorbed. The K_d value of Pu (V) was 10^4 mL/g in both waters.

Sorption of Plutonium-239 onto Silica Colloids–Generally, silica colloids sorbed less ^{239}Pu in both natural and simulated waters than iron oxide and montmorillonite colloids did. Silica-PST-1 and Silica-ST-ZL have similar sorption behavior. Silica-PST-1 colloids sorbed 69 percent of Pu (IV) in natural groundwater and 76 percent in the simulated water during the first 1 hr. (Figure 10.6-6). The initial rate was 10.4 pCi/mg/min. in natural groundwater and 13.0 pCi/mg/min. in the simulated water. By the end of the sorption process, approximately 78 percent of Pu (IV) in natural groundwater and approximately 95 percent in simulated groundwater were adsorbed. The K_d value was 5×10^3 mL/g in natural groundwater and 3×10^4 mL/g in the simulated water.

10.6.4.4.2 Sorption Kinetics of Americium-243 onto Colloids

Generally, adsorption of ^{243}Am by colloids was in the order of hematite > montmorillonite > silica in both natural and simulated groundwater. The amount of Am sorbed by these three types of colloids was not significantly different between natural and simulated groundwater.

Sorption of Americium-243 onto Hematite Colloids–Hematite colloids sorbed almost 100 percent of Am in both natural and simulated groundwater during the first 1 hr. (Figure 10.6-7). The initial rate was 6.1 pCi/mg/min. in natural groundwater and 3.9 pCi/mg/min. in the simulated water. After 1 hr., the amount of sorbed Am decreased gradually during the remaining 239 hr. in natural groundwater. However, in the simulated water, sorption of Am showed a fluctuation with time. The amount of sorbed ^{234}Am decreased slightly during the period from 1 to 48 hr., then it increased up to the original sorption level (approximately 100 percent) at 96 hr. Thereafter, the amount of sorbed Am decreased during the remaining 144 hr. This result indicates that partial desorption of Am from hematite colloids occurs after 1 hr. in both waters. At the end of the sorption process, approximately 90 percent of Am in the natural groundwater and approximately 93 percent in the simulated water were adsorbed. The K_d value was 10^5 mL/g in both natural and simulated groundwaters.

Sorption of Americium-243 onto Montmorillonite Colloids–Montmorillonite colloids sorbed approximately 61 percent of Am in natural groundwater and 79 percent in the simulated groundwater during the first hour (Figure 10.6-7). The initial rate was 3.8 pCi/mg/min. in natural groundwater and 3.2 pCi/mg/min. in the simulated water. After 1 hr., the amount of sorbed Am increased and reached a maximum at 96 hr. in natural and simulated groundwater. After 96 hr., the amount of sorbed Am decreased during the remaining 144 hr. This result indicates that partial desorption of Am from montmorillonite occurs after 96 hr. of the sorption. At the end of the sorption process, approximately 63 percent of Am in natural groundwater and 73 percent in the simulated water were adsorbed. The K_d value was 10^4 mL/g in both natural and simulated groundwater, which was 10 times lower than the K_d value on hematite.

Sorption of Americium-243 onto Silica Colloids–Generally, silica colloids sorbed less ^{243}Am in both natural and simulated waters than iron-oxide and montmorillonite colloids did. Silica-PST-1 colloids sorbed 28 percent of Am in both natural and simulated groundwater during the first hour (Figure 10.6-7). The initial rate was 1.7 pCi/mg/min. in natural groundwater and 1.1 pCi/mg/min. in the simulated water. After 1 hr., the amount of sorbed Am increased and reached a maximum at 48 hr., and then it decreased gradually during the remaining 192 hr. in the simulated water. However, in the simulated water, sorption of Am shows a fluctuation with time. The amount of sorbed ^{234}Am decreased to 35 percent at 96 hr., and then it increased up to 60 percent at the end of sorption process. The K_d values were 10^4 mL/g in natural groundwater and 5×10^3 mL/g in the simulated water.

10.6.4.4.3 The Effect of Colloidal Concentration on the Sorption of Plutonium (V)

To examine the effect of colloidal concentration on the sorption of Pu (V) onto colloids of hematite, montmorillonite, and two types of silica, an additional experiment was conducted using the following colloidal concentrations: 0.01, 0.05, 0.1, 0.15, 0.2, and 1.0 g/L. The results show that, per unit of colloid, sorption of Pu (V) was much higher at low colloid concentrations than at

high colloid concentrations (Figure 10.6-8). Silica colloids also show a similar pattern, as montmorillonite colloids did. Therefore, the results from silica colloids are not presented here.

With extremely high colloidal concentration (1,000 mg/L), montmorillonite sorbed approximately 100 pCi/mg of Pu (V) in both natural and simulated groundwaters after 240 hr. sorption. The K_d values were 4×10^3 mL/g in natural groundwater and 7×10^2 mL/g in the simulated groundwater. Hematite colloids sorbed 106 pCi/mg of Pu (V) in natural groundwater and approximately 500 pCi/mg in simulated groundwater. The K_d values were 8×10^3 mL/g in natural groundwater and 6×10^5 mL/g in simulated water.

At relatively low colloidal concentrations (10 mg/L), montmorillonite sorbed approximately 2,300 pCi/mg of Pu (V) in natural and approximately 2,900 pCi/mg in simulated groundwater after 240 hr. sorption. The K_d values were 3×10^3 mL/g in natural groundwater and 5×10^2 mL/g in the simulated water. Hematite colloids sorbed approximately 2,900 pCi/mg of Pu (V) in natural groundwater and approximately 3,200 pCi/mg in simulated groundwater. The K_d values were 4×10^4 mL/g in natural groundwater and 2×10^5 mL/g in the simulated groundwater. Moreover, hematite colloids sorbed more Pu (V) in the simulated water than in natural groundwater, whereas montmorillonite colloids sorbed more Pu (V) in natural groundwater than in simulated water.

10.6.4.4.4 Desorption of Plutonium-239 From Colloids

Little Pu was desorbed from hematite colloids after 150 days, even under vigorous shaking conditions (Figure 10.6-9). As much as 0.5 percent of colloidal Pu (IV) and 0.8 percent of soluble Pu (V) were desorbed from goethite colloids. Desorption of ^{239}Pu from montmorillonite or silica colloids was faster and higher than from hematite and goethite colloids. As much as 8 percent of colloidal Pu (IV) and 0.7 percent of soluble Pu (V) were desorbed from montmorillonite colloids after 150 days. However, as much as 20 percent of colloidal Pu (IV) and 6 percent of soluble Pu (V) were desorbed from silica colloids (Figure 10.6-9). The results suggest that desorption of ^{239}Pu from colloids of hematite, goethite, or montmorillonite in groundwater is much slower than the sorption process.

Therefore, colloids of iron oxide and clay in groundwater may enhance the transport of ^{239}Pu along the potential flow paths.

10.6.4.5 Summary of Most Recent Results

Sorption of radionuclides onto colloids of iron oxide, clays, and silica in groundwater may play an important role in their transport. Laboratory batch-sorption experiments were conducted to evaluate (1) sorption of ^{239}Pu and ^{243}Am onto different colloids (e.g., hematite, goethite, montmorillonite, and silica), (2) sorption kinetics of ^{239}Pu and ^{243}Am onto these colloids, (3) effect of colloidal concentrations on the sorption of soluble Pu (V) and ^{243}Am, (4) stability of colloidal Pu (IV) in groundwater, and (5) desorption of ^{239}Pu or ^{243}Am from ^{239}Pu-loaded or ^{243}Am-loaded colloids as a function of time. Natural groundwater and carbonate-rich simulated groundwater were used.

The results show that colloidal Pu (IV) and soluble Pu (V) were rapidly sorbed by colloids of hematite, goethite, montmorillonite, and silica in both natural and synthetic groundwater. The

initial sorption rates of Pu onto these colloids are summarized in Table 10.6-5. Sorption of Pu (V) per unit colloid was higher at low colloidal concentrations than at high colloidal concentrations. At high colloidal concentrations, the K_d values of Pu (V) range from 10^3 to 10^5 mL/g for hematite colloid and from 10^2 to 10^3 mL/g for montmorillonite colloid. At low colloidal concentrations, the K_d values of Pu (V) range from 10^4 to 10^5 mL/g for hematite and from 10^2 to 10^3 mL/g for montmorillonite.

Desorption of ^{239}Pu from colloids of hematite, goethite, and montmorillonite was much slower than the sorption process. Desorption of ^{239}Pu from silica colloids was faster than from the other three types of colloids. Table 10.6-6 summarizes the initial desorption rates from Pu-loaded colloids.

Adsorption of ^{243}Am by hematite colloids was faster and greater than by montmorillonite and silica colloids. Maximum sorption of ^{243}Am occurred at 1 hr. for hematite, 48 hours for silica, and 96 hr. or more for montmorillonite. After these time periods, partial desorption of ^{243}Am from colloids occurred. With the maximum sorption, the sorption distribution coefficient, K_d, for ^{243}Am was of the order of 10^4 mL/g for silica, and 10^5 mL/g for hematite and montmorillonite. The study with ^{243}Am is incomplete. Two experiments, which include different colloid concentrations and desorption of ^{243}Am from Am-loaded colloids, are in progress.

10.6.5 Mineralogy of Colloids

Colloid researchers define upper size limits of 1 to 10 μm for colloidal particles. For these studies, colloids are adequately defined as fine particulates that were transported and deposited in aqueous suspension. The selection of a particular size limit is not so important for alteration history studies because the relict colloidal materials preserved in Yucca Mountain rocks have been texturally modified by recrystallization. Most of the colloidal deposits identified in alteration history studies existed locally at some time as gels, semisolid colloid-water systems, with the macroscopic appearance and behavior of a jelly or paste. Liquid-rich gels have been observed in underground workings at Rainier Mesa, north of Yucca Mountain, and dried or crystallized gels have been identified in drill cores and in the ESF at Yucca Mountain itself.

X-ray diffraction analysis of dried gel from Rainier Mesa reveals a very pure, well-crystallized smectite. The mineral component of most gels in the Rainier Mesa tunnels, including drip pendants, is probably smectite. In addition to the smectite, there are fragments and clast coatings of silica-rich dried gels. Mineral phases identified by morphology and energy-dispersive x-ray spectra include silica, barite, copper-iron sulfides or sulfates, and possible zeolites, as well as the smectite (Levy 1992, pp. 83 to 84). The smectite has a moderately Fe-rich composition, with K as the main exchangeable cation (Levy 1992, Table 1).

Liquid-rich free gels (as distinguished from gel layers on hydrated glass surfaces) have not yet been found at Yucca Mountain, in either drill cores or the ESF. Prominent dried smectite gels are present in the Tiva Canyon Tuff exposed by the ESF North Ramp box cut and starter tunnel. Laminated deposits of smectite, up to several centimeters thick, coat fractures and fill the bottoms of lithophysal cavities. The abundance of this material gradually diminishes inward from the portal. Although this diminution corresponds to increasing depth below the surface in

the ESF, the smectite probably is not derived from present-day surficial deposits, because clay coatings are absent from the Tiva Canyon Tuff exposed at the ESF South Portal.

A clay-rich fracture filling from the Tptrn in the ESF offers a dramatic example of particulate transport. The wall rock is densely welded, devitrified tuff, but the fracture filling consists of devitrified rock fragments in a fine-grained matrix of Topopah Spring glass pyroclasts. Several sequences of graded bedding are preserved within the fillings. The glassy constituents had to come from tens of meters higher in the stratigraphic section.

Of the former gels and colloidal accumulations observed in altered rocks at Yucca Mountain, those in altered basal Topopah Spring Tuff vitrophyre are especially relevant, because the alteration conditions may represent a natural analog to a radioactive waste repository environment. The chief hydrous products of glass alteration are smectite and heulandite-clinoptilolite. Smectite commonly crystallized as spherical aggregates, 2 to 50 μm across, adhering to each other, with a small amount of intergrown, extremely fine-grained zeolite. Perhaps because of this growth habit, there is little evidence of free smectite gels in this altered zone. Relict colloidal accumulations of silica also fill dissolution cavities in altered vitrophyre and primary and secondary pores in moderately welded tuffs below the vitrophyre. Some of these are uraniferous opal deposits, with relevance to radionuclide transport. Experimental coprecipitation of dissolved U and silica gel showed that $[U]_{\text{dried silica gel}}/[U]_{\text{solution}}$ = 400 to 1,000 at pH = 7.0 to 8.5, ΣCO_2 = 0.001 to 0.01 M, and T = 25° to 80°C, indicating that silica has a very strong affinity for U.

The most common examples of former gels at Yucca Mountain are microscopic geopetal deposits in pores of the zeolitized nonwelded tuffs. Layers within silica deposits are distinguished by color, by variations in incipient birefringence related to differences in crystallinity, or by differences in granularity. Zeolite and silica occur commonly in separate layers, with the zeolite lowermost. Another variety of relict gel fills only primary pores and is a major cementing constituent in certain well-sorted bedded tuffs that originally contained little or no fine-grained ash; heulandite-clinoptilolite and opal, in variable proportions, are the main constituents. The infilling of virtually all primary porosity, but only primary porosity, by gel in this kind of tuff indicates that the gel constituents were externally derived and transported into the bedded tuff by moving water before the tuff itself began to be altered.

INTENTIONALLY LEFT BLANK

10.7 FIELD TRANSPORT STUDIES

10.7.1 Data Sources

Data for field transport studies generally come from two sources: measured data from samples taken from the field (the Busted Butte unsaturated zone transport test or the C-holes complex) or data derived from model simulations. Measured data include mineralogy, hydrologic parameters, sorption, solubility, tracer concentrations, and breakthroughs from collection pad analyses. Simulation input data include as-needed measured data and some data from other Yucca Mountain Site Characterization Project (YMP) sources, as noted in the text. Simulation output data include fluid distributions, tracer distribution in the rock, and tracer breakthrough times.

Input data for the Busted Butte unsaturated zone transport test are described in (CRWMS M&O 2000, Table 1d and 1f); input data for C-holes field and laboratory transport testing are described in (CRWMS M&O 2000, Table 1e).

10.7.2 Busted Butte Unsaturated Zone Transport Test

10.7.2.1 Overview

10.7.2.1.1 Unsaturated Zone Transport Test Location

The Busted Butte test facility is located in Area 25 of the Nevada Test Site, approximately 160 km northwest of Las Vegas, Nevada, and 8 km southeast of the potential Yucca Mountain repository area. The site was chosen based on the presence of a readily accessible exposure of the Topopah Spring Tuff and the Calico Hills Formation and the similarity of these units to those beneath the potential repository horizon.

10.7.2.1.2 Unsaturated Zone Transport Test Concept

The unsaturated zone transport test at Busted Butte is designed to validate and continuously improve the YMP's flow and transport site-scale model for the unsaturated zone. In terms of transport, the principal barrier to radionuclide migration in the unsaturated zone at Yucca Mountain is the Calico Hills Formation. For this purpose, the test block was located at Busted Butte where the exposure of Calico Hills rocks represents a distal extension of the formation located immediately beneath the potential repository horizon. This location means that the site is not an analog site but, to the best of the YMP's knowledge, it represents both the Calico Hills Formation and the Topopah Spring Tuff units as they exist beneath the potential repository horizon west of the Ghost Dance fault.

The unsaturated zone transport test was designed for two test phases. The first phase, including test Phases 1A and 1B, was designed as a scoping study to assist in design and analysis of Phase 2. The second phase is the mesoscale study, which incorporates a larger region than Phase 1, with a broader, more complex scope of tracer injection, monitoring, and collection.

In addition to field testing, parallel laboratory analytical and testing programs in geochemistry, tracer evaluation, hydrology, and mineralogy are designed to help interpret the field results. The

geochemistry program includes measurement of in situ pore-water chemistry and development of a synthetic injection matrix. The tracer evaluation program includes batch-sorption studies on Busted Butte samples using Phase 1 and Phase 2 conservative and reactive analog and radioactive tracers, as well as modeling of the geochemical behavior of those tracers in the ambient water chemistry. The hydrology program involves the measurement of the matric potentials and conductivities as a function of saturation for core samples from Busted Butte. The porosity of each sample is also characterized. The mineralogy/petrology program involves the mineralogic characterization of the Busted Butte samples from quality cores (obtained in conformance with quality assurance procedures) from Phases 1 and 2. When possible, splits from the quality-core samples are used in all three characterization programs.

Because the principal objective of the test is to evaluate the validity of the flow and transport site-scale process models used in total system performance assessment (TSPA) abstractions, a flow and transport modeling program was implemented. This effort allows the site-scale flow and transport model to be updated by simulating and predicting experimental field results and by addressing the effects of scaling from laboratory to field scales. Initial predictions of the field tests are included here.

10.7.2.1.3 Test Objectives

The principal objectives of the test are to address uncertainties associated with flow and transport in the unsaturated zone site-process models for Yucca Mountain as identified by the TSPA working group in February 1997. These include, but are not restricted to, the following:

- The effect of heterogeneities on flow and transport in unsaturated and partially saturated conditions in the Calico Hills. In particular, the test aims to address issues relevant to fracture/matrix interactions and permeability contrast boundaries.
- The migration behavior of colloids in fractured and unfractured Calico Hills rocks.
- The validation through field testing of laboratory sorption experiments in unsaturated Calico Hills rocks.
- The evaluation of the three-dimensional, site-scale, flow and transport process model (i.e., equivalent-continuum/dual-permeability/discrete-fracture-fault representations of flow and transport) used in the TSPA abstractions for the License Application.
- The effect of scaling from laboratory scale to field scale and site scale.

10.7.2.2 Test Design

10.7.2.2.1 Site Description

The foremost objective of the underground testing is to ensure minimal disturbance of the in situ test block in the initial stages of unsaturated tracer transport testing. Design, construction, and scientific teams were all involved in ensuring that the test block itself remained undisturbed by construction activities.

The Busted Butte site was mapped and sampled for the purposes of test design and construction during the fall of 1997. The site characterization of the potential test block involved the mapping of the main drift wall, core sampling for mineralogy/petrology, and hydrologic characterization of the reconnaissance geochemical laboratory tests. Additional characterization of the site included the recovery of samples from outcrops, which were used for the initial laboratory characterization studies of hydrologic properties and mineralogy. The geological context and lithological descriptions of core samples from the test site were used to provide further information on the geometry of the beds at the site in order to guide the construction of the tunnel.

Quality samples were collected from the dry drilling of the boreholes from the main drift and the Test Adit to provide core samples for geologic, hydrologic, and geochemical laboratory investigations and scoping calculations. The boreholes were then surveyed and instrumented for the injection tests. Laboratory measurements of hydrologic, mineralogic, and tracer sorption and matrix diffusion properties of the core samples collected once the tunnel was excavated are now providing needed information for predictive modeling studies.

10.7.2.2.2 Experimental Design for Test Phases

The Busted Butte test is meant to provide tangible results for the total system performance assessment License Application (TSPA-LA). Details of the test plan can be found in Bussod et al. (1997).

10.7.2.2.2.1 Test Phase 1

Phase 1 represents a simple test program that serves both as a precursor or scoping phase to Phase 2 and as a short-term (approximately 9 months) experiment aimed at providing initial transport data for early fiscal year 1999 model updates. Phase 1 involves six single-point injection boreholes and two inverted-membrane collection boreholes (Figure 10.7-1). All Phase 1 boreholes are 2 m in length and 10 cm in diameter. A mixture of conservative tracers (bromide, fluorescein, pyridone, and fluorinated benzoic acids), a reactive tracer (Li), and fluorescent polystyrene microspheres are being used to track flow, reactive transport, and colloid migration, respectively.

Phase 1A, located in the hydrologic Calico Hills nonwelded unit (CHn), is a noninstrumented or "blind" test consisting of four single-point injection boreholes (Figure 10.7-1). Continuous injection started on April 2, 1998. Injection rates varied from 1 mL/hr. (boreholes 2 and 4) to 10 mL/hr. (boreholes 1 and 3). The field test was completed through excavation by "mini-mineback" and auger sampling in early fiscal year 1999. Test predictions are included in Section 10.7.2.6.1. Initial model predictions associated with Phase 1A were done "blind" and are meant to test the YMP's ability to predict the flow and transport results given present YMP databases and modeling capabilities.

Phase 1B involved both injection and collection membranes and injection started on May 12, 1998, in the lower section of the Topopah Spring Tuff basal vitrophyre (Tptpv2) (Figure 10.7-1). Phase 1B involved two injection rates, 1 mL/hr. in borehole 7 and 10 mL/hr. in borehole 5. Because of the paucity of data on fracture matrix interactions in these lithologies, this test serves

as a "calibration" test for fracture/matrix interactions to be used in Phase 2 conceptual models. Results of Phase 1B are presented and discussed in Section 10.7.2.5.

10.7.2.2.2.2 Test Phase 2

Phase 2 testing involves a large 7-m-high, 10-m-wide, and 10-m-deep block comprising all the lithologies of Phase 1 (Figure 10.7-1). Unlike the single-point injection geometries in Phase 1, the injection systems in Phase 2 are designed to activate large surfaces of the block. Due to the short time frame available for testing, both high-injection and low-injection planes are used for testing in Phase 2. The injection points for this phase are distributed in two horizontal, parallel planes arranged to test the properties of the lower Topopah Spring Tuff basal vitrophyre and the hydrologic Calico Hills (Figure 10.7-2). Phase 2 mixed-tracer solutions include those used in Phase 1, three additional fluorinated benzoic acids, a mixture of new reactive tracers (Ni^{2+}, Co^{2+}, Mn^{2+}, Sm^{3+}, Ce^{3+}, and Rhodamine WT), and, starting in August 1999, an additional conservative tracer (I^-).

Phase 2 is divided into three subphases (2A, 2B, and 2C) according to location and the injection rates used. Phase 2A consists of a single borehole instrumented with 10 injection points and 10 moisture sensors, one at each injection point. The injection rate is 1 mL/hr. per injection point, which corresponds to an overall infiltration rate of 30 mm/yr. This borehole is restricted to the Tptpv2 lithology, which consists of fractured, moderately welded tuff from the basal vitrophyre. Phase 2A injection began on July 23, 1998, and is ongoing.

Phase 2B consists of four injection boreholes, each instrumented with 10 injection points and 10 moisture sensors, one at each injection point. The injection rate is 10 mL/hr. per injection point, which corresponds to an overall infiltration rate of 380 mm/yr. This injection plane is restricted to the Calico Hills Formation (Tac) and is meant to activate the lower section of the test block simultaneously with the upper section (Phases 2A and 2C). Phase 2B injection began on July 30, 1998, and is ongoing.

Phase 2C consists of three injection boreholes, each instrumented with 9 injection points and 12 moisture sensors, one at each injection point and two additional sensors located toward the borehole collar to detect tracer movement toward the front of the borehole. The injection rate is 50 mL/hr. per injection point, which corresponds to an overall infiltration rate of 1,550 mm/yr. As in Phase 2A, this injection system is restricted to a horizontal plane in the Tptpv2 lithology. Phase 2C injection was initiated on August 5, 1998, and is ongoing.

Natural infiltration rates at Yucca Mountain vary between 0.01 and 250 mm/yr. with an average of 5 mm/yr. (Flint et al. 1996). Phase 2A falls within the range of natural present-day infiltration rates at Yucca Mountain, whereas Phase 2B lies at the high end of predicted values for a pluvial climate scenario. Phase 2C infiltration rates are artificially higher than expected natural infiltration rates for the region but provide for the best testing conditions given the short duration of the experiment. Model simulations indicate that even at these high injection rates, the system is expected to remain unsaturated. The validity of this assumption and the relevance of the highest injection-rate experiments (i.e., Phase 2C) will be evaluated using the results from the other two injection-rate experiments (i.e., Phases 2A and 2B).

The high injection plane consists of fractured Topopah Spring Tuff (Tptpv2). As in Phase 1B, this unit represents the base of the Topopah Spring welded (TSw) basal vitrophyre and is characterized by subvertical fractured surfaces representing columnar joints. Thirty-seven injection points distributed along four injection holes, each approximately 8 m deep, are used for tracer injection along a horizontal surface. The natural fracture pattern present in this unit serves as the conduit for tracer migration into the CHn. The lower horizontal injection plane is located in the Calico Hills Formation (Tac) and involves 40 injection points distributed in four horizontal and parallel boreholes. This test (Phase 2B) is meant to activate the lower part of the block in the event that the top injection system does not activate the entire block in the short duration ($\leq$2 years) of the testing program.

Whereas all injection boreholes are located in the Test Alcove, the 12 collection boreholes associated with Phase 2 are located in the Main Adit. These boreholes are 8.5 to 10.0 m in length, and each contains 15 to 20 collection pads evenly distributed on inverted membranes. Because of the complexity of the flow fields expected in this block, several techniques (i.e., electrical resistance tomography, ground-penetrating radar, and neutron logging) are used to image the two-dimensional and three-dimensional saturation state of the block in monthly to bimonthly intervals.

10.7.2.2.3 Borehole Injection and Sampling Systems

Injection and sampling of the liquid tracers was accomplished by two pneumatically inflated borehole sealing and measurement systems (Figure 10.7-3). To allow visual inspection of the injection points under both standard and ultraviolet illumination, a transparent packer system was developed for the injection holes. Moisture sensing and sampling were accomplished using pneumatically emplaced inverting membranes.

A special transparent packer was developed for use in the tracer-injection systems (Figure 10.7-4). The design incorporates moisture sensors mounted to the outside of the packers to monitor both ambient soil moisture and injection moisture. The transparent nature of the packer allows viewing of the interior of the test borehole at any desired depth under both visible and ultraviolet illumination.

Moisture Sensors–Simple resistive moisture sensors were installed to diagnose the relative moisture state of the injection pads and the arrival of liquid tracer at the sampling-pad membranes. These sensors operate by measuring resistance across the exposed leads of two wires. Moisture absorbed by the fabric reduces the resistance between the two wires: the wetter the fabric, the lower the resistance. Although the sensor output is not quantitative, the values successfully indicated the general state of the sensing location. These moisture indications were meant to guide the inverting-membrane sampling operations (indicating tracer arrival) and diagnose the injection-pad moisture state, indicating loss of injection or over-injection.

10.7.2.2.4 Conservative and Reactive Tracers and Microspheres

Although the behavior of radionuclides of concern was extensively studied in the laboratory, regulatory and environmental concerns prevent the use of these materials in the field. For the Busted Butte field tests, analog conservative and reactive tracers are used as surrogates for

radionuclides. To validate the use of these tracers and the site-scale use of the minimum-K_d approach for sorption and the processes of matrix diffusion and colloid migration, laboratory batch studies of radionuclide sorption onto Busted Butte core samples were completed; results are presented and discussed in Section 10.7.2.5. Batch studies of tracer sorption onto the same rocks are under way, as described in that section. The tracers were chosen so that conservative, reactive, and colloid-like behaviors could be monitored in a single, continuous, injection scenario. The tracers were mixed together to normalize the hydrologic conditions of the injection. The tracer matrix was synthetic pore water, based on the measured composition of Busted Butte pore waters collected from the test area on January 30, 1998.

10.7.2.2.4.1 Phase 1 Tracers

Phase 1 tracers were chosen based on the list of tracers permitted for use in the C-wells tests. Analog conservative and reactive tracers and colloids are mixed together to normalize the hydrologic conditions they experience and provide for higher accuracy of the results. The tracers used in the Busted Butte experiments of Phase 1 include the following:

- Lithium bromide
- Fluorescent polystyrene latex microspheres
- Sodium fluorescein
- "Pyridone" (3-carbomoyl-2 (1H)-pyridone)
- 2,6-difluorobenzoic acid
- Pentafluorobenzoic acid.

The reactive tracer used is Li (K_d value of 1.0 mL/g), and the colloid analogs are fluorescent polystyrene latex microspheres of two sizes: 0.3 and 1 μm diameters. The 2,6-difluorobenzoic acid and pentafluorobenzoic acid tracers are conservative ones used to tag the various injection boreholes according to injection rates (i.e., 1- and 10-mL/hr. rates). Sodium fluorescein and pyridone are ultraviolet fluorescent and are used as conservative tracer markers that can be detected in the field at a concentration level of approximately 10 ppm using ultraviolet illumination.

- Phase 1A–10 mL/hr. Injection Rate; boreholes 1 and 3:
  - 500 mg/L lithium bromide
  - 500 mg/L sodium fluorescein
  - 100 mg/L 2,6-difluorobenzoic acid
  - 1 mL/L fluorescent polystyrene microspheres.
- Phase 1A–1 mL/hr. Injection Rate; boreholes 2 and 4:
  - 500 mg/L lithium bromide
  - 500 mg/L sodium fluorescein
  - 100 mg/L pentafluorobenzoic acid
  - 1 mL/L fluorescent polystyrene microspheres.

- Phase 1B–10 mL/hr. Injection Rate; borehole 5:
  - 500 mg/L lithium bromide
  - 500 mg/L sodium fluorescein
  - 100 mg/L 2,6-difluorobenzoic acid
  - 100 mg/L pyridone
  - 1 mL/L fluorescent polystyrene microspheres.
- Phase 1B–1 mL/hr. Injection Rate; borehole 7:
  - 500 mg/L lithium bromide
  - 500 mg/L sodium fluorescein
  - 100 mg/L pentafluorobenzoic acid
  - 100 mg/L pyridone
  - 1 mL/L fluorescent polystyrene microspheres.

10.7.2.2.4.2 Phase 2 Tracers

Phase 2 tracers include those used in Phase 1, three additional fluorinated benzoic acids (2,4-difluorobenzoic acid, 2,4,5-tri-fluorinated benzoic acid, 2,3,4,5-tetra-fluorinated benzoic acid), iodide, a fluorescent reactive tracer (Rhodamine WT), and additional reactive ions that serve as analogs for Np, Pu, and Am:

- Neptunium analogs (NpO_2^+, Np (V)):
  - Nickel (Ni^{2+})
  - Cobalt (Co^{2+})
  - Manganese (Mn^{2+})
- Plutonium analog (Pu^{3+}):
  - Samarium (Sm^{3+})
- Plutonium analogs (colloidal form):
  - Polystyrene microspheres
- Americium analog (Am^{3+}):
  - Cerium (Ce^{3+}).

Phase 2 tracer recipes are as follows:

- Phase 2A–1 mL/hr. Injection Rate; borehole 23:
  - 1,000 mg/L lithium bromide
  - 10 mg/L sodium fluorescein
  - 100 mg/L 2,4,5-tri-fluorinated benzoic acid
  - 10 mg/L pyridone
  - 1 mL/L microspheres.
- Starting October 7, 1998:
  - 10 mg/L rhodamine WT
  - 10 mg/kg $NiCl_2 \cdot 6H_2O$ (2.47 mg/kg of Ni^{2+})
  - 10 mg/kg $MnCl_2 \cdot 4H_2O$ (2.78 mg/kg of Mn^{2+})
  - 10 mg/kg $CoCl_2 \cdot 6H_2O$ (2.48 mg/kg of Co^{2+})
  - 5 mg/kg $SmCl_3 \cdot 6H_2O$ (2.06 mg/kg of Sm^{3+})
  - 5 mg/kg $CeCl_3 \cdot 7H_2O$ (1.88 mg/kg of Ce^{3+}).

On September 30, 1999, the Phase 2A recipe was changed with the elimination of the microspheres and the addition of 500 mg/kg potassium iodide.

- Phase 2B–10 mL/hr. Injection Rate; boreholes 24, 25, 26, 27:
  - 1,000 mg/L lithium bromide
  - 10 mg/L sodium fluorescein
  - 100 mg/L 2,6-difluorobenzoic acid (boreholes 26, 27)
  - 100 mg/L 2,3,4,5-Tetra-fluorinated benzoic acid (boreholes 24, 25)
  - 10 mg/L pyridone
  - 10 mg/L rhodamine WT
  - 1 mL/L microspheres.
- Starting September 2, 1998:
  - 10 mg/kg $NiCl_2 \cdot 6H_2O$ (2.47 mg/kg of Ni^{2+})
  - 10 mg/kg $MnCl_2 \cdot 4H_2O$ (2.78 mg/kg of Mn^{2+})
  - 10 mg/kg $CoCl_2 \cdot 6H_2O$ (2.48 mg/kg of Co^{2+})
  - 5 mg/kg $SmCl_3 \cdot 6H_2O$ (2.06 mg/kg of Sm^{3+})
  - 5 mg/kg $CeCl_3 \cdot 7H_2O$ (1.88 mg/kg of Ce^{3+}).

On August 18, 1999, the Phase 2B recipe was changed, with the elimination of the microspheres and the addition of 500 mg/kg potassium iodide.

- Phase 2C–50 mL/hr. Injection Rate; boreholes 18, 20, and 21:

  - 1,000 mg/L lithium bromide
  - 10 mg/L sodium fluorescein
  - 100 mg/L 2,6-difluorobenzoic acid (borehole 18)
  - 100 mg/L pentafluorobenzoic acid (borehole 20)
  - 100 mg/L 2,4-difluorobenzoic acid (borehole 21)
  - 10 mg/L pyridone
  - 10 mg/L rhodamine WT
  - 1 mL/L microspheres.

- Starting September 2, 1998:

  - 10 mg/kg $NiCl_2 \cdot 6H_2O$ (2.47 mg/kg of Ni^{2+})
  - 10 mg/kg $MnCl_2 \cdot 4H_2O$ (2.78 mg/kg of Mn^{2+})
  - 10 mg/kg $CoCl_2 \cdot 6H_2O$ (2.48 mg/kg of Co^{2+})
  - 5 mg/kg $SmCl_3 \cdot 6H_2O$ (2.06 mg/kg of Sm^{3+})
  - 5 mg/kg $CeCl_3 \cdot 7H_2O$ (1.88 mg/kg of Ce^{3+}).

On August 18, 1999, the Phase 2C recipe was changed, with the elimination of the microspheres and the addition of 500 mg/kg potassium iodide.

10.7.2.2.4.3 Synthetic Pore Water Recipe

To minimize the reactivity of the tracer solution with the country rock, a synthetic pore water, based on measured in situ composition, is used as a matrix for the tracers in solution.

- Phase 1 synthetic pore water:

  - 76.8 mg/kg $SiO_2 \cdot nH_2O$ (amorphous silica)
  - 36.8 mg/kg $CaCl_2 \cdot 2H_2O$ (calcium chloride dihydrate)
  - 44.8 mg/kg $Ca(NO_3)_2 \cdot 4H_2O$ (calcium nitrate tetrahydrate)
  - 3.8 mg/kg NaF (sodium fluoride)
  - 10.7 mg/kg Na_2SO_4 (sodium sulfate)
  - 51.2 mg/kg $NaHCO_3$ (sodium bicarbonate)
  - 9.0 mg/kg $KHCO_3$ (potassium bicarbonate)
  - 36.9 mg/kg $MgSO_4 \cdot 7H_2O$ (magnesium sulfate heptahydrate)
  - 7.8 mg/kg $Ca(OH)_2$ (calcium hydroxide).

- Phase 2 synthetic pore water:
  - Phase 2 was identical to Phase 1 with the exception that, due to the large quantities required, the source of water was J-13 water that had been deionized using resin cartridges. This resulted in a deionized water with approximately 30 ppm Si, so that no additional silica was added.

10.7.2.2.5 Use of Numerical Simulations for Test Design

10.7.2.2.5.1 Scoping Calculations for Test Injection Design

Prior to starting Phase 1A, scoping simulations were run to help design Phase 1A and subsequent tests. These scoping simulations were used to identify how the planned injection system would work and to estimate reasonable injection rates for the test. For the simulations, the same single borehole model system was used with a few modifications. The most significant modification was to use Bandelier Tuff Unit-1a properties (Krier et al. 1997) for the rock matrix. Bandelier Tuff properties were used to try to compare simulation results with preliminary experiments that Science & Engineering Associates, Inc. was running in the laboratory. Science & Engineering Associates, Inc.'s experiments were used to test the injection system and to make preliminary estimates of water and tracer travel distance in Phase 1A.

Initial conditions in the model were set up to mimic those of the experiment. The system was allowed to equilibrate from an initial rock-matrix saturation of 60 percent, initial pad saturation of 25 percent, side boundary conditions with saturation fixed at 60 percent, and air pressure fixed at atmospheric.

The experiment was stopped at 1.8 days, and measurements of the spread of the fluorescing tracer were made. The concentration of the observable fluorescein from the experiments was estimated to be 50 percent. Output from the numerical model showed that the average apparent radius of the 50 percent concentration isosurface was 0.09 to 0.10 m, which compares reasonably well with the radii observed in the experiment.

In addition to the Bandelier Tuff, the Tac was also used in these simulations. For these two materials, modeling showed that the size and shape of the pad do not influence the fluid movement due to the overwhelming capillarity of the porous rock and the similar basic material parameters between the polypropylene and the rock. All simulations for these two materials showed that the pad wets only locally to the injection point.

10.7.2.2.5.2 Sample Collection Analyses Simulating Performance of a Filter Paper Pad

Increasing attention has been paid in recent years to the collection of comprehensive large-scale field data. Considerable effort was expended during the last few decades for various modifications in solution sampler design and improved collection techniques, leading to a better performance and ease of operation in various sampling conditions. To date, a variety of modified sampler types are available depending on their shapes, materials, functions, and operations (Litaor 1988; Dorrance et al. 1991). Unfortunately, little attention was paid to how such instruments and the related operations might influence their surroundings and alter the background flow field and the resulting solute transport.

The objective of this study was to test the performance of the filter paper sampling system used in the Busted Butte field test site using numerical experiments. The simulation results were subsequently analyzed to evaluate any significant effect the sampler pads may have on the interpretation of transport phenomena and the underlying process hypothesis.

Numerical Experiments–Numerical simulations were designed to closely approximate the experimental setup of the sampler system at the Busted Butte field test site. For the purpose of testing the general performance of this new methodology, soil hydraulic properties representing Calico Hills Tuff (Bussod et al. 1998) and a loamy sand (Carsel and Parrish 1988) were chosen for this study. The simulations were conducted using the code FEHM (Zyvoloski et al. 1997), assuming two-dimensional, air-water flow under isothermal conditions.

Model Description–The performance of the filter paper sampling system was tested by applying a narrow pulse of solute after a sufficient period of constant, uniform irrigation to establish a reasonably steady water flow field within the simulation domain. The subsequent leaching of solute is observed frequently at selected nodes representing a sampling pad during the numerical experiments. In general, a pad is replaced periodically after the water potential within the pad reaches equilibrium with its ambient flow condition. The time required to reach this equilibrium depends highly upon the hydraulic properties of the pad and the soil.

The simulations were conducted in a homogeneous, two-dimensional, vertical cross section of 2 by 2 m with a 0.1-m-diameter access borehole located at the center of the domain. A 3.175-mm-thick pad of 0.05 m diameter was located on the inner upper center of the borehole. The hydraulic properties of the pad and the two selected soils are given in Table 10.7-1 The lateral boundaries were assumed to be a no-flux condition for both water flow and solute transport. A prescribed water potential was assumed on the surface boundary. The corresponding water input rate was calculated internally by the code and used subsequently for solute flux calculations. The pulse of solute input lasted for 1 day. The lower boundary was assumed to be a gravity-drained or natural drainage flux condition for water flow. At the bottom boundary, solute leaves the system freely with water at a water flux rate equal to the unsaturated hydraulic conductivity of a given water potential.

The filter-paper sampling system contains three major components that can adversely affect the flow field and the resulting solute transport. These three components are the borehole, the pad, and the effect due to periodic replacement of the pad. A borehole within the unsaturated flow domain acts like an obstacle to water flow (Philip et al. 1989). The collection pad disturbs the flow field due to the difference of its hydraulic properties from the neighboring porous material even under equilibrium condition with the ambient flow field. Finally, the periodic replacement of a new pad causes a highly transient flow condition, at least in the vicinity of the sampling location. To best evaluate and analyze the influence of the experimental setup to the overall behavior of the physical system, each component is tested separately during steady water flow conditions.

Modeling Results: Water Flow–Simulations were run for both the Calico Hills Tuff and the loamy sand. The background water saturation was assumed to be 0.35 for Calico Hills Tuff, and 0.5 for the loamy sand. When a borehole is constructed within an unsaturated domain, water tends to build up on the upstream side of the borehole and creates different shapes of so-called

roof-drip lobes depending largely upon the soil hydraulic properties (Philip et al. 1989, p. 16). The addition of a filter paper pad changes slightly the pattern of the water potential (or saturation) distributions. Figure 10.7-5 shows the saturation distributions for the Calico Hills Tuff when a borehole and a filter paper pad are added to the system. Flow patterns are not distinguishable for the loamy sand soil for the cases with and without a filter paper pad.

The dynamic responses of both systems to a filter paper pad plotted at three selected observation nodes are shown in Figure 10.7-6. The results show the water extraction rate and the equilibrium time needed when a new pad is added to a steady-state flow system. The background saturation during steady-state flow was 0.35 for the Calico Hills Tuff and 0.4 for the loamy sand. Two observation nodes were located within the pad. The rock node in Figure 10.7-6 indicates an observation immediately upstream of the pad within the porous media domain. The results revealed that for Calico Hills Tuff, it took approximately 10 days to reach equilibrium, whereas for loamy sand, the equilibrium time was less than half a day.

Solute Transport–Figure 10.7-7 shows the solute resident concentrations plotted as a function of time for various simulation scenarios for the Calico Hills Tuff. Solute transport was delayed when a borehole and a pad were added to the physical system. On the other hand, the periodic replacement of a filter paper pad caused an early arrival for the solute as illustrated in the figure for a step input of solute. The pad was assumed to be replaced every week during the simulations. As can be observed on the upper panel of Figure 10.7-8, the concentrations dropped periodically to a value of zero, corresponding to the replacement operations. The periodic change of concentrations on a nearby porous rock node, as depicted on the lower panel of Figure 10.7-8, also shows a reduction of concentration when the soil-water solution was sucked into the pad.

The dimensionless mean and variance of travel times were plotted as a function of steady-state fluid saturation in Figure 10.7-9 for Calico Hills Tuff. The normalized dimensionless quantities give a relative quantification of each separate effect that influences system behavior. For instance, the influence of a pad can be evaluated on a relative basis when the effect caused by a borehole plus pad is normalized with the corresponding quantities for a borehole without pad. It should be noted again that the resident concentrations observed as a function of time at a given location do not have an obvious physical implication in terms of parameter estimation and moment analysis as discussed above. Indirect estimations were used following the procedures given by Vanderborght et al. (1996) and Jacques et al. (1998). The results revealed that the disturbance of both a borehole and a pad to the solute transport is highly dependent upon the fluid saturation of the system. In a natural situation when the flow field is inherently transient, the saturation-dependent condition must be integrated into the system for the evaluation of the possible influence to solute transport.

Future Efforts–The last step in completing this effort to develop an application tool is to derive relationships between measured data and undisturbed true system behavior using available information. After that, this methodology will be applied to the Phase 1A and Phase 1B tests using U.S. Geological Survey (USGS) hydraulic property data as part of model-calibration and validation. The calibrated model can then be applied to the Phase 2 test evaluation and in performance assessment to more accurately represent anthropogenically altered sites.

10.7.2.3 Geology and Geologic Properties

10.7.2.3.1 Geology of the Busted Butte Test Facility

Busted Butte is a small (2.5 km by 1 km), north-trending mountain block primarily made up of thick ignimbrite deposits of the Paintbrush Group. This fault-block uplift is bound by northeast-trending and north-trending normal faults and is split by a north-trending down-to-the-west normal fault, which gives it a distinctive appearance. Tuff units generally have dips less than 10°, except where affected by drag near large faults. Small windows of older volcanic units, including the Calico Hills Formation, Wahmonie Formation, and Prow Pass Tuff, are exposed through colluvial deposits on the north and southeast sides of Busted Butte.

The test facility is located within a small horst on the southeast side of Busted Butte. The horst is 300 to 350 m wide and is bound by the down-to-the-west Paintbrush Canyon fault on the west and by a down-to-the-east splay of the Busted Butte fault on the east (Scott and Bonk 1984). Geologic units exposed in the vicinity of the test facility include, in ascending order, the Wahmonie Formation, the Calico Hills Formation, and Topopah Spring Tuff (Figure 10.7-10). The test facility is constructed in the Topopah Spring Tuff and the Calico Hills Formation.

A brief description of geologic units in the underground test facility is given below. The Topopah Spring Tuff is described in terms of its thermomechanical subunits because this nomenclature best represents rock properties that control groundwater movement. It should be noted, however, that ignimbrite depositional units in the lower part of the Topopah Spring Tuff cross thermomechanical boundaries. In the lower Topopah Spring Tuff, thermomechanical properties are controlled by compaction and welding features, and these features are superimposed on depositional units whose surfaces have up to a couple of meters of relief.

10.7.2.3.1.1 Calico Hills Formation

Up to 1 m of Calico Hills Formation is exposed in the test area of the facility in the lower walls of both the Main Adit and the Test Alcove. The Calico Hills Tuff consists of alternating beds of poorly cemented, salmon-pink massive tuff and well-cemented, white ash beds.

The salmon-pink tuffs contain round to slightly elongated, white vitric pumices that are generally less than 1 cm in diameter. The matrix is a mixture of fine ash, phenocrysts, and locally abundant fragments of black glass. The salmon-pink tuffs gradually become more deeply colored upsection, suggesting the upper parts of these units are more oxidized and may represent weakly developed paleosols. The clay content in these tuffs appears to be low, based on x-ray diffraction results (Section 10.7.2.3.2).

There are two well-cemented ash beds intercalated with the salmon-pink tuffs in the Main Adit and Test Alcove. These ash beds are about 130 cm apart on the right rib of the Main Adit. The ash beds are 15 to 20 cm thick and typically form resistant ledges in outcrops outside of the test facility and resistant layers inside the facility. Hand-augering results suggest that there may be additional ash beds in unexposed portions of the Calico Hills Formation below the floor of the test facility.

10.7.2.3.1.2 Topopah Spring Tuff

Tptpv1–The lowermost 1 to 1.5 m of the Topopah Spring Tuff is thermomechanical unit Tptpv1. The base of Tptpv1 is locally marked by a 3- to 4-cm coarsely bedded fall deposit. This deposit consists of 0.5- to 3-cm pumice fragments and 0.25-cm black perlitic lava clasts. This thin deposit pinches out laterally and is similar to thin discontinuous beds of fall deposits at the base of the Topopah Spring Tuff in outcrops outside of the test facility. A 4.5-cm-thick, crudely laminated shardy tuff overlies the fall deposit. The shardy tuff is also discontinuous laterally.

Above the thin bedded deposits, Tptpv1 consists of light-gray nonwelded ignimbrites. The ignimbrite flow units contain medium-gray pumices in a pink-gray matrix. Near the top of Tptpv1, pumices are tan. Glassy lava fragments and red-brown lithics are common. Pumices increase in size and abundance upsection in individual ignimbrite flow units. The two lowermost ignimbrite flow units are separated by a bedded tuff that is 0.2 to 8 cm thick. The character of these bedded tuffs is variable, consisting of laminated shardy tuff in some places and clast-supported pumiceous deposits in others. Because of the relief on the surface that these bedded tuffs were deposited on, they fall within Tptpv1 in the Test Alcove and within Tptpv2 toward the back of the Main Adit.

In the Test Alcove, the upper part of Tptpv1 is characterized by a distinctive zone of clay alteration, typically about 70 cm thick. The clay occurs both as rinds around pumice clasts and as complete replacement of the pumices. The clay is typically reddish brown but also includes small round bodies of white clay within the reddish-brown clay (giving it a mottled appearance). In some replaced pumices, white clay overlies layers of reddish-brown clay. Clay alteration also occurs in the tuff matrix and along subhorizontal fractures. One such fracture contains four different layers of clay up to 1.5 cm thick. The lower boundary of clay alteration is undulatory and has up to 0.5 m of relief.

Tptpv2–Thermomechanical unit Tptpv2 is the highest stratigraphic unit exposed in the back of the Main Adit and in the Test Alcove area. It is characterized by tan, partly welded ignimbrite that has well-developed columnar joints. The matrix of these ignimbrites has a distinctive salt and pepper appearance due to the presence of black glass shards in a tan ashy matrix. Pumices are typically 1 to 6 cm in their long dimension and exhibit flattening ratios from 6:1 to 8:1. Welding increases upsection through Tptpv2, and rocks in this unit yield a distinctive clink when hit with a hammer.

10.7.2.3.2 Mineralogy of the Busted Butte Locality

Samples from outcrops were collected at the Busted Butte site on different days for mineralogy/petrology analyses and site characterization activities. Some of these samples were also used for hydrologic property determinations. Other samples from the test block walls were also collected throughout the year for the study, and descriptions of the lithologies present in the test area were gathered.

Table 10.7-2 to 10.7-4 summarize the quantitative x-ray diffraction data from surface samples at the Busted Butte test locality. Table 10.7-2 to 10.7-4 are for the Tpt samples. Table 10.7-2

provides the stratigraphic descriptions for the samples in Tables 10.7-3 and 10.7-4. The calcite and gypsum reported in the Tpt samples represent calcrete contamination in the surface samples.

The erionite detected in the altered sample from the Tptpln/Tptpv3 contact zone (Table 10.7-3) is the only occurrence of this hazardous mineral found at the site. A survey for erionite occurrence shows no other detectable erionite (detection limits of 250 ppm) in the strata below the Tptpln/Tptpv3 contact, where the Busted Butte test facility was excavated.

The samples from the Tptpv2 and Tptpv3 intervals show that the poorly welded to nonwelded vitric portions of the lower Topopah Spring Tuff at this site are largely unaltered, without zeolites, but with modest smectite occurrences.

Table 10.7-5 covers the Calico Hills Formation (Tac) and the Wahmonie Formation surface samples at the Busted Butte site. These samples are arranged in Table 10.7-5 by relative depth and show that the lowermost part of the Tac contains appreciable amounts of clinoptilolite. The upper part of the Tac at this site, however, is characterized more by smectite than by zeolite alteration. Access to both types of alteration is therefore possible at this site. The lowest three samples from an auger hole (AUG-1) into the floor of the Busted Butte Alcove were analyzed (Table 10.7-6) for comparison with the vitric Tac samples from outcrop. Alteration in the alcove samples is generally similar, with smectite dominating over clinoptilolite. The mineral constituents in the alcove (especially the low biotite and feldspar components) are characteristic of the Calico Hills Tuff, indicating that Wahmonie Formation deposits are more than 396 cm below the present alcove floor.

10.7.2.3.2.1 Comparative Data for H-5 and SD-6

The excavated section at Busted Butte is in the lower Topopah Spring Tuff (Tptpv2 and Tptpv1; Tpbt1 poorly represented) and the upper Tac. The vitric nature of this section and the relatively low abundances of smectite and clinoptilolite alteration are similar to those found in drill holes near the crest of Yucca Mountain, such as USW H-5 (Table 10.7-7) and USW SD-6 (Table 10.7-8). The increase in zeolitization at the base of the Tac, particularly in the Tacbt unit, is comparable to the localized zeolitization in the lower part of the Tac at Busted Butte (Tables 10.7-5 and 10.7-6). The more detailed data from SD-6 are unfortunately pending an additional sample. However, the data that are available indicate a distribution of alteration similar to that at Busted Butte. In considering the SD-6 and H-5 data, however, it is important to bear in mind that both drill holes had only partial core or cuttings recovery, potentially skewing the mineralogic information. A much more accurate picture of these poorly indurated vitric units could be obtained by excavation, as was accomplished at Busted Butte.

10.7.2.3.2.2 Influence of Partial Zeolitization on Hydrologic Properties: Evidence from the Exploratory Block

The data displayed in Figure 10.7-11 show that zeolite abundances as low as 8 to 2 percent correlate with the sample porosity. Significant differences in the structure of sample porosity even occur in the transition from 0 percent zeolite content to 2 percent zeolite content. Whether such small differences in alteration mineralogy impact transport will be determined by the experiments being conducted at Busted Butte.

As part of a recent revision of the three-dimensional mineralogic model of Yucca Mountain (Carey et al. 1998), comparisons were made between hydrologic properties and the extent of zeolitization in the lower Topopah Spring Tuff and upper Calico Hills Formation from drill-core samples. Samples that were analyzed by the USGS for porosity properties were analyzed as subsplits to obtain quantitative x-ray diffraction mineralogy on the same sample. This approach allows the direct comparison of laboratory-measured matrix properties and mineralogy. Samples from USW SD-7, SD-9, and SD-12 were analyzed in this manner and the results are summarized in Table 10.7-9. The columns for mineral or glass abundance and the quantitative x-ray diffraction total report data were collected by standard Los Alamos National Laboratory methods for analyses of Yucca Mountain tuffs. The column for "δ porosity" represents the difference between relative humidity (65 percent), 60°C oven-dried porosity and 105°C oven-dried porosity (cm^3/cm^3), as reported by Flint (1998). The data in Table 10.7-9 allow direct comparison of not only zeolite abundance but the total abundance of hydrous minerals (clays and zeolites) versus the laboratory measurement of δ porosity in the unsaturated zone where a vitric-to-zeolitic transition occurs. Outliers may occur for a variety of reasons. Although the anomalously high hydrous mineral content in sample SD-7 1494 could be a result of differing trends in chabazite-bearing samples, the anomalously low hydrous mineral content and high δ porosity of SD-12 1456.6 occurs in a sample with no mineralogic distinction from neighboring samples that are not anomalous (Table 10.7-9). These results suggest that rock texture or fabric may be a significant factor in the ability of samples to retain water within pores. The data also indicate that a statistically useful relationship between hydrous-mineral abundance and porosity properties might be derived for Yucca Mountain samples with applicability down to very low abundances of hydrous minerals (Figure 10.7-12).

10.7.2.3.3 Hydrology

10.7.2.3.3.1 Introduction

Samples of Calico Hills and Topopah Spring formation rocks from Busted Butte outcrops were collected in Fall 1997 and were used to estimate the hydrologic properties of the formations in the test block. (The six USGS samples are discussed in Table 10.7-10).

10.7.2.3.3.2 Analyses Using Ultracentrifuge Induced Flow

The samples, collected from Busted Butte on November 7, 1997, are described below.

SPC 7047, Los Alamos National Laboratory Number 2825,X1–This sample was cored vertical to horizontal, as measured in the field area, from the Topopah Spring Tuff (Tptpv2) unit with a strong fabric, as indicated by flattened lapilli, low permeability, and moderate fracture density in the field. This partly welded, salt-and-pepper tuff unit is transitional between the basal vitrophyre (Tptpv3) and the base of the Topopah Spring Tptpv2 lower (sample 3). The core had no visible fractures and was of perfect dimensions:

- Diameter: from 3.790 to 3.795 cm
- Usable core length: about 5.850 cm.

SPC 7048, Los Alamos National Laboratory Number 2826,X1–The second sample was cored vertical to horizontal, as measured in the field area, from the Calico Hills Tuff Tac unit, which is a white ash-fall tuff located at the top of the sequence 40 cm below SPC 7049 2827,X1 (see below). The unit is ledge forming and approximately 50 to 70 cm thick. This sample had no visible fabric, had visible fractures, and was extremely fragile and friable. There were no visible fractures in the field outcrop except in the vicinity of faults. The permeability of this sample is expected to be very high (greater than 100 Darcys). The core quality was fair to poor, as a 2-in. core bit was used to core the sample. The diameter was consequently highly variable, and the core was somewhat curved:

- Diameter: from 3.715 to 3.850 cm
- Usable core length: about 5.000 cm.

SPC 7048, Los Alamos National Laboratory Number 2826,X2–The third sample was cored in the horizontal plane (as measured in field area) and perpendicular to SPC 7048F 2826,X1 above. This sample also had no visible fabric but contained at least two fractures at approximately 70° to the core axis and subparallel to each other (subhorizontal). The first fracture extended from one of the core extremities over one-third of the core length and the other extends through the center of the core. The core quality was similar to sample SPC 7048 2826,X1 with the following dimensions:

- Diameter: from 3.790 to 3.890 cm
- Usable core length: about 4.300 cm.

SPC 7048, Los Alamos National Laboratory Number 2826,X3–This is the same sample as above, but the shavings were used in a reconstruction experiment.

SPC 7049, Los Alamos National Laboratory Number 2827,X1–The fourth sample was cored vertical to horizontal, as measured in the field area, from a 60- to 70-cm-thick, pumice-rich base of the Topopah Spring Formation (TpTpv1) located 40 cm above sample SPC 7048 2820,X1, consisting of very large (centimeter size) pumice fragments defining a moderate fabric. This is a high permeability unit with little to no through-going fractures, with the exception of fault zones. The sample had no visible fractures. The core quality was good considering the mechanical heterogeneity of the sample:

- Diameter: from 3.720 to 3.605 cm
- Usable core length: about 4.700 cm.

SPC 7049, Los Alamos National Laboratory Number 2827,X2–This is the same sample as above, but the shavings are to be used in a reconstruction experiment.

SPC 7050, Los Alamos National Laboratory Number 2828,X1–The fifth sample was cored vertical to horizontal, as measured in the field area, from the nonwelded to partly welded Topopah Spring, tan, ash-flow tuff (TpTpv2) which was an approximately 90-cm (3-ft.)-thick

unit with some fractures, transitional with sample SPC 7047 2825,X1. With a weak to moderate fabric, the sample was very fragile, permeable, and contained no visible fractures. The core quality was good:

- Diameter: from 3.635 to 3.650 cm
- Usable core length: about 3.425 cm.

The Calico Hills (Tac) sample (SPC 7048) has a total porosity of 50 to 56 percent and a saturated conductivity (K) of approximately 2×10^{-3} cm/s. The Topopah Spring (Tptpv1) sample (SPC 7049) has a total porosity of 64 percent and a saturated conductivity (K) of approximately 6×10^{-4} cm/s. Both samples represent the nonwelded Calico Hills unit (CHn). Conversely, samples collected from the top of the test block represent the base of the basal vitrophyre (Tptpv2) and exhibited lower saturated conductivities (K), varying from 4×10^{-4} to less than 4×10^{-10} cm/s (for SPC 7050 and 7047 collected during Phases 1 and 2, respectively). These results are used in conjunction with YMP database parameters to run the model simulations presented in Section 10.7.2.6.

10.7.2.4 Tomographic Studies Overview of Geophysical Techniques Used at the Busted Butte Unsaturated Zone Test Facility

The original test plan for Busted Butte (Bussod et al. 1997) relied on inverting-membrane collection-pad systems to collect unsaturated zone water samples for detailed tracer analysis at discrete points in the block and during final destructive mineback of the entire block. Recent successes of combined real-time geophysical monitoring techniques using ground-penetrating radar tomography and electrical-resistance tomography at the Large Block Facility and the Exploratory Studies Facility thermal tests suggest that these techniques may be used to provide real-time data on the advance of the tracer front through the block. This will optimize the collection-pad sampling schedule to collect data. Each of the techniques has advantages and drawbacks; by combining techniques, detailed high-resolution, three-dimensional, calibrated, real-time monitoring of moisture and tracer movement through the unsaturated fractured medium can be obtained. Specifically, electrical-resistance tomography provides three-dimensional global coverage, ground-penetrating radar tomography provides high spatial resolution, and neutron logging enables absolute moisture-content calibration.

10.7.2.4.1 Ground-Penetrating Radar Tomography

10.7.2.4.1.1 Experimental Objective

The objective of the borehole radar data acquisition is to monitor the tracer injection of the Busted Butte unsaturated zone transport test, and to investigate the nature of fluid migration through the Calico Hills member of the Yucca Mountain lithologic sequence. The data presented in this section include the preinjection baseline measurements, as well as several measurements made after the start of tracer injection. Subsequent measurements are to be made as determined by tracer breakthrough in an attempt to monitor the tracer distribution over time.

10.7.2.4.1.2 Background

The borehole radar method is one in which modified ground-penetrating radar antennas are lowered into the ground and high-frequency electromagnetic signals are transmitted through subsurface material to a receiving antenna. The electrical properties of the subsurface material influence the properties of the transmitted electromagnetic signal. In particular, the dielectric permittivity of the rock has a strong influence on the speed of propagation of the signal. The moisture content and chemical composition also have such an effect, so that any increase in background moisture content or chemical composition resulting from the tracer injection should result in changes in the received radar wave velocity and amplitude. A tomographic image may be obtained through computer processing that includes the following information: (1) transit time, which depends on wave velocity, and (2) amplitude, which depends on attenuation. This information, in the form of a processed tomogram, offers a high-resolution approach to monitoring the changes occurring in the rock over the duration of the tracer-injection experiment.

10.7.2.4.1.3 Results of Radar Data Acquisition in the Busted Butte Unsaturated Zone Transport Test

The radar data were acquired in eight of the Phase 2 collection boreholes orthogonal to the direction of the Phase 2 injection boreholes. Additionally, two Phase 2 injection boreholes were used to acquire data after the holes were affected by grout infiltration resulting from nearby electrical-resistance tomography borehole grouting.

Of the data processed so far, several well-pair images deserve particular attention: 48-46, 46-9, 46-16, and 22-19. The large horizontal surface defined by the 48-46 and 46-9 well pairs shows an area of lower velocity in the vicinity of the injection boreholes that differs dramatically from the pre-injection data (Figures 10.7-13 and 10.7-14). Lower velocities are likely the result of elevated moisture content or changing chemical composition. Therefore, these low velocities are possibly the result of the injected tracer moving through the plane of the well pairs. The close proximity of several of the injection boreholes to the collection boreholes (10.0 cm), however, might be the cause of the low-velocity zones. That is, the low-velocity zone might be due to the nature of the injection assemblies and any metallic or other velocity-affecting materials being present in such close proximity to the radar well pairs. Subsequent measurements in these well pairs should reconcile the problem because the injection assemblies will remain static, whereas the injected tracer will continue to pass through and be distributed throughout the well pairs. Differencing tomography (i.e., the subtraction of one set of radar measurements from another) will result in only those areas of tracer being imaged, as the tracer is all that will change over the duration of the experiment.

Similarly, well results from pair 46-16 suggest areas of variable velocity and the possible presence of tracer (Figure 10.7-15). The image is plotted with the injection and electrical-resistance tomography boreholes shown as black dots intersecting the well pair. Particularly in the area of the lower injection boreholes (nearest borehole 46), low velocities are found directly beneath the boreholes. Again, this may represent either the tracer or the injection assemblies, with subsequent data differencing needed to remove the influence of the assemblies. Additionally, a striking feature between the two boreholes resembles a low-velocity zone with high-angle dip. This feature was also present in the baseline data acquired using the lower-

resolution, 100-MHz antennas. It may be the result of elevated moisture content along the highly permeable fault zone mapped along the face of the Main Adit, thus explaining the lower velocities. The apparent strike of the fault would bring it into intersection with well pair 46-16 at roughly the observed location of the low-velocity zone. If this zone does represent the fault, then future data acquisition may be able to illuminate the tracer transport properties of the fault zone versus those of the matrix.

Finally, well pair 22-19 is notable due to the possible imaging of the pathway taken by the grout moving from an electrical-resistance tomography borehole to the planned injection borehole 22. The grout was apparently injected under sufficient pressure and at sufficient volume to travel from one borehole to another, likely along a fracture or similar fast pathway. The properties of the grout and their impact on radar wave propagation are similar in effect to those of the tracer.

Any zones of low or anomalous velocity are potential evidence of the presence of grout. Such a zone is clearly present in well pair 22-19 (Figure 10.7-16). The point of grout injection between injection boreholes 20 and 21 is shown as a low velocity (i.e., elevated water content) region in the tomogram. This low-velocity zone appears to connect with borehole 22 and is present laterally 2.50 m down the length of borehole 22. Based on the grout-injection history, this scenario appears to be the one experienced by the personnel present at the time. Another low-velocity zone in the area near the bottom of injection borehole 19 should also be noted. This zone, if located spatially with respect to well pair 46-16, nearly intersects the low-velocity zone imaged in the tomogram of well pair 46-16. It, too, may be another representation of the elevated moisture content along the fault zone and may have nothing to do with the electrical-resistance tomography grouting infiltration.

10.7.2.4.1.4 Conclusions

The radar data collected thus far in support of the Busted Butte unsaturated zone transport test suggest that the method is appropriate for investigating subsurface velocity anomalies that may be related to tracer injection. Such anomalies are the result of changes in the dielectric permittivity or chemical composition of the rock mass. As noted above, such changes are most likely the result of both the injected tracer and/or the downhole injection and electrical-resistance tomography assemblies. Although the data presented above describe areas of unusually low velocity, subsequent radar data acquisition should remove the effects of the downhole assemblies and result in the singular imaging of the tracer front. This effort, combined with the ongoing processing of the radar-wave amplitude data, should allow for the most accurate imaging of the injected tracer to date.

10.7.2.4.2 Electrical-Resistance Tomography

The objective of this work is to provide three-dimensional electrical-resistance tomography images of the movement of a tracer through the test block at the unsaturated zone transport test at Busted Butte. Electrical-resistance tomography was chosen as an appropriate technology based on its success at many other locations, including the Drift Scale Test at Yucca Mountain. This section describes the results obtained during four separate data collections from July to early September 1998.

Electrical-resistance tomography is a geophysical imaging technique that can be used to map subsurface liquids as flow occurs during natural or man-induced processes and to map geologic structure. Electrical-resistance tomography is a technique for reconstructing of subsurface electrical resistivity. The result of such reconstruction is a two-dimensional or three-dimensional map of the electrical resistivity distribution underground made from a series of voltage and current measurements from buried electrodes. The electrical-resistance tomography approach followed here relies on detection and mapping of the changes in electrical resistivity associated with tracer movement through the test block at the unsaturated zone transport test site.

10.7.2.4.2.1 Results of Data Collections From July to Early September

Electrical-resistance tomography data were collected four times on July 2, July 14, August 19, and September 9, 1998. It is most useful to compare images when changes are taking place over time. The results presented here consider difference images that compare the resistivity of the block on August 19 and September 9 to July 2. Because the water injected during Phase 2 of the unsaturated-zone transport test experiment was approximately eight times more conductive than the pore water, resistivity decreases in the images were looked for.

Figure 10.7-17 shows an absolute image of the baseline condition of July 2 (top) and the difference between August 19 and July 2 (bottom). The baseline image shows a layered structure consistent with the lithology in the rear half of the block. That is, a high-resistivity layer was shown over most of the middle of the block, Tptpv1, with a lower-resistivity region, Tptpv2, at the top, and a low-resistivity region, Tac, at the bottom. The image also shows an anomalously low resistivity region in the front half of the block, particularly near the bottom.

The difference image of Figure 10.7-17 shows regions of resistivity decrease near injection holes 18, 20, and 21, as expected from the injection of conductive water. Also apparent is a resistivity decrease that is very pronounced in the slice 2.66 m from the front of the block, which could be associated with water moving downward in the block. The region of the block between 1.33 and 4.0 m, which contains this slice, also appears to be a low-resistivity region in the absolute image.

The September 9 to July 2 difference (Figure 10.7-18) also shows regions of resistivity decrease near injection holes 18, 20, and 21. The effect is even stronger in the 5.33-m slice. Moreover, the effect of water moving down into the block seems to be more pronounced in the 1.33- and 4.0-m slices compared to August 19 (CRWMS M&O 2000, Section 6.8.4.2).

10.7.2.4.2.2 Conclusions

The electrical-resistance tomography baseline images show a resistivity structure that is consistent with the known lithology in the rear part of the block. There appears to be a low-resistivity region in the front half of the block, particularly near the bottom. This is not well understood and should be confirmed, if possible, by other means.

The difference images from August 19 and September 9 show clear and consistent resistivity decreases in the region near holes 18, 20, and 21 that can be associated with the injection of conductive water. This effect appears to be stronger on September 9 in the 5.33-m slice. The images show very little effect in the region around the other injection holes, 23 and 24 through 27, where far less water was injected.

In addition, the difference images from August 19 and September 9 show resistivity decreases that could be interpreted as water moving down into the block between the 1.33- and 4.0-m slices. This is the same region that has an anomalously low resistivity in the baseline image.

These results should be considered preliminary and subject to change based on new information, such as new borehole radar data and, perhaps, neutron data.

10.7.2.5 Geochemistry and Tracer Migration

This section discusses all aspects of chemical and geochemical measurements that were conducted in association with the Busted Butte project. These include laboratory measurements of sorption of both radionuclides and tracers onto Busted Butte rocks, measurements of in situ pore-water chemistry used to formulate the field tracer mixture, and measurements of field-scale tracer transport.

10.7.2.5.1 Laboratory Sorption Studies

For the Busted Butte field tests, analog conservative and reactive tracers are used as surrogates for radionuclides. To validate the use of these tracers and the site-scale use of the minimum-K_d approach for sorption and the processes of matrix diffusion and colloid migration, a series of laboratory batch-sorption studies were conducted. Preliminary tracer sorption studies used in tracer selection are complete, detailed radionuclide sorption studies are complete, and detailed tracer sorption studies are in progress. Each study will be discussed in turn.

10.7.2.5.1.1 Preliminary Studies

A large number of possible tracers were proposed in the Busted Butte work plan. Final determination of tracer selection and concentration was dependent on both rock and pore-water characteristics. Rock and pore-water samples became available in early 1998, and a set of fast-turnaround batch studies and geochemical modeling efforts was initiated.

Preliminary batch-sorption studies were conducted using proposed reactive tracers and two rock samples from the Main Adit at Busted Butte. Tracers tested included Li, Mn, cobalt, Ni, molybdate, and perrhenate; rocks were samples of the Calico Hills Formation (Tac) and Topopah Spring Tuff (Tptpv2) from Phase 1 boreholes 4 and 7. Because of the need for rapid turnaround on these results, the sorption studies differed from standard YMP procedures in two important respects: preequilibration and equilibration times were shorter than normal and fewer concentration levels were studied. Therefore, these results are preliminary and will be supplanted by the results of the detailed tracer sorption measurements that are underway.

The results of the preliminary sorption studies for Li, Mn, cobalt, and Ni are presented in Table 10.7-11. The results indicate that the Tac sample sorbed the metals more strongly than the Tptpv2 sample and that, on both samples, the metals showed a consistent sequence of sorption: Li « Mn « Ni < cobalt. Based on these results, all four metals show significant sorption and may be useful reactive tracers in the field. Neither of the proposed pertechnetate analogs (molybdate and perrhenate) displayed any significant sorption and were therefore eliminated from further consideration in the testing.

10.7.2.5.1.2 Detailed Studies

Three core samples were selected for detailed sorption and mineralogic characterization, and are described in Table 10.7-12. These rock samples were uniformly ground, sieved, and homogenized, and subsamples were used for radionuclide sorption, tracer sorption, and quantitative x-ray diffraction studies.

The sorption of Np, Pu, and Am to the three Busted Butte rock samples was measured at three different concentration levels. Average results for each nuclide are summarized in Table 10.7-13.

Laboratory batch measurements of the sorption of the field tracers onto the same three rock samples were begun in fiscal year 1999. At the time this Site Description was prepared, the laboratory data were not published.

10.7.2.5.2 In Situ Pore Water Chemistry

Field-scale transport behavior is primarily a function of the ambient flow field and the interactions between the geologic host and the material being transported. Secondary influences include details of the pore water chemistry, including pH, Eh, ionic strength, and chemical composition. Changes in any of these variables may affect solute sorption behavior and colloid stability and may lead to dissolution or precipitation of minerals resulting in permeability changes. These considerations lead to a fundamental conflict in field-tracer studies: on the one hand, alteration of the in situ water chemistry should be limited to minimize the artificial perturbations introduced by chemistry variations; on the other hand, introduction of any artificial tracer will inherently alter water chemistry. (One exception might be the use of miniscule amounts of isotopic tracers, which is not a practical alternative at this phase of the Busted Butte studies.)

The plan at Busted Butte was to introduce artificial tracers in a matrix designed to mimic natural pore-water chemistry as closely as practical, acknowledging that some alterations were inevitable. Accordingly, pore water samples were collected and analyzed from rock cores collected in the Adit, a recipe was developed for "synthetic" Busted Butte water that closely resembled the in situ chemistry, and synthetic water was used as the injection matrix. Results of the chemical analyses are presented here, and details of the synthetic pore water recipe were presented in Section 10.7.2.2.4.3.

A set of quality rock samples were collected in the Test Alcove from the Tac horizon. Pore water was extracted from a subset of these samples by ultracentrifugation. Gravimetric moisture contents of the rock samples and the chemical composition of the extracted pore water were measured (Table 10.7-14). Because the analyses involve a bicarbonate buffer, the bicarbonate numbers listed in Table 10.7-14 are estimated by charge balance.

The results in Table 10.7-14 show that the pore water is a mixed-ion water (Ca-Na-HCO_3-SO_4) with an average total dissolved solids of approximately 200 mg/L. Compared to more typical groundwater compositions, the pore water shows high nitrate (probably due to soil biological activity) and high silica content (due to relatively rapid equilibration with amorphous silica in the tuff). Sample 3B, from near the adit wall, differs somewhat from the other samples, perhaps due

to the influence of construction water and atmospheric CO_2 levels. The compositions of the other three pore-water samples were averaged (as shown in the table), and these average values were used to develop the synthetic pore-water recipe presented in Section 10.7.2.2.4.3.

Also listed in Table 10.7-14 are the pH values measured on extracted pore water. Despite obvious opportunities for pH alteration due to CO_2 exchange during sample collection, extraction, and analysis, these pH values were the best available at the time of Phase 1 planning. Thus, Phase 1 tracer mixtures were pH-adjusted to a value of 8.4 ± 0.1. During Phase 2 installation, attempts were made to measure pH in situ by inserting pH paper into boreholes for a few days. Results were mixed but seemed to indicate lower in situ pH values than those measured in the laboratory (consistent with degassing of excess soil CO_2 before lab analysis). Accordingly, Phase 2 tracer mixtures were pH adjusted to a value of 7.0 ± 0.1.

10.7.2.5.3 Field-Scale Tracer Transport

10.7.2.5.3.1 Phase 1A

10.7.2.5.3.1.1 Description

Phase 1A consisted of four, 2-m-injection boreholes (boreholes 1 to 4). The Phase 1A tracer mixture was described in Section 10.7.2.2.4.1. The tracer mixture was injected at 10 mL/hr. in boreholes 1 and 3, and at 1 mL/hr. in boreholes 2 and 4. Phase 1A injection ran continuously from April 2, 1998, to January 12, 1999. The mineback of the Phase 1A test block began on January 15, 1999, and ended on March 3, 1999. During the mineback, as successive layers of the Adit wall were removed, digital photographs under visible and ultraviolet illumination were taken, rock samples were collected by augering, and the exposed phase was accurately surveyed.

10.7.2.5.3.1.2 Results

The visualization of the tracer plume using ultraviolet illumination of the fluorescein tracer serves as the primary result of Phase 1A. Detailed comparison of the digital plume imagery and numerical modeling results is under way, and will be completed in fiscal year 2000.

A small number of augered rock samples are currently being analyzed for bromide and moisture content.

10.7.2.5.3.2 Phase 1B

Phase 1B consisted of two 2-m injection boreholes (boreholes 5 and 7) and two 2-m collection boreholes (boreholes 6 and 8) with the tracer mixture, described in Section 10.7.2.2.4.1, injected at 10 mL/hr. in borehole 5 and at 1 mL/hr. in borehole 7. At the conclusion of the experiment, overcoring of the Phase 1B boreholes was conducted.

One hundred seventy-six selected pads were extracted for tracers and analyzed for trace concentrations. Breakthrough of all five solute tracers (Section 10.7.2.2.4.1) was detected in borehole 6, directly below the 10 mL/hr. injection site in borehole 5. No breakthrough was detected in borehole 8, below the 1 mL/hr. injection site in borehole 7. No clear evidence of microsphere breakthrough was detected in either borehole, but this may be due to analytical

difficulties. The borehole 6 breakthrough results are summarized in Figures 10.7-19a to 10.7-19e. Detailed modeling analyses of these results are under way; the following discussion provides some initial comments on the breakthrough patterns.

All five tracers shown in Figure 10.7-19 show clear evidence of breakthrough by the end of the experiment. All of the figures show peak concentrations at a (horizontal) depth of approximately 130 cm, directly below the injection port in borehole 5, but maximum recovery varies greatly. Bromide and 2,6-difluorobenzoic acid, both anionic supposedly nonreactive tracers, show similar and reasonable breakthrough patterns, with initial breakthrough detected after approximately 1 mo. of injection. Both bromide and 2,6-difluorobenzoic acid reached 50 percent injection concentrations after 2 mo. of injection. The fluorescein breakthrough pattern is more erratic. In particular, the peak concentration measured is over twice the injected concentration, which is clearly not reasonable. These anomalies probably reflect analytical difficulties associated with the extremely high concentration of fluorescein injected. The high concentration succeeded in its goal of improving field visualization of the plumes during mineback and overcore, even though it hurt the laboratory quantification. This analytical problem will be less severe for Phase 2, in which injected fluorescein concentrations are just 1/50 of those used in Phase 1. The late breakthrough and low detected concentrations of pyridone may also reflect analytical difficulties; if real, they may indicate either sorption or degradation of this supposedly conservative tracer. Ongoing laboratory sorption and degradation studies will provide more information. Finally, although detected Li concentrations are quite low, their contrast with background levels and their consistent location both in time and space indicate that true Li breakthrough was observed in the field. The low and late breakthrough indicates that Li was sorbed quite significantly. Ongoing numerical analyses will provide quantitative field retardation estimates, to be compared with lab sorption estimates.

10.7.2.5.3.3 Phase 2

10.7.2.5.3.3.1 Introduction

Phase 2 involves 8 injection boreholes and 12 collection boreholes drilled into the Phase 2 test block from the Test Alcove. The injection boreholes are subdivided into three subphases. Phase 2A consists of a single horizontal borehole (borehole 23) in the Tptpv2 horizon. The borehole has 10 injection points, each injecting tracer at 1 mL/hr. Phase 2A injection began on July 23, 1998, and is ongoing. Phase 2B consists of four parallel horizontal injection boreholes, (boreholes 24, 25, 26, 27) in the Tac horizon. Each borehole is fitted with 10 injection points at a rate of 10 mL/hr. Phase 2B injection began on July 30, 1998, and is ongoing. Phase 2C consists of three parallel horizontal injection boreholes (boreholes 18, 20, 21) coplanar with the Phase 2A borehole in the Tptpv2 horizon. Each borehole is equipped with nine injection points at a rate of 50 mL/hr. Phase 2C injection was initiated on August 5, 1998, and is ongoing. Details on the tracer mixtures for each borehole are presented in Section 10.7.2.2.4.2.

The 12 collection boreholes are drilled into the Phase 2 test block from the Main Adit and are thus perpendicular to the injection boreholes. Ten of the collection boreholes are horizontal, whereas the two deepest boreholes (boreholes 11 and 47) are dipping downward beneath the block. The collection boreholes are arranged to allow interception of the tracer plumes after varying travel distances. Figure 10.7-20 is a schematic layout of the collection boreholes.

10.7.2.5.3.3.2 Status

Between the initiation of Phase 2 activities and September 21, 1999, a total of 9,188 sampling pads were collected. Of these, more than 2,200 were extracted for the Phase 2 extraction/analysis scheme. More than 10,000 individual analyses were conducted and more are being received on a day-to-day basis. A summary of the results to date is being prepared and will help guide decisions on the future course of the field test.

Tracer Degradation–One concern that has been raised is the possible biodegradation of some of the tracers on the collection pads during transportation and storage. This concern only applies to the organic tracers (dyes and fluorinated benzoic acids); the metals, inorganic anions (bromide and iodide), and polystyrene microspheres are not subject to degradation. Among the organic tracers, fluorinated benzoic acids are unlikely to degrade rapidly due to their strong F-C bonds; the dyes' primary purpose is field-screening, so degradation, if occurring, is not particularly damaging to the overall goals of the test. Nevertheless, to address this concern, a long-term tracer biodegradation study was initiated in fiscal year 1999 and will be concluded in fiscal year 2000, at which time, data and discussion of the potential impacts of tracer degradation will be submitted to the YMP.

10.7.2.6 Phase 1A Predictions

10.7.2.6.1 Deterministic Model

The purpose of the unsaturated zone transport test at Busted Butte is to obtain new information about flow and transport behavior and to apply that information toward improving computational models used to predict flow and transport in the vadose zone. The field experiments at Busted Butte examine flow in unfractured, fractured, and composite systems. These experiments were carefully designed to provide specific information to improve database and models. Data collected through the unsaturated zone transport test will help to check the accuracy and value of data currently in the database for future improvements. Improved increased experimental data about the site will improve computational models of the various flow and transport processes occurring in the system. The accuracy of current concepts for unsaturated zone flow and transport, and the iterative improvement of the model through incorporation of new data, can then be shown through increased model accuracy. As more data become available, it should be possible to demonstrate the validity of refined flow and transport models, as well as the worth of the data collection effort at Busted Butte. Upon the completion of the testing and modeling activity, an improved model that adequately describes the flow and transport behavior in the unsaturated zone at the site will result. In addition, refinements to the radionuclide transport model of the potential repository site should follow. This cyclic process of prediction, measurement, and model refinement will result in increased confidence in the unsaturated zone model.

This section provides a preliminary "blind" numerical simulation of the Phase 1A. In this section, numerically based "blind" predictions of the tracer distribution for Phase 1A were made. These predictions were made prior to the beginning of any measurements at the site. Thus, the accuracy of the understanding of the system and the representation of the computational model

can be tested. The blind prediction was intended to test the current modeling concepts and tools available to the integrated site-scale model and their abstractions.

This prediction used existing parameters available from the Yucca Mountain hydrologic database, as well as initial laboratory values on samples taken from the Busted Butte site. As more data become available from the unsaturated zone transport test, they will be incorporated into refined versions of the models employed in these preliminary predictions.

The numerical experiments presented here were set up to determine the ability of numerical models to predict actual field response of flow and transport in porous media. The simulations are not intended to be a one-time prediction; rather, they are intended to provide insight into the quality and extent of information needed to accurately represent a physical system and to identify physical processes that are not adequately represented in numerical models.

The computer code FEHM (Zyvoloski et al. 1997) was used to develop the predictions presented in this section. FEHM is a multi-dimensional finite element code for simulating transient, saturated and unsaturated flow in transport problems. FEHM has been the code used by the YMP for radionuclide migration studies and therefore was chosen for predictions of the unsaturated zone transport test. At Yucca Mountain, detailed geologic and hydrologic property distributions in three dimensions are not available at present, and the Tac unit in question is not fractured so a homogeneous, isotropic description of the porous media was selected. However, it is expected that more site data will also become available, and three-dimensional effects might very well become apparent during the test. Therefore, the model was made three-dimensional from the outset to allow the capture of these effects and to anticipate the three-dimensional property database that will be built for the test block.

In Phase 1A simulations, the focus was on the injection of a conservative tracer into the vitric Calico Hills Formation (Tac) via a single injection point in a 10-cm-diameter borehole. The model for assumed a homogeneous, unfractured rock matrix. A 0.05-m-radius borehole was placed in the center of the computational domain. The tracer solution was injected through a polypropylene pad located 0.75 m down the length of the borehole. The base prediction was made using data measured on Busted Butte samples, with information about the injection pad provided from Science & Engineering Associates, Inc., the contracted field-implementation team.

An 82,000-node, three-dimensional, unstructured grid that represents the single borehole configuration was generated using the LAGRIT computer code (CRWMS M&O 2000, Section 3, Item 4). This grid was used for the Phase 1A blind prediction as well as for the ongoing preliminary scoping calculation. The grid contains the full representation of the injection borehole, the 25-cm^2 injection pad, and 54 m^3 of the surrounding rock mass (Figure 10.7-21).

The Phase IA simulations were made assuming a 6-mo. (180-day) test duration, which represents a mineback and auger schedule for Phase 1A of October 2, 1998. Measurements of the tracer concentrations from collected samples are to be conducted after that date. After the auger samples are collected and analyzed and mineback completed, the numerical predictions will be compared against the measured values, and the accuracy of the model configuration will be addressed.

Using the experimental injection rate of 10 mL/hr, the model-predicted tracer transport distances after 180 days are shown in the Table 10.7-15. (In all the simulations discussed in this section, the tracer is injected at a concentration of "1," and cited concentration values are relative to this initial value.)

The predicted distribution of the tracer is generally uniform in all directions (spherical) (Figure 10.7-22). Changes in saturation from the background (in situ) level are generally small. Table 10.7-16 shows the saturation at different distances from the injection point at 180 days for the base-case simulation. Note that the initial background saturation for this simulation is 35 percent, based on measured moisture contents of 14.0 ± 2.5 percent and a porosity of approximately 0.5.

Additional simulations were run to assess the effect of variability of the hydrogeologic parameters used in the modeling. In the event that the predictions from the base simulation do not agree with field measurements, these sensitivity analyses will be used to identify potential discrepancies between the model and the data.

10.7.2.6.1.1 Model Configuration and Parameter Set

The simulations of the Phase 1A field experiment were run in a model system that approximates the field configuration as closely as possible. The model system was a single borehole with a 0.10-m diameter embedded in a matrix of tuff in the Tac unit. The model domain for the simulations is 6 by 6 by 1.5 m. The borehole extended the full 1.5-m length of the z direction, and gravity acts in the $-x$ direction. The system configuration is shown in Figure 10.7-21. Both two-dimensional and three-dimensional simulations of the system were run. The two-dimensional system was a vertical plane, an x-y slice through the injection point at z = 0.75 m.

The model attempted to capture the experimental setup as closely as possible, including accurately capturing the actual configuration of the injection pad. The injection pad resided inside the borehole, centered at (0.0, 0.05, 0.75). The pad was a 0.05- by 0.05-m polypropylene pad, with material parameters shown in Table 10.7-17. Injection occurred at a single point in the center of the pad, consistent with the actual physical injection system. For Phase 1A, the injection point is located on the side of the borehole, 90° off vertical, as shown in Figure 10.7-21.

The boundary conditions for the simulation were no flow for the lateral sides ($y = \pm 3$ m) and the front face of the borehole ($z = 0$ m). The exposed face of the rock in the field ($z = 0$) was sealed to minimize evaporative losses resulting from the experimental tunnel. The top and bottom faces ($x = \pm 3$ m) of the model, as well as the back side ($z = 1.5$ m), were held at a fixed capillary pressure. Capillary pressures were chosen to match measured in situ saturation and capillary-pressure conditions. The use of capillary-pressure boundary conditions provide the most accurate means of capturing the real saturation distribution of the system. Although for a homogeneous rock matrix, capillary pressure can readily be converted to a constant saturation boundary, in a heterogeneous system, the saturation may vary drastically around the boundary, though the capillary pressure is relatively constant. In the vadose zone, the capillary pressure provides a much better representation of the steady-state condition of the system, and measured in situ saturations can be much better captured by a model.

As mentioned previously, the simulations were conducted to scope calculations for Phase 1A injection tests and to assess the viability of current models. In the simulations, the influence of a number of model parameters were assessed that can, at best, be only approximately known. These parameters include rock permeability, relative permeability, porosity, and in situ conditions (saturation). For these simulations, the constitutive relationships (relative permeability versus saturation and capillary pressure versus saturation) are characterized using the van Genuchten curve fit (van Genuchten 1980). The van Genuchten method fits the data points of permeability versus saturation measured in the laboratory to a two-parameter function. The two parameters are typically denoted as α and n. The α parameter represents the air entry pressure and is given here in units of 1/m. The n parameter controls the slope of the capillary-pressure saturation curve, and is nondimensional.

Table 10.7-17 and 10.7-18, respectively, list the different parameter combinations that were run in two-dimensional and three-dimensional representations of Phase 1A. The base case represents the current knowledge of the properties and conditions of the system. Using available data, a range for each parameter was simulated. The response of the system to various rates of injection of the tracer fluid was also assessed. Injection rates simulated were 1, 10, and 50 mL/hr. These injection rates were chosen to span the range of rates being considered for the various unsaturated zone transport test phases.

10.7.2.6.1.2 Modeling Results

10.7.2.6.1.2.1 Overview of Simulations

The large three-dimensional system size required relatively long simulation times. In an effort to minimize computer time and use the time most effectively, two-dimensional simulations were initially used. These simulations were used primarily as scoping calculations to identify the important simulations to run in three dimensions. As will be seen from the numerical results, the two-dimensional simulations showed shorter travel distances for the tracer than did the same simulation in three dimensions. The differences in tracer movement between two-dimensional and three-dimensional simulations at the same effective injection rate are primarily due to the effective volume of injection. The two-dimensional system is implicitly 1 m in depth, resulting in a lower, effective point-injection rate. Therefore, all quantitative predictions are made using values from the three-dimensional simulations. However, the two-dimensional simulations can be used to identify the relative response of one set of conditions versus another. The results indicate that trends in the two-dimensional simulations mirror those in the three-dimensional simulations.

A series of two-dimensional simulations (Table 10.7-17) were run to identify the relative importance of different parameters and injection scenarios. Figure 10.7-22, a graph of concentration versus distance from the borehole center, indicates that this system is relatively insensitive to many parameters but is quite sensitive to some. Three-dimensional simulations were chosen from the parameter sets to which the system was most sensitive. Six parameter combinations were chosen and are listed as numbers 1 through 6 in Table 10.7-18. From these simulations, both spatial and temporal concentration profiles will be presented. Although time-history concentration profiles are presented here, for this prediction, the concentration

distribution at 180 days after injection is of most interest, as this is the time when overcoring begins.

The most influential parameter, based on Figure 10.7-22, is the value of the van Genuchten power *n*. The values of both van Genuchten parameters, α and *n*, for the base case were taken from laboratory measurements made on cores from the Busted Butte site. Available data for the Tac unit were also collected from other sources (Flint 1998; Bodvarsson et al. 1997, Chapter 6; data tracking number LB970601233129.001) to reduce the uncertainty in these parameters. From these data, high and low values of α and *n* were chosen and tested for the range of responses for the combinations of those values. The value of *n* strongly controls the relative influence of capillary forces and gravity forces. Increasing *n* decreases the capillary forces, resulting in more gravity-driven flow.

Another parameter that clearly influenced the tracer transport was porosity. Although flow is only slightly affected by even relatively large changes in porosity, transport is more strongly affected. Porosity affects transport because the bulk velocity of the fluid is divided by the porosity to get the pore velocity. Two-dimensional and three-dimensional simulations were run with porosity increased and decreased by 10 to 15 percent. The higher porosity did not substantially change the tracer transport, but the lower porosity resulted in an observable increase in tracer concentrations.

A third factor affecting tracer transport was the injection rate. Prior to starting Phase 1A, simulations were run using different injection rates to help select a rate for Phase 1A that would allow the tracer to move sufficient distances to produce readily measurable distributions, but not so far that the tracer could not be fully recovered. Testing multiple injection rates is also intended to help select injection rates for Phase 2. An injection rate of 10 mL/hr. was chosen for Phase 1A. Therefore, the discussion here will focus on simulation results using 10 mL/hr. Results with other injection rates are presented later, for completeness. These other injection scenarios are also useful for making predictions for Phase 2.

10.7.2.6.1.2.2 Discussion of Simulations

Base Case–The base case parameters were taken from values measured in core samples collected from the unsaturated zone transport test site. These parameters are given in Tables 10.7-17 and 10.7-18. These simulations make predictions of the water and tracer distribution in Phase 1A.

Measurements from the core samples suggested that in situ saturations are in the range of 20 to 40 percent. In the simulations, initial capillary pressures of 5.6, 0.55, and 0.07 MPa correspond to saturations of 20 percent, 35 percent, and 60 percent, respectively. Comparing locally measured values and those reported for the Tac unit, the saturation of approximately 35 percent most closely represented the Phase 1A in situ conditions.

The saturation of the system changed only slightly over the 180-day period for the base case. After 180 days, at a distance of 0.125 m below the injection point, the saturation had increased by only 5 percent, whereas at 1 m, it had increased by only 0.7 percent. The tracer distributed relatively evenly in all directions, centered at the injection point. Some asymmetry was

introduced, however, by the presence of the borehole and by injecting 90° off vertical. Water and tracer had to move around the borehole to flow out in the negative horizontal direction where there was no impedance in the positive horizontal direction. Thus, flow and transport would be somewhat asymmetric.

The relatively even distribution of tracer and the lack of increase in saturation near the borehole indicate that this system is dominated by capillary forces over gravitational forces. Gravitationally dominated flows have a much more asymmetric character. It can be seen by these simulations that a 10 mL/hr injection rate should not introduce enough water to change the overall flow and transport processes that occur in the undisturbed system.

At 180 days, for the two-dimensional run, the approximate radii of the tracer at concentrations of 0.01 and 0.5 are 0.75 m and 0.30 m, respectively. Concentrations of 0.01 and 0.5 for the three-dimensional simulation are observed 0.85 and 0.45 m respectively, from the insertion point. Figure 10.7-23 plots the concentration as a function of distance from the borehole center at 180 days for the two-dimensional and three-dimensional systems. In the three-dimensional simulation, the concentration at a distance of 0.125 m is 0.96 percent of the injection concentration, whereas at 1 m the concentration is only 0.02 percent of the injection concentration.

Figure 10.7-24 plots the time history of concentration at a vertical distance of 0.25, 0.5, and 1 m below the center of the borehole for the three-dimensional simulation. Figure 10.7-24 shows that the tracer concentration at 180 days and a distance of 0.125 m has almost reached the injection concentration of 1.0, whereas the concentration at 0.5 m is still increasing rapidly.

Sensitivity Analyses–The accuracy of these numerical simulations will not be known until site measurements are made. It is known that the existing hydrologic and material properties are subject to some uncertainty. Furthermore, these properties will also vary somewhat within the hydrogeologic units, as reflected in variations in measured values from different cores. Using stochastic methods, these uncertainties can be incorporated directly into the calculations. Such predictions will be presented in Section 10.7.2.6.2. Within this deterministic modeling approach, an attempt has been made to account for and understand the influence of such uncertainty by assessing the sensitivity of the simulation to various system parameters. Figures 10.7-25 to 10.7-28 compare the results of these simulations. Figure 10.7-25 shows the effect of water injection on matrix saturation with time for the different sensitivity runs. Figure 10.7-26 plots concentration against distance from the borehole that the measurement was made, for the three-dimensional simulations from numbers 1 through 6. Figure 10.7-27 shows the same information plotted as concentration versus time, with each graph plotting a different distance from the borehole. Figure 10.7-28 compares the three-dimensional concentration versus time values against those for two-dimensional values.

If the predictions of the base case simulation do not match the measurements made in the field, it will be possible to use this series of simulations to identify parameter values that might be in error. From this knowledge, it will be possible to modify the model to improve accuracy.

Figure 10.7-25 shows that saturation for the Phase 1A model system is not really affected by any of the simulation scenarios. Further, the saturation is not particularly sensitive to many of the

parameters. The biggest changes are observed for conditions that increase the relative influence of gravity forces over the otherwise prevailing viscous forces. Both a higher α and the much higher injection rate produce relatively rapid and apparent increases in saturation. Otherwise, little change in saturation is observed.

At 180 days, Figure 10.7-26 demonstrates that, based on measurements at a distance of 0.25 m from the borehole, the tracer concentration distribution within short distances from injection is not sensitive to material properties and field conditions. At 0.25 m, there is negligible difference in concentrations among the different simulations. At a distance of 0.5 m, however, variations in system characteristics result in a 60 percent range of concentrations. Figure 10.7-26 shows that a system with intrinsic permeability an order of magnitude lower [Figure 10.7-26, case labeled k_base (s = 1) × 0.1] is indistinguishable from one with a value of van Genuchten power *n* that is at the low end of reported values [Figure 10.7-26, case labeled vG(a_high, n_low)]. Both of these cases are very similar to the base case. This fact indicates that transport in this system is not particularly sensitive to the values of *k* or α; errors in these values are not expected to demonstrably influence the accuracy of predictions in this system.

If the porosity is 0.20 instead of 0.35 an error of 15 percent), tracer concentration at 0.5 m and 180 days is expected to be 0.58, which differs by 25 percent from the base value. By 365 days, as seen in Figure 10.7-27, the difference in concentration has decreased somewhat but is still a substantial 10 percent. At shorter distances from the injection point, the low-porosity system is very close to the fastest transport system—one with high van Genuchten *n*—and leads the base case prediction by 10 percent concentration.

Figures 10.7-26 and 10.7-27 show that flow in the simulation that starts with an in situ saturation of 60 percent, instead of the estimated 35 percent, is actually dominated by gravity rather than capillarity. For this simulation, tracer is carried much farther down than in any of the lateral directions. At 180 days and a vertical distance of 0.5 m below the borehole, the relative concentrations are 0.62 and 0.36, respectively, in the 60 percent saturation case and the base case. The transport rate is substantially faster than the base case, as demonstrated by much higher concentrations at greater distances (Figure 10.7-26). At 0.5 m below the borehole, tracer concentrations resulting from decreased porosity and increased saturation are virtually indistinguishable but they differ significantly in the three-dimensional simulations. The lower-porosity transport is capillary driven, producing a relatively uniform tracer plume, whereas the high-saturation system produces a highly elongated tracer profile. It should be noted that saturation as high as 60 percent is not indicated by the reported capillary pressures measured in this system. The measured pressures indicate an in situ saturation in the vicinity of 25 to 35 percent.

The simulation results were most sensitive to the value of the van Genuchten parameter *n*. Reported values for this parameter ranged from 1.2 to 1.8, with the value from Busted Butte samples being 1.31. At a value of $n = 1.8$, transport was strongly gravity-dominated. The resulting concentration profiles were long vertically and thin laterally. This effect was much stronger than that observed for the high-saturation simulation. The resulting concentration at a vertical distance of 0.5 m was 0.88 [Figure 10.7-26, case labeled vG(a_high, n_high)], versus 0.04 at the same lateral distance. At a vertical distance of 0.5 m, tracer concentration was 60 percent higher than the base case and 30 percent higher than the high-saturation case

(Figure 10.7-26). Furthermore, by 180 days, this system had just about reached its steady-state distribution [Figure 10.7-27, case labeled vG(a_high, n_high)]), whereas even at 365 days, the other systems were continuing to change. If the actual value of *n* is significantly higher from the measured value for the Busted Butte core, it should be recognizable by the distinct, long and thin tracer distribution and by the high vertical concentrations.

The two-dimensional simulations Figure 10.7-22) indicated that the value of α appears to have little influence on the transient system as compared to *n*. As a result, three-dimensional simulations were only done for the two different variations in van Genuchten parameters presented.

Two-Dimensional Versus Three-Dimensional Simulations–The two-dimensional and three-dimensional simulations followed very much the same trends in tracer concentrations distribution. Figure 10.7-28 shows concentrations as a function of time, simulated for a distance of 0.5 m vertically below the borehole center for both simulations. For intermediate times, the numerical difference in concentration between equivalent two-dimensional and three-dimensional systems remains relatively constant. The differences were approximately 10 to 15 percent after approximately 90 days of injection. Concentration values between the two-dimensional runs and the three-dimensional runs were much closer at early times and began to converge at later times, as all concentrations approached the injection concentration.

10.7.2.6.1.3 Implications for Unsaturated Zone Transport Test Phase 2 Design and Analysis

The above simulations also act as a tool for selecting injection rates for the Phase 2 experiment, as well as to help understand how the used injection rates will influence what is observed at different monitoring locations. For example, after 180 days at an injection rate of 10 mL/hr., concentrations had increased to greater than 0.20 within a radius of 0.4 m from the injection point, but fell off rapidly beyond that and were below 1 percent beyond 0.9 m. Thus, a 2-m spacing between boreholes and injection points within boreholes would probably produce a system in which transport from each injection location was distinct from one another.

Faster injection rates, such as 50 mL/hr., can be expected to strongly modify natural flow patterns, producing gravity-dominated flow. At this injection rate, relative saturation concentrations 0.5 m from the injection point are predicted to rise to 0.80 in only 3 mo. Thus, boreholes or injection points spaced 1-m apart are expected to start influencing each other very early in the experiment.

On the other hand, an injection rate of 1 mL/hr. is seen to hardly influence the system at all. Even after 1 yr., concentrations do not rise to 0.05 at the 0.5-m distance. At such a low injection rate, it would take an extremely long time to analyze the system or identify important physical and chemical processes that are occurring. Further, at such slow rates of movement, it is difficult to distinguish differences in tracer movement that might arise due to geochemical effects.

Using different tracers at various injection rates and injection separation distances can provide an opportunity to differentiate controlling processes and material features.

10.7.2.6.1.4 Summary

This section describes the results of the blind predictions of the Phase 1A injection test being run in the Tac unit at Busted Butte. For these preliminary predictions, it was assumed that the matrix is homogeneous and unfractured. Using these assumptions and the described system configuration, expected tracer distribution can be predicted after 5 mo. of injection, at which time field test measurements will begin.

Based on the available information about Tac hydrologic properties and properties measured on samples taken from this site, a baseline numerical simulation was set up that ideally should reflect the actual system. From this simulation, it was predicted that a nonsorbing tracer will have traveled approximately 0.81 m (at a relative concentration of 0.01) over the 5-mo. injection period. It is also expected that the tracer will travel as far in the horizontal direction as the vertical. This uniform spread of the tracer indicates that the Tac system is more strongly controlled by capillary forces than by gravitational forces.

There is a possibility, however, that the baseline prediction is not correct. Errors in prediction may be caused by uncertainty in the value of many of the hydrologic and physical parameters. For each of these parameters, the sensitivity of flow and transport was analyzed. These analyses will allow the identification of aspects of the model system that might be in error if the baseline case predictions do not match the observations in the field. If, for example, the tracer has traveled much farther than predicted and predominantly in the vertical direction, then the gravitational forces are dominating. This outcome could be the result of a much higher in-situ saturation or an error in the van Genuchten parameter α. If the tracer plume has traveled farther than expected, but has retained a rather symmetric shape, the matrix porosity estimate may be in error. If the field data do not match the baseline case, alternative simulations will help to identify potential differences in the actual material characteristics and the properties used in the simulations.

The similarity in tracer distributions simulated by the two-dimensional and three-dimensional models suggests that if a correction was made to the injection rate, a two-dimensional simulation might be sufficient for predicting flow and transport in this homogeneous system. This suggestion does not imply that a two-dimensional simulation is adequate for more complex geology. In fact, all of the above predictions are based on a homogeneous rock matrix. If the matrix is not homogeneous, these predictions may be in error.

10.7.2.6.2 Stochastic Model

10.7.2.6.2.1 Introduction

This section documents the use of stochastic predictions made for Phase 1A of the Busted Butte testing program. The phase 1A test is located in the Calico Hills Formation vitrified tuff. At this time, there is a paucity of physical-properties information on the lithologies of that site, and the spatial variability of rock properties cannot be accurately depicted. Although this lack of information results in uncertain flow and transport predictions, this section attempts to use stochastic predictions for the site using current YMP databases. The input uncertainties from these databases are directly incorporated into flow predictions through a recently developed

stochastic model. This model requires that the first two statistical moments of rock properties be specified (i.e., saturated hydraulic conductivity and pore-size-distribution parameter α). The predictions represent the first two moments (expected value and standard deviation) of flow quantities, and these two moments are used to construct confidence intervals for the flow quantities. These flow moments serve as a basis for future stochastic predictions of tracer migration.

In the near future, field-test results of flow parameters, such as saturation, will be used to compare with the predicted confidence intervals of these same quantities. The confidence intervals are a measure of the uncertainty caused by incomplete knowledge of material heterogeneities. The field-test results are expected to fall within the predicted confidence intervals with a 95 percent probability. However, because the statistical and other input parameters are taken or estimated from the YMP databases, these parameters may or may not represent the rock properties at the test site, thereby introducing another level of uncertainty in the analyses. Some sensitivity analyses were performed on these parameters and it was found that the flow predictions are sensitive to the background saturation, the mean and variance of pore-size-distribution parameter α, the mean and variance of the logarithm of the saturated hydraulic conductivity, and the injection rate. This indicates the importance of refining these parameters.

10.7.2.6.2.2 Existing Stochastic Models

Although geologic media exhibit a high degree of spatial variability, rock properties, including fundamental parameters such as permeability and porosity, are usually observed only at a few locations due to the high cost associated with subsurface measurements. This combination of significant spatial heterogeneity with a relatively small number of observations leads to uncertainty about the values of material properties and, thus, to uncertainties in predicting flow and solute transport in such media. It has been recognized that the theory of stochastic processes provides a natural method for evaluating flow and transport uncertainties. In the last two decades, many stochastic theories were developed to study the effects of spatial variability on flow and transport in both saturated (e.g., Gelhar and Axness 1983; Dagan 1984, 1989; Winter et al. 1984; Neuman et al. 1987; Graham and McLaughlin 1989; Rubin 1990; Zhang and Neuman 1995, 1996a, 1996b) and unsaturated zones (e.g., Yeh et al. 1985a, 1985b; Mantoglou and Gelhar 1987; Mantoglou 1992; Russo 1993, 1995a, 1995b; Harter and Yeh 1996a, 1996b; Zhang and Winter 1998; Zhang et al. 1998). In the unsaturated zone, the problem is complicated by the fact that the flow equations are nonlinear because unsaturated hydraulic conductivity depends on pressure head.

Many of these existing theories involve a number of simplifying assumptions such as gravity-dominated flow (for steady-state cases) and slow-varying gradient (for transient flow), which restrict their applications of the existing theories. For example, the assumption of gravity-dominated flow excludes the presence of domain boundaries and the existence of a water table. In addition, a slow-varying gradient does not permit local injection or fast-varying recharge. Recently, Zhang (1999) developed a stochastic model for transient unsaturated flow in bounded domains free of the above-mentioned assumptions. The model results are the first two moments of the flow quantities, which may be used to construct confidence intervals for these quantities.

10.7.2.6.2.3 Phase 1A Modeling

A two-dimensional vertical stochastic flow model was developed for Phase 1A simulations. The input uncertainties from YMP databases were directly incorporated into flow predictions using the stochastic model of Zhang (1999). This model requires that the first two statistical moments for rock properties, such as saturated hydraulic conductivity and pore-size-distribution parameter α, be specified. Because the variabilities of porosity and residual water content are likely to be small compared to that of hydraulic conductivity, both are assumed to be known with certainty. To model unsaturated flow, the constitutive relationships between capillary pressure and unsaturated hydraulic conductivity and between capillary pressure and saturation must also be specified. Although the parameters characterizing these relationships are reported in the YMP databases (Schenker et al. 1995; Flint 1998), they are based on the van Genuchten model (van Genuchten 1980). Conversely, the current stochastic model of Zhang (1999) assumes the constitutive relationships to obey the Gardner-Russo model (Gardner 1958; Russo 1988). In this study, the Gardner-Russo parameter α is estimated from the reported van Genuchten parameters by matching the main features of the retention curves for these two models. The first row of Table 10.7-19 summarizes the relevant parameters that were taken or estimated from the YMP databases (Schenker et al. 1995; Flint 1998). No information was found with respect to the correlation lengths of the logarithm of the hydraulic conductivity and pore size distribution. The value of 20 cm is assumed for both of these parameters.

Baseline Case–In the baseline case, the model domain is 200 cm by 200 cm with material properties specified in Table 10.7-19. The steady-state simulations are run with the following boundaries conditions: specified flux at the top, a constant head of -488 cm at the bottom, and no-flow boundaries at the sides. The specified flux is consistent with the constant head at the bottom such that at steady-state (t = 0), the flow is gravity-dominated with a constant mean pressure head (h = -488 cm) and a constant saturation (S = 30 percent) through the whole domain. Specifically, it was assumed that initial mean saturation was 30 percent. The initial mean head was then computed to be -488 cm using the gravity-dominated condition and the specified characteristic curves. However, the head standard deviation is not uniform in such a bounded domain. The head standard deviation is zero at the bottom boundary, increases with distance from there, and reaches its maximum at the top. Figure 10.7-29 shows the confidence intervals for the pressure head h and the saturation S along horizontal (y) and vertical (z) lines passing through the injection point. The profiles are obtained by adding one standard deviation to the result and subtracting it from the mean quantity. This result corresponds to the 68 percent confidence intervals for the flow quantities. By comparing the vertical profiles for pressure head and saturation (Figure 10.7-29), it is seen that unlike the head standard deviation, the saturation standard deviation is not zero at the bottom boundary of constant head. This result happens because the uncertainty in saturation comes from the uncertainty in the soil parameter α, even though the head is specified with certainty there. The behaviors of these flow moments under steady-state conditions were discussed in detail by Zhang and Winter (1998).

An injection rate of Q = 1 mL/hr. starts at time t = 0, and lasts for 150 days. The actual injection at the field test site is a point in three dimensions, whereas the model is in two dimensions. In the model, the injection is approximated by a line source of length L_3 perpendicular to the two-dimensional domain. Therefore, the injection rate is Q/L_3 in two dimensions. In the baseline case, it was assumed that L_3 = 50 cm. It should be realized that the two-dimensional

representation is an approximation, and the accuracy of this approximation highly depends on the choice of L_3, which is, in turn, a strong function of injection rate. The two-dimensional predictions should yield the same general trend as the three-dimensional predictions, however.

Figure 10.7-30 shows the vertical and horizontal profiles of pressure head and saturation at 150 days. The impact of injection is the increase of pressure head and saturation in the vicinity of injection. The effects seem to be even in all directions near the injection. This is because the injection rate is overwhelmingly large compared to the background unsaturated hydraulic conductivity. The approximate radius of noticeable pressure head and saturation changes is 40 cm.

Other flow quantities (e.g., flux and velocity) and their associated uncertainties can be evaluated similarly. In principle, the concentration field and its associated uncertainty might be predicted based on this information. However, at this stage, there is no existing model for solute transport in a nonstationary, unsaturated flow field. The ongoing related research may provide a model during Phase 2 prediction.

Sensitivity Cases–Because the actual measurements at the site are too few to perform any statistical analysis, the statistical parameters are either taken or estimated from the relevant YMP databases. There is another level of uncertainty associated with inaccurate statistical and other parameters. Some sensitivity studies were performed below, using the stochastic model.

As mentioned before, there is no information regarding the correlation lengths of the log of the saturated hydraulic conductivity and the rock pore-size distribution parameter α. Case 2 investigates the effect of the correlation lengths by changing it from 20 to 30 cm. Figure 10.7-31 shows the corresponding profiles of pressure head and saturation. Comparing Figures 10.7-30 and 10.7-31 reveals that the prediction is insensitive to the correlation lengths.

In the base case, the model domain was set to be $L_1 = 200$ cm by $L_2 = 200$ cm. However, the size of the test site is much larger. In Case 3, the values used were $L_1 = 400$ cm and $L_2 = 400$ cm. It can be seen from Figure 10.7-32 that, in areas away from the boundaries and the injection point, the confidence intervals are quite insensitive to the domain size.

Cases 4 to 6 investigate the effect of background saturation by changing the specified flux at the top and the constant head at the bottom. Figures 10.7-33 to 10.7-35 show the cases for S_o = 20 percent, 40 percent, and 60 percent, respectively. It can be seen that the peak pressure head and saturation at the injection location decrease with the increase of the background saturation, but the impact radius increases with it. The width of confidence intervals for pressure head decreases with the increase of background saturation, whereas that for saturation profiles is quite insensitive to the background saturation.

In Case 7, the porosity is varied from $\phi = 0.5$ to 0.3 (Figure 10.7-36). A comparison of Figures 10.7-36 and 10.7-30 reveals that a lower porosity results in a slight increase in both the peak saturation and the radius of influence. However, the effect of porosity on solute transport is expected to be greater.

In Case 8, the mean of the log of the saturated hydraulic conductivity is increased from $\langle f \rangle$ = -6.258 to -4.258 (where f = ln K_s and K_s is in centimeters per second). As expected, a larger hydraulic conductivity renders a lower peak saturation and a larger radius of influence (Figure 10.7-37). In this case, the size of the domain was changed to 400 by 400 cm to accommodate the increase of saturation at large distance. In Case 9, the mean of α is varied from 0.01 to 0.02 cm, while the variance of α is kept the same. It can be seen that the mean head has increased significantly with a larger α for a given saturation (Figure 10.7-38). The confidence intervals are qualitatively similar to those in Figure 10.7-30, but the intervals are tighter in Figure 10.7-38. This difference occurs because the variability in α is actually reduced by keeping the same variance but with an increased mean value. As expected, the prediction—in particular, the width of confidence intervals—is sensitive to the variabilities in saturated hydraulic conductivity and pore size distribution α. In case 10 the variability of α is set to zero. It can be seen from Figure 10.7-39 that the width of the confidence intervals is significantly reduced in the absence of variability in α. In this case, the prediction uncertainties are entirely caused by the variability in saturated hydraulic conductivity K_s. In the baseline case, $Cv_\alpha = \sigma_\alpha/\langle\alpha\rangle = 0.3$, while $Cv_{Ks} = 3.27$. That is, the variability in saturated hydraulic conductivity K_s is much larger than that in pore size distribution α. Therefore, it may be concluded that the results are much more sensitive to the variability in α than to that in K_s.

As expected, the behaviors of pressure head and saturation profiles are very sensitive to the injection rate. In Case 11, the injection rate is Q = 10 mL/hr. (Figure 10.7-40). The peak saturation is much higher than that in Case 1 (Figure 10.7-30) and the radius of influence is also larger. This difference is even clearer from Case 12 (Figure 10.7-41), for which Q = 50 mL/hr.

In the last two cases, the mean saturated hydraulic conductivity $\langle K_s \rangle$ is taken to be 4.68 cm/hr. This value is based on some site-specific measurements and is three orders of magnitude larger than the value found in the YMP databases mentioned earlier. As for sensitivity runs, this value is taken as the mean and $Cv_{Ks} = \sigma_{Ks}/\langle K_s \rangle = 3.27$, as in the baseline case. Equivalently, $\langle f \rangle = 0.314$ and $\sigma_f^2 = 2.459$. In Case 13, Q = 10 mL/hr and L_3 = 50 cm (Figure 10.7-42); in Case 14, Q = 50 mL/hr. and L_3 = 100 cm (Figure 10.7-43). As found in Case 8 (Figure 10.7-37), a larger hydraulic conductivity renders a lower peak saturation and a larger radius of influence. It is expected that the tracer travels significantly faster in these cases.

10.7.2.6.2.4 Nonstationarity

The stochastic model of transient fluid flow in unsaturated, stationary (statistically homogeneous) media was modified to account for nonstationary features, such as distinct layers in the rock properties. First, the theory of Zhang (1999) was extended to generally nonstationary media, in which the statistical moments of the rock properties vary with location in the domain. This theoretical extension was then implemented into the stochastic model developed during fiscal year 1998 and tested with some two-dimensional examples. In these examples, some special cases of medium nonstationarity are considered: trending in the statistical moments of the log of saturated hydraulic conductivity and pore size distribution parameter; zones of different rock properties existing in the domain; and different layers present in the domain. The effect of an embedded thin layer on fluid flow for the Phase 1A test was investigated with this modified stochastic model. It was found that this thin layer acts like a barrier to fluid flow and

induces lateral fluid spreading. Only after accounting for this thin layer did the stochastic model produce fluid redistribution behaviors that are qualitatively similar to those observed by the mineback. A quantitative comparison can be made in fiscal year 2000 after the site-specific statistical parameters are obtained from the ongoing geostatistical analysis of the rock property measurements at the site. During fiscal year 1999, some issues for solute transport through nonstationary, unsaturated flow in heterogeneous media were also examined. It was found that the flow nonstationarity, under unsaturated conditions, significantly affects the behaviors of solute migration in such flow fields. The effect of the thin layer in the Phase 1A area on the migration of injected tracers can be assessed with site-specific statistical parameters.

10.7.2.6.2.5 Summary

This section describes the results of the stochastic predictions of the Phase 1A injection test at Busted Butte. Because a detailed description of the spatial variability of the rock properties at the site is lacking, a stochastic model for the Busted Butte field test site was developed to incorporate input parameter uncertainties into flow predictions during fiscal year 1998. This stochastic model requires the first two statistical moments of rock properties to be specified (i.e., saturated hydraulic conductivity and pore size distribution parameter). The results of the stochastic model are the first two moments (expected value and standard deviation) of the flow quantities of interest, and these two moments are used to construct confidence intervals of the flow quantities such as pressure head and saturation. The stochastic predictions of the Phase 1A injection test at Busted Butte were reported in the fiscal year 1998 milestone report. There, the statistical moments of the rock properties were taken or estimated from the YMP databases. Further, the rock in the modeling domain was assumed to be statistically homogeneous, implying that there is one type of material in the domain, from a statistical point of view. However, the plume obtained based on the mineback of the Phase 1A injection area revealed that a thin layer of different rock exists below the injection points, and this thin layer has significantly impacted the migration of injected fluid and tracers.

The combination of inherent spatial variability in rock properties and insufficient measurements for these properties leads to uncertainties in the input parameters for any model and, thus, to uncertainties in flow and transport predictions. These uncertainties were incorporated directly into the flow predictions through a stochastic model. The results from this model are the first two moments (expected value and standard deviation) of flow quantities, and these two moments can be used to construct confidence intervals for the flow quantities. The statistical moments of flow quantities served as a basis for future stochastic predictions of solute transport developed in fiscal year 1999.

Field-test results of flow quantities, such as pressure head and saturation, if available, can be used to compare these values with the predicted confidence intervals of the same quantities (Case 1). It is expected that the field-test results fall within the predicted confidence intervals with a 95 percent probability. However, statistical and other input parameters are taken or estimated from the YMP databases. These parameters may or may not represent the rock properties at the test site. Therefore, there is another level of uncertainty, and there have been some sensitivity analyses regarding these parameters. It is found that the flow predictions are sensitive to the background saturation, the mean and variance of pore-size-distribution parameter

α, the mean and variance of the log of the saturated hydraulic conductivity, and the injection rate. This sensitivity indicates that a refinement of these parameters is important.

10.7.2.6.3 Monte Carlo Flow and Transport Simulations

10.7.2.6.3.1 Introduction

To augment the results of the sensitivity analyses for the homogeneous-model calculations and the stochastic-model results, a series of Monte Carlo analyses were carried out in two dimensions. The goal of these simulations is to bracket the range of possible transport behavior that could arise due to variability in the hydrologic parameters. To accomplish this goal, a refined two-dimensional grid was generated (Figure 10.7-44) for performing flow and transport calculations. As in the homogeneous simulations using FEHM, the top and bottom boundaries of the model are held at constant capillary pressure. A single realization of the model consists of two simulations: a background simulation (without fluid injection at the borehole) to establish a steady-state flow condition followed by a simulation in which fluid of unit concentration (arbitrary concentration units) is injected for 180 days, the duration of the Phase 1A experiments. To simulate a heterogeneous system, the model is populated with a distribution of permeability values with a given mean value and an assumed correlation length. Figure 10.7-45 shows a permeability distribution chosen at random from the Case-1 simulations (see Table 10.7-20 for a summary of the different cases treated in the Monte Carlo simulations; detailed discussion of the individual cases considered is provided below). The contrasting permeability within the region of rock in which fluid is injected is expected to affect the flow and transport behavior by providing preferential pathways for fluid migration through the rock.

10.7.2.6.3.2 Methodology

The Monte Carlo approach considers the results of all individual realizations to be equally likely outcomes of the behavior of the system. Therefore, once a metric is chosen for quantifying the behavior of the system, statistical properties of the behavior of the system can be established. In the present study, the movement of a conservative solute injected with the fluid is used because the post-test measurements will consist of a mineback or selective drilling to collect rock and water samples and chemical analysis of tracer concentrations. The maximum penetration distance in all four directions away from the injection point is recorded for several different concentrations to establish the movement tracer direction. Then, for all 50 realizations in a given case, the mean values for these distances are recorded along with the standard deviation. The mean values establish the general location of the concentration front, whereas the standard deviation is a measure of uncertainty in the predictions of concentration-front movement due to rock mass heterogeneities.

10.7.2.6.3.3 Statistical Results

One advantage of the Monte Carlo approach is that an individual realization can be examined in detail to understand the behavior of the system, after which the multiple realizations can be used to quantify the uncertainty. The behavior of the flow and transport system is now examined (Figure 10.7-46) for the permeability distribution shown in Figure 10.7-45. The background saturation distribution shows little or no variability. This result is in contrast to the variability in

predicted fluid saturation for the cases in which permeability and van Genuchten α are correlated.

For that type of heterogeneous field, the fluid saturation is a strong function of α. The left-hand panels of Figure 10.7-46 show the movement of the saturation front into the rock mass for various times during the injection phase, and the right-hand panels are the concentrations of the conservative tracer for those same times. For this rock at this injection rate, there appears to be a relatively uniform migration of fluid and tracer away from the injection point in all directions, even upward. Under these conditions, the capillary-pressure driving forces are strong enough to pull water against the force of gravity. The presence of the borehole produces a shadow effect in which fluid must migrate around the borehole to reach the rock on the opposite side of the injection pad. Regarding the influence of heterogeneities, there is some tendency for fluid to be drawn preferentially into portions of the rock with higher capillary suction. The resulting saturation and concentration fronts exhibit an irregular pattern that tracks the heterogeneities. Nevertheless, the general patterns of movement of fluid and solute match fairly closely those of the homogeneous simulations.

The results of the statistical analyses of the Monte Carlo simulations are now examined. Table 10.7-21 shows the mean and standard-deviation values for the four cases summarized in Table 10.7-20. The y coordinate in the table represents the vertical direction, with negative values below the borehole injection point. The x coordinate is laterally away from the borehole, with positive values located on the side at which the injection pad is located. Results of Case 1, in which the permeability field is assumed to vary but the van Genuchten α value is constant, are examined first. The mean values for the minimum and maximum y values illustrate the degree to which the transport occurs uniformly upward and downward. Case 1 results show that capillary forces tend to pull water (and tracer) uniformly upward and downward with little or no tendency for downward migration due to gravity. The $C = 0.01$ iso-concentration value is meant to represent the migration of the front edge of the concentration plume; it travels approximately 40 to 45 cm in upward, downward, and outward (positive x) directions, on average. The injection point is located at approximately $x = 5$ cm and $y = 0$. The travel distance for the $C = 0.5$ iso-concentration value is more indicative of bulk plume movement, rather than the leading edge. This front travels approximately 30 cm in the three directions. The x_{min} values suggest a slight asymmetry in plume migration. This asymmetry is caused by the shadow effect due to the presence of the borehole, as described above.

The borehole causes the plume to have more difficulty migrating in the negative x direction. The standard deviation values reflect the uncertainty in the predicted migration of the plume caused by the heterogeneous permeability distribution. For Case 1, the uncertainty in the $C = 0.01$ iso-concentration value is about 8 to 12 cm (depending on direction), whereas for the $C = 0.5$ value, the uncertainty ranges from about 7 to 10 cm. Therefore, for Case 1, the heterogeneous permeability field (with no variability in α) adds considerable uncertainty to the predictions.

A comparison of Cases 1 and 2 (Table 10.7-21) illustrates the effect of imposing a correlation of permeability and α on the uncertainty of the predictions. The mean values for the spreading of the plume in all directions are very similar for the two cases, but the uncertainty due to heterogeneity is much smaller when α is assumed to be correlated with permeability (Case 2).

The correlation imposes a larger α for lower permeability, resulting in a larger capillary suction for rock regions with lower permeability. This result counteracts the tendency for fluid to travel preferentially through higher permeability rock, as in Case 1. Therefore, the spreading of tracer in Case 2 is more uniform, and the standard deviation values are consequently smaller. A series of hydrologic measurements on samples collected at the site will help to evaluate which situation is more likely for the Calico Hills tuffs.

Finally, the influence of correlation length on plume spreading can be examined by comparing Cases 2, 3, and 4, which assumed correlation lengths of 0.2, 0.1, and 0.5 m, respectively (Table 10.7-21). The mean behavior of the plumes is very insensitive to the correlation length. Regarding the uncertainty in plume prediction (as measured by the standard deviation), there is a trend toward larger uncertainty as the correlation length increases, as expected. Nevertheless, the uncertainty for these cases is much smaller than the correlation length itself. This result is caused by the assumed correlation of permeability and α for each of these cases, which, as mentioned above, largely negates the distribution of permeability values. Therefore, the largest uncertainty in these simulations appears to be the nature of the correlation (or lack thereof) of different hydrologic properties. Permeability and the van Genuchten α parameter were correlated in these simulations. Altman et al. (1996, Section 3.2.1.2, p. 28) also proposed correlations between permeability and porosity for Yucca Mountain tuffs. Therefore, the most important data that could be collected to further constrain these predictions are hydrologic property measurements on a much larger set of samples from the test block. A full suite of property measurements (porosity, permeability, and unsaturated hydrologic parameters) on samples collected from known locations in the block would be useful to set correlations between parameters and assign correlation lengths for future simulations.

10.7.2.6.3.4 Preliminary Interpretations

Critical evaluation and iterative improvement of the flow and transport conceptual and numerical models await the data collection, which is in progress. Focus over the past year has been on flow and transport field data collection, and this focus has now shifted to compiling, analyzing, and interpreting these data. Observations of the data collected so far, and the modeling of these data, lead to several key conclusions of relevance to performance assessment.

The modeling analyses for Phase 1A indicate that strong capillary forces in the rock matrix of the Tac unit are likely to modulate fracture flow from overlying units, thereby dampening pulses of infiltrating water and providing a large degree of contact between radionuclides and the rock matrix. Several modeling approaches, from deterministic to Monte Carlo to stochastic models, were used to simulate the Phase 1A experiments. All yielded similar qualitative results. From these results, it is concluded tentatively that the deterministic modeling approach taken at the site scale may be adequate. The parameterizations used to perform these calculations must be evaluated after data from the unsaturated zone transport test are available.

A particularly interesting observation from the Phase 1B experiment is that, even when injection occurs immediately adjacent to a fracture, water appears to be imbibed quickly into the surrounding matrix. The transport times observed immediately below the injection point were on the order of 30 days, whereas pure fracture flow would have resulted in travel times of minutes to hours at this flow rate. Site-scale models must be evaluated in light of this observation.

Models that predict significant fracture flow at percolation rates low enough for the matrix to transmit the flow may be inconsistent with the Phase 1B experiment.

10.7.2.7 Initial Phase 2 Model Predictions

10.7.2.7.1 Introduction

The predictions presented here were first presented to the YMP Management and Operating Contractor as a white paper on July 15, 1997, 8 days prior to the commencement of Phase 2 injections. This work constitutes the first "blind" prediction of the behavior of the Phase 2 block of the Busted Butte transport test prior to injection. This prediction is intended to test the modeling concepts and tools available to the integrated site-scale model and the validity of the abstractions of that model for performance assessment. The prediction uses parameters from available Yucca Mountain hydrologic and geochemical databases. At this stage, no model calibration has been performed. As data become available from the various phases of the unsaturated zone transport test, they will be incorporated into refined versions of the model. The new information will be used to make improved predictions. All simulation results presented in this section were data logged into the YMP Management and Operating Contractor file system to guarantee that all predictions herein preceded the injection of Phase 2 tracers.

The YMP-qualified computer code FEHM used in the site-scale unsaturated zone flow and transport model and its abstractions for performance assessment was also used in the development of the three-dimensional model presented in this section. Specifically, this code is used by the YMP for radionuclide migration predictions using the calibrated site-scale flow models (Bodvarsson et al. 1997, Chapter 19) and, therefore, is ideal for predicting unsaturated zone transport test results. Although detailed geologic and hydrologic property distributions in three dimensions are not yet available, it is anticipated that during the course of the testing, these data will become available. Three-dimensional effects will probably become important as data specific to the test block become available for the Phase 2 block. The model is, therefore, being developed in three dimensions at the outset to capture these effects and to anticipate the three-dimensional property database that will be collected for the test block.

In this section, conservative and reactive tracer breakthrough times are predicted for each sampling borehole for up to 1 yr. from the start time, the planned input time of the test results into the TSPA-LA.

10.7.2.7.2 Model Description

The Phase 2 test block at Busted Butte encompasses, from top to bottom, the lower section of the Topopah Spring Tuff vitrophyre (Tptpv2) and the hydrologic Calico Hills unit (Tptpv1 and Tac) (Figure 10.7-2). The first step in constructing a three-dimensional, finite-element model of the Phase 2 test was to build a finite-element mesh using the coordinates of the injection and collection boreholes. The file used in this work contains the surveyed local coordinates of the boreholes and the layered stratigraphy at the site.

Figure 10.7-2 shows a representation of the Phase 2 block with the boreholes represented as colored lines. The block is approximately 7 by 10 m deep by 10 m wide and contains 28 boreholes ranging from 7.5 to 10.0 m in length. The eight injection boreholes (shown in red)

all originate in the left rib of the Test Alcove (located in front of the figure). These boreholes are subparallel, distributed along two horizontal planes, and are perpendicular to the 12 collection boreholes (dark blue) coming from the right rib of the Main Adit (to the left of the vertical *yz* lane). The other boreholes (light blue) are dedicated to electrical-resistance tomography and ground-penetrating radar tomography.

For modeling purposes, the model domain was extended from +2 to +14 m in the *x*-direction, +60 to +72 m in the *y*-direction, and -8.2845 to +2.5015 m in the *z*-direction. These coordinates are consistent with the surveyed local coordinates and the stratigraphy of the block. Figure 10.7-47 shows a top view of the finite-element grid with the borehole locations.

In general, the mesh was refined between the injection and collection boreholes to accurately capture the migration of the tracers and heterogeneities at scales smaller than the layer thickness. In the *x*-direction, a grid spacing of 0.25 m was chosen close to the boreholes. In both the *x*- and *y*-directions, a coarse mesh spacing was chosen at the block boundaries, because no transport is expected at these locations. In the *y*-direction, a mesh spacing of 0.125 m was chosen close to boreholes. A slightly finer grid spacing was used in the *y*-direction than the *x*-direction to accurately capture the location of the injection points, which are spaced 0.61 m apart in the *y*-direction (10 injection points per injection borehole). In the *z*-direction, the stratigraphy is represented with six distinct layers: five layers to represent the hydrologic Calico Hills unit (Tac: three layers; Tptpv1: two layers), and one layer to represent Tptpv2. The discretization in the *z*-direction is dependent on the particular layer because some layers are thicker than others. The discretization ranged from 0.15 to 0.25 m. The entire model is composed of 128,570 nodes. Figures 10.7-48 and 10.7-49 show views of the grid from the Test Alcove and the Main Adit, respectively. Once the mesh was constructed, the next step was to assign properties to the model. Table 10.7-22 contains the property sets used in the different layers.

For this preliminary investigation, layers 1 through 3 were lumped together as one Calico Hills unit (Tac), layers 4 to 5 were assigned Tptpv1 properties, and layer 6 was assigned Tptpv2 properties. As additional data become available, layers 1 through 3 and 4 through 5 will all be treated as distinct layers. Porosity values were obtained from a few samples from the Busted Butte site. Permeabilities and van Genuchten relative-permeability parameters for the matrix were obtained from Flint (1998). Flint (1998) was chosen because this study represents the existing YMP database for the unsaturated zone and contained sufficient samples to generate statistics on the variability of key parameters, such as matrix permeability and matrix van Genuchten parameters. Ideally, a database of fracture properties for the Busted Butte site would be used, but these data are not yet available. Instead, fracture van Genuchten parameters were taken from the calibrated flow model of Bodvarsson et al. (1997, Chapter 6, p. 6-22), which data were obtained by fitting field data at the site scale. Although there is a great amount of uncertainty in fracture properties, this data set is considered to be a reasonable representation of YMP material properties applicable to Busted Butte.

For this preliminary investigation, and in view of the absence of data on fracture-matrix interactions in the Calico Hills, the equivalent-continuum model was used to model Phase 2. Isotropic and anisotropic dual-permeability models and stochastic models will be used in addition to the equivalent-continuum model, if necessary, to refine the predictions. The

equivalent-continuum model was also used to scope calculations done during test design and is currently being used to understand both Phases 1A and 1B.

Tracer breakthrough occurred in the 10 mL/hr. injection system of Phase 1B (borehole 6). Specifically, tracer was detected at the pad 35 days after injection. This result means the time of breakthrough occurred between 28 and 35 days in relation to the collection-pad schedule. To compare model predictions with test breakthrough times as defined by the appearance of fluorescein tracer on a collection pad, the tracer concentration must be known. For example, if the breakthrough time is defined to be when the normalized concentration reaches 0.5, then for Tptpv2, the equivalent-continuum model predicts a breakthrough at 47 days for a distance tracer travel of 28 cm (Figure 10.7-50). At a normalized concentration of 0.3, the model predicts breakthrough at 31 days for the same distance, which is close to the observed breakthrough time for borehole 6.

In the future, as data become available, it will be possible to use the Phase 1 results to improve on the current predictions of Phase 2. However, in the absence of appropriate data, the first phase of predictive modeling used the database listed in Table 10.7-22, with no attempt at calibration. The background flow conditions are obtained by setting a capillary pressure at the top and bottom boundaries and allowing the block to equilibrate to a steady-state saturation profile. A capillary pressure of 200 m of water was chosen, which is within the range of capillary-pressure measurements at Yucca Mountain (Altman et al. 1996). The capillary pressure was set so that a saturation of about 0.35 to 0.45 was obtained in the block. Moisture measurements and preliminary porosity data from test-block lithologies indicate that these saturation values are reasonable. Once the background conditions were set, the next step was to begin pumping and injecting tracer.

Three different pumping rates are to be used in Phase 2: (1) 1 mL/hr. (one upper borehole), (2) 10 mL/hr. (four lower boreholes), and (3) 50 mL/hr. (three upper boreholes). The 1 mL/hr rate is equivalent to an infiltration rate of approximately 30 mm/yr., which is well within the range of infiltration rates at Yucca Mountain. The predictions made (given below) show that during a 1-yr. test, the 1-mL/hr. pumping rate is not expected to transport any tracer to the sampling wells. Injection borehole 23 will be the only one that pumps at 1 mL/hr. The 10-mL/hr. injection rate is equivalent to an infiltration rate of approximately 380 mm/yr., which is slightly higher than the highest anticipated infiltration that will occur at Yucca Mountain. The lower injection boreholes, 24, 25, 26, and 27, will operate at 10 mL/hr. Finally, 50 mL/hr. is equivalent to an approximate infiltration rate of 1,550 mm/yr., which well exceeds the expected at Yucca Mountain even under wetter climate scenarios. The purpose of the 50-mL/hr. rate is to obtain enough separation in travel times between the conservative and reactive tracers so as to be visible and distinct in the field test. Boreholes 18, 20, and 21 will pump continuously at 50 mL/hr.

10.7.2.7.3 Predictions

The predictions below are borehole specific and can therefore be used to compare directly to test-block results. Table 10.7-23 shows the distance between the closest sampling point and the injection planes. Table 10.7-24 to 10.7-32 present the predicted tracer breakthroughs at each location.

For all predictions, three criteria for tracer-breakthrough times were used: (1) a 5 percent concentration limit, (2) a 50 percent concentration limit, and (3) the concentration after 1 yr. from the time of injection (the time of submittal of results for TSPA-LA). Note that it is assumed that the concentration of tracer in the injection fluid is unity, and tracers are continuously injected for the duration of the test.

A diffusion coefficient of 1×10^{-11} m^2/s was used for all tracers. Longitudinal and transverse dispersivities were zeroed out for this preliminary set of calculations. However, as with any finite-element model, some numerical dispersion is present. Due to the fine-mesh spacing and small time steps taken in these simulations, numerical dispersion is not expected to play a significant role in these simulations. A bulk-rock density of 2,580 kg/m was used for all layers. This parameter only affects the reactive-tracer breakthrough times. The values chosen are considered to be reasonable representations of Yucca Mountain properties, given the existing database. As more data become available, all of these parameters will be adjusted.

Conservative Tracers–First, the travel times for fluorescein, a conservative tracer, are predicted. Uniform properties for porosity, permeability, and van Genuchten model parameters within each of the six layers of the test block are assumed. In the last part of this section, the effect of heterogeneous property distributions is briefly examined. Figure 10.7-51 depicts a concentration plume for fluorescein after 1 yr.

Table 10.7-24 and 10.7-25 show the predicted breakthrough times of tracer for the upper and lower collection sampling points, respectively. As expected, sampling locations closer to the injection planes exhibit tracer breakthrough times that are earlier than those from more distant locations. As discussed in the next section, for simulations involving heterogeneous property distributions, this result may be modified due to preferential flow paths. The results indicate that tracer breakthrough is expected at several sampling locations within the first year and some are expected within the first month. Conservative-tracer breakthroughs could occur at earlier times than predicted by the equivalent-continuum model if the model assumptions are erroneous. Fracture flow through Tptpv2, for example, could result in faster travel times. Even so, an additional year of operation may be required to achieve transport distances on the order of the entire length of the block.

Nonconservative Tracers–Table 10.7-26 shows the distribution coefficients, K_d, for the reactive, nonconservative tracers determined by parallel laboratory studies and used in Phase 2 for the various units. The measurements are preliminary but provide a starting point for the modeling effort. Travel times for reactive tracers are extremely sensitive to these distribution coefficients and errors in these parameters strongly bias the results. One major deficiency in the preliminary measurements is that these results do not include reversible sorption, and equilibrium may not have been achieved when obtaining the distribution coefficients.

The next set of tables shows the predicted breakthroughs for the three reactive tracers: Li (Table 10.7-27 and 10.7-28), Mn (Table 10.7-29 and 10.7-30), and Ni or cobalt (Table 10.7-31 and 10.7-32).

The data indicate that Li does not sorb in Tptpv2, but mildly sorbs in Tac and Tptpv1. Although Li sorption in Tac is mild when compared to Mn and Ni or cobalt, the sorption has a large effect

on travel times over the time scale of interest. The Li only breaks through at locations that are extremely close to the injection boreholes (i.e., boreholes 16, 17, 46, 48, and 9).

Manganese is predicted to sorb much more strongly than Li. For this reason, Mn is only expected to breakthrough at boreholes 46 and 48 within 1 yr. Cobalt or Ni sorbs even more strongly than Mn, and is not expected to break through at any borehole during the test.

There are many caveats that could strongly affect the predicted travel times of the reactive tracers. First, the model is extremely sensitive to the values of K_d, and the current K_d measurements are uncertain at this time. A simple K_d may not be sufficient to model sorption of these tracers due to chemical heterogeneities and nonlinear reactions. More rigorous reactive transport models will be used in the future to check the linear-K_d assumption. Finally, these immobile reactive tracers may sorb onto colloids, thereby enhancing their mobility.

Heterogeneous System–A major assumption of the above modeling results is that properties are homogeneous within a layer. In this section, the effects of the heterogeneity of properties within the layers are explored. In these simulations, permeability values are distributed within each layer. It is assumed that the mean of the permeability is the same as the permeability values used in the homogeneous simulations. In each layer, a log-normal distribution of permeability with a ln (k) variance of 2.0 and a correlation length of 1 m in the x, y, and z directions is assumed. In the Calico Hills and Tptpv1 units, the van Genuchten parameter α_m has been shown to be correlated to matrix permeability (Altman et al. 1996, Section 3.2.1.3). This correlation is used to distribute α_m throughout the hydrologic Calico Hills or Tac and Tptpv1 units.

Figure 10.7-52 shows the background saturation profile and the saturation profile after 1 yr. of continuous injection. The saturation profile shows that the 50-mL/hr. boreholes have a strong effect on the saturation profile. There are two reasons for this effect: the first reason is that 50 mL/hr. is the high injection; the second reason is that the 50-mL/hr. boreholes inject into the lower section Topopah Spring basal vitrophyre (Tptpv2), which has a much lower matrix permeability than the hydrologic Calico Hills (Tac and Tptpv1). The 10 mL/hr. injections in the Tac unit do not have a large effect on the saturation profile. The simulations indicate that capillary action is an important process around the 10 mL/hr. injections, which is mostly due to the high matrix permeabilities in this unit.

Table 10.7-33 and 10.7-34 show the fluorescein breakthrough times for two realizations. As expected, heterogeneities do add some fluctuations in the previously observed trends; however, many trends still hold. Many more realizations are required to gauge the spread or uncertainty in travel times. The methodology for performing these Monte Carlo simulations now exists, and the next step will be to run many realizations.

10.7.2.7.4 Summary and Interpretation

This section presents a preliminary "blind" prediction of the behavior of the Phase 2 block of the unsaturated zone transport test at Busted Butte. The prediction was intended to test the current modeling concepts and tools available to the integrated site-scale model and their abstractions for performance assessment. This prediction uses parameters from the available Yucca Mountain hydrologic and geochemical databases. No calibrations were performed using information from

Busted Butte. As more data become available from the unsaturated zone transport test, they will be incorporated into refined versions of the models employed in these preliminary predictions.

Modeling results for fluorescein, a conservative tracer, indicate that tracer breakthrough is expected at several sampling locations within the first year of testing. For some sampling locations, tracer breakthrough is predicted for travel times of less than 1 mo. Tracer breakthroughs could be even quicker than predicted if the equivalent-continuum model assumption does not hold. Fracture flow through the Topopah Spring formation (Tptpv2) could result in faster travel times. The fracture parameters for the van Genuchten model are not known to a high degree of accuracy. Sensitivity analyses on these parameters will be performed to determine how sensitive travel times are to these fracture parameters. Another caveat in these modeling results is the effect of physical heterogeneities within each layer. Small-scale heterogeneities could result in preferential flow paths, which result in faster flow paths in some parts of the block and slow flow paths in other parts of the block. In the future, Monte Carlo simulations and more elegant stochastic techniques will be employed to attempt to capture the uncertainty in the travel times.

More uncertainty exists in the predicted travel times of the reactive tracers when compared with the conservative-tracer predictions. The strongly sorbing tracers Mn cobalt (or Ni) are not expected to break through within the first year of testing. Even weakly sorbing Li only reaches a few collection boreholes. Therefore, an additional year of operation may be required to achieve transport distances that reach more sampling points. At this stage, it is important to note that the model is extremely sensitive to the values of K_d used, which are preliminary. In addition, a linear-K_d model may not be sufficient to model sorption of these tracers due to chemical heterogeneities and nonlinear reactions. More rigorous reactive transport models will be used in the future to check the linear-K_d assumption. Finally, these immobile reactive tracers may sorb onto colloids, thereby enhancing their mobility.

10.7.2.8 Summary of the Implications for Performance Assessment

The unsaturated zone transport test is designed to provide information suitable for assessing the validity of flow and transport models used in the site characterization and performance assessment programs for Yucca Mountain. This section is a summary of the experimental and modeling work performed to date for the unsaturated zone transport test. Critical evaluation and iterative improvement of the flow and transport conceptual and numerical models awaits data collection, which is in progress. The first step in this process is reported here, namely the blind predictions of flow and transport behavior for both the Phase 1 and Phase 2 experiments.

Although flow and transport field data collected to date are limited, observations of the available data collected, and modeling of these data, lead to several key conclusions of relevance to performance assessment. The conclusions summarized below were categorized with respect to the particular field or modeling activity in this section.

- **Laboratory Measurements**–The collection of unsaturated hydrologic property data using the unsaturated flow apparatus provides data of particular relevance to flow and transport models because they are direct measurements under unsaturated conditions rather than indirect, model-derived parameters. Future laboratory data for unsaturated

zone rocks should be collected under unsaturated conditions to confirm or supplement the large existing database of hydrologic parameters. The Monte Carlo analyses (Section 10.7.2.6.3) indicate that the nature of the correlations between parameters such as permeability and the van Genuchten α parameter have a strong impact on the predictability of the flow and transport system. Therefore, a full suite of measurements of hydrologic and transport parameters should be made on each rock sample to constrain models and develop correlations.

- **Phase 1A and 1B Model Results**–The modeling analyses for Phase 1A indicate that strong capillary forces in the rock matrix of the Tac unit are likely to modulate fracture flow from overlying units, thereby dampening pulses of infiltrating water and providing a large degree of contact between radionuclides and the rock matrix. Several modeling approaches, from deterministic to Monte Carlo and stochastic models, were used to simulate the Phase 1A experiments (Sections 10.7.2.6 and 10.7.2.7). All yielded similar qualitative results. From this, it is tentatively concluded that the deterministic modeling approach taken at the site scale may be adequate. The parameterizations used to perform these calculations must be evaluated after data from the unsaturated zone transport test are available.

  A particularly interesting observation from the Phase 1B experiment is that, even when injection occurs immediately adjacent to a fracture, water appears to be imbibed quickly into the surrounding matrix. The transport times observed immediately below the injection point were on the order of 30 days, whereas pure fracture flow would have resulted in travel times of minutes to hours at this flow rate. Site-scale models must be evaluated in light of this observation. Models that predict significant fracture flow at percolation rates low enough for the matrix to transmit the flow may be inconsistent with the Phase 1B experiment.

- **Phase 2 Modeling**–Because field-test results from this part of the test are not available yet, it is difficult to draw conclusions relevant to the evaluation of models. Significant uncertainties uncovered by the modeling include the adequacy of continuum models in nonwelded units of high matrix permeability and the nature of the transition from fracture flow to matrix flow at contacts between hydrogeologic units. These are exactly the issues being studied within the unsaturated zone transport test. Therefore, preliminary answers to these important questions are anticipated in the next few months, after the first 9 months of test data have been collected and analyzed.

10.7.3 C-Holes Field and Laboratory Transport Testing

10.7.3.1 Introduction

To test conceptual saturated zone transport models for the YMP, two major cross-hole, forced-gradient tracer tests were conducted at the C-holes complex (UE-25 c#1, UE-25 c#2, and UE-25 c#3), located approximately 2 km southeast of the potential repository footprint (Figure 10.7-53) and completed in fractured volcanic tuffs. Groundwater flow at this location is thought to be toward the southeast, which puts the C-holes directly downgradient of the southern end of the potential repository. The tracer tests were conducted in two different saturated intervals that

differed in horizontal hydraulic conductivity by about two orders of magnitude: the lower Bullfrog Tuff, with a conductivity of 70 to 210 m/day (Geldon et al. 1997, Table 8), and the lower Prow Pass Tuff, with a conductivity of 0.8 to 1.0 m/day (Reimus et al. 1999, Table 3-2). Figure 10.7-54 depicts the hydrogeology of the C-holes and shows the packer locations of the tracer tests. It should be noted from Figure 10.7-54 that the vast majority of the water produced at the C-holes comes from a small number of relatively discrete zones, most of which are located in the lower portion of the Bullfrog Tuff. Both tracer tests were conducted between wells c#2 and c#3 (a linear distance of approximately 30 m); c#3 was the production well in the Bullfrog Tuff test and c#2 was the production well in the Prow Pass Tuff test.

The two tracer tests featured the simultaneous injection of several different tracers having different physical and chemical characteristics: (1) nonsorbing solutes with different diffusion coefficients (Br^- and pentafluorobenzoate), (2) a weakly-sorbing solute (Li^+), and (3) carboxylate-modified latex polystyrene microspheres, which served as colloidal tracers. Two additional tracer tests were conducted in the Bullfrog Tuff, each of which involved the injection of only a single nonsorbing solute (Reimus et al. 1999, Appendix C). These tests were conducted primarily to determine the optimal injection well for the test involving multiple tracers, and they will not be discussed further here except in the context of how they supported the interpretation of the multiple-tracer test in the Bullfrog Tuff. The simultaneous injection of multiple tracers offers significant advantages over single-tracer injections because it allows transport processes to be better distinguished and quantified by comparing the responses of the different tracers.

A series of laboratory studies were conducted in parallel with the field testing efforts to help support and constrain the interpretations of the field tests. These studies included (1) batch-sorption tests to characterize Li^+ sorption to C-holes tuffs, (2) diffusion-cell tests to determine matrix diffusion coefficients of tracers used in the field, and (3) dynamic transport tests to study tracer transport in fractured and crushed tuffs under more controlled conditions than in the field. The batch-sorption tests and dynamic transport tests provided estimates of Li sorption parameters for comparison with sorption parameters derived from the field tests. Such comparisons are important because they indicate whether laboratory-derived radionuclide sorption parameters can be used defensibly in field-scale predictive calculations.

10.7.3.2 Summary of Field Test Results and Interpretations

Figure 10.7-55 shows the normalized tracer responses (concentrations divided by injection masses) in the multiple tracer test in the Bullfrog Tuff. Figure 10.7-56 shows the normalized tracer responses in the Prow Pass Tuff multiple-tracer test. It should be noted that the concentrations and times for the Bullfrog Tuff test in Figure 10.7-55 are shown on log-log axes. The test conditions and tracer injection masses in the two tests are described in detail in Reimus et al. (1999, Chapter 5 [Prow Pass Tuff] and Appendix C [Bullfrog Tuff]). Both tests featured partial recirculation of the water produced from the pumped well; about 3.5 percent recirculation in the Bullfrog Tuff and about 30 percent recirculation in the Prow Pass Tuff.

The most striking feature of the tracer breakthrough curves in the Bullfrog Tuff test (Figure 10.7-55) is their bimodal (double-peaked) behavior. This behavior is attributed to a relatively small fraction (about 13 percent) of the tracer solution exiting the injection borehole in

short residence time pathways in the upper half of the injection interval, whereas the remaining tracer mass exited the borehole primarily in pathways of longer travel time deeper in the interval. The greater density of the tracer solution (injected just below the top packer) relative to the groundwater would have caused it to preferentially sink to the bottom of the relatively long (and unmixed) injection interval. Figure 10.7-57 shows that there was only one pentafluorobenzoic acid peak in a tracer test conducted earlier in the Bullfrog Tuff (same interval, same flow rates). The only difference between the two tests was that about 1,000 L of tracer solution were injected in the first test, whereas about 12,000 L were injected in the second test. The packed-off injection interval volume was about 4,300 L, so in the first test, only about one-fourth of an interval volume was injected. Therefore, it is likely that only flow pathways in the lower part of the injection interval conducted tracers out of the borehole because of the tendency of the tracers to sink. In contrast, in the second test, approximately three interval volumes of tracer solution were injected, so the volume between the packers should have eventually filled with tracer solution, and tracers would have thus accessed flow pathways throughout the entire length of the interval. The flow survey information depicted in Figure 10.7-54 suggests that the zone of highest flow in the injection well (c#2) occurred in the upper half of the injection interval.

The pentafluorobenzoic acid and bromide responses in both the Bullfrog Tuff tracer test and the Prow Pass Tuff test show clear qualitative evidence of matrix diffusion. The peak normalized pentafluorobenzoic acid concentrations are higher than the peak normalized bromide concentrations in both tests, and the second bromide peak in the Bullfrog Tuff test is somewhat delayed relative to the pentafluorobenzoic acid with a tail that appears to cross over the pentafluorobenzoic acid at long times. These features are all consistent with greater matrix diffusion of the more diffusive tracer (bromide) relative to the less diffusive tracer (pentafluorobenzoic acid). Another qualitative indication of matrix diffusion in the Prow Pass Tuff test is the jump in solute tracer concentrations after each of the three major flow interruptions during the tailing portion of the test, which indicates diffusion of tracers out of the matrix and into fractures during the interruptions. Thus, the two tests support the concept of dual-porosity behavior in the saturated, fractured system at the C-holes (i.e., flow occurs primarily in fractures, but there is a great deal of stagnant water available for tracer/contaminant storage in the near-stagnant water of the rock matrix). The Li responses in the two tests show obvious attenuation relative to the nonsorbing tracers, which is indicative of Li sorption. The attenuation in the Prow Pass Tuff test and in the first peak of the Bullfrog Tuff test is almost exclusively a lowering of the peak concentration with little or no delay in arrival time. This behavior is consistent with Li sorption in the matrix (after diffusion into the matrix). The attenuation in the second peak of the Bullfrog Tuff test involves a clear time delay along with a dramatic lowering of concentration. This behavior is consistent with sorption in both the fracture flow pathways and the matrix.

The carboxylate-modified latex microsphere responses in the two tests indicate that the microspheres were significantly attenuated relative to the solute tracers in both tests, with the attenuation relative to solutes being greater in the Prow Pass Tuff test. The microsphere responses in the Prow Pass Tuff test are shown more clearly on a plot of log-normalized concentration versus time in Figure 10.7-58. The responses in both tests (including both sizes of spheres in the Prow Pass test) are characterized by truncated tails relative to the solutes but with measurable concentrations that persist throughout the tests. This behavior is consistent with filtration followed by some sort of nonlinear or stochastic resuspension of the microspheres.

It should be noted that the concentration of microspheres in the injection solution was well below any stability limit. All of the injected microspheres were obtained from the manufacturer in less than 1 L of solution. They were stored at this concentration for several weeks before the injection. For the injection, the microspheres were diluted by a factor of about 5,000. In regard to the destabilizing effect of the high concentration of solute tracers in the injection solution, several samples were taken of the injection solution, and microsphere aggregation in these samples was minimal, even after sitting for more than a week. Thus it is very unlikely that microsphere stability limits were exceeded either due to microsphere concentrations being too high or solute concentrations being too high.

The tracer responses in both tests were interpreted by simultaneously fitting the breakthrough curves using a semianalytical, dual-porosity transport model, RELAP, described in detail in Reimus et al. (1999, Appendix D). RELAP is part of the Reactive Transport Application software package. It solves Laplace-domain "transfer functions," which describe tracer injection, wellbore mixing, recirculation, and tracer transport in a dual-porosity system. The equations used for transport in the flow system can take various forms depending on whether (1) the flow is assumed to be linear or radial, (2) the matrix is assumed to be finite or semi-infinite, or (3) sorption is assumed to be equilibrium or rate limited (Reimus et al. 1999, Appendix D).

The interpretation strategy in the Bullfrog Tuff test was to (1) fit the first tracer peaks, (2) subtract the fitted responses from the complete breakthrough curve(s), and (3) fit the resulting residual second peak(s) with a second set of transport parameters. In the Prow Pass Tuff test, a single set of transport parameters was sufficient to fit the single-modal tracer responses. The sequence of fitting the different tracer responses in each test was as follows:

- The Br^- and pentafluorobenzoic acid responses were fit simultaneously using RELAP (CRWMS M&O 2000, Section 3, Item 3) and assuming that both tracers experienced the same mean residence time and longitudinal dispersivity (because they were injected simultaneously), but they had diffusion coefficients that differed by a factor of three. Both tracers were assumed to be conservative (nonsorbing).

- The Li response was fit by assuming that the Li experienced the same mean residence time and dispersivity as the bromide and pentafluorobenzoic acid, but it had a diffusion coefficient two-thirds that of bromide and twice that of pentafluorobenzoic acid. The only parameters adjusted to obtain a fit to the Li data were sorption parameters.

- The microsphere responses were fitted assuming the same mean residence times and dispersion coefficients as the solute tracers, but without any diffusion into the matrix (diffusion coefficient of zero). The rate-limited sorption features of RELAP were used to adjust filtration and resuspension rate constants until a fit to the data was obtained.

- To simulate the flow interruptions in the Prow Pass Tuff tracer test, a numerical code called RETRAN, also part of the Reactive Transport Application software package, was used. Unlike RELAP, RETRAN is capable of simulating nonlinear behavior and flow transients (Laplace transforms are limited to linear functions and steady-state flow behavior). RELAP fits were extended beyond the flow interruptions by using the

transport parameters obtained from RELAP (up until the time of the flow interruptions) as inputs to RETRAN. RETRAN was also used to simulate the nonlinear sorption behavior of Li.

The model fits to the tracer breakthrough curves are not shown graphically here; graphical representations of the fits can be found in Reimus et al. (1999, Chapter 5, Appendix C). All transport parameters obtained from the fits, with the exception of Li sorption parameters, are listed in Table 10.7-35 and 10.7-36 for the Bullfrog and Prow Pass tuff tests, respectively. It should be noted that there are separate estimates of mean residence times and dispersivities depending on whether "radial" or "linear" flow is assumed (the two possible extremes for flow to a pumped well in a confined aquifer). These values reflect the parameter uncertainty associated with the true nature of the flow field. Figure 10.7-59 shows the range of longitudinal dispersivities deduced from the C-holes tracer tests on a plot of dispersivity versus length scale taken from Neuman (1990). It is apparent that the C-holes longitudinal dispersivities (the darkened box) are in relatively good agreement with Neuman's published relationship of dispersivity versus length scale. Note that the lower end of the range of length scales associated with the darkened box corresponds to the interwell separation in the tracer tests, and the upper end corresponds to the test interval thickness (used as an upper bound for the transport distance). The effective flow porosities listed in Table 10.7-35 and 10.7-36 were calculated from the deduced mean tracer residence times using the following expression (Reimus et al. 1999, Chapter 5, p. 5-17 Equation 5.7), which assumes radial convergent flow in a homogeneous, isotropic medium:

$$\eta = \frac{Q\tau}{\pi R^2 L} \qquad \text{(Eq. 10.7-1)}$$

where

η = flow porosity
Q = production rate (cubic meters per hour)
τ = mean tracer residence time (hours)
R = distance between boreholes (meters)
L = formation thickness (meters)

The "mass fraction" of tracer participating in each test (listed in Table 10.7-35 and 10.7-37) was an adjustable parameter used to account for unrecoverable loss of tracer mass during the tests. Such mass loss is possible given the open, heterogeneous nature of the system and the density of the tracer solution (which may have resulted in tracers "sinking" out of the zone of influence of the pump). Finite but slow flow through the matrix may also have resulted in some tracer being pushed out of the injection well into the matrix (rather than fractures), where it would have been effectively lost from the fracture flow system.

The parameter describing matrix diffusion in Table 10.7-35 and 10.7-37 is actually a lumped parameter

$$\frac{\phi}{b}\sqrt{D_m} \qquad \text{(Eq. 10.7-2)}$$

consisting of the matrix porosity, ϕ, the fracture half-aperture, b, and the matrix diffusion coefficient, D_m. These parameters cannot be easily separated because it is not possible to obtain independent estimates of their in situ values. It should be noted that the simultaneous fits to the nonsorbing tracer responses were not significantly improved by assuming a finite matrix (versus an infinite matrix) or by assuming multiple pathways with different matrix diffusion mass transfer coefficients (versus a single mass transfer coefficient).

Lithium sorption parameters deduced from the field tracer tests are listed in Table 10.7-37. Laboratory-derived Li sorption parameters (Section 10.7.3.2) are also listed in Table 10.7-37 to allow a comparison between field-derived and laboratory-derived sorption data. Table 10.7-37 indicates that Li sorption in the field was always approximately equal to or greater than the sorption measured in the laboratory. It should be noted that although Table 10.7-37 lists only linear, equilibrium sorption parameters (K_d values), the first Li peak in the Bullfrog Tuff tracer test was actually a better fit assuming either rate-limited sorption or nonlinear sorption. A discussion of these and other alternative approaches to fitting the early Li peak in the Bullfrog Tuff test is provided by Reimus et al. (1999, Appendix C). For the second Li peak in the Bullfrog Tuff test and the only peak in the Prow Pass test, the assumption of linear, equilibrium sorption provided very good fits to the data.

The microsphere fitting procedure in the Bullfrog Tuff test is described in detail in Reimus et al. (1999, Appendix C, Section C.5). Two sets of pathways were assumed, each having a unique linear filtration rate constant. However, to fit the long tailing behavior, it was necessary to assume that there were multiple resuspension rate constants for different mass fractions of the spheres within each pathway. To match the low recovery of the spheres, a relatively large fraction of mass in each pathway was assumed to be irreversibly filtered (a resuspension rate constant of zero). The filtration rate constants resulting in a good fit to the complete microsphere response are given in Table 10.7-35. In the Prow Pass Tuff test, the microsphere responses were fit assuming only linear forward filtration with no resuspension (Reimus et al. 1999, Chapter 5, p. 5.10, Figure 5-11). The resulting filtration rate constants are provided in Table 10.7-36. The fits provided a good match to the data until the tails of the breakthrough curves began to flatten out. The long flat tails could probably be explained by multiple resuspension rate constants, but this was not attempted.

10.7.3.3 Summary of Laboratory Test Results and Interpretations

10.7.3.3.1 Batch-Sorption Testing of Lithium Ion

Batch-sorption tests were conducted to determine equilibrium sorption isotherms of Li ion to seven different C-holes tuff lithologies over a three-order-of-magnitude range of Li solution concentrations that effectively spanned the range of concentrations in field tests (about 1 to 1,000 mg/L). The resulting best-fitting Langmuir isotherms for each lithology are shown in Figure 10.7-60 (without the fitted data, which would excessively clutter the plot) (Reimus et al. 1999, Chapter 6, p. 6.4). In most cases, a Langmuir isotherm offered a better fit to the data than either a linear or Freundlich isotherm because of the tendency of the Langmuir isotherm to plateau at higher concentrations, suggesting a saturation of the surface with Li. These tests and their results are described in more detail in Reimus et al. (1999, Chapter 6).

In conjunction with the batch-sorption tests, all tuffs tested were analyzed quantitatively for major mineral phases by quantitative X-ray diffraction. Cation exchange capacity experiments were also conducted on each rock. Not surprisingly, the tuffs that had the highest Li sorption capacity (bedded Prow Pass and lower Bullfrog tuffs) also had the highest percentages of smectite clays and/or zeolites and the highest cation exchange capacities (Reimus et al. 1999, Chapter 6). The primary cations exchanging with the Li in the cation exchange capacity tests were Na and Ca.

10.7.3.3.2 Diffusion Cell Testing

Laboratory diffusion cell tests involved measuring the diffusion coefficients of the nonsorbing tracers used in field tests in intact blocks of saturated matrix material. The experimental apparatus and details of the test interpretations are presented in Reimus et al. (1999, Chapter 8). The diffusion coefficients of pentafluorobenzoic acid and bromide were measured in five different tuff lithologies, listed in Table 10.7-38. Each lithology could have been involved in the field tests. Table 10.7-38 also gives the measured matrix porosities and tuff permeabilities. It is evident that the diffusion coefficients are positively correlated with both of these rock properties, although the correlation is better with permeability. The two diffusion cell tests conducted in the lower Prow Pass Tuff indicate very good experimental reproducibility using two different pieces of core from this lithological unit.

The ratio of bromide to pentafluorobenzoic acid diffusion coefficients in the diffusion cell tests was consistently about 3:1, regardless of the absolute values of the diffusion coefficients. This ratio was used as a constraint when simultaneously fitting the responses of these tracers in the field tests.

10.7.3.3.3 Flowing Transport Experiments in Crushed and Fractured Tuffs

Two types of flowing transport experiments were conducted to support field test: (1) crushed-tuff column experiments, and (2) fractured-core column experiments. In the former, LiBr solutions were eluted through columns of the same crushed central Bullfrog Tuff at different concentrations and different flow rates. These tests showed that Li sorption under flowing conditions was in very good agreement with batch-sorption measurements, and that Li sorption kinetics were rapid enough that Li sorption in the field should be well approximated by assuming local equilibrium between the solution and solid phases. More details of the crushed-tuff column experiments and their results are given in Reimus et al. (1999, Chapter 7). The tests were interpreted using the RELAP and RETRAN components of the Reactive Transport Application software package.

The fractured core experiments offered more realistic laboratory simulations of the field tracer tests. These tests were conducted in induced (unnatural) fractures in both the upper and central Prow Pass Tuff lithologies (16 to 17 cm long). Experimental methods are described in Reimus et al. (1999, Chapter 7, Section 7.2). Two different sets of tests were conducted in each fracture: (1) multiple tests at different flow rates using only iodide as a tracer, and (2) tests involving the simultaneous injection of Li, bromide, and pentafluorobenzoic acid (analogous to the field experiments). The first set of tests consistently exhibited higher peak concentrations of iodide at higher flow rates, consistent with matrix diffusion (more iodide would be expected to diffuse

into the matrix as residence times increase). Simultaneous RELAP fits of these data sets allowed estimates of matrix diffusion parameters in the columns. The second test set exhibited behavior that was very consistent with the field observations; that is, peak normalized pentafluorobenzoic acid concentrations were greater than peak Br concentrations, and Li concentrations were lower yet but not significantly attenuated in time (Reimus et al. 1999, Chapter 7, pp. 7.8 to 7.11). All these features are consistent with dual-porosity transport behavior in the columns. These tests were interpreted using the same techniques (Reactive Transport Application) as the field tests involving multiple tracers. For brevity, the test results and interpretations are not presented here (Reimus et al. 1999, Chapter 7). In general, apparent matrix diffusion mass transfer coefficients were greater in the laboratory than in the field, and Li sorption parameters in the laboratory were smaller than in the field.

10.7.3.4 Conclusions from C-Holes Field and Laboratory Testing

The C-holes field and laboratory tests resulted in the following conclusions relevant to performance assessments of the potential Yucca Mountain repository.

- The responses of nonsorbing tracers in all field and laboratory tracer tests in fractured rocks are consistent with matrix diffusion behavior. This result supports the use of a dual-porosity conceptual model to describe radionuclide transport through the saturated, fractured volcanic rocks near Yucca Mountain.

- Sorption of Li ion in the field was greater than or equal to its measured sorption in the laboratory (see Table 10.7-37 for a comparison of laboratory-derived and field-derived sorption parameters). Although Li does not behave identically to any radionuclide, this result suggests that the use of laboratory-derived radionuclide sorption parameters in field-scale transport predictions is defensible and may even be conservative.

- The effective flow porosities deduced from the field tests were less than 1 percent for all tracer responses except for the second tracer peak(s) in the Bullfrog Tuff test, for which the deduced flow porosity was several percent (even after apportioning 75 percent of the production flow to the first tracer peak). However, if the second peak was really the result of only 10 percent of the production flow, then the effective flow porosity would be only about 1 percent, and if it were only 5 percent of the production flow, then the flow porosity would be less than 1 percent. Such small percentages of production flow resulting in the second tracer response(s) are entirely possible in a heterogeneous fracture flow system such as that at the C-holes.

- The longitudinal dispersivities deduced from the field-scale experiments are consistent with published relationships of dispersivity versus length scale (e.g., Figure 10.7-59).

- Matrix diffusion mass transfer coefficients in the field experiments were less than in the laboratory experiments, and they generally decreased as tracer residence times increased. There are several possible explanations for this behavior, including (1) larger average fracture apertures as length (and time) scales increase, (2) an increasingly greater influence of true matrix diffusion, as opposed to diffusion into stagnant free water, as test durations increase, and/or (3) a greater tendency to encounter diffusion

barriers in longer duration tests where characteristic diffusion distances are greater. It should be noted that all tracer responses could be adequately fitted assuming a single matrix diffusion mass transfer rate for each tracer peak.

INTENTIONALLY LEFT BLANK

10.8 SUMMARY OF FACTORS AFFECTING RADIONUCLIDE TRANSPORT

Section 10 addresses factors affecting radionuclide transport in the far field under ambient conditions. Radionuclide transport experiments have been conducted in the laboratory to determine solubility concentration limits and to determine K_d values under batch and dynamic transport conditions. Results of experiments have been tested under field conditions at the Busted Butte unsaturated zone transport test site and, for the saturated zone, at the C-holes complex.

Retardation of radionuclides may take place via sorption onto fracture-filling minerals or zeolites in the matrix. Ion exchange and surface complexation are both sorptive mechanisms. Matrix diffusion also plays a role in retarding radionuclides such as Np and U. Organic complexes may enhance sorption, but organics are formed in low concentration in Yucca Mountain groundwaters.

Colloids in groundwater have the potential to lower retardation of radionuclides by transporting them. Colloidal transport of Pu is an important mechanism to include in performance assessment calculations.

INTENTIONALLY LEFT BLANK

10.9 REFERENCES

10.9.1 Documents Cited

Allard, B. 1982. *Sorption of Actinides in Granitic Rock.* KBS TR 82-21. Goteborg, Sweden: Chalmers University of Technology. TIC: 205892.

Altman, S.J.; Arnold, B.W.; Barnard, R.W.; Barr, G.E.; Ho, C.K.; McKenna, S.A.; and Eaton, R.R. 1996. *Flow Calculations for Yucca Mountain Groundwater Travel Time (GWTT-95).* SAND96-0819. Albuquerque, New Mexico: Sandia National Laboratories. ACC: MOL.19961209.0152.

Ames, L.L., Jr. 1960: "The Cation Sieve Properties of Clinoptilolite." *American Mineralogist, 45,* 689-700. Washington, D.C.: Mineralogical Society of America. TIC: 235507.

Ames, L.L., Jr.; McGarrah, J.E.; and Walker, B.A. 1983. "Sorption of Trace Constituents from Aqueous Solutions onto Secondary Minerals: 1. Uranium." *Clays and Clay Minerals, 31,* (5), 321-334. Long Island City, New York: Pergamon Press. TIC: 238914.

Andersson, K. 1988. *SKI Project-90: Chemical Data.* SKI Technical Report 91:21. Stockholm, Sweden: Swedish Nuclear Power Inspectorate. TIC: 242643.

Baeyens, B. and Bradbury, M.H. 1995a. *A Quantitative Mechanistic Description of Ni, Zn and Ca Sorption on Na-Montmorillonite, Part I: Physico-Chemical Characterization and Titration Measurements.* PSI Bericht 95-10. Villigen, Switzerland: Paul Scherrer Institute. TIC: 237271.

Baeyens, B. and Bradbury, M.H. 1995b. *A Quantitative Mechanistic Description of Ni, Zn and Ca Sorption on Na-Montmorillonite, Part II: Sorption Measurements.* PSI Bericht 95-11. Villigen, Switzerland: Paul Scherrer Institute. TIC: 237272.

Balistrieri, L.S. and Chao, T.T. 1987. "Selenium Adsorption by Goethite." *Soil Science Society of America Journal, 51,* (5), 1145-1151. Madison, Wisconsin: Soil Science Society of America. TIC: 223172.

Balistrieri, L.S. and Murray, J.W. 1982. "The Adsorption of Cu, Pb, Zn, and Cd on Goethite from Major Ion Seawater." *Geochimica et Cosmochimica Acta, 46,* 1253-1265. New York, New York: Pergamon Press. TIC: 238913.

Barnard, R.W.; Wilson, M.L.; Dockery, H.A.; Gauthier, J.H.; Kaplan, P.G.; Eaton, R.R.; Bingham, F.W.; and Robey, T.H. 1992. *TSPA 1991: An Initial Total-System Performance Assessment for Yucca Mountain.* SAND91-2795. Albuquerque, New Mexico: Sandia National Laboratories. ACC: NNA.19920630.0033.

Barrer, R.M. and Townsend, R.P. 1976. "Transition Metal Ion Exchange in Zeolites, Part 1.– Thermodynamics of Exchange of Hydrated Mn^{2+}, Co^{2+}, Ni^{2+}, Cu^{2+} and Zn^{2+} Ions in Ammonium Mordenite." *Journal of the Chemical Society, Faraday Transactions 1, 72,* 661-673. London, England: Royal Society of Chemistry. TIC: 239144.

Bar-Yosef, B. and Meek, D. 1987. "Selenium Sorption by Kaolinite and Montmorillonite." *Soil Science, 144,* (1), 11-19. Philadelphia, Pennsylvania: Lippincott Williams & Wilkins. TIC: 237321.

Bates, J.K.; Bradley, J.P.; Teetsov, A.; Bradley, C.R.; and Buchholtz ten Brink, M. 1992. "Colloid Formation During Waste Form Reaction: Implications for Nuclear Waste Disposal." *Science, 256,* 649-651. Washington, D.C.: American Association for the Advancement of Science. TIC: 239138.

Bates, J.K.; Tani, B.S.; Veleckis, E.; and Wronkiewicz, D.J. 1990. "Identification of Secondary Phases Formed During Reaction of UO_2 with EJ-13 Water." *Scientific Basis for Nuclear Waste Management XIII, Symposium held November 27-30, 1989, Boston, Massachusetts.* Oversby, V.M. and Brown, P.W., eds. *176,* 499-506. Pittsburgh, Pennsylvania: Materials Research Society. TIC: 203658.

Beckman, R.; Thomas, K.; and Crowe, B. 1988. *Preliminary Report on the Statistical Evaluation of Sorption Data: Sorption as a Function of Mineralogy, Temperature, Time, and Particle Size.* LA-11246-MS. Los Alamos, New Mexico: Los Alamos National Laboratory. ACC: NNA.19890918.0500.

Benjamin, M.M. 1983. "Adsorption and Surface Precipitation of Metals on Amorphous Iron Oxyhydroxide." *Environmental Science and Technology, 17,* 686-692. Easton, Pennsylvania: American Chemical Society. TIC: 239143.

Bennett, D.A.; Hoffman, D.; Nitsche, H.; Russo, R.E.; Torres, R.A.; Baisden, P.A.; Andrews, J.E.; Palmer, C.E.A.; and Silva, R.J. 1992. "Hydrolysis and Carbonate Complexation of Dioxoplutonium(V)." *Radiochimica Acta, 56,* 15-19. München, Germany: R. Oldenbourg Verlag. TIC: 224778.

Bish, D.L. 1989. *Evaluation of Past and Future Alterations in Tuff at Yucca Mountain, Nevada, Based on the Clay Mineralogy of Drill Cores USW G-1, G-2, and G-3.* LA-10667-MS. Los Alamos, New Mexico: Los Alamos National Laboratory. ACC: NNA.19890126.0207.

Bish, D.L. and Aronson, J.L. 1993. "Paleogeothermal and Paleohydrologic Conditions in Silicic Tuff from Yucca Mountain, Nevada." *Clays and Clay Minerals, 41,* (2), 148-161. Long Island City, New York: Pergamon Press. TIC: 224613.

Bish, D.L. and Chipera, S.J. 1989. *Revised Mineralogic Summary of Yucca Mountain, Nevada.* LA-11497-MS. Los Alamos, New Mexico: Los Alamos National Laboratory. ACC: NNA.19891019.0029.

Bish, D.L. and Chipera, S.J. 1991. "Detection of Trace Amounts of Erionite Using X-Ray Powder Diffraction: Erionite in Tuffs of Yucca Mountain, Nevada, and Central Turkey." *Clays and Clay Minerals, 39,* (4), 437-445. [Long Island City, New York]: Pergamon Press. TIC: 203789.

Bish, D.L. and Post, J.E. 1989. "Thermal Behavior of Complex, Tunnel-Structure Manganese Oxides." *American Mineralogist, 74,* 177-186. Washington, D.C.: Mineralogical Society of America. TIC: 222519.

Bish, D.L.; Vaniman, D.T.; Rundberg, R.S.; Wolfsberg, K.; Daniels, W.R.; and Broxton, D.E. 1983. *Natural Sorptive Barriers in Yucca Mountain, Nevada, for Long-Term Isolation of High-Level Waste.* IAEA-CN-43/461. Vienna, Austria: International Atomic Energy Agency. TIC: 228652.

Blanchard, G.; Maunaye, M.; and Martin, G. 1984. "Removal of Heavy Metals from Waters by Means of Natural Zeolites." *Water Research, 18,* (12), 1501-1507. Oxford, Great Britain: Pergamon Press. TIC: 239004.

Bodvarsson, G.S.; Bandurraga, T.M.; and Wu, Y.S., eds. 1997. *The Site-Scale Unsaturated Zone Model of Yucca Mountain, Nevada, for the Viability Assessment.* LBNL-40376. Berkeley, California: Lawrence Berkeley National Laboratory. ACC: MOL.19971014.0232.

Bolt, G.H. and Bruggenwert, M.G.M., eds. 1978. *Soil Chemistry, A. Basic Elements.* Developments in Soil Science 5A. 2nd Revised Edition. New York, New York: Elsevier Scientific Publishing Company. TIC: 243742.

Borovec, Z. 1981. "The Adsorption of Uranyl Species by Fine Clay." *Chemical Geology, 32,* 45-58. Amsterdam, The Netherlands: Elsevier Science Publishing Company. TIC: 237323.

Bouwer, H. 1991. "Simple Derivation of the Retardation Equation and Application to Preferential Flow and Macrodispersion." *Ground Water, 29,* (1), 41-46. Dublin, Ohio: Water Well Publishing Company. TIC: 224079.

Bowman, R.S. and O'Connor, G.A. 1982. "Control of Nickel and Strontium Sorption by Free Metal Ion Activity." *Soil Science Society of America Journal, 46,* 933-936. Madison, Wisconsin: Soil Science Society of America. TIC: 236910.

Bradbury, M.H.; Green, A.; Lever, D.; and Stephen, I.G. 1986. *Diffusion and Permeability Based Sorption Measurements in Sandstone, Anhydrite and Upper Magnesian Limestone Samples.* AERE-R 11995. Oxfordshire, United Kingdom: Harwell Laboratory. TIC: 237243.

Breck, D.W. 1984. "Ion Exchange Reactions in Zeolites." Chapter 7 of *Zeolite Molecular Sieves, Structure, Chemistry, and Use.* Malabar, Florida: Robert E. Krieger Publishing Company. TIC: 245213.

Brookins, D.G. 1983. "Migration and Retention of Elements at the Oklo Natural Reactor." *Environmental Geology, 4,* 201-208. New York, New York: Springer-Verlag. TIC: 239003.

Brookins, D.G. 1988. *Eh-pH Diagrams for Geochemistry.* New York, New York: Springer-Verlag. TIC: 237943.

Broxton, D.E.; Warren, R.G.; Hagan, R.C.; and Luedemann, G. 1986. *Chemistry of Diagenetically Altered Tuffs at a Potential Nuclear Waste Repository, Yucca Mountain, Nye*

County, Nevada. LA-10802-MS. Los Alamos, New Mexico: Los Alamos National Laboratory. ACC: MOL.19980527.0202.

Bruton, C.J. 1991. "Equilibrium Controls of Radionuclide Concentrations in Nevada Test Site Waters: Preliminary Results for Th, U, Np, Pu, Am, Sr, Ra and Pb." Appendix D of *Waste Inventory and Preliminary Source Term Model for the Greater Confinement Disposal Site at the Nevada Test Site.* Chu, M.S.Y. and Bernard, E.A. SAND91-0170. Albuquerque, New Mexico: Sandia National Laboratories. ACC: MOL.19990211.0489.

Buddemeier, R.W. and Hunt, J.R. 1988. "Transport of Colloidal Contaminants in Groundwater: Radionuclide Migration at the Nevada Test Site." *Applied Geochemistry, 3,* 535-548. Oxford, England: Pergamon Press. TIC: 224116.

Buscheck, T.A. and Nitao, J.J. 1992. "The Impact of Thermal Loading on Repository Performance at Yucca Mountain." *High Level Radioactive Waste Management, Proceedings of the Third International Conference, Las Vegas, Nevada, April 12-16, 1992. 1,* 1003-1017. La Grange Park, Illinois: American Nuclear Society. TIC: 204231.

Bussod, G.Y. 1998. Busted Butte On-Site Logbook #1, UZ Transport Field Test (LA-EES-5-NBK-98-010). Scientific Notebook SN-LANL-SCI-040-V1. ACC: MOL.20000321.0288.

Bussod, G.Y.; Robinson, B.A.; Vaniman, D.T.; Broxton, D.E.; and Viswanathan, H.S. 1997. *UZ Field Transport Test Plan.* Deliverable SP341SM4. Los Alamos, New Mexico: Los Alamos National Laboratory. ACC: MOL.19980806.0715.

Bussod, G.Y.; Robinson, B.A.; Wolfsberg, A.V.; Gable, C.W.; and Viswanathan, H.S. 1998. "An Integrated UZ Flow and Transport Model for Yucca Mountain, Nevada, U.S.A." *Modelling the Effects of Spatial Variability on Radionuclide Migration, Synthesis and Proceedings of an NEA Workshop, Paris, France, 9-11 June 1997.* Pages 165-192. Paris, France: Nuclear Energy Agency, Organisation for Economic Co-operation and Development. TIC: 247752.

Carey, J.W.; Chipera, S.J.; Vaniman, D.T.; and Bish, D.L. 1998. *Three-Dimensional Mineralogic Model of Yucca Mountain, Nevada Rev 2.0.* Deliverable SP32B1M4. Draft R2. Los Alamos, New Mexico: Los Alamos National Laboratory, Earth and Environmental Sciences Division. Submit to RPC URN-0440

Carlos, B.A. 1985. *Minerals in Fractures of the Unsaturated Zone from Drill Core USW G-4, Yucca Mountain, Nye County, Nevada.* LA-10415-MS. Los Alamos, New Mexico: Los Alamos National Laboratory. ACC: NNA.19920506.0037.

Carlos, B.A. 1987. *Minerals in Fractures of the Saturated Zone from Drill Core USW G-4, Yucca Mountain, Nye County, Nevada.* LA-10927-MS. Los Alamos, New Mexico: Los Alamos National Laboratory. ACC: NNA.19900222.0149.

Carlos, B.A. 1989. *Fracture-Coating Minerals in the Topopah Spring Member and Upper Tuff of Calico Hills from Drill Hole J-13.* LA-11504-MS. Los Alamos, New Mexico: Los Alamos National Laboratory. TIC: 202383.

Carlos, B.A. 1994. *Field Guide to Fracture-Lining Minerals at Yucca Mountain, Nevada.* LA-12803-MS. Los Alamos, New Mexico: Los Alamos National Laboratory. ACC: MOL.19950717.0113.

Carlos, B.A.; Bish, D.L.; and Chipera, S.J. 1990. *Manganese-Oxide Minerals in Fractures of the Crater Flat Tuff in Drill Core USW G-4, Yucca Mountain, Nevada.* LA-11787-MS. Los Alamos, New Mexico: Los Alamos National Laboratory. ACC: NNA.19900206.0163.

Carlos, B.A.; Bish, D.L.; and Chipera, S.J. 1991. "Fracture-Lining Minerals in the Lower Topopah Spring Tuff at Yucca Mountain." *High Level Radioactive Waste Management, Proceedings of the Second Annual International Conference, Las Vegas, Nevada, April 28-May 3, 1991. 1,* 486-493. La Grange Park, Illinois: American Nuclear Society. TIC: 204272.

Carlos, B.A.; Chipera, S.J.; Bish, D.L.; and Craven, S.J. 1993. "Fracture-Lining Manganese Oxide Minerals in Silicic Tuff, Yucca Mountain, Nevada, U.S.A." *Chemical Geology, 107,* 47-69. Amsterdam, The Netherlands: Elsevier Science Publishers B.V. TIC: 208629.

Carsel, R.F. and Parrish, R.S. 1988. "Developing Joint Probability Distributions of Soil Water Retention Characteristics." *Water Resources Research, 24,* (5), 755-769. Washington, D.C.: American Geophysical Union. TIC: 247697.

Champ, D.R.; Merritt, W.F.; and Young, J.L. 1982. "Potential for the Rapid Transport of Plutonium in Groundwater as Demonstrated by Core Column Studies." *Scientific Basis for Nuclear Waste Management V, Proceedings of the Materials Research Society Fifth International Symposium held June 7-10, 1982, Berlin, Germany.* Lutze, W., ed. *11,* 745-754. New York, New York: North-Holland. TIC: 204398.

Chipera, S.J.; Bish, D.L.; and Carlos, B.A. 1995. "Equilibrium Modeling of the Formation of Zeolites in Fractures at Yucca Mountain, Nevada." *Natural Zeolites '93: Occurrence, Properties, Use, Proceedings of the 4th International Conference on the Occurrence, Properties, and Utilization of Natural Zeolites, June 20-28, 1993, Boise, Idaho.* Ming, D.W. and Mumpton, F.A., eds. Pages 565-577. Brockport, New York: International Committee on Natural Zeolites. TIC: 243086.

Choi, J.S. and Pigford, T.H. 1981. "Water Dilution Volumes for High-Level Wastes." *[Transactions of the American Nuclear Society Winter Meeting, San Francisco, California, 1981, 39],* 176-177. [La Grange Park, Illinois: American Nuclear Society]. TIC: 236930.

Choppin, G.R. 1992. "The Role of Natural Organics in Radionuclide Migration in Natural Aquifer Systems." *Radiochimica Acta, 58/59,* 113-120. New York, New York: Academic Press. TIC: 222387.

Choppin, G.R. and Rao, L.F. 1984. "Complexation of Pentavalent and Hexavalent Actinides by Fluoride." *Radiochimica Acta, 37,* 143-146. München, Germany: R. Oldenbourg Verlag. TIC: 237580.

Clark, D.L. 1994. *Letter Report on the Status of Pu(IV) Colloid Studies.* Milestone 4026. Draft. Los Alamos, New Mexico: Los Alamos National Laboratory. ACC: MOL.19951002.0234.

Cleveland, J.M. 1979a. "Critical Review of Plutonium Equilibria of Environmental Concern." Chapter 16 of *Chemical Modeling in Aqueous Systems, Speciation, Sorption, Solubility, and Kinetics.* Jenne, E.A., ed. ACS Symposium Series 93. Washington, D.C.: American Chemical Society. TIC: 236752.

Cleveland, J.M. 1979b. *The Chemistry of Plutonium.* La Grange Park, Illinois: American Nuclear Society. TIC: 10231.

Combes, J.M.; Chisholm-Brause, C.J.; Brown, G.E., Jr.; Parks, G.A.; Conradson, S.D.; Eller, P.G.; Triay, I.R.; Hobart, D.E.; and Meijer, A. 1992. "EXAFS Spectroscopic Study of Neptunium(V) Sorption at the a-FeOOH/Water Interface." *Environmental Science & Technology, 26,* (2), 376-382. Washington, D.C.: American Chemical Society. TIC: 224053.

Conca, J.L. and Wright, J. 1992a. "A New Technology for Direct Measurements of Unsaturated Transport." *Proceedings of the International Topical Meeting on Nuclear and Hazardous Waste Management, Spectrum '92, August 23-27, 1992, Boise, Idaho. 2,* 1546-1555. La Grange Park, Illinois: American Nuclear Society. TIC: 205023.

Conca, J.L. and Wright, J. 1992b. "Diffusion and Flow in Gravel, Soil, and Whole Rock." *Applied Hydrogeology, 1,* 5-24. Hanover, Germany: Verlag Heinz Heise GmbH. TIC: 224081.

Cotton, F.A. and Wilkinson, G. 1988. *Advanced Inorganic Chemistry.* 5th Edition. New York, New York: John Wiley & Sons. TIC: 236867.

Cramer, J.J. and Sargent, F.P. 1994. "The Cigar Lake Analog Study: An International R&D Project." *High Level Radioactive Waste Management, Proceedings of the Fifth Annual International Conference, Las Vegas, Nevada, May 22-26, 1994. 4,* 2237-2242. La Grange Park, Illinois: American Nuclear Society. TIC: 210984.

CRWMS M&O 1994. *Total System Performance Assessment - 1993: An Evaluation of the Potential Yucca Mountain Repository.* B00000000-01717-2200-00099 REV 01. Las Vegas, Nevada: CRWMS M&O. ACC: NNA.19940406.0158.

CRWMS M&O 1995. *Total System Performance Assessment - 1995: An Evaluation of the Potential Yucca Mountain Repository.* B00000000-01717-2200-00136 REV 01. Las Vegas, Nevada: CRWMS M&O. ACC: MOL.19960724.0188.

CRWMS M&O 1997. *Summary Report Geochemistry/Transport Laboratory Tests.* Deliverable SP23QM3. Las Vegas, New York: CRWMS M&O. ACC: MOL.19980122.0053.

CRWMS M&O 2000. *Unsaturated Zone and Saturated Zone Transport Properties (U0100).* ANL-NBS-HS-000019 REV 00. Las Vegas, Nevada: CRWMS M&O. ACC: MOL.20000817.0546.

Curtis, D. and Fabryka-Martin, J. 1988. *Report on Trip to Alligator River Analogue Project Workshop held in Tucson, Arizona, November 21-22, 1988.* Los Alamos, New Mexico: Los Alamos National Laboratory. TIC: 242711.

Curtis, D.B.; Fabryka-Martin, J.; Dixon, P.; Aguilar, R.; and Cramer, J. 1994. "Radionuclide Release Rates from Natural Analogues of Spent Nuclear Fuel." *High Level Radioactive Waste Management, Proceedings of the Fifth Annual International Conference, Las Vegas, Nevada, May 22-26, 1994. 4,* 2228-2236. La Grange Park, Illinois: American Nuclear Society. TIC: 210984.

Dagan, G. 1984. "Solute Transport in Heterogeneous Porous Formations." *Journal of Fluid Mechanics,* (145), 151-177. Cambridge, United Kingdom: Cambridge University Press. TIC: 247700.

Dagan, G. 1989. *Flow and Transport in Porous Formations.* New York, New York: Springer-Verlag. TIC: 234219.

Daniels, W.R.; Erdal, B.R.; and Vaniman, D.T., eds. 1983. *Research and Development Related to the Nevada Nuclear Waste Storage Investigations, July 1—September 30, 1982.* LA-9577-PR. Los Alamos, New Mexico: Los Alamos National Laboratory. ACC: NNA.19870406.0180.

Daniels, W.R.; Wolfsberg, K.; Rundberg, R.S.; Ogard, A.E.; Kerrisk, J.F.; Duffy, C.J.; Newton, T.W.; Thompson, J.L.; Bayhurst, B.P.; Bish, D.L.; Blacic, J.D.; Crowe, B.M.; Erdal, B.R.; Griffith, J.F.; Knight, S.D.; Lawrence, F.O.; Rundberg, V.L.; Skyes, M.L.; Thompson, G.M.; Travis, B.J.; Treher, E.N.; Vidale, R.J.; Walter, G.R.; Aguilar, R.D.; Cisneros, M.R.; Maestas, S.; Mitchell, A.J.; Oliver, P.Q.; Raybold, N.A.; and Wanek, P.L. 1982. *Summary Report on the Geochemistry of Yucca Mountain and Environs.* LA-9328-MS. Los Alamos, New Mexico: Los Alamos National Laboratory. ACC: NNA.19870406.0243.

Davis, J.A.; James, R.O.; and Leckie, J.O. 1978. "Surface Ionization and Complexation at the Oxide/Water Interface: I. Computation of Electrical Double Layer." *Journal of Colloid and Interface Science, 63,* (3), 480-499. New York, New York: Academic Press. TIC: 223904.

Decarreau, A. 1985. "Partitioning of Divalent Transition Elements Between Octahedral Sheets of Trioctahedral Smectites and Water." *Geochimica et Cosmochimica Acta, 49,* 1537-1544. New York, New York: Pergamon Press. TIC: 237522.

Degueldre, C.; Grauer, R.; Laube, A.; Oess, A.; and Silby, H. 1996b. "Colloid Properties in Granitic Groundwater Systems. II: Stability and Transport Study." *Applied Geochemistry, 11,* 697-710. Oxford, England: Elsevier Science. TIC: 236569.

Degueldre, C.; Laube, A.; and Scholtis, A. 1994. *WLB: A Study of Colloids in Ground-Waters at the Wellenberg Site: Status Report.* Interner Bericht 94-41. Wettingen, Switzerland: Nationale Genossenschaft für die Lagerung Radoaktiver Abfalle. TIC: 246054.

Degueldre, C.; Pfeiffer, H.R.; Alexander, W.; Wernli, B.; and Bruetsch, R. 1996a. "Colloid Properties in Granitic Groundwater Systems. I: Sampling and Characterization." *Applied Geochemistry, 11,* 677-694. Oxford, England: Elsevier Science. TIC: 236886.

de Marsily, G. 1986. *Quantitative Hydrogeology: Groundwater Hydrology for Engineers.* San Diego, California: Academic Press. TIC: 208450.

DOE (U.S. Department of Energy) 1988. *Site Characterization Plan Yucca Mountain Site, Nevada Research and Development Area, Nevada.* DOE/RW-0199. Nine volumes. Washington, D.C.: U.S. Department of Energy, Office of Civilian Radioactive Waste Management. ACC: HQO.19881201.0002.

DOE (U.S. Department of Energy) 1998. *Total System Performance Assessment.* Volume 3 of *Viability Assessment of a Repository at Yucca Mountain.* DOE/RW-0508. Washington, D.C.: U.S. Department of Energy, Office of Civilian Radioactive Waste Management. ACC: MOL.19981007.0030.

Doi, K.; Hirono, S.; and Sakamaki, Y. 1975. "Uranium Mineralization by Groundwater in Sedimentary Rocks, Japan." *Economic Geology, 70,* 628-646. El Paso, Texas: Economic Geology Publishing Company. TIC: 236987.

Dorrance, D.W.; Wilson, L.G.; Everett, L.G.; and Cullen, S.J. 1991. "Compendium of In Situ Pore-Liquid Samplers for Vadose Zone." Chapter 19 of *Groundwater Residue Sampling Design.* Nash, R.G. and Leslie, A.R., eds. ACS Symposium Series 465. Washington, D.C.: American Chemical Society. TIC: 247154.

Dozol, M. and Hageman, R. 1993. "Radionuclide Migration in Groundwaters: Review of the Behaviour of Actinides." *Pure and Applied Chemistry, 65,* (5), 1081-1102. Oxford, United Kingdom: Blackwell Scientific Publishers. TIC: 236897.

Drever, J.I. 1988. *The Geochemistry of Natural Waters.* 2nd Edition. Englewood Cliffs, New Jersey: Prentice-Hall. TIC: 242836.

Eckhardt, R.C. 2000. "Site Description, Sec. 5 & 10, Selected Tables and Figures." Letter from R.C. Eckhardt (LANL) to A. Simmons (LBNL), EES-13-06-00-176, June 27, 2000, with enclosures. ACC: MOL.20000808.0058.

Efurd, D.W.; Runde, W.; Banar, J.C.; Roensch, F.R.; Palmer, P.D.; Clark, D.L.; and Tait, C.D. 1996. *Measured Solubilities and Speciation of Neptunium and Plutonium in J-13 Groundwater.* Milestone 3411. Los Alamos, New Mexico: Los Alamos National Laboratory. TIC: 237839.

Fabryka-Martin, J.T.; Flint, A.L.; Sweetkind, D.S.; Wolfsberg, A.V.; Levy, S.S.; Roemer, G.J.C.; Roach, J.L.; Wolfsberg, L.E.; and Duff, M.C. 1997. *Evaluation of Flow and Transport Models of Yucca Mountain, Based on Chlorine-36 Studies for FY97.* LA-CST-TIP-97-010. Los Alamos, New Mexico: Los Alamos National Laboratory. ACC: MOL.19980204.0916.

Fabryka-Martin, J.T.; Wolfsberg, A.V.; Dixon, P.R.; Levy, S.S.; Musgrave, J.A.; and Turin, H.J. 1997. *Summary Report of Chlorine-36 Studies: Sampling, Analysis, and Simulation of*

Chlorine-36 in the Exploratory Studies Facility. LA-13352-MS. Los Alamos, New Mexico: Los Alamos National Laboratory. ACC: MOL.19980812.0254.

Felmy, A.R.; Rai, D.; and Fulton, R.W. 1990. "The Solubility of $AmOHCO_3$(c) and the Aqueous Thermodynamics of the System Na^+-Am^{3+}-HCO_3^--CO_3^{2-}-OH^--H_2O." *Radiochimica Acta, 50,* 193-204. München, Germany: R. Oldenbourg Verlag. TIC: 236870.

Finch, R.J.; Miller, M.L.; and Ewing, R.C. 1992. "Weathering of Natural Uranyl Oxide Hydrates: Schoepite Polytypes and Dehydration Effects." *Radiochimica Acta, 58/59,* 433-443. München, Germany: R. Oldenbourg Verlag. TIC: 238032.

Flexser, S. and Wollenberg, H.A. 1992. "Radioelements and Their Occurrence with Secondary Minerals in Heated and Unheated Tuff at the Nevada Test Site." *High Level Radioactive Waste Management, Proceedings of the Third International Conference, Las Vegas, Nevada, April 12-16, 1992. 2,* 1593-1598. La Grange Park, Illinois: American Nuclear Society. TIC: 204231.

Flint, A.L.; Hevesi, J.A.; and Flint, L.E. 1996. *Conceptual and Numerical Model of Infiltration for the Yucca Mountain Area, Nevada.* Milestone 3GUI623M. Denver, Colorado: U.S. Geological Survey. ACC: MOL.19970409.0087.

Flint, L.E. 1998. *Characterization of Hydrogeologic Units Using Matrix Properties, Yucca Mountain, Nevada.* Water-Resources Investigations Report 97-4243. Denver, Colorado: U.S. Geological Survey. ACC: MOL.19980429.0512.

Fuger, J. 1992. "Thermodynamic Properties of Actinide Aqueous Species Relevant to Geochemical Problems." *Radiochimica Acta, 58/59,* (I), 81-91. München, Germany: R. Oldenbourg Verlag. TIC: 245944.

Gardner, W.R. 1958. "Some Steady-State Solutions of the Unsaturated Moisture Flow Equation with Application to Evaporation from a Water Table." *Soil Science, 85,* 228-232. Baltimore, Maryland: Williams and Wilkins. TIC: 240150.

GCX 1994. *Ground Water Compositional Parameters Most Critical to the Sorption Behavior of Radionuclides-of-Concern to the Yucca Mountain Project.* Milestone 4032. Draft. Albuquerque, New Mexico: GCX. ACC: MOL.19950630.0308.

Geldon, A.L.; Umari, A.M.A.; Fahy, M.F.; Earle, J.D.; Gemmell, J.M.; and Darnell, J. 1997. *Results of Hydraulic and Conservative Tracer Tests in Miocene Tuffaceous Rocks at the C-Hole Complex, 1995 to 1997, Yucca Mountain, Nye County, Nevada.* Milestone SP23PM3. Denver, Colorado: U.S. Geological Survey. ACC: MOL.19980122.0412.

Gelhar, L.W. and Axness, C.L. 1983. "Three-Dimensional Stochastic Analysis of Macrodispersion in Aquifers." *Water Resources Research, 19,* (1), 161-180. Washington, D.C.: American Geophysical Union. TIC: 222815.

George-Aniel, B.; Leroy, J.L.; and Poty, B. 1991. "Volcanogenic Uranium Mineralizations in the Sierra Peña Blanca District, Chihuahua, Mexico: Three Genetic Models." *Economic*

Geology, 86, (2), 233-248. El Paso, Texas: Economic Geology Publishing Company. TIC: 237050.

Giblin, A.M. and Snelling, A.A. 1983. "Application of Hydrogeochemistry to Uranium Exploration in the Pine Creek Geosyncline, Northern Territory, Australia." *Journal of Geochemical Exploration, 19,* 33-55. Amsterdam, The Netherlands: Elsevier Science Publishers B.V. TIC: 237423.

Goodwin, B.W.; Cramer, J.J.; and McConnell, D.B. 1989. "The Cigar Lake Uranium Deposit: An Analogue for Nuclear Fuel Waste Disposal." Appendix B of *Natural Analogues in Performance Assessments for the Disposal of Long Lived Radioactive Wastes.* Technical Reports Series 304. Vienna, Austria: International Atomic Energy Agency. TIC: 7851.

Graham, W. and McLaughlin, D. 1989. "Stochastic Analysis of Nonstationary Subsurface Solute Transport, 2. Conditional Moments." *Water Resources Research, 25,* (11), 2331-2355. Washington, D.C.: American Geophysical Union. TIC: 239451.

Gregg, S.J. and Sing, K.S.W. 1967. *Adsorption, Surface Area and Porosity.* Pages 182-185. New York, New York: Academic Press. TIC: 217459.

Grenthe, I.; Fuger, J.; Konings, R.J.M.; Lemire, R.J.; Muller, A.B.; Nguyen-Trung, C.; and Wanner, H. 1992. *Chemical Thermodynamics of Uranium.* Volume 1 of *Chemical Thermodynamics.* Wanner, H. and Forest, I., eds. Amsterdam, The Netherlands: North-Holland Publishing Company. TIC: 224074.

Hakanen, M. and Lindberg, A. 1991. "Sorption of Neptunium Under Oxidizing and Reducing Groundwater Conditions." *Radiochimica Acta, 52/53,* 147-151. München, Germany: R. Oldenbourg Verlag. TIC: 237041.

Harter, T. and Yeh, T.-C.J. 1996a. "Stochastic Analysis of Solute Transport in Heterogeneous, Variably Saturated Soils." *Water Resources Research, 32,* (6), 1585-1595. Washington, D.C.: American Geophysical Union. TIC: 247170.

Harter, T. and Yeh, T.-C.J. 1996b. "Conditional Stochastic Analysis of Solute Transport in Heterogeneous, Variably Saturated Soils." *Water Resources Research, 32,* (6), 1597-1609. Washington, D.C.: American Geophysical Union. TIC: 247169.

Haschke, J.M. and Ricketts, T.E. 1997. "Adsorption of Water on Plutonium Dioxide." *Journal of Alloys and Compounds, 252,* 148-156. Lausanne, Switzerland: Elsevier Science B.V. TIC: 241047.

Hayes, K.F.; Roe, A.L.; Brown, G.E., Jr.; Hodgson, K.O.; Leckie, J.O.; and Parks, G.A. 1987. "In Situ X-Ray Absorption Study of Surface Complexes: Selenium Oxyanions on a-FeOOH." *Science, 238,* 783-786. Washington, D.C.: American Association for the Advancement of Science. TIC: 237033.

Hiester, N.K. and Vermeulen, T. 1952. "Saturation Performance of Ion-Exchange and Adsorption Columns." *Chemical Engineering Progress, 48,* (10), 505-516. New York, New York: American Institute of Chemical Engineers. TIC: 224052.

Hingston, F.J.; Posner, A.M.; and Quirk, J.P. 1971. "Competitive Adsorption of Negatively Charged Ligands on Oxide Surfaces." *Surface Chemistry of Oxides, Discussions of the Faraday Society, 52,* 334-351. London, England: Royal Society of Chemistry. TIC: 237679.

Ho, C.H. and Miller, N.H. 1986. "Adsorption of Uranyl Species from Bicarbonate Solution onto Hematite Particles." *Journal of Colloid and Interface Science, 110,* (1), 165-171. New York, New York: Academic Press. TIC: 226326.

Hobart, D.E. 1990. "Actinides in the Environment." Chapter XIII of *Proceedings of the Robert A. Welch Foundation Conference on Chemical Research XXXIV, Fifty Years with Transuranium Elements, Houston, Texas, October 22-23, 1990.* [Houston, Texas: Robert A. Welch Foundation]. TIC: 237030.

Hobart, D.E.; Morris, D.E.; Palmer, P.D.; and Newton, T.W. 1989. "Formation, Characterization, and Stability of Pu(IV) Colloid: A Progress Report." *Proceedings of the Topical Meeting on Nuclear Waste Isolation in the Unsaturated Zone, Focus '89, September 17-21, 1989, Las Vegas, Nevada.* Pages 118-124. La Grange Park, Illinois: American Nuclear Society. TIC: 212738.

Howard, J.H., III 1977. "Geochemistry of Selenium: Formation of Ferroselite and Selenium Behavior in the Vicinity of Oxidizing Sulfide and Uranium Deposits." *Geochimica et Cosmochimica Acta, 41,* 1665-1678. New York, New York: Pergamon Press. TIC: 239142.

Hsi, C-K.D. and Langmuir, D. 1985. "Adsorption of Uranyl onto Ferric Oxyhydroxides: Application of the Surface Complexation Site-Binding Model." *Geochimica et Cosmochimica Acta, 49,* 1931-1941. New York, New York: Pergamon Press. TIC: 224090.

Itagaki, H.; Nakayama, S.; Tanaka, S.; and Yamawaki, M. 1992. "Effect of Ionic Strength on the Solubility of Neptunium(V) Hydroxide." *Radiochimica Acta, 58/59,* 61-66. München, Germany: R. Oldenbourg Verlag. TIC: 240833.

Jacques, D.; Kim, D-J.; Diels, J.; Vanderborght, J.; Vereecken, H.; and Feyen, J. 1998. "Analysis of Steady State Chloride Transport Through Two Heterogeneous Field Soils." *Water Resources Research, 34,* (10), 2539-2550. Washington, D.C.: American Geophysical Union. TIC: 247171.

Janecky, D.R.; Duffy, C.J.; Tait, C.D.; and Clark, D. 1997. *Letter Report on Thermochemical Data on Actinides for Modeling.* Milestone 4025. Los Alamos, New Mexico: Los Alamos National Laboratory. TIC: 243470.

Janecky, D.R.; Enter, J.; Duffy, C.; and Tait, C.D. 1995. *Modeled Actinide Solubilities and Speciation.* Milestone 3463. Draft. Los Alamos, New Mexico: Los Alamos National Laboratory. ACC: MOL.19960417.0131.

Kaplan, D.I.; Bertsch, P.M.; Adriano, D.C.; and Orlandini, K.A. 1994. "Actinide Association with Groundwater Colloids in a Coastal Plain Aquifer." *Radiochimica Acta, 66/67,* 181-187. München, Germany: R. Oldenbourg Verlag. TIC: 245939.

Katz, J.J.; Seaborg, G.T.; and Morss, L.R., eds. 1986. *The Chemistry of the Actinide Elements.* 2nd Edition. Two volumes. New York, New York: Chapman and Hall. TIC: 243942.

Keeney-Kennicutt, W.L. and Morse, J.W. 1985. "The Redox Chemistry of $Pu(V)O^{+2}$ Interaction with Common Mineral Surfaces in Dilute Solutions and Seawater." *Geochimica et Cosmochimica Acta, 49,* 2577-2588. New York, New York: Pergamon Press. TIC: 237000.

Kersting, A.B.; Efurd, D.W.; Finnegan, D.L.; Rokop, D.J.; Smith, D.K.; and Thompson, J.L. 1999. "Migration of Plutonium in Ground Water at the Nevada Test Site." *Nature, 397,* 56-59. London, England: Macmillan Publishers. TIC: 243597.

Kim, J.I. and Sekine, T. 1991. "Complexation of Neptunium(V) with Humic Acid." *Radiochimica Acta, 55,* 187-192. München, Germany: R. Oldenbourg Verlag. TIC: 240875.

Kim, J.I.; Zeh, P.; and Delakovitz, B. 1992. "Chemical Interactions of Actinide Ions with Groundwater Colloids in Gorleben Aquifer Systems." *Radiochimica Acta, 58/59,* 147-154. München, Germany: R. Oldenbourg Verlag. TIC: 236935.

Knight, S.D. and Lawrence, F.O. 1988. *Sorption of Nickel and Neptunium in Tuff Using Groundwaters of Various Compositions.* Milestone R505. Los Alamos, New Mexico: Los Alamos National Laboratory. ACC: NN1.19881028.0004.

Knight, S.D. and Thomas, K.W. 1987. *Sorption of Radionuclides Using Different Groundwater Compositions.* [Milestone M316]. Los Alamos, New Mexico: Los Alamos National Laboratory. ACC: MOL.19980625.0236; NNA.19870902.0098.

Krier, D.; Longmire, P.; Gilkeson, R.; and Turin, H.J. 1997. *Geologic, Geohydrologic, and Geochemical Data Summary of Material Disposal Area G, Technical Area 54, Los Alamos National Laboratory.* LAUR-95-2696. Los Alamos, New Mexico: Los Alamos National Laboratory. TIC: 247472.

Kung, K-H. and McBride, M.B. 1989a. "Adsorption of Para-Substituted Benzoates on Iron Oxides." *Soil Science Society of America Journal, 53,* 1673-1678. Madison, Wisconsin: Soil Science Society of America. TIC: 237036.

Kung, K-H. and McBride, M.B. 1989b. "Coordination Complexes of p-Hydroxybenzoate on Fe Oxides." *Clay and Clay Minerals, 37,* (4), 333-340. Boulder, Colorado: Clay Minerals Society. TIC: 236863.

Kung, K-H.S. and McBride, M.B. 1991. "Bonding of Chlorophenols on Iron and Aluminum Oxides." *Environmental Science & Technology, 25,* (4), 702-709. Washington, D.C.: American Chemical Society. TIC: 236864.

Kunze, G.W. and Dixon, J.B. 1986. "Pretreatment for Mineralogical Analysis." Chapter 5 of *Method of Soil Analysis, Part 1, Physical and Mineralogical Methods.* Klute, A., ed. 2nd Edition. Madison, Wisconsin: Soil Science Society of America. TIC: 217566.

Laaksoharju, M.; Degueldre, C.; and Skårman, C. 1995. *Study of Colloids and Their Importance for Repository Performance Assessment.* SKB Technical Report 95-24. Stockholm, Sweden: Swedish Nuclear Fuel and Waste Management Company. TIC: 223428.

Langmuir, D. 1997. *Aqueous Environmental Geochemistry.* Upper Saddle River, New Jersey: Prentice Hall. TIC: 237107.

Langmuir, D. and Riese, A.C. 1985. "The Thermodynamic Properties of Radium." *Geochimica et Cosmochimica Acta, 49,* 1593-1601. New York, New York: Pergamon Press. TIC: 241035.

Lemire, R.J. and Garisto, F. 1989. *The Solubility of U, Np, Pu, Th and Tc in a Geological Disposal Vault for Used Nuclear Fuel.* AECL-10009. Pinawa, Manitoba, Canada: Atomic Energy of Canada Limited. TIC: 213161.

Lemire, R.J. and Tremaine, P.R. 1980. "Uranium and Plutonium Equilibria in Aqueous Solutions to 200°C." *Journal of Chemical and Engineering Data, 25,* (4), 361-370. Washington, D.C.: American Chemical Society. TIC: 222175.

Levy, S.S. 1984. "Studies of Altered Vitrophyre for the Prediction of Nuclear Waste Repository-Induced Thermal Alteration at Yucca Mountain, Nevada." *Scientific Basis for Nuclear Waste Management VII, Symposium held November 1983, Boston, Massachusetts.* McVay, G.L., ed. *26,* 959-966. New York, New York: Elsevier Science. TIC: 204393.

Levy, S.S. 1991. "Mineralogic Alteration History and Paleohydrology at Yucca Mountain, Nevada." *High Level Radioactive Waste Management, Proceedings of the Second Annual International Conference, Las Vegas, Nevada, April 28-May 3, 1991. 1,* 477-485. La Grange Park, Illinois: American Nuclear Society. TIC: 204272.

Levy, S.S. 1992. "Natural Gels in the Yucca Mountain Area, Nevada, USA." *Applied Clay Science, 7,* (1-3), 79-85. Amsterdam, The Netherlands: Elsevier Science Publishers B.V. TIC: 225196.

Levy, S.S. and O'Neil, J.R. 1989. "Moderate-Temperature Zeolitic Alteration in a Cooling Pyroclastic Deposit." *Chemical Geology, 76,* (3/4), 321-326. Amsterdam, The Netherlands: Elsevier Science. TIC: 237819.

Liang, L. and McCarthy, J.F. 1995. "Colloidal Transport of Metal Contaminants in Groundwater." Chapter 4 of *Metal Speciation and Contamination of Soil.* Boca Raton, Florida: Lewis Publishers. TIC: 236979.

Lieser, K.H. and Bauscher, C. 1988. "Technetium in the Hydrosphere and in the Geosphere, II. Influence of pH, of Complexing Agents, and of Some Minerals on the Sorption of Technetium." *Radiochimica Acta, 44/45,* 125-128. München, Germany: R. Oldenbourg Verlag. TIC: 237071.

Lieser, K.H. and Muhlenweg, U. 1988. "Neptunium in the Hydrosphere and in the Geosphere, I. Chemistry of Neptunium in the Hydrosphere and Sorption of Neptunium from Groundwaters on Sediments Under Aerobic and Anaerobic Conditions." *Radiochimica Acta, 43,* 27-35. München, Germany: R. Oldenbourg Verlag. TIC: 236783.

Litaor, M.I. 1988. "Review of Soil Solution Samplers." *Water Resources Research, 24,* (5), 727-733. Washington, D.C.: American Geophysical Union. TIC: 247172.

Longworth, G.; Ross, C.A.M.; Degueldre, C.; and Ivanovich, M. 1989. *Interlaboratory Study of Sampling and Characterization Techniques for Groundwater Colloids.* AERE-R 13393. Oxfordshire, United Kingdom: Harwell Laboratory. TIC: 242340.

Lorens, R.B. 1981. "Sr, Cd, Mn and Co Distribution Coefficients in Calcite as a Function of Calcite Precipitation Rate." *Geochimica et Cosmochimica Acta, 45,* 553-561. New York, New York: Pergamon. TIC: 247351.

Machesky, M.L. 1990. "Influence of Temperature on Ion Adsorption by Hydrous Metal Oxides." *Chemical Modeling of Aqueous Systems II, Los Angeles, California, September 25-30, 1988.* Melchior, D.C. and Bassett, R.L., eds. ACS Symposium Series 416. Pages 282-292. Washington, D.C.: American Chemical Society. TIC: 241139.

Mantoglou, A. 1992. "A Theoretical Approach for Modeling Unsaturated Flow in Spatially Variable Soils: Effective Flow Models in Finite Domains and Nonstationarity." *Water Resources Research, 28,* (1), 251-267. Washington, D.C.: American Geophysical Union. TIC: 247176.

Mantoglou, A. and Gelhar, L.W. 1987. "Stochastic Modeling of Large-Scale Transient Unsaturated Flow Systems." *Water Resources Research, 23,* (1), 37-46. Washington, D.C.: American Geophysical Union. TIC: 223510.

Maya, L. 1982. "Sorbed Uranium(VI) Species on Hydrous Titania, Zirconia, and Silica Gel." *Radiochimica Acta, 31,* 147-151. München, Germany: R. Oldenbourg Verlag. TIC: 236887.

McBride, M.B. and Wesselink, L.G. 1988. "Chemisorption of Catechol on Gibbsite, Boehmite, and Noncrystalline Alumina Surfaces." *Environmental Science and Technology, 22,* (6), 703-708. Washington, D.C.: American Chemical Society. TIC: 237431.

McCarthy, J.F. and Degueldre, C. 1993. "Sampling and Characterization of Colloids and Particles in Groundwater for Studying Their Role in Contaminant Transport." Chapter 6 of *Environmental Particles.* Buffle, J. and van Leeuwen, H.P., eds. Volume 2. Boca Raton, Florida: Lewis Publishers. TIC: 245905.

McCarthy, J.F. and Zachara, J.M. 1989. "Subsurface Transport of Contaminants." *Environmental Science & Technology, 23,* (5), 496-502. Easton, Pennsylvania: American Chemical Society. TIC: 224876.

McGraw, M.A. 1996. *The Effect of Colloid Size, Colloid Hydrophobicity, and Volumetric Water Content on the Transport of Colloids Through Porous Media.* Ph.D. dissertation. Berkeley, California: University of California. TIC: 245722.

Means, J.L.; Crerar, D.A.; and Borcsik, M.P. 1978. "Adsorption of Co and Selected Actinides by Mn and Fe Oxides in Soils and Sediments." *Geochimica et Cosmochimica Acta, 42,* 1763-1773. New York, New York: Pergamon Press. TIC: 218336.

Meece, D.E. and Benninger, L.K. 1993. "The Coprecipitation of Pu and Other Radionuclides with $CaCO_3$." *Geochimica et Cosmochimica Acta, 57,* 1447-1458. New York, New York: Pergamon. TIC: 247349.

Meijer, A. 1990. *Yucca Mountain Project Far-Field Sorption Studies and Data Needs.* LA-11671-MS. Los Alamos, New Mexico: Los Alamos National Laboratory. ACC: NNA.19920131.0363.

Meijer, A. 1992. "A Strategy for the Derivation and Use of Sorption Coefficients in Performance Assessment Calculations for the Yucca Mountain Site." *Proceedings of the DOE/Yucca Mountain Site Characterization Project Radionuclide Adsorption Workshop at Los Alamos National Laboratory, September 11-12, 1990.* Canepa, J.A., ed. LA-12325-C. Los Alamos, New Mexico: Los Alamos National Laboratory. ACC: NNA.19920421.0117.

Meijer, A. 1993. "Far-Field Transport of Carbon Dioxide: Retardation Mechanisms and Possible Validation Experiments." *Proceedings of the Topical Meeting on Site Characterization and Model Validation, FOCUS '93, September 26-29, 1993, Las Vegas, Nevada.* Pages 110-112. La Grange Park, Illinois: American Nuclear Society. TIC: 102245.

Meijer, A.; Triay, I.; Knight, S.; and Cisneros, M. 1990. "Sorption of Radionuclides on Yucca Mountain Tuffs." *Proceedings of the Topical Meeting on Nuclear Waste Isolation in the Unsaturated Zone, Focus '89, September 17-21, 1989, Las Vegas, Nevada.* Pages 113-117. La Grange Park, Illinois: American Nuclear Society. TIC: 212738.

Miekeley, N.; Couthinho de Jesus, H.; Porto da Silveira, C.L.; and Degueldre, C. 1992. "Chemical and Physical Characterization of Suspended Particles and Colloids in Waters from the Osamu Utsumi Mine and Morro do Ferro Analogue Study Sites, Poços-de-Caldas, Brazil." *Journal of Geochemical Exploration, 45,* 409-437. Amsterdam, The Netherlands: Elsevier Science Publishers B.V. TIC: 245687.

Milton, G.M. and Brown, R.M. 1987. "Adsorption of Uranium from Groundwater by Common Fracture Secondary Minerals." *Canadian Journal of Earth Sciences, 24,* 1321-1328. Ottawa, Ontario, Canada: National Research Council of Canada. TIC: 247350.

Moskvin, A.I. 1971. "Hydrolytic Behavior of Neptunium (IV,V,VI)." *Soviet Radiochemistry, 13,* (1), 700-705. New York, New York: Consultants Bureau. TIC: 245661.

Murphy, W.M. 1992. "Natural Analog Studies for Geologic Disposal of Nuclear Waste." *Technology Today,* Pages 16-21. San Antonio, Texas: Southwest Research Institute. TIC: 238853.

Neal, R.H.; Sposito, G.; Holtzclaw, K.M.; and Traina, S.J. 1987. "Selenite Adsorption on Alluvial Soils: I. Soil Composition and pH Effects." *Soil Science Society of America Journal, 51,* 1161-1165. Madison, Wisconsin: Soil Science Society of America. TIC: 237059.

Neck, V.; Kim, J.I.; and Kanellakopulos, B. 1992. "Solubility and Hydrolysis Behavior of Neptunium(V)." *Radiochimica Acta, 56,* 25-30. Munich, Germany: R. Oldenbourg Verlag. TIC: 224093.

Neck, V.; Runde, W.; and Kim, J.I. 1995. "Solid-Liquid Equilibria of Neptunium(V) in Carbonate Solutions of Different Ionic Strengths: II. Stability of the Solid Phases." *Journal of Alloys and Compounds, 225,* 295-302. Lausanne, Switzerland: Elsevier Science. TIC: 237061.

Neck, V.; Runde, W.; Kim, J.I.; and Kanellakopulos, B. 1994. "Solid-Liquid Equilibrium Reactions of Neptunium (V) in Carbonate Solution at Different Ionic Strength." *Radiochimica Acta, 65,* 29-37. München, Germany: R. Oldenbourg Verlag. TIC: 237467.

Neretnieks, I. 1990. *Solute Transport in Fractured Rock — Applications to Radionuclide Waste Repositories.* SKB Technical Report 90-38. Stockholm, Sweden: Swedish Nuclear Fuel and Waste Management Company. TIC: 208618.

Neuman, S.P. 1990. "Universal Scaling of Hydraulic Conductivities and Dispersivities in Geologic Media." *Water Resources Research, 26,* (8), 1749-1758. Washington, D.C.: American Geophysical Union. TIC: 237977.

Neuman, S.P.; Winter, C.L.; and Newman, C.M. 1987. "Stochastic Theory of Field-Scale Fickian Dispersion in Anisotropic Porous Media." *Water Resources Research, 23,* (3), 453-466. Washington, D.C.: American Geophysical Union. TIC: 225294.

Newton, T.W. 1975. *The Kinetics of the Oxidation-Reduction Reactions of Uranium, Neptunium, Plutonium, and Americium in Aqueous Solutions.* TID-26506. Oak Ridge, Tennessee: U.S. Energy Research and Development Administration. TIC: 239297.

Nimmo, J.R. and Akstin, K.C. 1988. "Hydraulic Conductivity of a Sandy Soil at Low Water Content After Compaction by Various Methods." *Soil Science Society of America Journal, 52,* (2), 303-310. Madison, Wisconsin: Soil Science Society of America. TIC: 224083.

Nimmo, J.R. and Mello, K.A. 1991. "Centrifugal Techniques for Measuring Saturated Hydraulic Conductivity." *Water Resources Research, 27,* (6), 1263-1269. Washington, D.C.: American Geophysical Union. TIC: 224084.

Nimmo, J.R.; Rubin, J.; and Hammermeister, D.P. 1987. "Unsaturated Flow in a Centrifugal Field: Measurement of Hydraulic Conductivity and Testing of Darcy's Law." *Water Resources Research, 23,* (1), 124-134. Washington, D.C.: American Geophysical Union. TIC: 216671.

Nitao, J.J. 1991. "Theory of Matrix and Fracture Flow Regimes in Unsaturated, Fractured Porous Media." *High Level Radioactive Waste Management, Proceedings of the Second Annual*

International Conference, Las Vegas, Nevada, April 28-May 3, 1991. 1, 845-852. La Grange Park, Illinois: American Nuclear Society. TIC: 204272.

Nitsche, H.; Gatti, R.C.; Standifer, E.M.; Lee, S.C.; Muller, A.; Prussin, T.; Deinhammer, R.S.; Maurer, H.; Becraft, K.; Leung, S.; and Carpenter, S.A. 1992. *Measured Solubilities and Speciations of Neptunium, Plutonium, and Americium in a Typical Groundwater (J-13) from the Yucca Mountain Region.* LBL-30958. Berkeley, California: Lawrence Berkeley National Laboratory. ACC: MOL.19960701.0272.

Nitsche, H.; Gatti, R.C.; Standifer, E.M.; Lee, S.C.; Muller, A.; Prussin, T.; Deinhammer, R.S.; Maurer, H.; Becraft, K.; Leung, S.; and Carpenter, S.A. 1993. *Measured Solubilities and Speciations of Neptunium, Plutonium, and Americium in Typical Groundwater (J-13) from the Yucca Mountain Region.* LA-12562-MS. Los Alamos, New Mexico: Los Alamos National Laboratory. ACC: MOL.19950621.0265.

Nitsche, H.; Roberts, K.; Prussin, T.; Muller, A.; Becraft, K.; Keeney, D.; Carpenter, S.A.; and Gatti, R.C. 1995. *Measured Solubilities and Speciations from Oversaturation Experiments of Neptunium, Plutonium and Americium in UE25p#1 Well Water from the Yucca Mountain Region.* LA-12563-MS. Los Alamos, New Mexico: Los Alamos National Laboratory. ACC: MOL.19951006.0171.

Noell, A.L.; Thompson, J.L.; Corapcioglu, M.Y.; and Triay, I.R. 1998. "The Role of Silica Colloids on Facilitated Cesium Transport Through Glass Bead Columns and Modeling." *Journal of Contaminant Hydrology, 31,* (1-2), 23-56. Amsterdam, The Netherlands: Elsevier Science B.V. TIC: 245510.

NRC (U.S. Nuclear Regulatory Commission) 1984. *Determination of Radionuclide Solubility in Groundwater for Assessment of High-Level Waste Isolation.* Washington, D.C.: U.S. Nuclear Regulatory Commission. ACC: HQS.19880517.2024.

Obeng, L.A.; Carrondo, M.J.T.; Perry, R.; and Lester, J.N. 1981. "The Influence of Zeolite Type A on Metal Concentrations in Water and Waste Water." *Journal of the American Oil Chemists' Society, 58,* (1), 81-85. Champaign, Illinois: American Oil Chemists' Society. TIC: 237902.

Ogard, A.E. and Kerrisk, J.F. 1984. *Groundwater Chemistry Along Flow Paths Between a Proposed Repository Site and the Accessible Environment.* LA-10188-MS. Los Alamos, New Mexico: Los Alamos National Laboratory. ACC: HQS.19880517.2031.

Ogard, A.E. and Vaniman, D.T., eds. 1985. *Research and Development Related to the Nevada Nuclear Waste Storage Investigations, July 1–September 30, 1984.* LA-10299-PR. Los Alamos, New Mexico: Los Alamos National Laboratory. ACC: NNA.19920922.0014.

Olhoeft, G.R. 1986. "Electrical Conductivity." *Eighth Workshop on Electromagnetic Induction in the Earth and Moon, Review Papers, Working Group 1-3, International Association of Geomagnetism and Aeronomy, August 25, 1986.* Pages 2-1 to 2-13. Neuchatel, Switzerland: Universite de Neuchatel, Observatoire Cantonal de Neuchatel. TIC: 247674.

O'Melia, C. and Tiller, C. 1993. "Physicochemical Aggregation and Deposition in Aquatic Environment." Chapter 8 of *Environmental Particles.* Buffle, J. and van Leeuwen, H.P., eds. Volume 2. Boca Raton, Florida: Lewis Publishers. TIC: 238504.

O'Melia, C.R. 1990. "Kinetics of Colloid Chemical Processes in Aquatic Systems." Chapter 16 of *Aquatic Chemical Kinetics, Reaction Rates of Processes in Natural Waters.* Stumm, W., ed. Pages 447-474. New York, New York: John Wiley & Sons. TIC: 245726.

Parks, G.A. and Pohl, D.C. 1988. "Hydrothermal Solubility of Uraninite." *Geochimica et Cosmochimica Acta, 52,* 863-875. New York, New York: Pergamon Press. TIC: 240879.

Payne, T.E.; Davis, J.A.; and Waite, T.D. 1990. "Modeling of Uranium Sorption to Substrates from the Weathered Zone in the Vicinity of the Koongarra Ore Body." *Alligator Rivers Analogue Project, First Annual Report 1988-89.* Duerden, P., ed. Menai, New South Wales, Australia: Australian Nuclear Science and Technology Organisation. TIC: 244780.

Pearcy, E.C.; Prikryl, J.D.; Murphy, W.M.; and Leslie, B.W. 1994. "Alteration of Uraninite from the Nopal I Deposit, Peña Blanca District, Chihuahua, Mexico, Compared to Degradation of Spent Nuclear Fuel in the Proposed U.S. High-Level Nuclear Waste Repository at Yucca Mountain, Nevada." *Applied Geochemistry, 9,* 713-732. New York, New York: Elsevier. TIC: 236934.

Pedersen, K. 1996. *Bacteria, Colloids, and Organic Carbon in Groundwater at the Bangombé Site in the Oklo Area.* SKB Technical Report 96-01. Stockholm, Sweden: Swedish Nuclear Fuel and Waste Management Company. TIC: 225494.

Penrose, W.R.; Polzer, W.L.; Essington, E.H.; Nelson, D.M.; and Orlandini, K.A. 1990. "Mobility of Plutonium and Americium Through a Shallow Aquifer in a Semiarid Region." *Environmental Science and Technology, 24,* 228-234. Washington, D.C.: American Chemical Society. TIC: 224113.

Philip, J.R.; Knight, J.H.; and Waechter, R.T. 1989. "Unsaturated Seepage and Subterranean Holes: Conspectus, and Exclusion Problem for Circular Cylindrical Cavities." *Water Resources Research, 25,* (1), 16-28. Washington, D.C.: American Geophysical Union. TIC: 239117.

Polzer, W.L. and Fuentes, H.R. 1988. "The Use of a Heterogeneity-Based Isotherm to Interpret the Transport of Reactive Radionuclides in Volcanic Tuff Media." *Radiochimica Acta, 44/45,* 361-365. München, Germany: R. Oldenbourg Verlag. TIC: 240183.

Pourbaix, M. 1966. *Atlas of Electrochemical Equilibria in Aqueous Solutions.* Long Island City, New York: Pergamon Press. TIC: 240774.

Rai, D.; Felmy, A.R.; and Ryan. J.L. 1990. "Uranium(IV) Hydrolysis Constants and Solubility Product of $UO_2.xH_2O$(am)." *Inorganic Chemistry, 29,* 260-264. Washington, D.C.: American Chemical Society. TIC: 237466.

Rai, D.; Serne, R.J.; and Moore, D.A. 1980. "Solubility of Plutonium Compounds and Their Behavior in Soils." *Soil Science Society of America Journal, 44,* 490-495. Madison, Wisconsin: Soil Science Society of America. TIC: 219108.

Rai, D. and Zachara, J.M. 1984. *A Critical Review.* Volume 1 of *Chemical Attenuation Rates, Coefficients, and Constants in Leachate Migration.* EPRI EA-3356. Palo Alto, California: Electric Power Research Institute. TIC: 237846.

Rard, J.A. 1983. *Critical Review of the Chemistry and Thermodynamics of Technetium and Some of Its Inorganic Compounds and Aqueous Species.* UCRL-53440. Livermore, California: Lawrence Livermore National Laboratory. ACC: MOL.19990908.0231.

Rechard, R.P., ed. 1995. *Executive Summary.* Volume 1 of *Performance Assessment of the Direct Disposal in Unsaturated Tuff of Spent Nuclear Fuel and High-Level Waste Owned by U.S. Department of Energy.* SAND94-2563/1. Albuquerque, New Mexico: Sandia National Laboratories. TIC: 237101.

Reimus, P.W.; Adams, A.; Haga, M.J.; Humphrey, A.; Callahan, T.; Anghel, I.; and Counce, D. 1999. *Results and Interpretation of Hydraulic and Tracer Testing in the Prow Pass Tuff at the C-Holes.* Milestone SP32E7M4. Los Alamos, New Mexico: Los Alamos National Laboratory. TIC: 246377.

Rimstidt, J.D.; Newcomb, W.D.; and Shettel, J.L., Jr. 1989. "A Vertical Thermal Gradient Experiment to Simulate Conditions in Vapor Dominated Geothermal Systems, Epithermal Gold Deposits, and High Level Radioactive Repositories in Unsaturated Media." *Proceedings of the 6th International Symposium on Water-Rock Interaction, WRI-6, Malvern, United Kingdom, August 3-8, 1989.* Miles, D.L., ed. Pages 585-588. Rotterdam, The Netherlands: A.A. Balkema. TIC: 241868.

Robinson, B.A.; Wolfsberg, A.V.; Zyvoloski, G.A.; and Gable, C.W. 1995. *An Unsaturated Zone Flow and Transport Model of Yucca Mountain.* Milestone 3468. Draft. Los Alamos, New Mexico: Los Alamos National Laboratory. ACC: MOL.19960415.0218.

Rogers, P.S.Z.; Meijer, A.; and Kung, K.H. 1994. *Sorption Characteristics of Yucca Mountain Tuffs as a Function of Particle Size.* Los Alamos, New Mexico: Los Alamos National Laboratory. ACC: NNA.19921105.0046.

Rosch, F.; Milanov, M.; Hung, T.K.; Ludwig, R.; Buklanov, G.V.; and Khalkin, V.A. 1987. "Electromigration of Carrier-Free Radionuclides, 5. Ion Mobilities and Hydrolysis of Np(V) in Aqueous Perchlorate Solutions." *Radiochimica Acta, 42,* (1), 43-46. München, Germany: R. Oldenbourg Verlag. TIC: 245662.

Rosholt, J.N.; Prijana; and Noble, D.C. 1971. "Mobility of Uranium and Thorium in Glassy and Crystallized Silicic Volcanic Rocks." *Economic Geology, 66,* 1061-1069. El Paso, Texas: Economic Geology Publishing Company. TIC: 219186.

Rubin, Y. 1990. "Stochastic Modeling of Macrodispersion in Heterogeneous Porous Media." *Water Resources Research, 26,* (1), 133-141. Washington, D.C.: American Geophysical Union. TIC: 247179.

Rundberg, R.S. 1987. *Assessment Report on the Kinetics of Radionuclide Adsorption on Yucca Mountain Tuff.* LA-11026-MS. Los Alamos, New Mexico: Los Alamos National Laboratory. ACC: NNA.19930405.0075.

Rundberg, R.S.; Ogard, A.E.; and Vaniman, D.T., eds. 1985. *Research and Development Related to the Nevada Nuclear Waste Storage Investigations, April 1–June 30, 1984.* LA-10297-PR. Los Alamos, New Mexico: Los Alamos National Laboratory. ACC: NNA.19920922.0018.

Rundberg, R.S.; Partom, I.; Ott, M.A.; Mitchell, A.J.; and Birdsell, K. 1987. *Diffusion of Nonsorbing Tracers in Yucca Mountain Tuff.* Milestone R524. Los Alamos, New Mexico: Los Alamos National Laboratory. ACC: NNA.19930405.0074.

Runde, W. and Kim, J.I. 1994. *Chemisches Verhalten von Drei- und Fünfwertigem Americium in Salinen NaCl-Lösungen.* RCM 01094. Garching, Germany: Technische Universitat München. TIC: 241857.

Runde, W.; Meinrath, G.; and Kim, J.I. 1992. "A Study of Solid-Liquid Phase Equilibria of Trivalent Lanthanide and Actinide Ions in Carbonate Systems." *Radiochimica Acta, 58/59,* 93-100. München, Germany: R. Oldenbourg Verlag. TIC: 237409.

Russo, D. 1988. "Determining Soil Hydraulic Properties by Parameter Estimation: On the Selection of a Model for the Hydraulic Properties." *Water Resources Research, 24,* (3), 453-459. Washington, D.C.: American Geophysical Union. TIC: 247182.

Russo, D. 1993. "Stochastic Modeling of Macrodispersion for Solute Transport in a Heterogeneous Unsaturated Porous Formation." *Water Resources Research, 29,* (2), 383-397. Washington, D.C.: American Geophysical Union. TIC: 247755.

Russo, D. 1995a. "On the Velocity Covariance and Transport Modeling in Heterogeneous Anisotropic Porous Formations, 2. Unsaturated Flow." *Water Resources Research, 31,* (1), 139-145. Washington, D.C.: American Geophysical Union. TIC: 247181.

Russo, D. 1995b. "Stochastic Analysis of the Velocity Covariance and the Displacement Covariance Tensors in Partially Saturated Heterogeneous Anisotropic Porous Formations." *Water Resources Research, 31,* (7), 1647-1658. Washington, D.C.: American Geophysical Union. TIC: 247180.

Ryan, J.L. and Rai, D. 1983. "The Solubility of Uranium(IV) Hydrous Oxide in Sodium Hydroxide Solutions Under Reducing Conditions." *Polyhedron, 2,* (9), 947-952. Oxford, United Kingdom: Pergamon Press. TIC: 236941.

Sanchez, A.L.; Murray, J.W.; and Sibley, T.H. 1985. "The Adsorption of Plutonium IV and V on Goethite." *Geochimica et Cosmochimica Acta, 49,* (11), 2297-2307. New York, New York: Pergamon Press. TIC: 224091.

Schenker, A.R.; Guerin, D.C.; Robey, T.H.; Rautman, C.A.; and Barnard, R.W. 1995. *Stochastic Hydrogeologic Units and Hydrogeologic Properties Development for Total-System Performance Assessments.* SAND94-0244. Albuquerque, New Mexico: Sandia National Laboratories. ACC: MOL.19960318.0528.

Scott, R.B. and Bonk, J. 1984. *Preliminary Geologic Map of Yucca Mountain, Nye County, Nevada, with Geologic Sections.* Open-File Report 84-494. Denver, Colorado: U.S. Geological Survey. TIC: 203162.

Seaman, J.C.; Bertsch, P.M.; and Miller, W.P. 1995. "Chemical Controls on Colloid Generation and Transport in a Sandy Aquifer." *Environmental Science and Technology, 29,* (7), 1808-1815. Washington, D.C.: American Chemical Society. TIC: 237337.

Siegel, M.D.; Hopkins, P.L.; Glass, R.J.; and Ward, D.B. 1992. "Design of an Intermediate-Scale Experiment to Validate Unsaturated-Zone Transport Models." *High Level Radioactive Waste Management, Proceedings of the Third International Conference, Las Vegas, Nevada, April 12-16, 1992. 2,* 1972-1984. La Grange Park, Illinois: American Nuclear Society. TIC: 4447.

Siegel, M.D.; Ward, D.B.; Cheng, W.C.; Bryant, C.; Chocas, C.S.; and Reynolds, C.G. 1993. "Preliminary Characterization of Materials for a Reactive Transport Model Validation Experiment." *High Level Radioactive Waste Management, Proceedings of the Fourth Annual International Conference, Las Vegas, Nevada, April 26-30, 1993. 1,* 348-356. La Grange Park, Illinois: American Nuclear Society. TIC: 208542.

Silva, R.J.; Bidoglio, G.; Rand, M.H.; Robouch, P.B.; Wanner, H.; and Puigdomenech, I. 1995. *Chemical Thermodynamics of Americium.* Volume 2 of *Chemical Thermodynamics.* Amsterdam, The Netherlands: Elsevier Science Publishers B.V. TIC: 237106.

Snelling, A.A. 1980. "Uraninite and Its Alteration Products, Koongarra Uranium Deposit." *Proceedings of International Uranium Symposium on the Pine Creek Geosyncline, 1980.* [Ferguson, J. and Goleby, A.B., eds.]. Pages 487-498. [Vienna, Austria: International Atomic Energy Agency]. TIC: 236806.

Snelling, A.A. and Dickson, B.L. 1979. "Uranium/Daughter Disequilibrium in the Koongarra Uranium Deposit, Australia." *Mineralium Deposita, 14,* 109-118. New York, New York: Springer-Verlag. TIC: 237067.

Snodgrass, W.J. 1980. "Distribution and Behavior of Nickel in the Aquatic Environment." Chapter 9 of *Nickel in the Environment.* Pages 203-274. New York, New York: John Wiley & Sons. TIC: 237686.

Sposito, G. 1989. *The Chemistry of Soils.* New York, New York: Oxford University Press. TIC: 237211.

Stakebake, J.L.; Larson, D.T.; and Haschke, J.M. 1993. "Characterization of the Plutonium-Water Reaction II: Formation of a Binary Oxide Containing Pu(VI)." *Journal of Alloys and Compounds, 202,* 251-263. Lausanne, Switzerland: Elsevier Seqouia. TIC: 241265.

Stephens, D.B. and Rehfeldt, K.R. 1985. "Evaluation of Closed-Form Analytical Models to Calculate Conductivity in a Fine Sand." *Soil Science Society of America Journal, 49,* 12-19. Madison, Wisconsin: Soil Science Society of America. TIC: 224082.

Sumner, M.E. and Miller, W.P. 1996. "Cation Exchange Capacity and Exchange Coefficients." *Methods of Soil Analysis, Part 3: Chemical Methods.* SSSA Book Series No. 5. Pages 1201-1229. Madison, Wisconsin: Soil Science Society of America. TIC: 245720.

Szabo, B.J. and Kyser, T.K. 1990. "Ages and Stable-Isotope Compositions of Secondary Calcite and Opal in Drill Cores from Tertiary Volcanic Rocks of the Yucca Mountain Area, Nevada." *Geological Society of America Bulletin, 102,* 1714-1719. Boulder, Colorado: Geological Society of America. TIC: 221927.

Tait, C.D.; Clark, D.L.; Neu, M.P.; and Hobart, D.E. 1996. *Specific Ion Interaction Theory Studies.* Milestone 3792M. Los Alamos, New Mexico: Los Alamos National Laboratory. ACC: MOL.19961231.0094.

Theis, T.L. and Richter, R.O. 1980. "Adsorption Reactions of Nickel Species at Oxide Surfaces." Chapter 4 of *[Particulates in Water: Characterization, Fate, Effects, and Removal.* Advances in Chemistry Series Volume 189. Kavanaugh, M.C. and Leckie, J.O., eds. Washington, D.C.]: American Chemical Society. TIC: 236944.

Thomas, K.W. 1987. *Summary of Sorption Measurements Performed with Yucca Mountain, Nevada, Tuff Samples and Water from Well J-13.* LA-10960-MS. Los Alamos, New Mexico: Los Alamos National Laboratory. ACC: NNA.19900604.0045.

Thomas, K.W. 1988. *Research and Development Related to the Nevada Nuclear Waste Storage Investigations, October 1-December 31, 1984.* LA-11443-PR. Los Alamos, New Mexico: Los Alamos National Laboratory. ACC: NNA.19920131.0372.

Torstenfelt, B.; Rundberg, R.S.; and Mitchell, A.J. 1988. "Actinide Sorption on Granites and Minerals as a Function of pH and Colloids/Pseudocolloids." *Radiochimica Acta, 44/45,* 111-117. München, Germany: R. Oldenbourg Verlag. TIC: 237496.

Travis, B.J. and Birdsell, K.H. 1991. *TRACR3D: A Model of Flow and Transport in Porous Media, Model Description and User's Manual.* LA-11798-M. Los Alamos, New Mexico: Los Alamos National Laboratory. TIC: 201398.

Triay, I.; Degueldre, C.; Wistrom, A.; Cotter, C.; and Lemons, W. 1996d. *Progress Report on Colloid-Facilitated Transport at Yucca Mountain.* LA-12959-MS. Los Alamos, New Mexico: Los Alamos National Laboratory. TIC: 225473.

Triay, I.; Simmons, A.; Levy, S.; Nelson, S.; Nuttall, H.; Robinson, B.; Steinkampf, W.; and Viani, B. 1995. *Colloid-Facilitated Radionuclide Transport at Yucca Mountain.* LA-12779-

MS. Los Alamos, New Mexico: Los Alamos National Laboratory. ACC: NNA.19930628.0067.

Triay, I.R.; Birdsell, K.H.; Mitchell, A.J.; and Ott, M.A. 1993b. "Diffusion of Sorbing and Non-Sorbing Radionuclides." *High Level Radioactive Waste Management, Proceedings of the Fourth Annual International Conference, Las Vegas, Nevada, April 26-30, 1993. 2,* 1527-1532. La Grange Park, Illinois: American Nuclear Society. TIC: 208542.

Triay, I.R.; Cotter, C.R.; Huddleston, M.H.; Leonard, D.E.; Weaver, S.C.; Chipera, S.J.; Bish, D.L.; Meijer, A.; and Canepa, J.A. 1996a. *Batch Sorption Results for Neptunium Transport Through Yucca Mountain Tuffs.* LA-12961-MS. Los Alamos, New Mexico: Los Alamos National Laboratory. ACC: MOL.19980924.0050.

Triay, I.R.; Cotter, C.R.; Kraus, S.M.; Huddleston, M.H.; Chipera, S.J.; and Bish, D.L. 1996b. *Radionuclide Sorption in Yucca Mountain Tuffs with J-13 Well Water: Neptunium, Uranium, and Plutonium.* LA-12956-MS. Los Alamos, New Mexico: Los Alamos National Laboratory. TIC: 226117.

Triay, I.R.; Furlano, A.C.; Weaver, S.C.; Chipera, S.J.; and Bish, D.L. 1996c. *Comparison of Neptunium Sorption Results Using Batch and Column Techniques.* LA-12958-MS. Los Alamos, New Mexico: Los Alamos National Laboratory. ACC: MOL.19980924.0049.

Triay, I.R.; Hobart, D.E.; Mitchell, A.J.; Newton, T.W.; Ott, M.A.; Palmer, P.D.; Rundberg, R.S.; and Thompson, J.L. 1991b. "Size Determinations of Plutonium Colloids Using Autocorrelation Photon Spectroscopy." *Radiochimica Acta, 52/53,* 127-131. Munich, Germany: R. Oldenbourg Verlag. TIC: 222703.

Triay, I.R.; Meijer, A.; Cisneros, M.R.; Miller, G.G.; Mitchell, A.J.; Ott, M.A.; Hobart, D.E.; Palmer, P.D.; Perrin, R.E.; and Aguilar, R.D. 1991a. "Sorption of Americium in Tuff and Pure Minerals Using Synthetic and Natural Groundwaters." *Radiochimica Acta, 52/53,* 141-145. München, Germany: R. Oldenbourg Verlag. TIC: 222704.

Triay, I.R.; Meijer, A.; Conca, J.L.; Kung, K.S.; Rundberg, R.S.; Strietelmeier, B.A.; and Tait, C.D. 1997. *Summary and Synthesis Report on Radionuclide Retardation for the Yucca Mountain Site Characterization Project.* Eckhardt, R.C., ed. LA-13262-MS. Los Alamos, New Mexico: Los Alamos National Laboratory. ACC: MOL.19971210.0177.

Triay, I.R.; Robinson, B.A.; Lopez, R.M.; Mitchell, A.J.; and Overly, C.M. 1993a. "Neptunium Retardation with Tuffs and Groundwaters from Yucca Mountain." *High Level Radioactive Waste Management, Proceedings of the Fourth International Conference, Las Vegas, Nevada, April 26-30, 1993. 2,* 1504-1508. La Grange Park, Illinois: American Nuclear Society. TIC: 208542.

Tsuji, M. and Komarneni, S. 1993. "Selectivity Study of Alkaline Earth and Divalent Transition Metal Ions on [Al^{3+}-Na^{+}]-Substituted Tobermorites." *Separation Science and Technology, 28,* (11&12), 2061-2071. New York, New York: Marcel Dekker. TIC: 236894.

Tsunashima, A.; Brindley, G.W.; and Bastovanov, M. 1981. "Adsorption of Uranium from Solutions by Montmorillonite: Compositions and Properties of Uranyl Montmorillonites." *Clays and Clay Minerals, 29,* (1), 10-16. Boulder, Colorado: Clay Minerals Society. TIC: 236914.

Vanderborght, J.; Vanclooster, M.; Mallants, D.; Diels, J.; and Feyen, J. 1996. "Determining Convective Lognormal Solute Transport Parameters from Resident Concentration Data." *Soil Science Society of America Journal, 60,* (5), 1306-1317. Madison, Wisconsin: Soil Science Society of America. TIC: 247183.

van Genuchten, M.T. 1980. "A Closed-Form Equation for Predicting the Hydraulic Conductivity of Unsaturated Soils." *Soil Science Society of America Journal, 44,* (5), 892-898. Madison, Wisconsin: Soil Science Society of America. TIC: 217327.

Vaniman, D.; Furlano, A.; Chipera, S.; Thompson, J.; and Triay, I. 1996. "Microautoradiography in Studies of Pu(V) Sorption by Trace and Fracture Minerals in Tuff." *Scientific Basis for Nuclear Waste Management XIX, Symposium held November 27-December 1, 1995, Boston, Massachusetts.* Murphy, W.M. and Knecht, D.A., eds. *412,* 639-646. Pittsburgh, Pennsylvania: Materials Research Society. TIC: 233877.

Vaniman, D.T. 1993a. *Calcite Deposits in Drill Cores USW G-2 and USW GU-3/G-3 at Yucca Mountain, Nevada.* TWS-EES-1-7-92-2, Rev. 1. Los Alamos, New Mexico: Los Alamos National Laboratory. ACC: NNA.19931018.0075.

Vaniman, D.T. 1993b. "Calcite Deposits in Fractures at Yucca Mountain, Nevada." *High Level Radioactive Waste Management, Proceedings of the Fourth Annual International Conference, Las Vegas, Nevada, April 26-30, 1993. 2,* 1935-1939. La Grange Park, Illinois: American Nuclear Society. TIC: 208542.

Vilks, P.; Cramer, J.J.; Bachinski, D.B.; Doern, D.C.; and Miller, H.G. 1993. "Studies of Colloids and Suspended Particles, Cigar Lake Uranium Deposit, Saskatchewan, Canada." *Applied Geochemistry, 8,* (6), 605-616. London, England: Pergamon Press. TIC: 237449.

Vilks, P. and Degueldre, C. 1991. "Sorption Behavior of ^{85}Sr, ^{131}I and ^{137}Cs on Colloids and Suspended Particles from the Grimsel Test Site, Switzerland." *Applied Geochemistry, 6,* 553-563. London, England: Pergamon Press. TIC: 236931.

Vilks, P.; Miller, H.G.; and Doern, D.C. 1991. "Natural Colloids and Suspended Particles in the Whiteshell Research Area, Manitoba, Canada, and Their Potential Effect on Radiocolloid Formation." *Applied Geochemistry, 6,* (5), 565-574. London, England: Pergamon Press. TIC: 237339.

Volkov, Y.F.; Visyashcheva, G.I.; Tomilin, S.V.; Kapshukov, I.I.; and Rykov, A.G. 1981. "Study of Carbonate Compounds of Pentavalent Actinides with Alkali-Metal Cations. X. Composition and Crystal Structure of Carbonates." *Radiokhimiya (English Translation), 23,* (2), 200-204. New York, New York: Plenum Publishing Corporation. TIC: 239010.

Volkov, Y.F.; Visyashcheva, G.I.; Tomilin, S.V.; Spiryakov, V.I.; Kapshukov, I.I.; and Rykov, A.G. 1980. "Carbonate Compounds of Pentavalent Actinides with Alkali Metal Cations. VII. Synthesis and Crystal Structure of Hydrate Compounds with the Composition $Na_{0.6}NpO_2(CO_3)_{0.8} \cdot nH_2O$." *Radiokhimiya (English Translation), 21,* (5), 583-590. New York, New York: Plenum Publishing Corporation. TIC: 240213.

Waite, T.O.; Davis, J.A.; Payne, T.E.; Waychunas, G.A.; and Xu, N. 1994. "Uranium(VI) Adsorption to Ferrihydrite: Application of a Surface Complexation Model." *Geochimica et Cosmochimica Acta, 58,* (24), 5465-5478. Oxford, England: Elsevier Science. TIC: 226322.

Wan, J. and Tokunaga, T.K. 1997. "Film Straining on Colloids in Unsaturated Porous Media: Conceptual Model and Experimental Testing." *Environmental Science and Technology, 31,* (8), 2413-2420. Washington, D.C.: American Chemical Society. TIC: 234804.

Whelan, J.F.; Vaniman, D.T.; Stuckless, J.S.; and Moscati, R.J. 1994. "Paleoclimatic and Paleohydrologic Records from Secondary Calcite: Yucca Mountain, Nevada." *High Level Radioactive Waste Management, Proceedings of the Fifth Annual International Conference, Las Vegas, Nevada, May 22-26, 1994. 4,* 2738-2745. La Grange Park, Illinois: American Nuclear Society. TIC: 210984.

White, A.F.; Benson, S.M.; Yee, A.W.; Wollenberg, H.A., Jr.; and Flexser, S. 1991. "Groundwater Contamination at the Kesterson Reservoir, California, 2. Geochemical Parameters Influencing Selenium Mobility." *Water Resources Research, 27,* (6), 1085-1098. Washington, D.C.: American Geophysical Union. TIC: 237455.

Wilson, C.N. 1990. *Results from NNWSI Series 3 Spent Fuel Dissolution Tests.* PNL-7170. Richland, Washington: Pacific Northwest Laboratory. ACC: NNA.19900329.0142.

Wilson, C.N. and Bruton, C.J. 1990. "Studies on Spent Fuel Dissolution Behavior Under Yucca Mountain Repository Conditions." *[Nuclear Waste Management III, Proceedings of the Fourth International Symposium on Ceramics in Nuclear Waste Management, held in Indianapolis, Indiana, April 24-26, 1989].* Pages 423-442. [Westerville, Ohio: American Ceramic Society]. TIC: 235673.

Wilson, M.L.; Gauthier, J.H.; Barnard, R.W.; Barr, G.E.; Dockery, H.A.; Dunn, E.; Eaton, R.R.; Guerin, D.C.; Lu, N.; Martinez, M.J.; Nilson, R.; Rautman, C.A.; Robey, T.H.; Ross, B.; Ryder, E.E.; Schenker, A.R.; Shannon, S.A.; Skinner, L.H.; Halsey, W.G.; Gansemer, J.D.; Lewis, L.C.; Lamont, A.D.; Triay, I.R.; Meijer, A.; and Morris, D.E. 1994. *Total-System Performance Assessment for Yucca Mountain – SNL Second Iteration (TSPA-1993).* SAND93-2675. Executive Summary and two volumes. Albuquerque, New Mexico: Sandia National Laboratories. ACC: NNA.19940112.0123.

Winter, C.L.; Newman, C.M.; and Neuman, S.P. 1984. "A Perturbation Expansion for Diffusion in a Random Velocity Field." *SIAM Journal of Applied Mathematics, 44,* (2), 411-424. Philadelphia, Pennsylvania: Society for Industrial and Applied Mathematics. TIC: 247189.

Yajima, T.; Kawamura, Y.; and Ueta, S. 1995. "Uranium(IV) Solubility and Hydrolysis Constants Under Reduced Conditions." *Scientific Basis for Nuclear Waste Management XVIII, Symposium held October 23-27, 1994, Kyoto, Japan.* Murakami, T. and Ewing, R.C., eds. *353,* 1137-1142. Pittsburgh, Pennsylvania: Materials Research Society. TIC: 216341.

Yeh, T.-C.; Gelhar, L.W.; and Gutjahr, A.L. 1985b. "Stochastic Analysis of Unsaturated Flow in Heterogeneous Soils, 2. Statistically Anisotropic Media with Variable α." *Water Resources Research, 21,* (4), 457-464. Washington, D.C.: American Geophysical Union. TIC: 239649.

Yeh, T.-C.J.; Gelhar, L.W.; and Gutjahr, A.L. 1985a. "Stochastic Analysis of Unsaturated Flow in Heterogeneous Soils 1. Statistically Isotropic Media." *Water Resources Research, 21,* (4), 447-456. Washington, D.C.: American Geophysical Union. TIC: 216857.

Zhang, D. 1999. "Nonstationary Stochastic Analysis of Transient Unsaturated Flow in Randomly Heterogeneous Media." *Water Resources Research, 35,* (4), 1127-1141. Washington, D.C.: American Geophysical Union. TIC: 247193.

Zhang, D. and Neuman, S.P. 1995. "Eulerian-Lagrangian Analysis of Transport Conditioned on Hydraulic Data, 1. Analytical-Numerical Approach." *Water Resources Research, 31,* (1), 39-51. Washington, D.C.: American Geophysical Union. TIC: 247195.

Zhang, D. and Neuman, S.P. 1996a. "Effect of Local Dispersion on Solute Transport in Randomly Heterogeneous Media." *Water Resources Research, 32,* (9), 2715-2723. Washington, D.C.: American Geophysical Union. TIC: 247197.

Zhang, D. and Neuman, S.P. 1996b. "Head and Velocity Covariances Under Quasi-Steady State Flow and Their Effects on Advective Transport." *Water Resources Research, 32,* (1), 77-83. Washington, D.C.: American Geophysical Union. TIC: 247196.

Zhang, D.; Wallstrom, T.C.; and Winter, C.L. 1998. "Stochastic Analysis of Steady-State Unsaturated Flow in Heterogeneous Media: Comparison of the Brooks-Corey and Gardner-Russo Models." *Water Resources Research, 34,* (6), 1437-1449. Washington, D.C.: American Geophysical Union. TIC: 247194.

Zhang, D. and Winter, C.L. 1998. "Nonstationary Stochastic Analysis of Steady State Flow Through Variably Saturated, Heterogeneous Media." *Water Resources Research, 34,* (5), 1091-1100. Washington, D.C.: American Geophysical Union. TIC: 247192.

Zielinski, R.A. 1980. "Uranium in Secondary Silica: A Possible Exploration Guide." *Economic Geology, 75,* 592-602. El Paso, Texas: Economic Geology Publishing Company. TIC: 237418.

Zielinski, R.A. 1983. *Evaluation of Ash-Flow Tuffs as Hosts for Radioactive Waste: Criteria Based on Selective Leaching of Manganese Oxides.* Open-File Report 83-480. Denver, Colorado: U.S. Geological Survey. ACC: HQS.19880517.1582.

Zielinski, R.A.; Bush, C.A.; Spengler, R.W.; and Szabo, B.J. 1986. "Rock-Water Interaction in Ash-Flow Tuffs (Yucca Mountain, Nevada, U.S.A.) – The Record from Uranium Studies."

Uranium, 2, 361-386. Amsterdam, The Netherlands: Elsevier Science Publishers B.V. TIC: 222472.

Zyvoloski, G.A.; Robinson, B.A.; Dash, Z.V.; and Trease, L.L. 1997. *User's Manual for the FEHM Application – A Finite-Element Heat- and Mass-Transfer Code.* LA-13306-M. Los Alamos, New Mexico: Los Alamos National Laboratory. TIC: 235999.

10.9.2 Source Data, Listed by Data Tracking Number

LA0003NL831352.001. Experimental Data on Sorption and Desorption Amounts for Plutonium Onto Clay Colloids. Submittal date: 03/16/2000.

LA0004NL831352.001. Pu(IV) and Pu(V) Sorption on Hematite and Geothite Colloids with Natural and Synthetic J-13 Water (1997-98 Data). Submittal date: 04/04/2000.

LA0004NL831352.003. Pu(IV) and Pu(V) Sorption and Desorption Studies with Silica Colloids, Utilizing Natural and Synthetic J-13 Water (1997-98 Data). Submittal date: 04/04/2000.

LA0005NL831352.001. The Kd Values of ^{243}Am on Colloids of Hematite, Montmorillonite and Silica in Natural and Synthetic Groundwater. Submittal date: 05/03/2000.

LA9909WS831372.013. Busted Butte Samples Used for Hydrologic Characterization. Submittal date: 10/13/1999.

LAIT831341AQ98.001. Effects of Organics on Plutonium Sorption. Submittal date: 09/30/1998.

LAJC831321AQ98.005. Quantitative XRD Results for Drill Core USW SD-7, USW SD-9, USW SD-12 and UE-25 UZ#16. Submittal date: 10/27/1998.

LB970601233129.001. The Site-Scale Unsaturated Zone Model of Yucca Mountain, Nevada for the Viability Assessment. Submittal date: 06/09/1997.

INTENTIONALLY LEFT BLANK

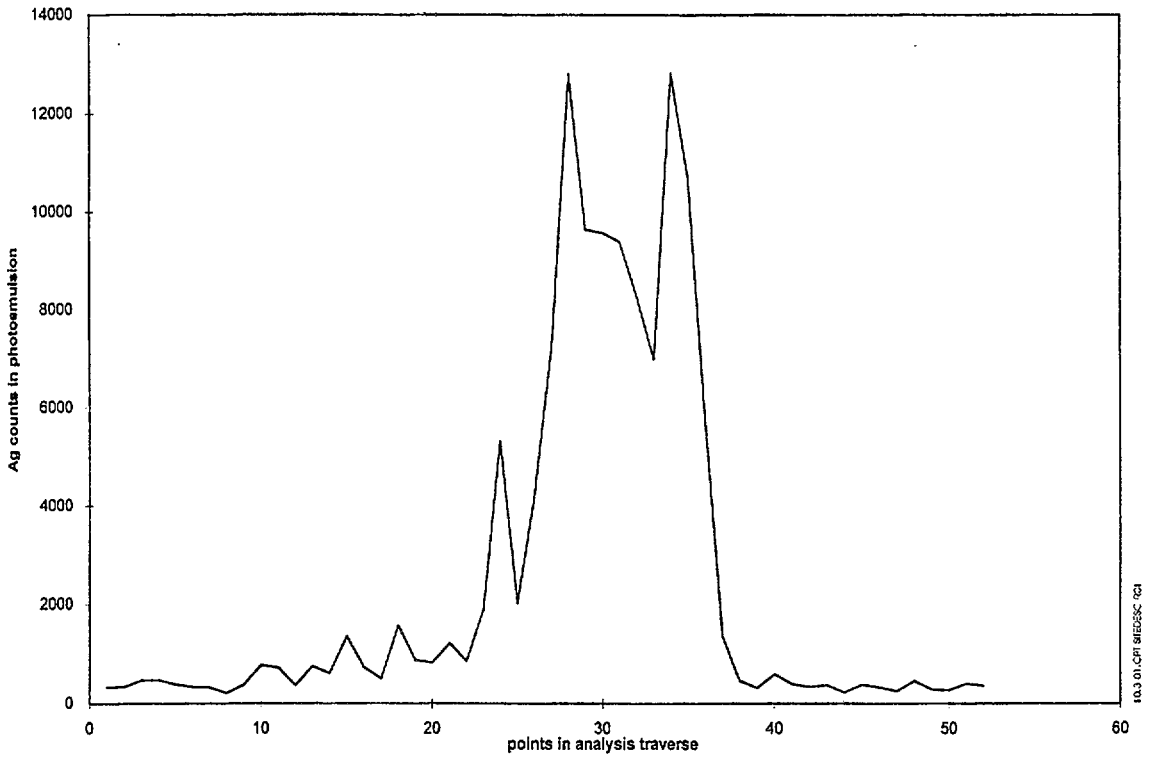

Source: CRWMS M&O (1997, Figure 1)

NOTE: The linescan crosses a fracture with smectite-lined walls; matrix on either side is zeolitic. Open fracture is approximately at point 33 (10 µm beam, 15 s/point, and 12 µm between analytical points).

Figure 10.3-1. Electron Microprobe Linescan for Silver in a Microautoradiography Photoemulsion

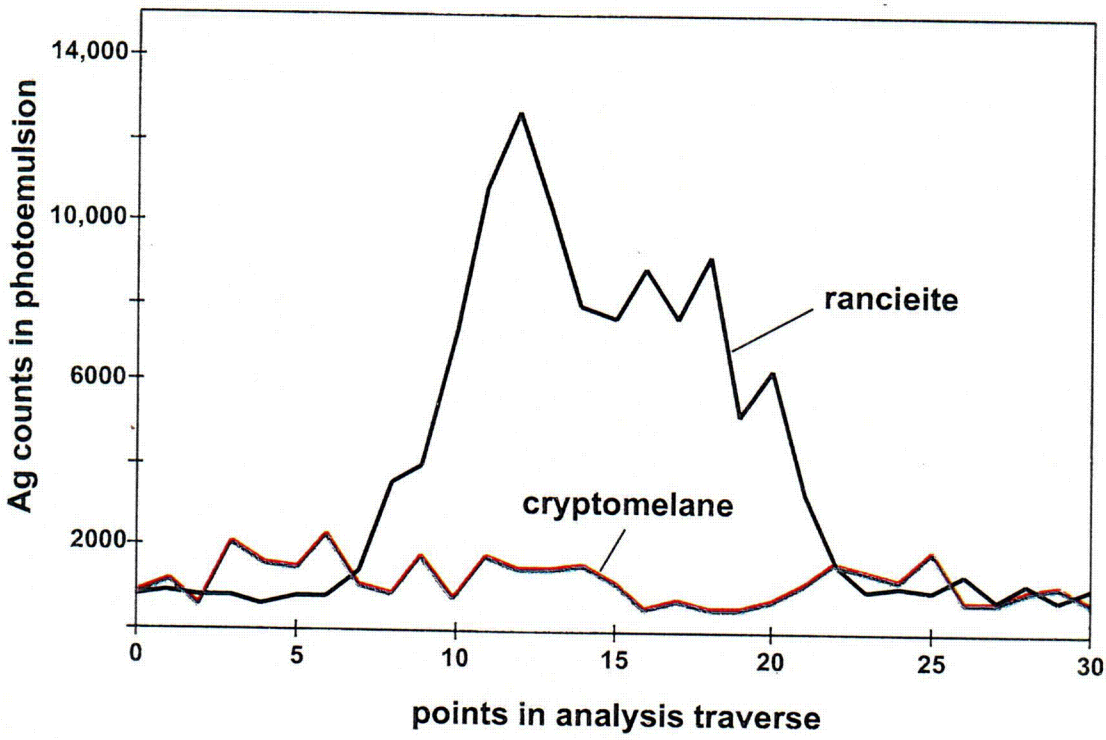

Source: Eckhardt (2000)

NOTE: The linescans cross two different manganese-oxide bodies exposed to similar plutonium-bearing solutions: (1) a rancieite body within zeolitic tuff and (2) cryptomelane lining a fracture in devitrified tuff (both linescans collected with a 10 µm beam, 15 s/point, and 12 µm between analytical points).

Figure 10.3-2. Electron Microprobe Linescans for Silver in Two Microautoradiography Photoemulsions

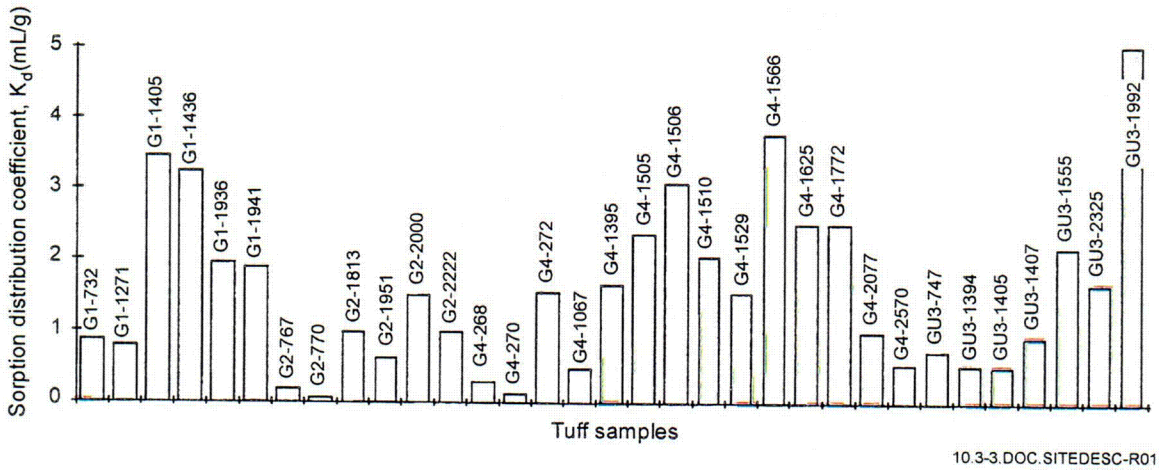

Source: CRWMS M&O (2000, Figure 1)

NOTE: These values of the batch-sorption distribution coefficient, K_d, illustrate the limited sorption of neptunium onto a large range of Yucca Mountain tuffs in J-13 well water under atmospheric conditions. The initial neptunium concentration ranged from 6 to 8 x 10^{-7} M. The tuffs were wet-sieved to particle sizes that ranged from 75 to 500 µm. The pretreatment period was 2 to 14 days; the sorption period was 3 to 23 days.

Figure 10.3-3. Neptunium Sorption in J-13 Well Water

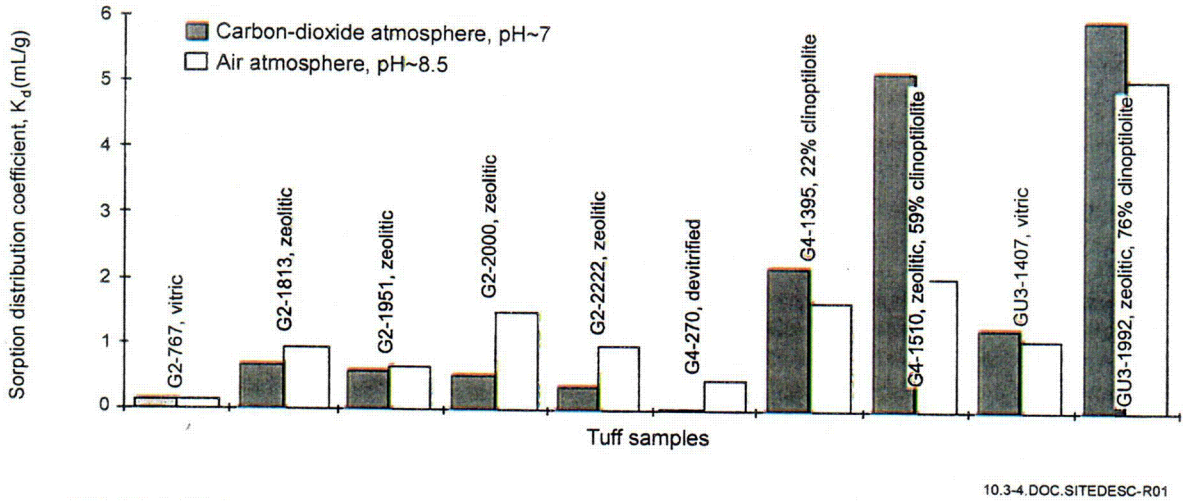

Source: CRWMS M&O (2000, Figure 2)

NOTE: Experimental values of K_d for the sorption of neptunium onto tuffs in J-13 water at initial concentrations of 6 to 7 x 10^{-7} M are compared for atmospheric conditions (pH of about 8.5) and a carbon-dioxide overpressure (pH of about 7). Tuffs were wet-sieved (75 to 500 µm); the pretreatment period was 2 to 3 days; the sorption period was 3 to 5 days.

Figure 10.3-4. The pH Dependence of Neptunium Sorption onto Tuffs at 10^{-7} M

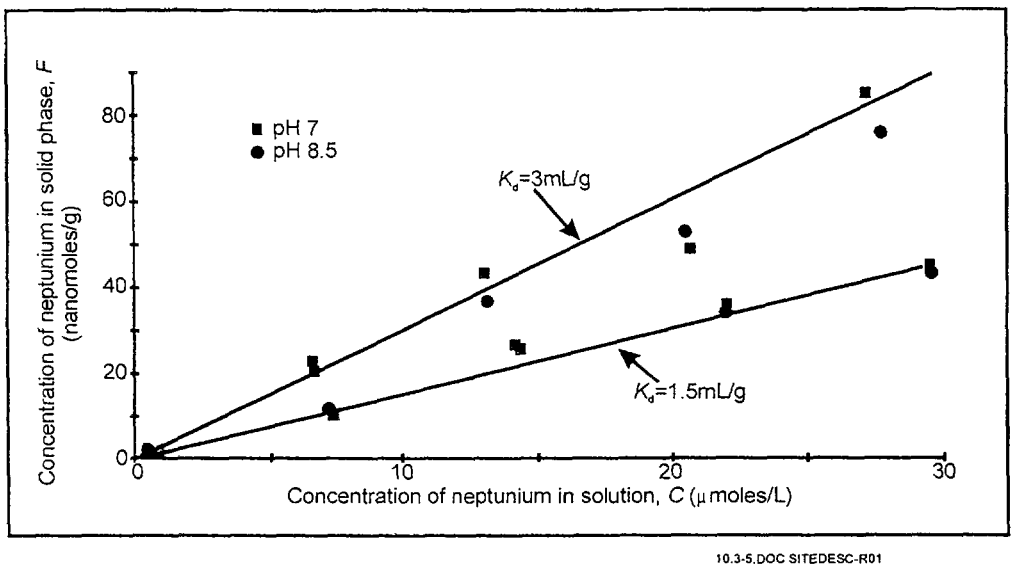

Source: CRWMS M&O (2000, Figure 3)

NOTE: A plot is shown of the concentration, *F*, of neptunium in the solid phase of the clinoptilolite-rich tuff G4-1510 versus the concentration, C, of neptunium in the solution phase of J-13 well water and linear (K_d) fits to the data for two values of pH.

Figure 10.3-5. Neptunium Sorption onto Clinoptilolite-Rich Tuff

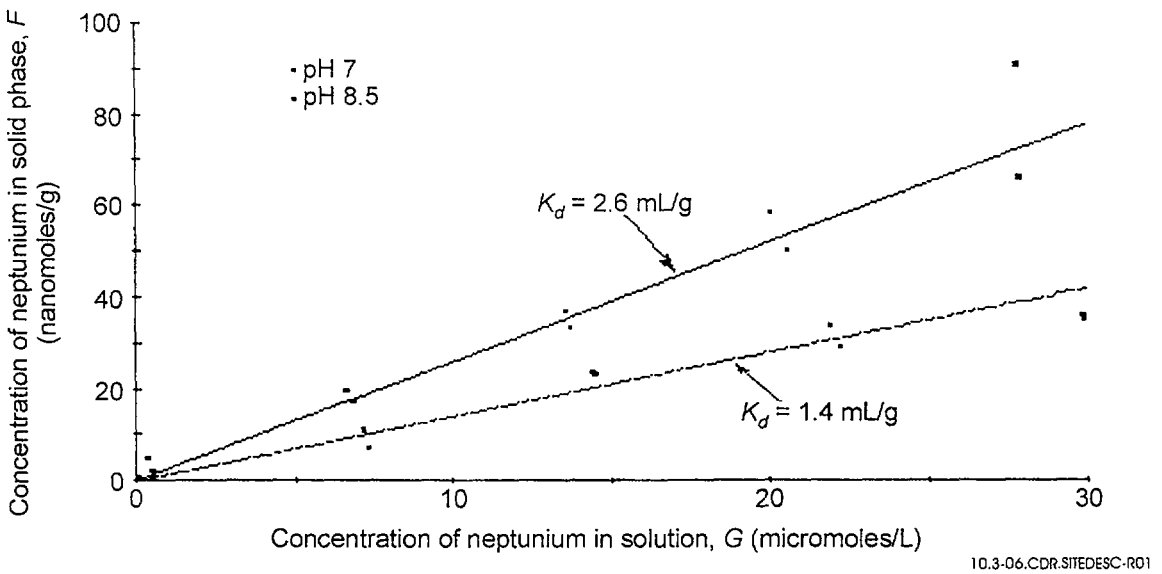

Source: CRWMS M&O (2000, Figure 4)

NOTE: A plot is shown of the concentration, *F*, of neptunium in the solid phase of clinoptilolite versus the concentration, *C*, of neptunium in the solution phase of J-13 well water and linear (K_d) fits to the data for two values of pH.

Figure 10.3-6. Neptunium Sorption onto Clinoptilolite

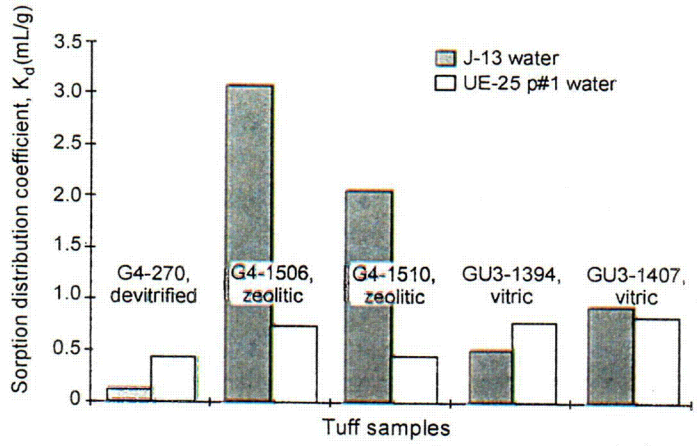

Source: CRWMS M&O (2000, Figure 5)

NOTE: Values of K_d for sorption of neptunium onto several tuffs that allow comparison of sorption (under atmospheric conditions) for the two types of groundwaters. The initial neptunium concentration ranged from 6×10^{-7} to 8×10^{-7} M. The tuffs were wet-sieved to particle sizes ranging from 75 to 500 µm. The pretreatment period was 2 to 14 days, and the sorption period was 3 to 23 days.

Figure 10.3-7. Dependence on Water for Neptunium Sorption onto Tuffs

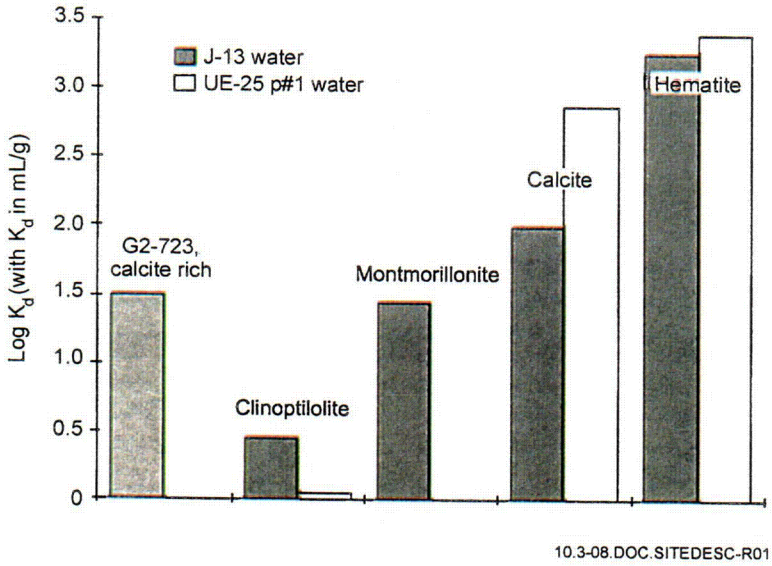

Source: CRWMS M&O (2000, Figure 6)

NOTE: Values of K_d for neptunium onto several minerals and a calcite-rich tuff that allow comparison of sorption (under atmospheric conditions) for the two groundwaters. The initial neptunium concentration ranged from 6×10^{-7} to 8×10^{-7} M. The tuff and the calcite were wet-sieved to particle sizes ranging from 75 to 500 µm; the montmorillonite was dry-sieved; the clinoptilolite and hematite were not sieved; the sorption period was 17 to 22 days.

Figure 10.3-8. Dependence on Water for Neptunium Sorption onto Minerals

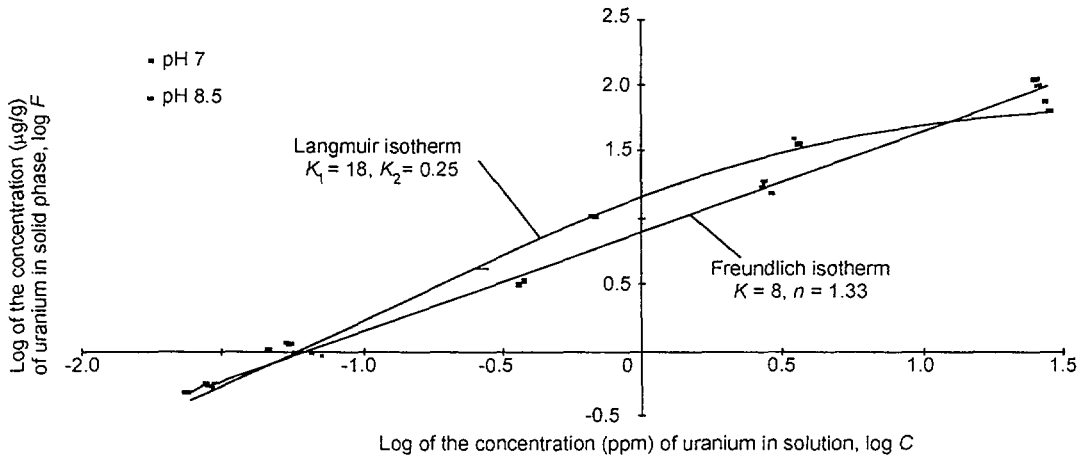

10.3-09.DOC.SITEDESC-R01

Source: CRWMS M&O (2000, Figure 7)

NOTE: This is a log-log plot of the concentration of uranium in the solid phase, F, of the clinoptilolite-rich tuff G4-1510 versus the concentration of uranium in the solution phase, C, of J-13 well water. The tuff was wet-sieved to give particles that ranged in size from 75 to 500 µm. The period of pretreatment was 2 to 4 days; the period of sorption was 3 to 4 days. The data for a pH of 7 have been fitted with a Langmuir isotherm; the data for a pH of 8.5 have been fitted with a Freundlich isotherm.

Figure 10.3-9. Uranium Sorption onto Clinoptilolite-Rich Tuff

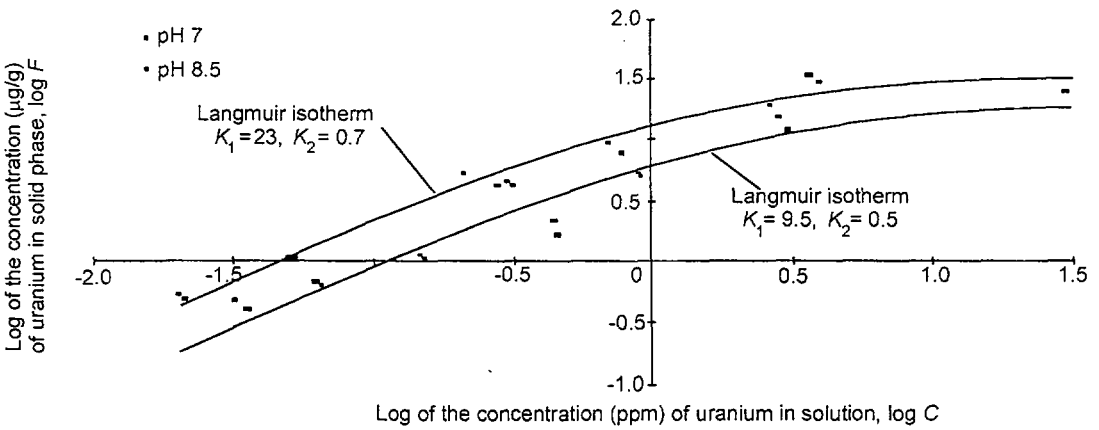

10.3-10.DOC.SITEDESC-R01

Source: CRWMS M&O (2000, Figure 8)

NOTE: This is a log-log plot of the concentration of uranium in the solid phase, F, of clinoptilolite versus the concentration of uranium in the solution phase, C, of J-13 water. The mineral was unsieved. The period of pretreatment was 2 to 4 days; the period of sorption was 3 to 4 days. The data for each pH (7 and 8.5) have been fitted with a Langmuir isotherm.

Figure 10.3-10. Uranium Sorption onto Clinoptilolite

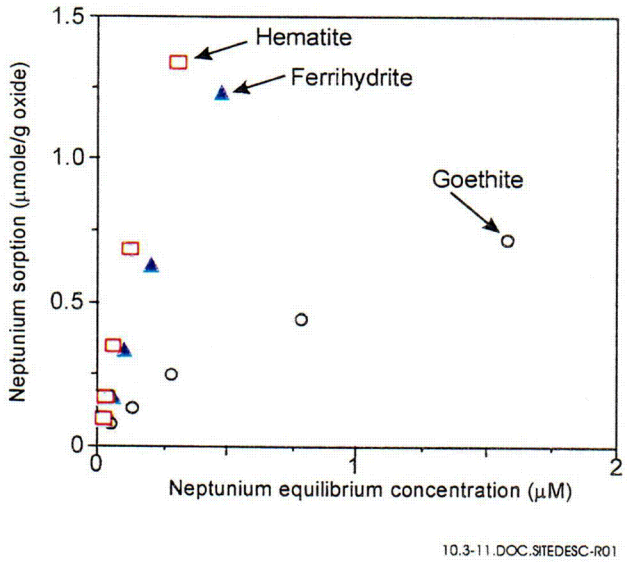

Source: Triay et al. (1997, Figure 76)

NOTE: The plot shows isotherms for the sorption of neptunium on three different iron oxides, calculated on the basis of unit mass.

Figure 10.3-11. Neptunium Sorption per Unit Mass on Iron Oxides

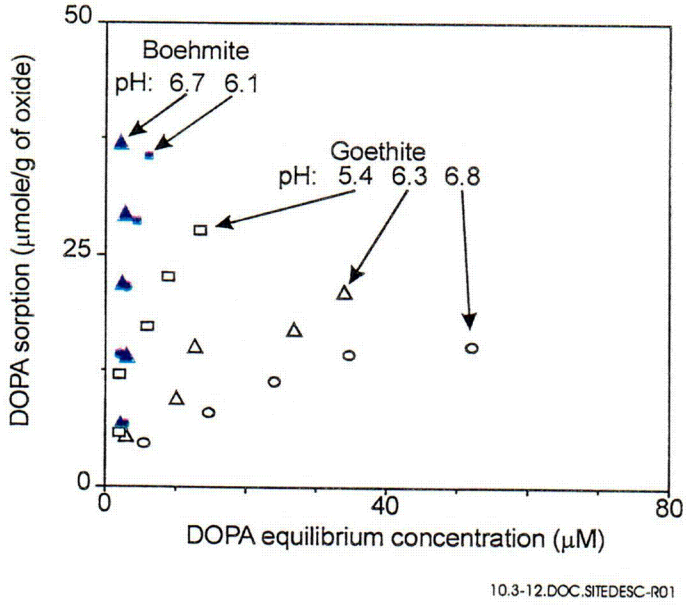

Source: Triay et al. (1997, Figure 78)

NOTE: This plot shows isotherms for the sorption of dihydroxyphenylalanine (DOPA) on goethite and on boehmite at different pH levels in the presence of 0.1 M KCl.

Figure 10.3-12. The pH Dependence of Dihydroxyphenylalanine Sorption on Oxides

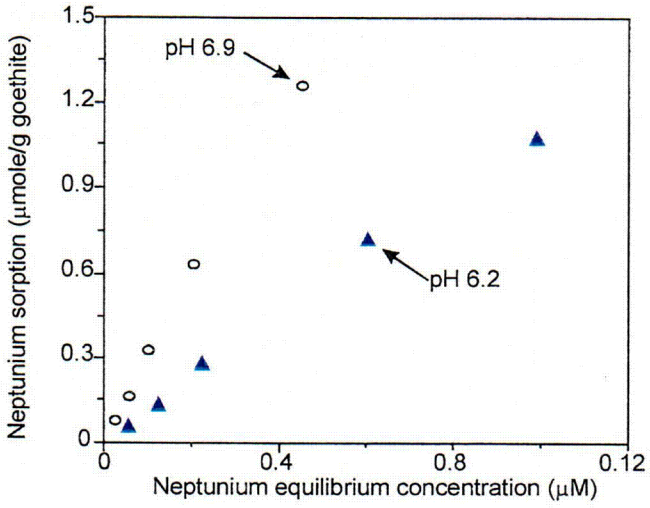

10.3-13.DOC.SITEDESC-R01

Source: Triay et al. (1997, Figure 79)

NOTE: This plot shows isotherms for the sorption of neptunium on goethite at a pH of 6.2 and 6.9.

Figure 10.3-13. Neptunium Sorption on Goethite

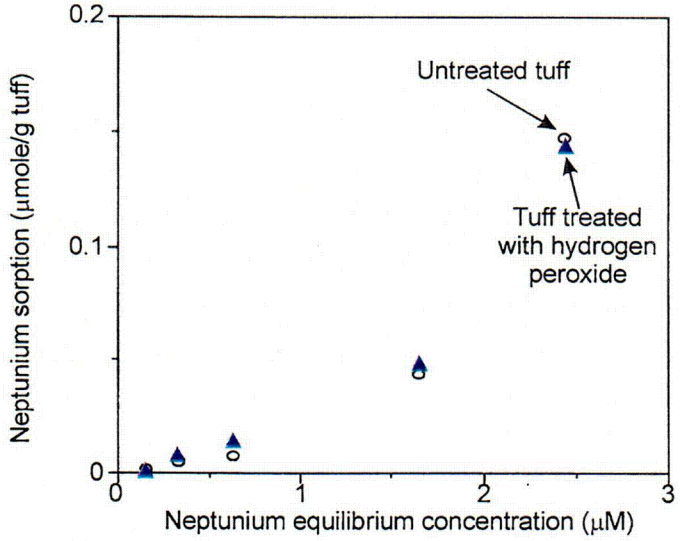

10.3-14.DOC.SITEDESC-R01

Source: Triay et al. (1997, Figure 80)

NOTE: This plot shows isotherms for the sorption of neptunium on devitrified tuff (G4-270) treated with hydrogen peroxide and untreated.

Figure 10.3-14. Neptunium Sorption on Treated and Untreated Tuff

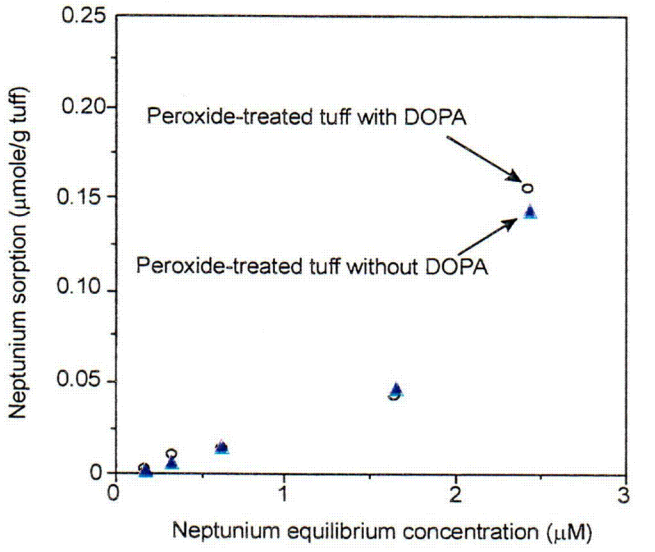

Source: Triay et al. (1997, Figure 81)

NOTE: This plot shows isotherms for the sorption of neptunium on hydrogen-peroxide-treated tuff materials (G4-270) with and without dihydroxyphenylalanine (DOPA).

Figure 10.3-15. Neptunium Sorption with and without Dihydroxyphenylalanine on Treated Tuff

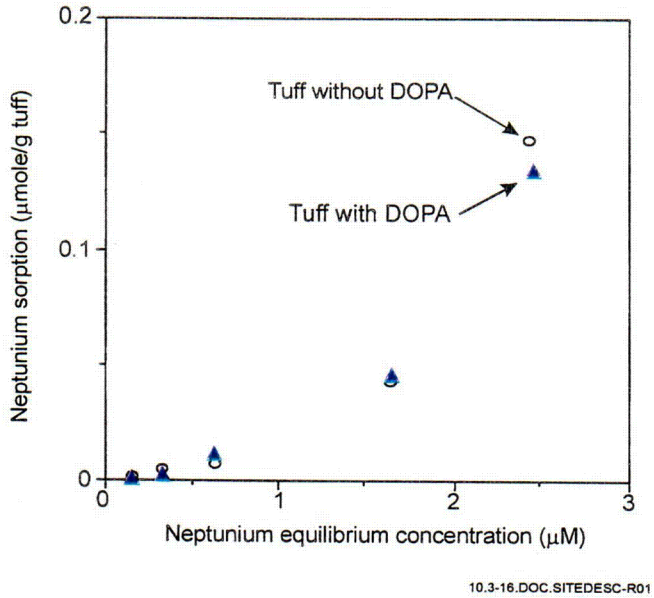

Source: Triay et al. (1997, Figure 82)

NOTE: This plot shows isotherms for the sorption of neptunium on untreated tuff samples (G4-270) with and without dihydroxyphenylalanine (DOPA).

Figure 10.3-16. Neptunium Sorption with and without Dihydroxyphenylalanine on Untreated Tuff

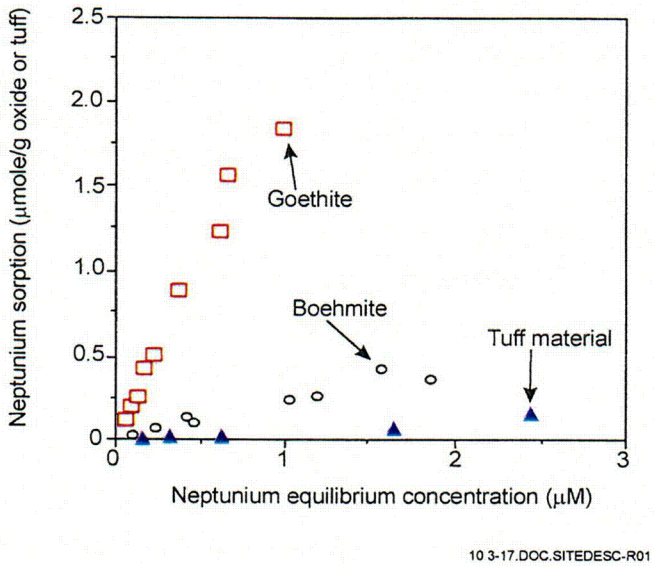

Source: Triay et al. (1997, Figure 83)

NOTE: This plot shows isotherms for the sorption of neptunium on goethite, boehmite, and tuff material (G4-270).

Figure 10.3-17. Neptunium Sorption on Oxides and Tuff

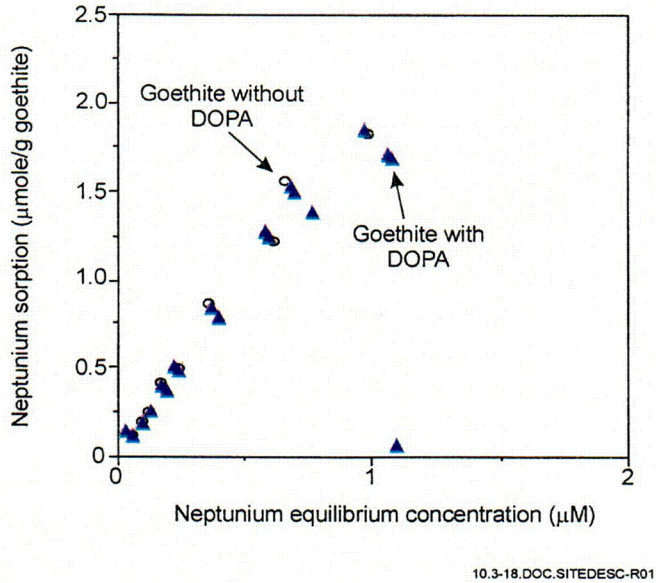

Source: Triay et al. (1997, Figure 84)

NOTE: This plot shows isotherms for the sorption of neptunium on goethite in the presence and absence of dihydroxyphenylalanine (DOPA) at a pH of 6.2.

Figure 10.3-18. Neptunium Sorption on Goethite with and without Dihydroxyphenylalanine

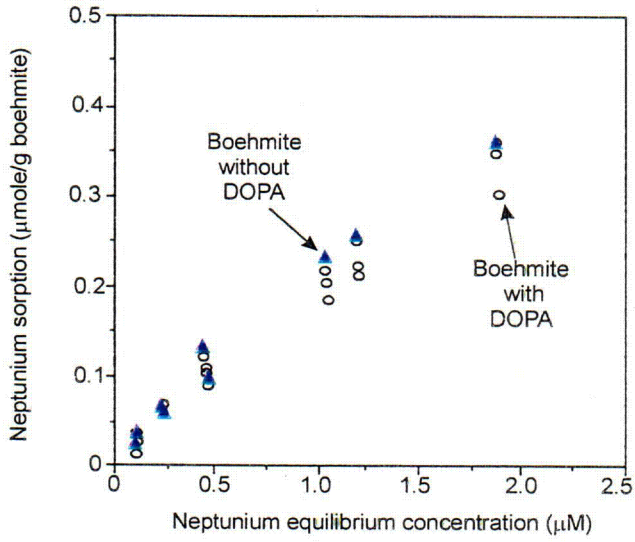

Source: Triay et al. (1997, Figure 85)

NOTE: This plot shows isotherms for the sorption of neptunium on boehmite in the presence and absence of dihydroxyphenylalanine (DOPA) at a pH of 6.2.

Figure 10.3-19. Neptunium Sorption on Boehmite with and without Dihydroxyphenylalanine

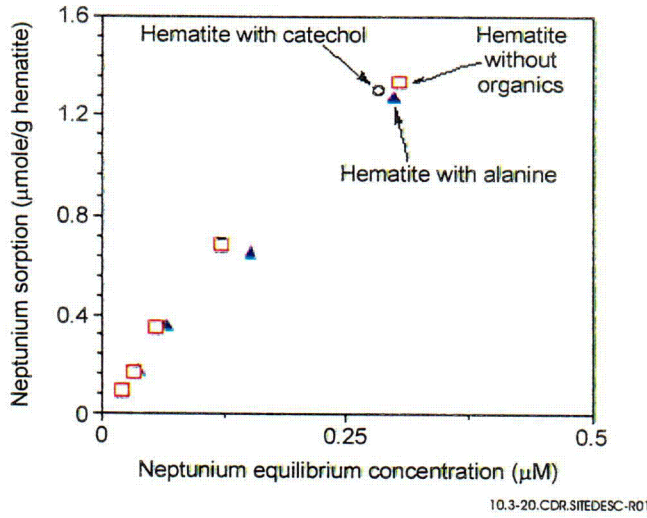

Source: Triay et al. (1997, Figure 86)

NOTE: This plot shows isotherms for neptunium sorption on hematite in the presence and absence of catechol or alanine (1 μM) at a pH of 6.9.

Figure 10.3-20. Neptunium Sorption on Hematite with and without Organics

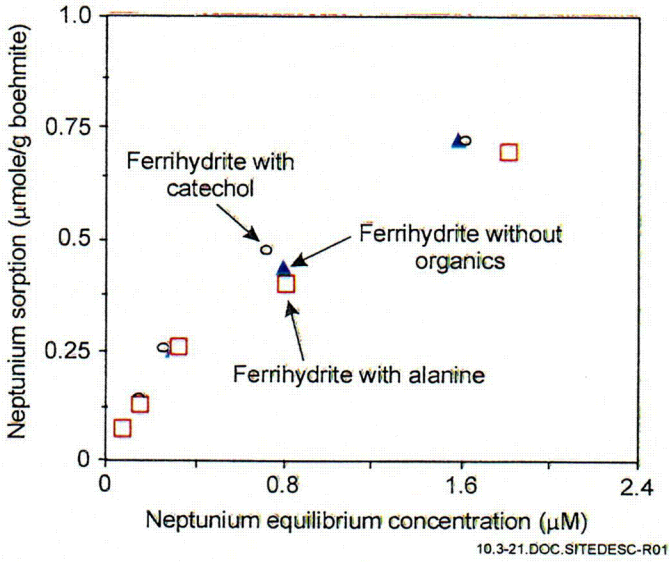

Source: Triay et al. (1997, Figure 87)

NOTE: The plot shows isotherms for sorption of neptunium on ferrihydrite in the presence and absence of catechol or alanine (1 µM) at pH 6.2.

Figure 10.3-21. Neptunium Sorption on Ferrihydrite with and without Organics

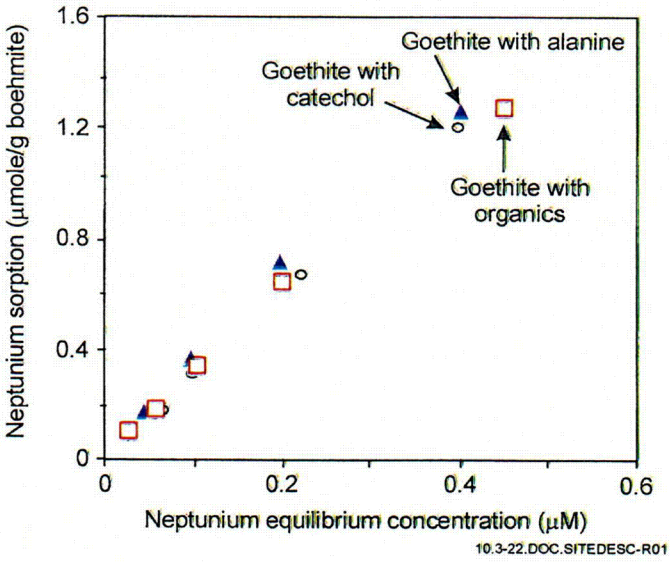

Source: Triay et al. (1997, Figure 88)

NOTE: This plot shows isotherms for the sorption of neptunium on goethite in the presence and absence of catechol or alanine (1 µM) at a pH of 6.9.

Figure 10.3-22. Neptunium Sorption on Goethite with and without Organics

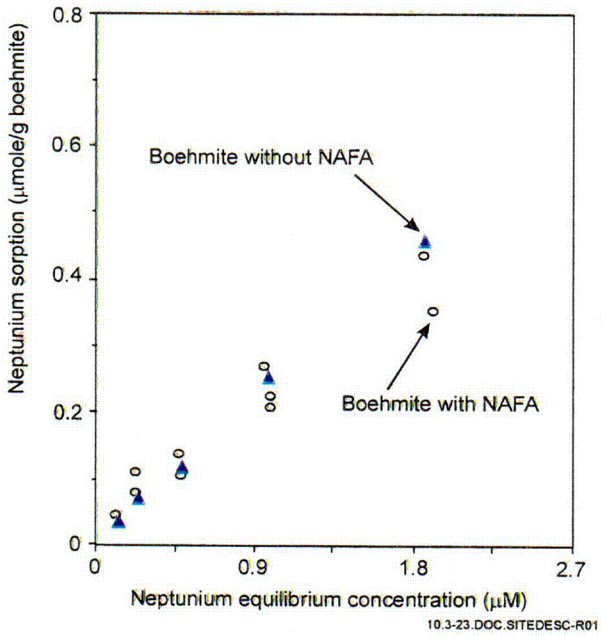

Source: Triay et al. (1997, Figure 89)

NOTE: This plot shows isotherms for the sorption of neptunium on boehmite with and without Nordic aquatic fulvic acid (NAFA).

Figure 10.3-23. Neptunium Sorption on Boehmite with and without Nordic Aquatic Fulvic Acid

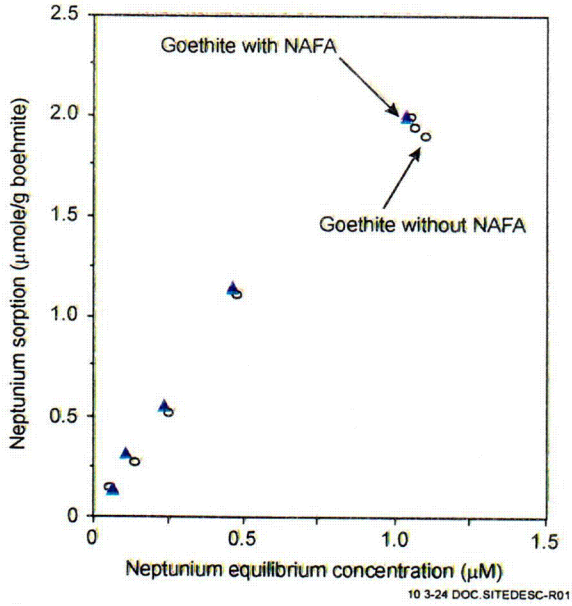

Source: Triay et al. (1997, Figure 90)

NOTE: This plot shows isotherms for the sorption of neptunium on goethite with and without Nordic aquatic fulvic acid (NAFA).

Figure 10.3-24. Neptunium Sorption on Goethite with and without Nordic Aquatic Fulvic Acid

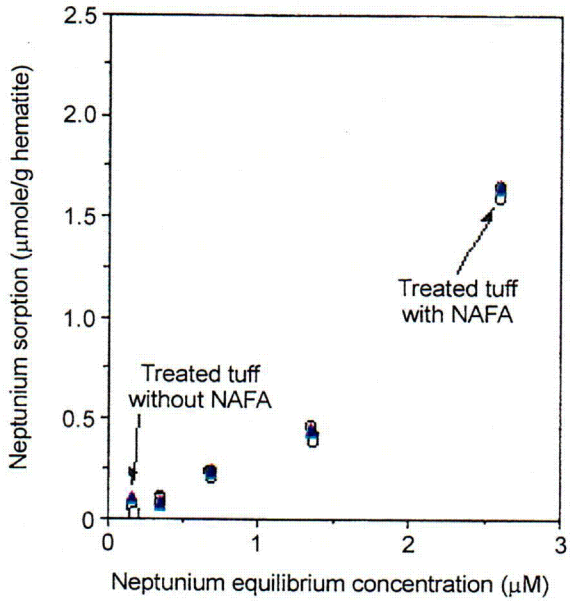

Source: CRWMS M&O (2000, Figure 65)

NOTE: This plot shows isotherms for neptunium sorption on treated tuff (G4-270) with and without Nordic aquatic fulvic acid (NAFA).

Figure 10.3-25. Neptunium Sorption on Treated Tuff with and without Nordic Aquatic Fulvic Acid

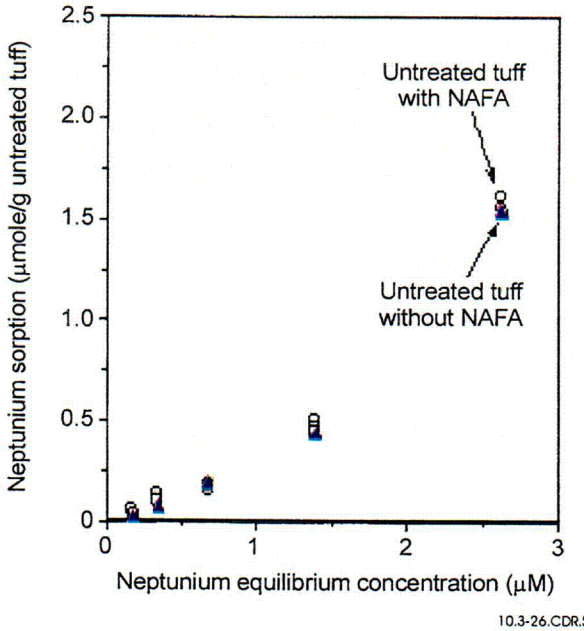

Source: CRWMS M&O (2000, Figure 66)

NOTE: This plot shows isotherms of neptunium sorption on untreated tuff (G4-270) with and without Nordic aquatic fulvic acid (NAFA).

Figure 10.3-26. Neptunium Sorption on Untreated Tuff with and without Nordic Aquatic Fulvic Acid

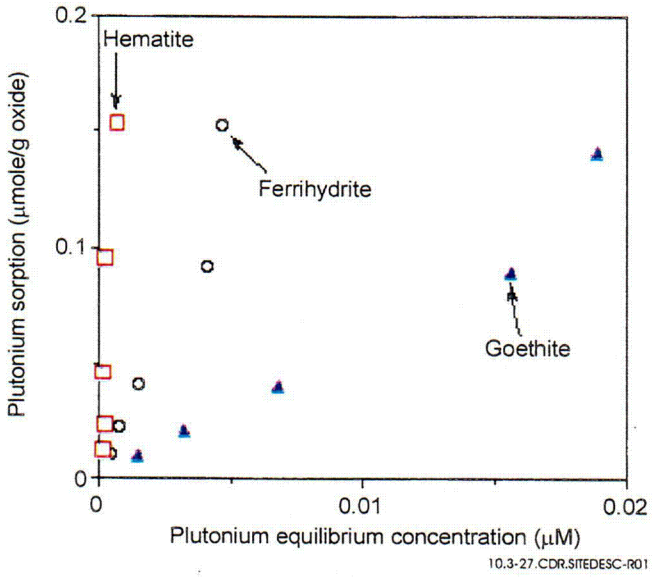

Source: Triay et al. (1997, Figure 93)

NOTE: This plot shows isotherms for the sorption of plutonium on three iron oxides, calculated on the basis of unit mass.

Figure 10.3-27. Plutonium Sorption per Unit Mass on Iron Oxides

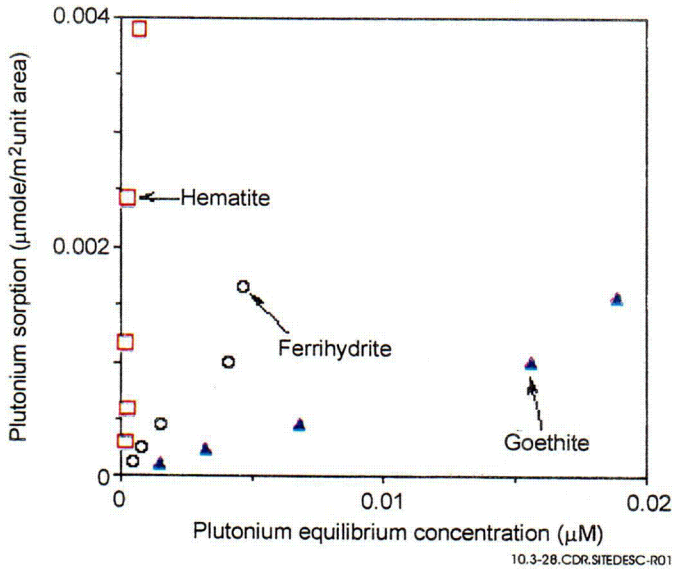

Source: Triay et al. (1997, Figure 94)

NOTE: This plot shows isotherms for the sorption of plutonium on three different iron oxides, calculated on the basis of unit surface area.

Figure 10.3-28. Plutonium Sorption per Unit Area on Iron Oxides

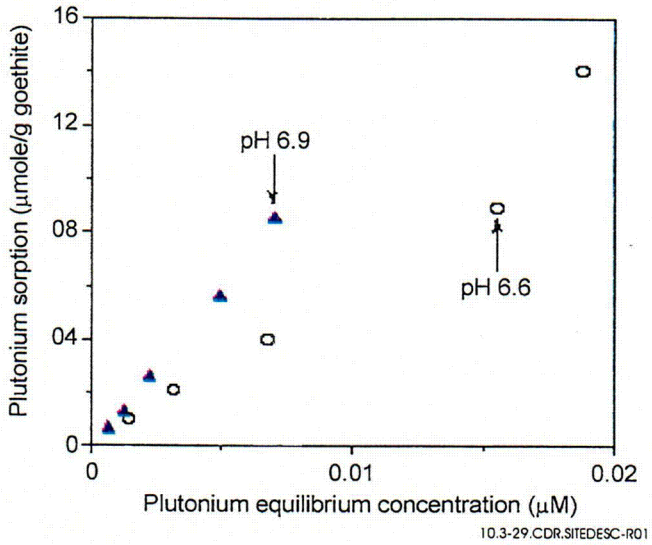

Source: Triay et al. (1997, Figure 95)

NOTE: This plot shows isotherms for the sorption of plutonium on goethite at two different values of pH.

Figure 10.3-29. The pH Dependence of Plutonium Sorption on Goethite

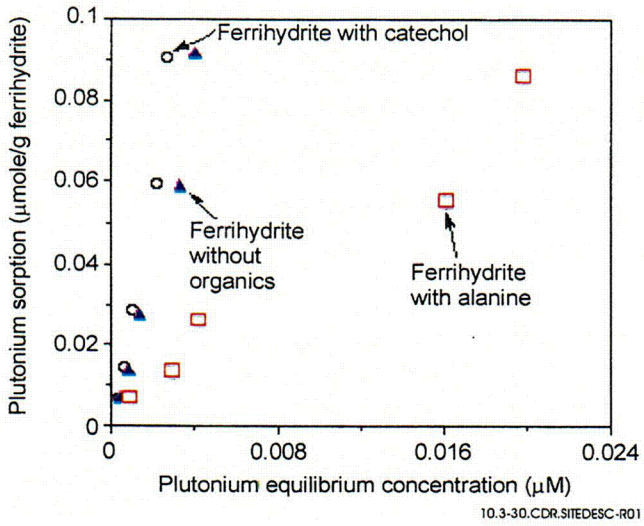

Source: Triay et al. (1997, Figure 96)

NOTE: This plot shows isotherms for plutonium sorption on ferrihydrite with and without catechol or alanine (1 µM) at a pH of 6.2 in 0.1 M KCl.

Figure 10.3-30. Plutonium Sorption on Ferrihydrite with and without Organics

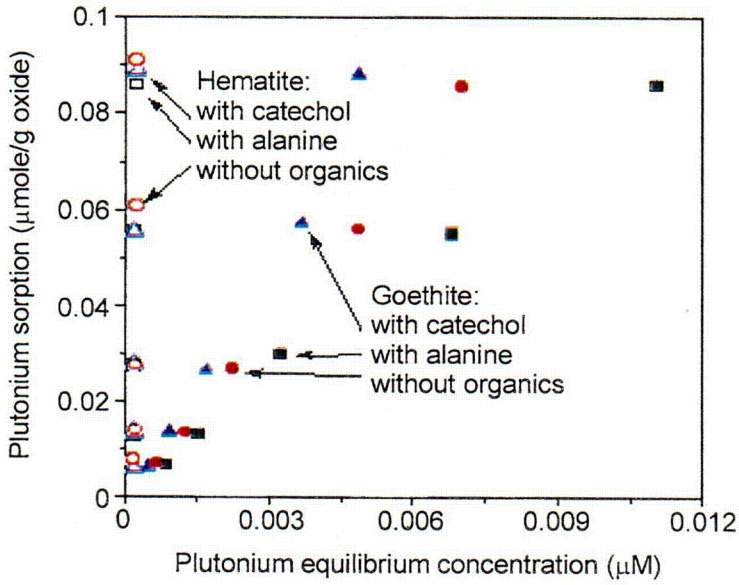

Source: Triay et al. (1997, Figure 97)

NOTE: This plot shows isotherms for the sorption of plutonium on hematite and goethite with and without catechol or alanine at a pH of 6.9 in 0.1 M KCl.

Figure 10.3-31. Plutonium Sorption with and without Organics

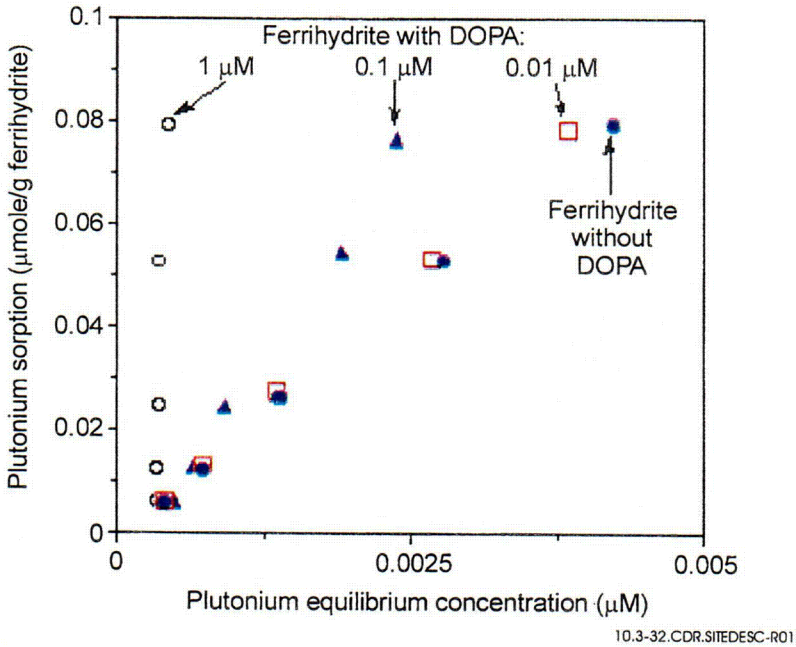

Source: Triay et al. (1997, Figure 98)

NOTE: This plot shows isotherms for the sorption of plutonium on ferrihydrite with and without dihydroxyphenylalanine (DOPA) at a pH of 6.2 in 0.1 M KCl.

Figure 10.3-32. Plutonium Sorption on Ferrihydrite with and without Dihydroxyphenylalanine

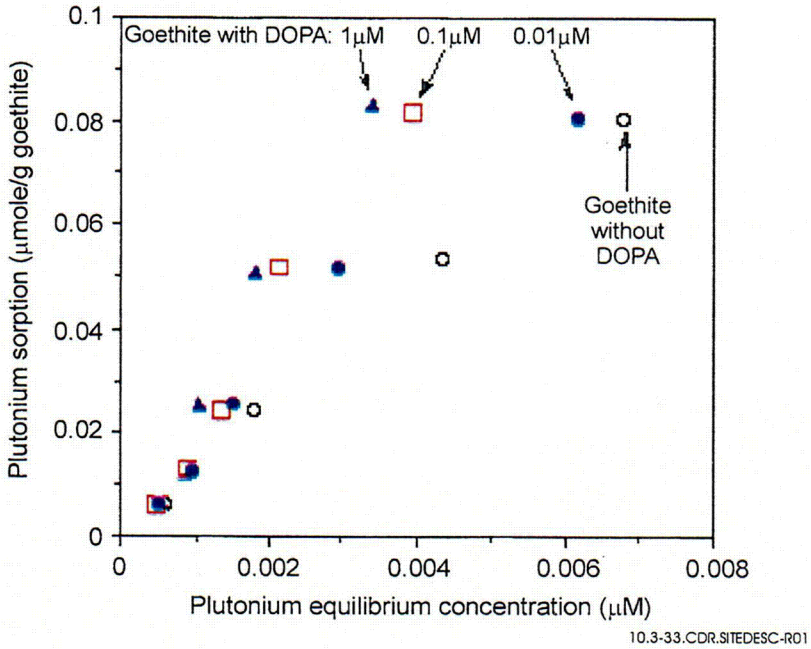

Source: Triay et al. (1997, Figure 99)

NOTE: This plot shows isotherms for the sorption of plutonium on goethite with and without dihydroxyphenylalanine (DOPA) at a pH of 6.9 in 0.1 M KCl.

Figure 10.3-33. Plutonium Sorption on Goethite with and without Dihydroxyphenylalanine

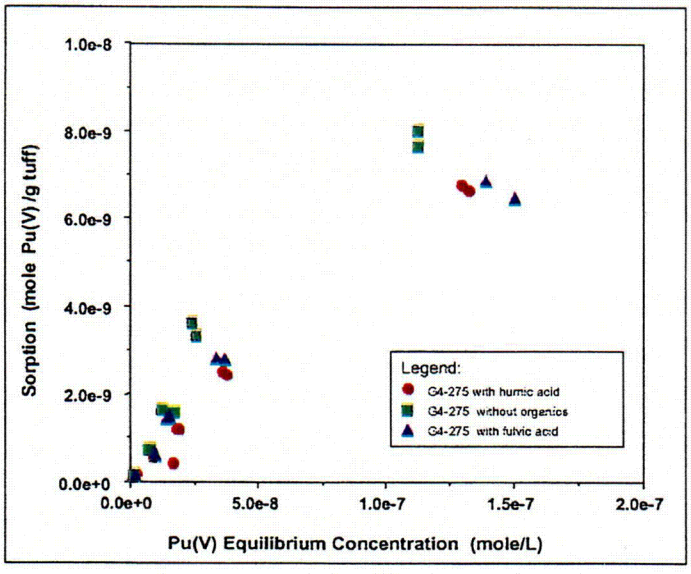

DTN: LAIT831341AQ98.001

Figure 10.3-34. Sorption Isotherms for Plutonium (V) on Devitric Tuff (G4-275) with and without Humic and Fulvic Acids in Natural J-13 Groundwater

C15

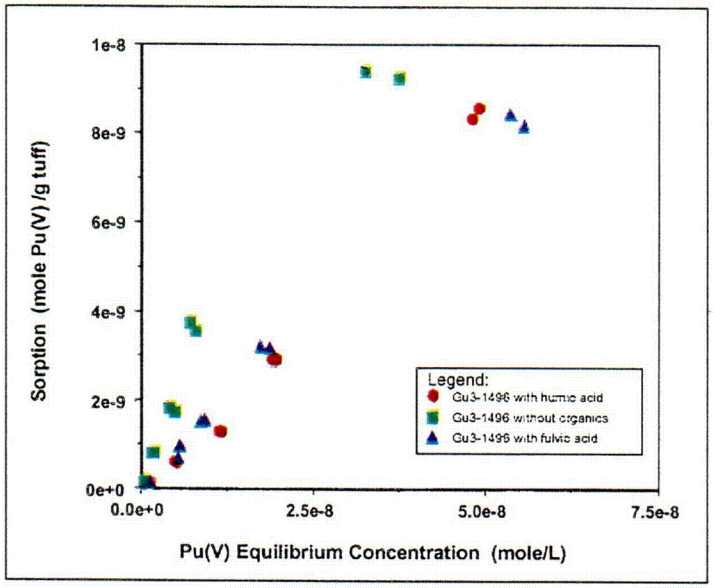

DTN: LAIT831341AQ98.001

Figure 10.3-35. Sorption Isotherms for Plutonium (V) on Vitric Tuff (Gu3-1496) with and without Humic and Fulvic Acids in Natural J-13 Groundwater

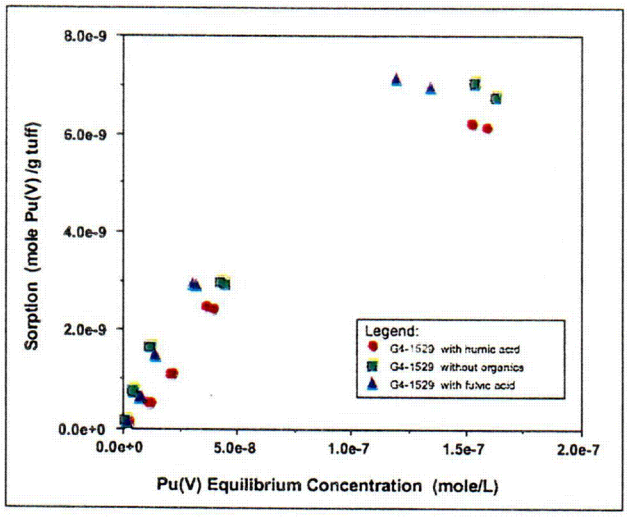

DTN: LAIT831341AQ98.001

Figure 10.3-36. Sorption Isotherms for Plutonium (V) on Zeolitic Tuff (G4-1529) with and without Humic and Fulvic Acids in Natural J-13 Groundwater

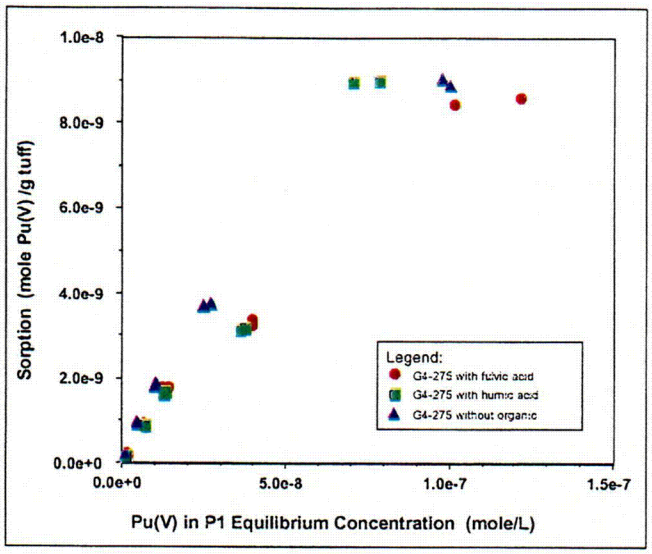

DTN: LAIT831341AQ98.001

Figure 10.3-37. Sorption Isotherms for Plutonium (V) on Devitric Tuff (G4-275) with and without Humic and Fulvic Acids in Synthetic UE-25 p#1 Groundwater

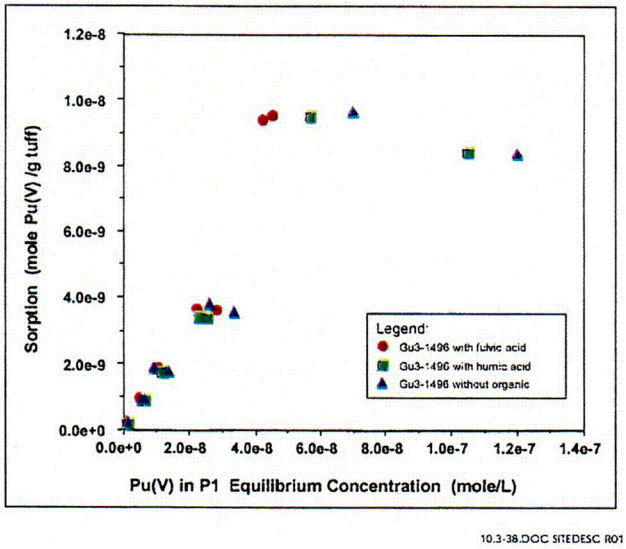

DTN: LAIT831341AQ98.001

Figure 10.3-38. Sorption Isotherms for Plutonium (V) on Vitric Tuff (GU3-1496) with and without Humic and Fulvic Acids in Synthetic UE-25 p#1 Groundwater

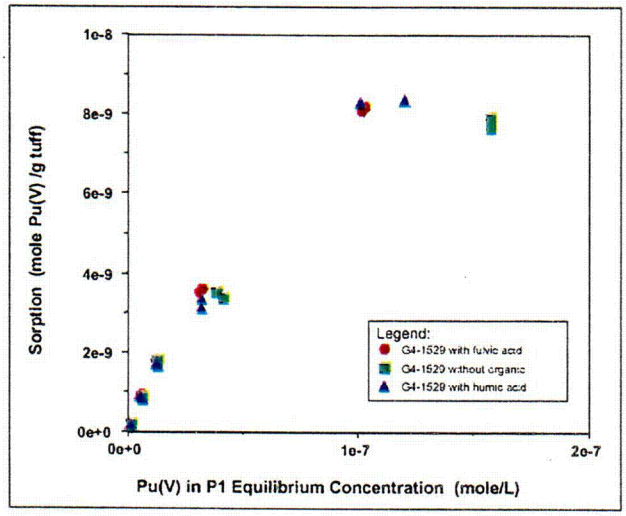

DTN: LAIT831341AQ98.001

Figure 10.3-39. Sorption Isotherms for Plutonium (V) on Zeolitic Tuff (G4-1529) with and without Humic and Fulvic Acids in Synthetic UE-25 p#1 Groundwater

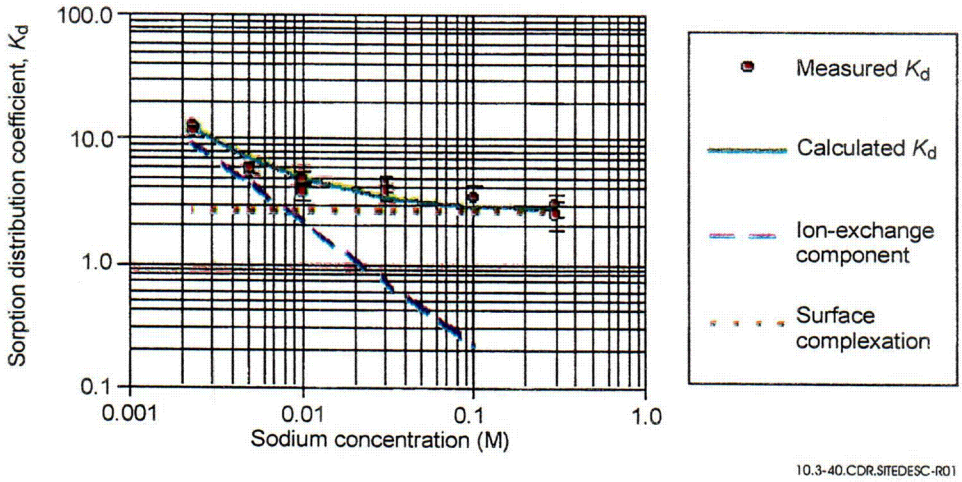

Source: Triay et al. (1997, Figure 100)

NOTE: The plot shows data points for the sorption distribution coefficient of neptunium on the zeolitic tuff sample G4-1506 at a pH of 8.4 as a function of sodium-ion concentration. Surface complexation should not vary with sodium concentration, so the horizontal dashed asymptote at high concentrations is a measure of surface complexation and the dashed linear slope at low concentrations is a measure of the ion-exchange component of the sorption.

Figure 10.3-40. Modeling of Neptunium Sorption

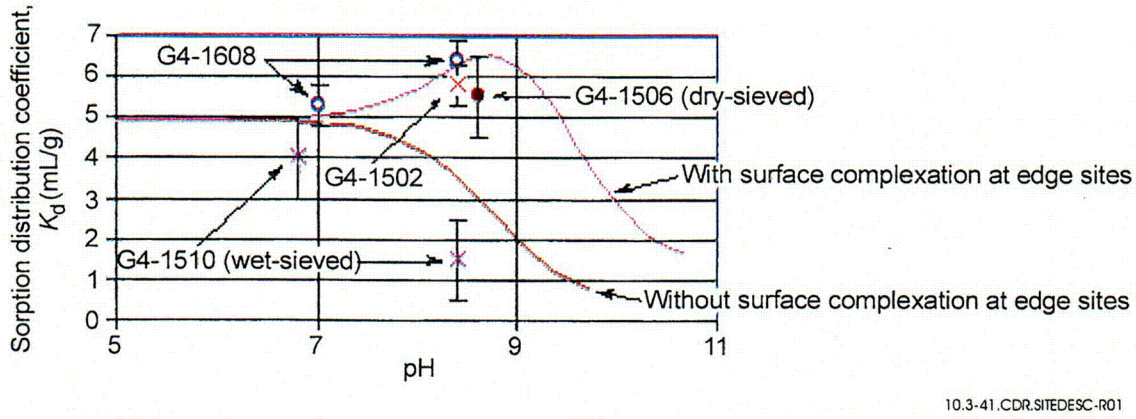

Source: Triay et al. (1997, Figure 102)

NOTE: This plot compares sorption data (points) with the predictions of the FITEQL code for the pH dependence of neptunium sorption on zeolitic tuff from J-13 water with and without surface complexation at edge sites (curves). The sorption data for samples G4-1608 and G4-1502 are from Thomas (1987).

Figure 10.3-41. Neptunium Sorption in J-13 Water

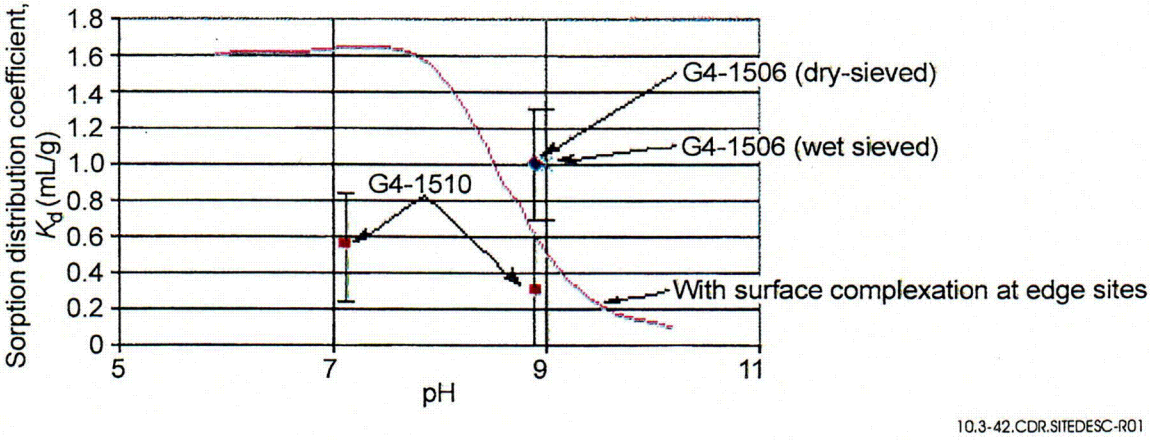

Source: Triay et al. (1997, Figure 103)

NOTE: This plot compares sorption data (points) with the predictions of the FITEQL code for the pH dependence of neptunium sorption on zeolitic tuff from UE-25 p#1 water with surface complexation at edge sites (curve).

Figure 10.3-42. Neptunium Sorption in UE-25 p#1 Water

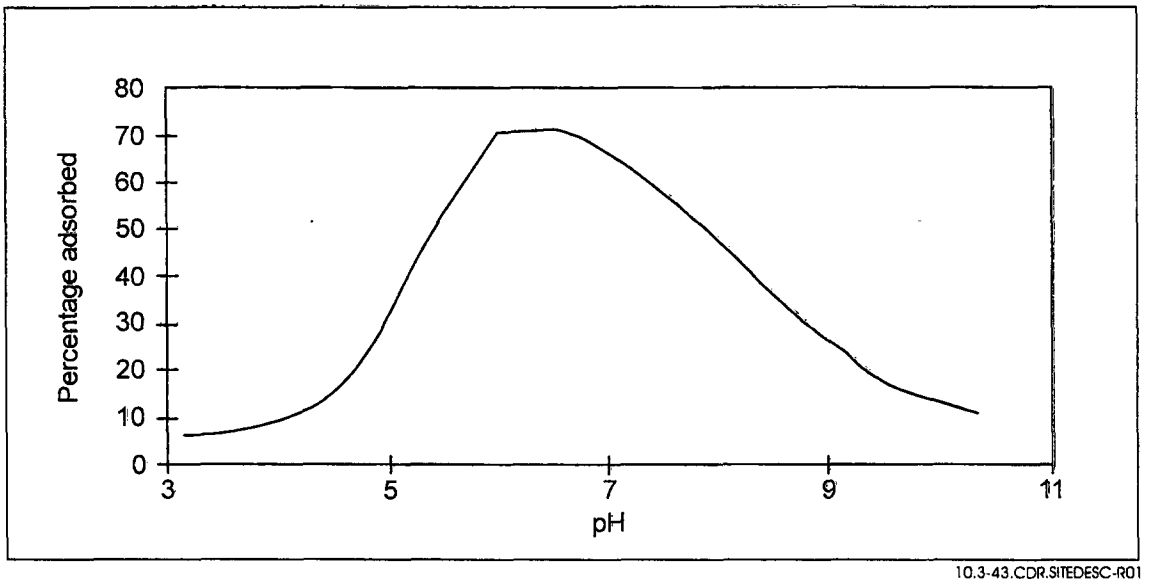

Source: Triay et al. (1997, Figure 104)

NOTE: The curve above shows the predictions of the FITEQL code for the adsorption of uranium onto crushed devitrified tuff from a 0.1 M NaCl solution in a controlled atmosphere with an initial uranium concentration of 1×10^{-6} M.

Figure 10.3-43. Uranium Adsorption

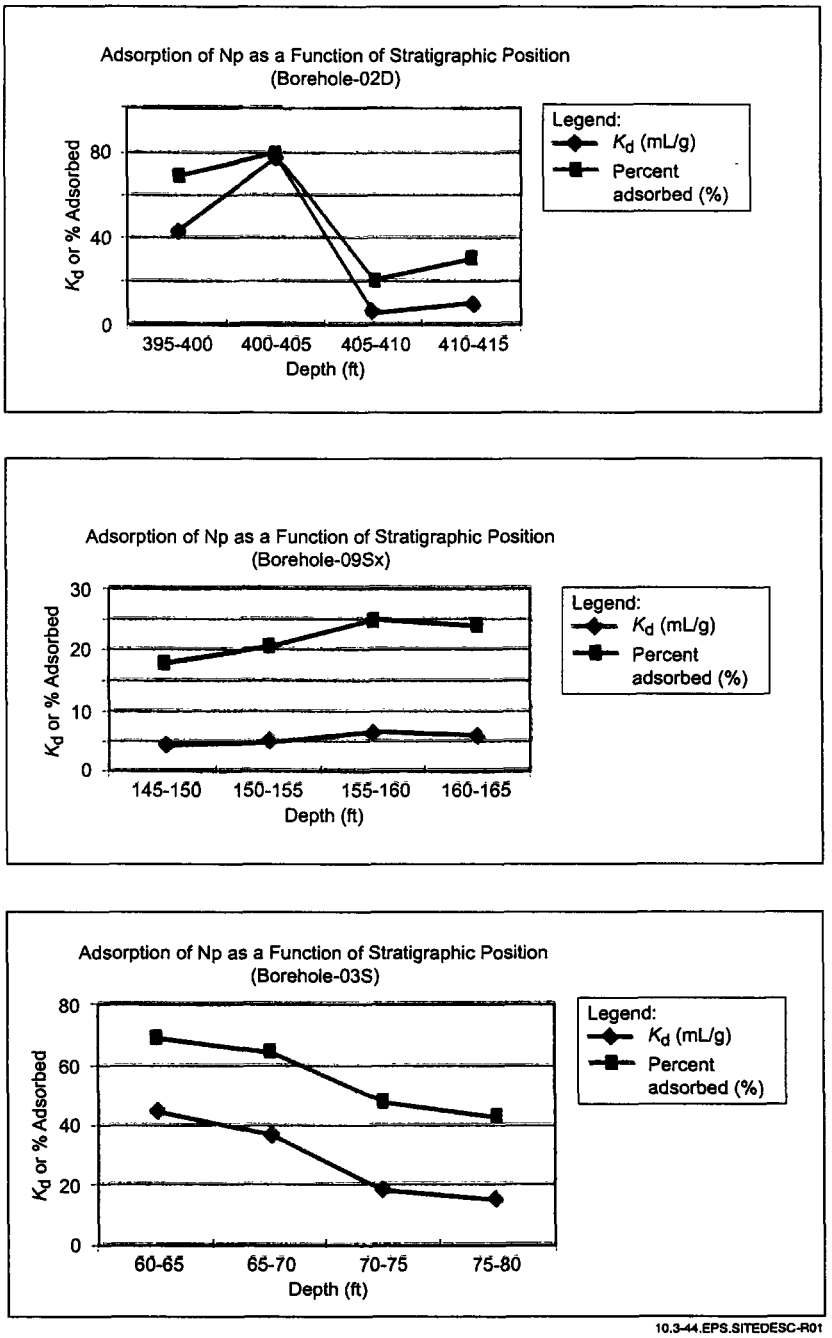

Source: CRWMS M&O (2000, Figure 9)

Figure 10.3-44. Adsorption of Neptunium-237 on Three Types of Alluvium

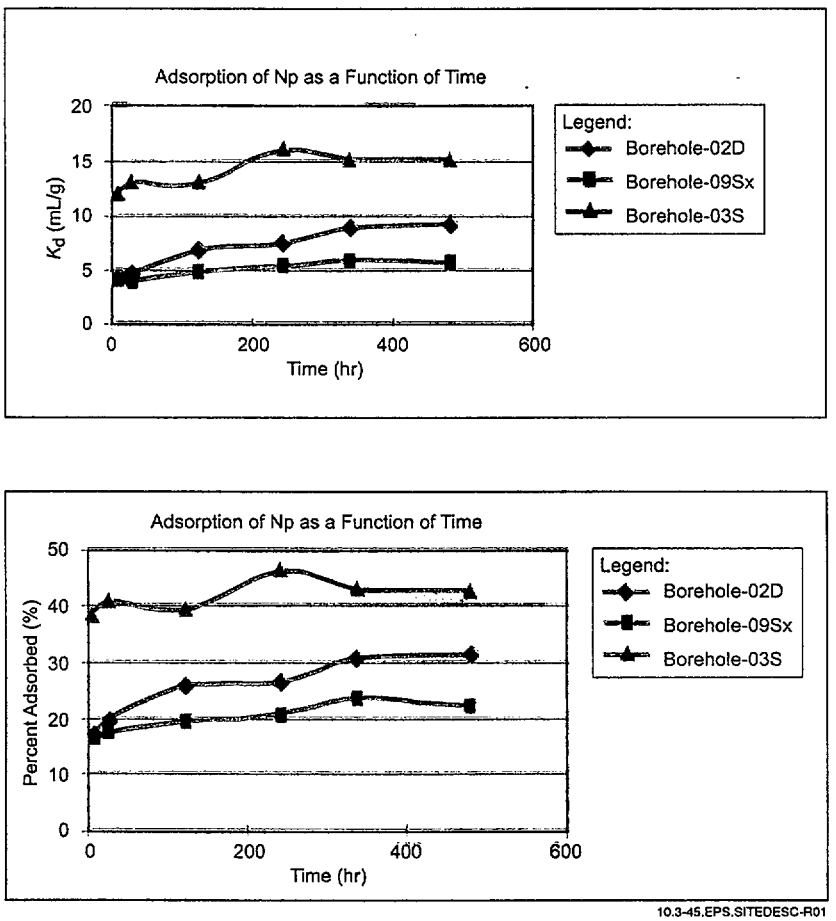

Source: CRWMS M&O (2000, Figure 10)

NOTE: The top panel shows the change in sorption coefficient (K_d) with time; the bottom panel, the percent adsorbed.

Figure 10.3-45. Kinetics of Neptunium-237 Adsorption in Three Types of Alluvium

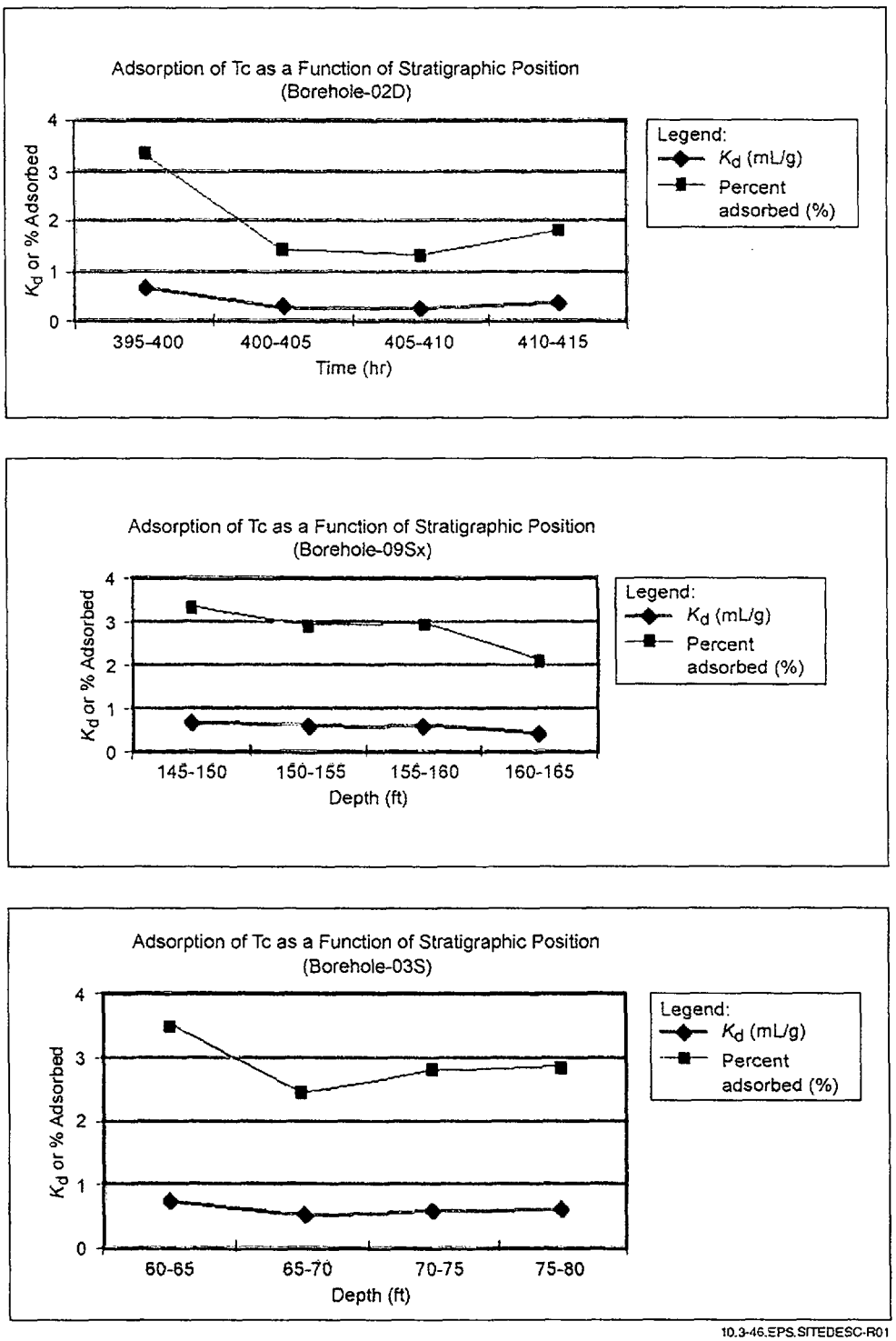

Source: CRWMS M&O (2000, Figure 11)

Figure 10.3-46. Adsorption of Technetium-99 on Three Types of Alluvium

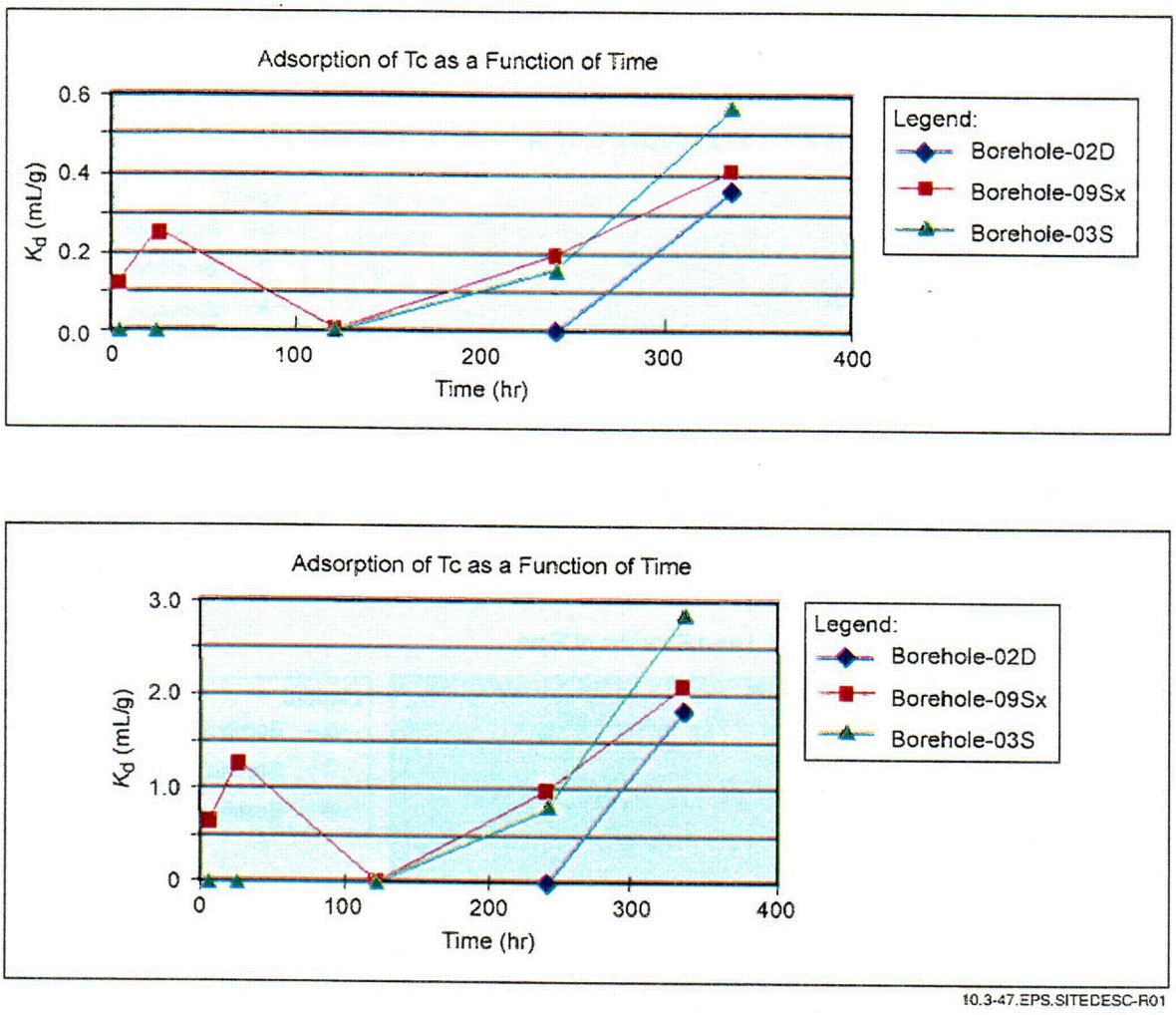

Source: CRWMS M&O (2000, Figure 12)

NOTE: The panels show the change in sorption coefficient (K_d) with time.

Figure 10.3-47. Kinetics of Technetium-99 Adsorption in Three Types of Alluvium

C20

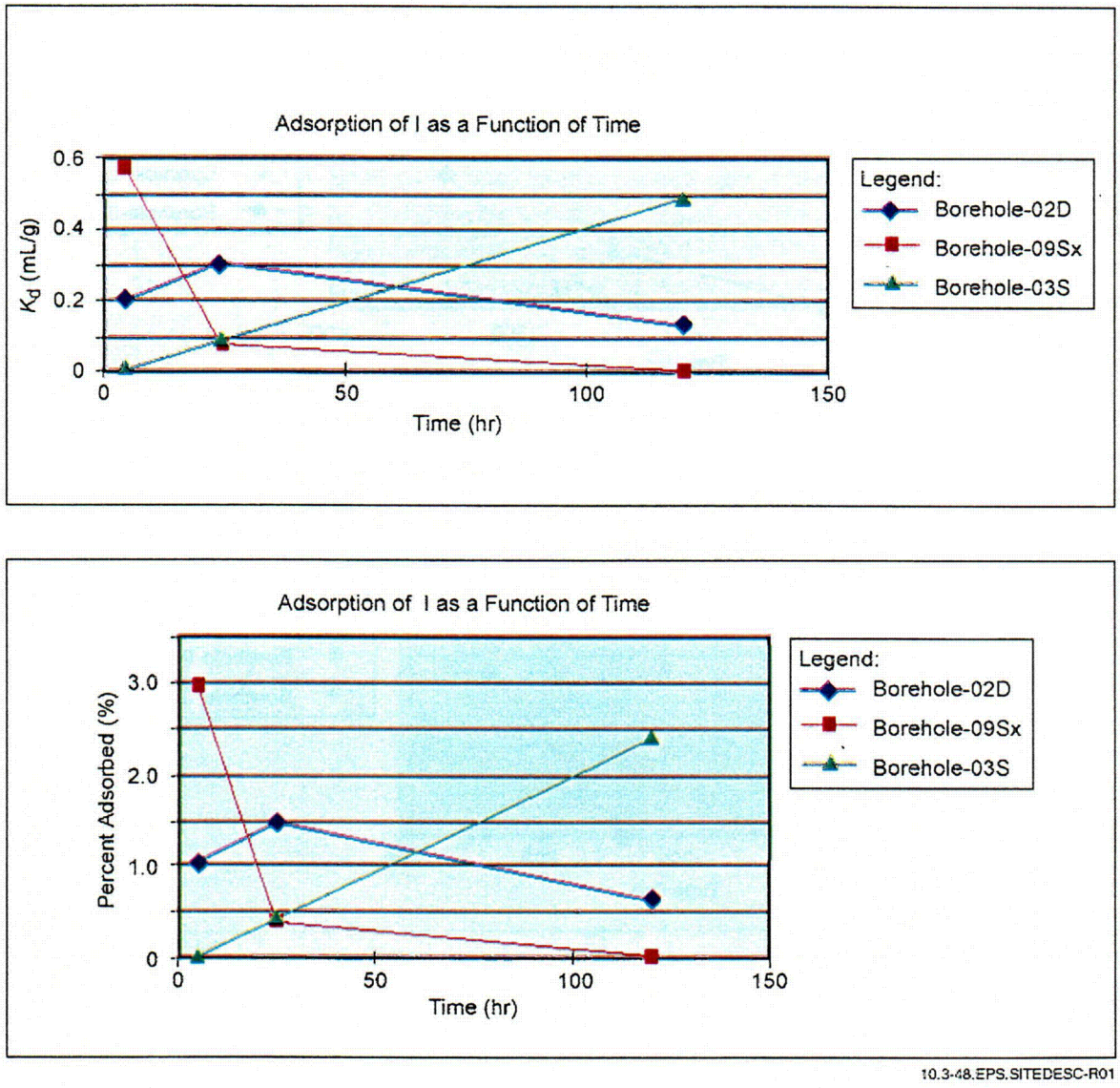

Source: CRWMS M&O (2000, Figure 13)

NOTE: The panels show the change in sorption coefficient (K_d) with time.

Figure 10.3-48. Kinetics of Iodine-129 Adsorption in Three Types of Alluvium

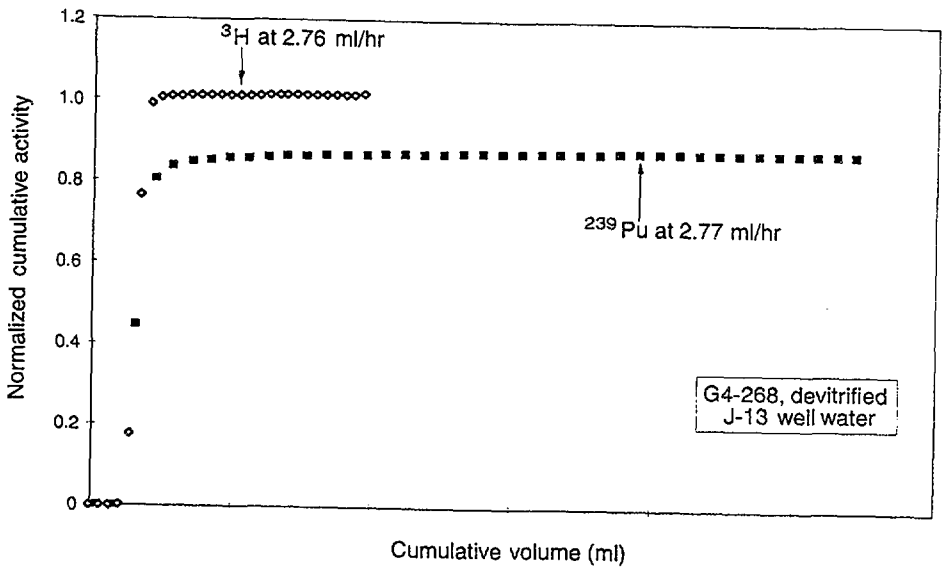

Source: Triay et al. (1997, Figure 107)

NOTE: This plot shows the elution curves for tritium and plutonium-239 through devitrified tuff sample G4-268 with J-13 well water. Cumulative concentration (in Figures 10.4-1 to 10.4-8) is the total activity of the recovered tracer divided by the total activity injected initially. As seen by the variation of the final part of the curves, this variable has an experimental error of about ± 20 percent.

Figure 10.4-1. Plutonium through Devitrified Tuff

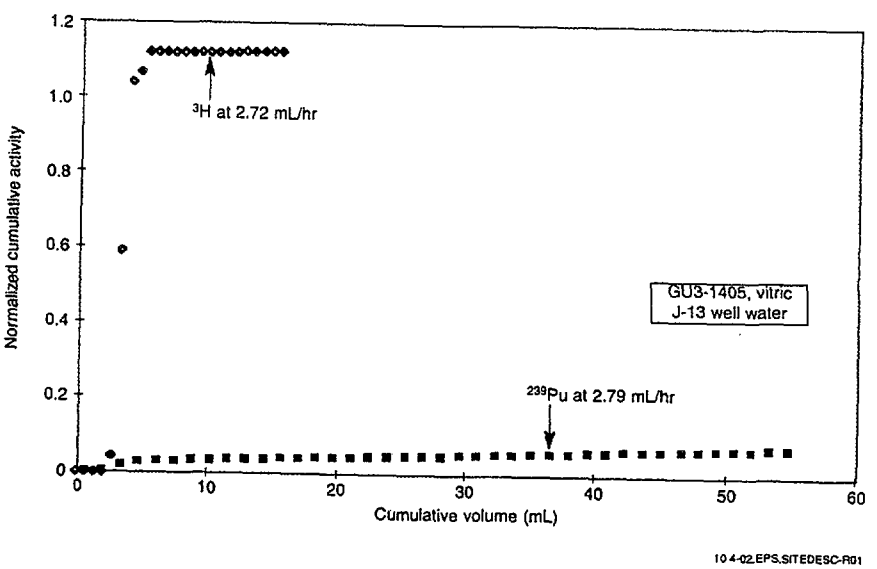

Source: CRWMS M&O (2000, Figure 14)

NOTE: This plot shows the elution curves for tritium and plutonium-239 through vitric tuff sample GU3-1405 with J-13 well water.

Figure 10.4-2. Plutonium through Vitric Tuff

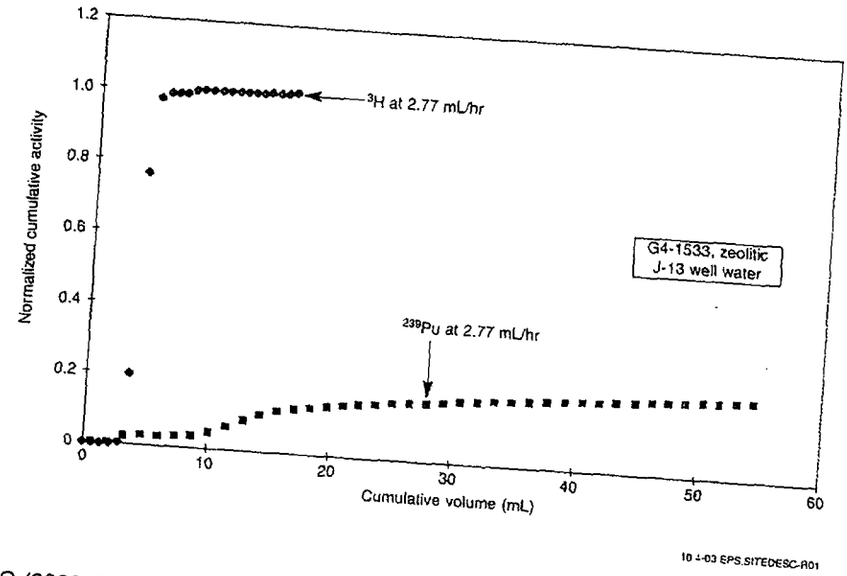

Source: CRWMS M&O (2000, Figure 15)

NOTE: This plot shows the elution curves for tritium and plutonium-239 through zeolitic tuff sample G4-1533 with J-13 well water.

Figure 10.4-3. Plutonium through Zeolitic Tuff

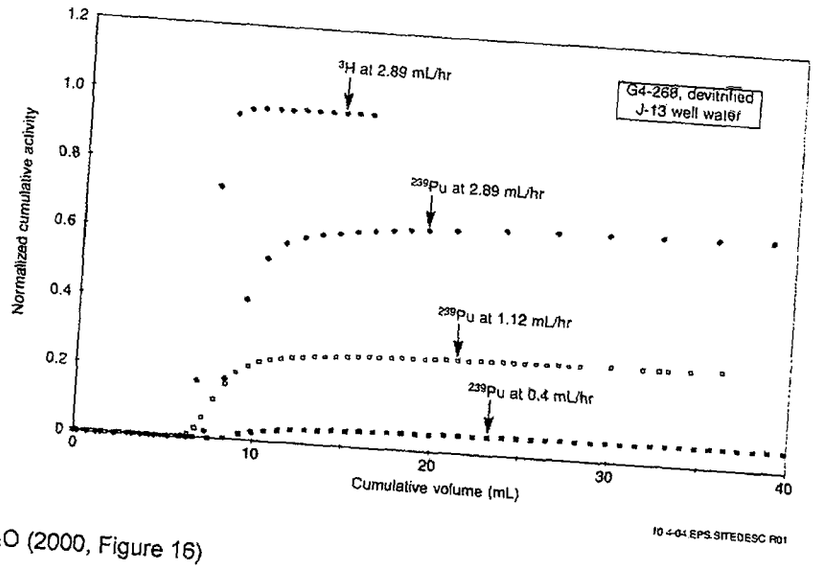

Source: CRWMS M&O (2000, Figure 16)

NOTE: This plot shows elution curves for tritium and plutonium-239 at different flow rates with J-13 water through devitrified tuff G4-268.

Figure 10.4-4. Plutonium in Devitrified Tuff (J-13 Well Water) at Various Flow Rates

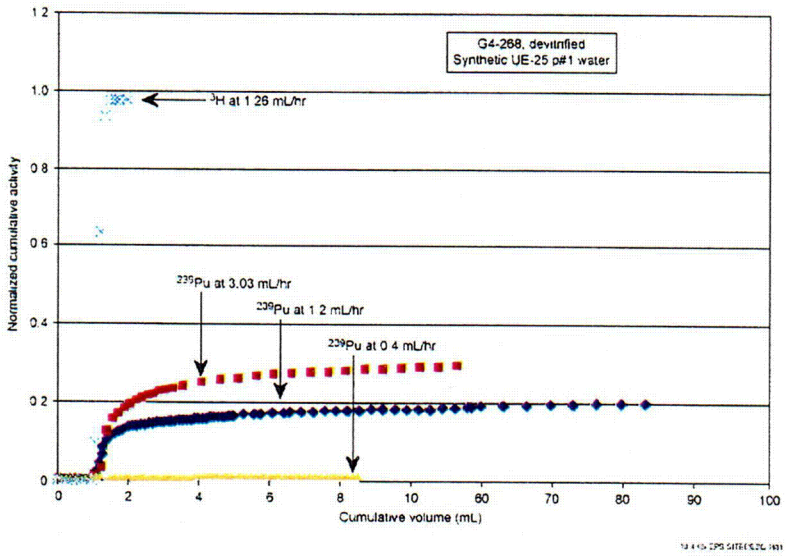

Source: CRWMS M&O (2000, Figure 17)

NOTE: This plot shows elution curves for tritium and plutonium-239 at different flow rates in synthetic UE-25 p#1 water and tuff G4-268.

Figure 10.4-5. Plutonium in Devitrified Tuff (UE-25 p#1 Water) at Various Flow Rates

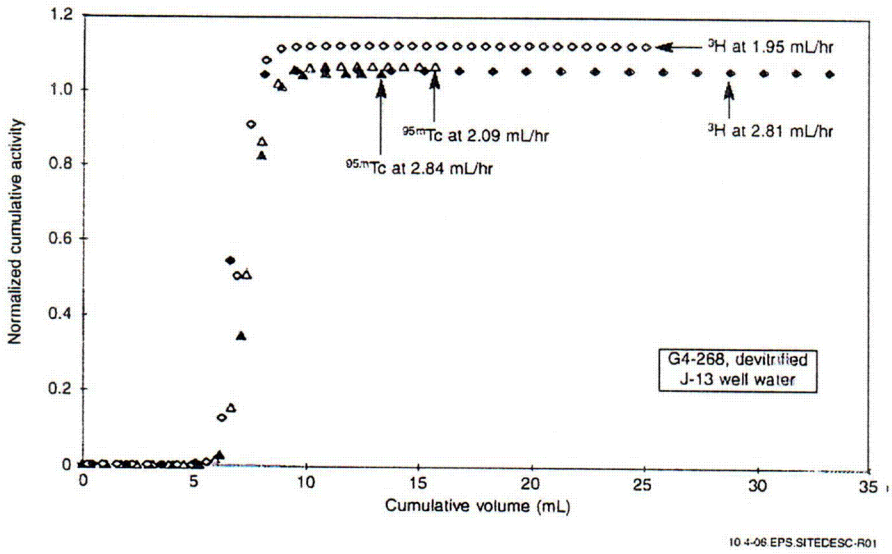

Source: CRWMS M&O (2000, Figure 18)

NOTE: This plot shows the elution curves for tritium and technetium-95m at different flow rates with J-13 well water through devitrified tuff sample G4-268.

Figure 10.4-6. Technetium in Devitrified Tuff at Various Flow Rates

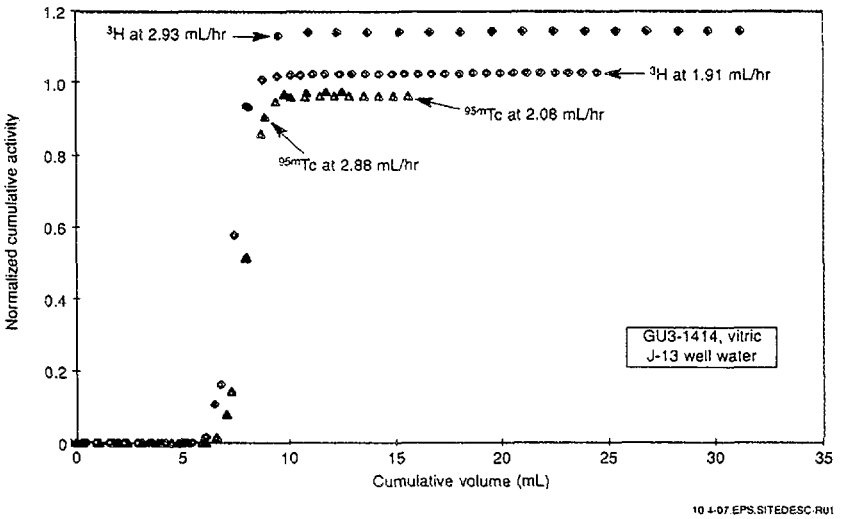

Source: CRWMS M&O (2000, Figure 19)

NOTE: This plot shows the elution curves for tritium and technetium-95m at different flow rates with J-13 well water through vitric tuff sample GU3-1414.

Figure 10.4-7. Technetium in Vitric Tuff at Various Flow Rates

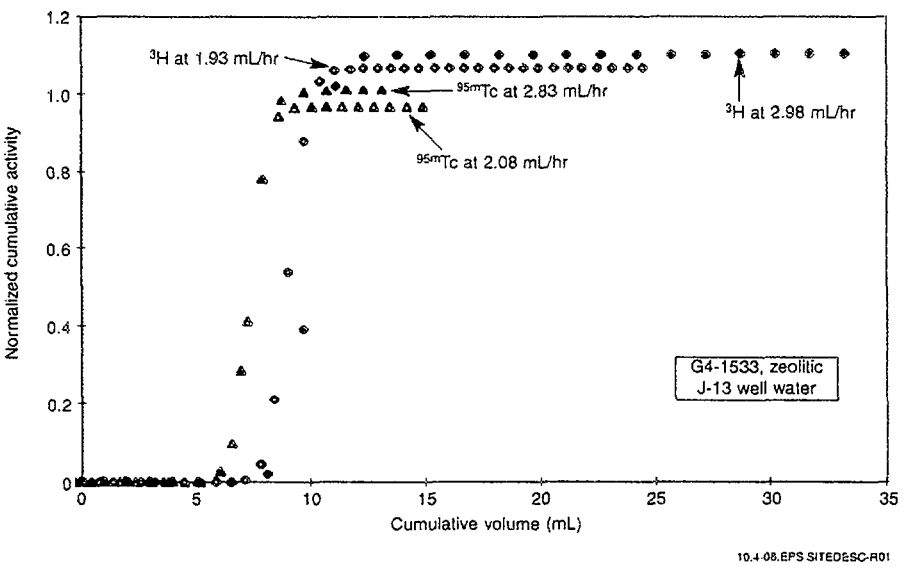

Source: CRWMS M&O (2000, Figure 20)

NOTE: This plot shows the elution curves for tritium and technetium-95m at different flow rates with J-13 well water through zeolitic tuff sample G4-1533.

Figure 10.4-8. Technetium in Zeolitic Tuff at Various Flow Rates

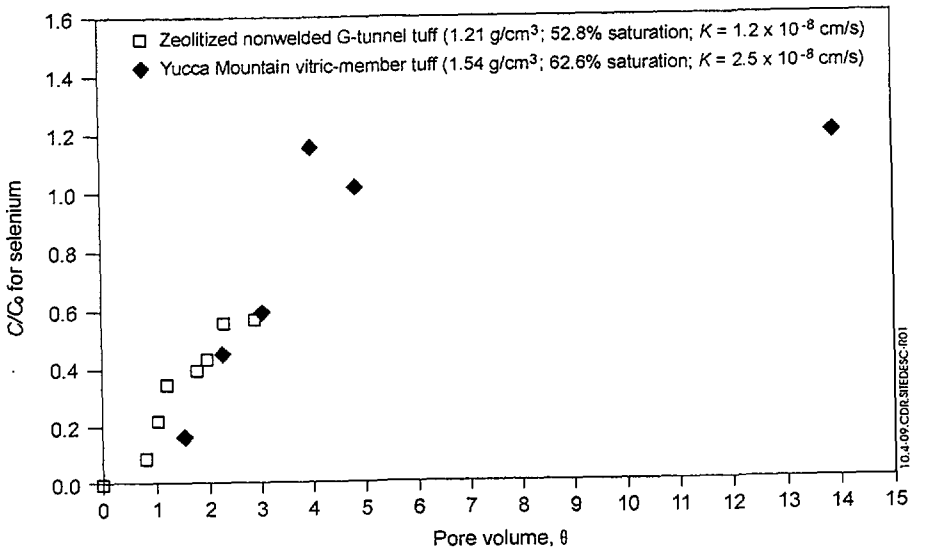

Source: CRWMS M&O (2000, Figure 21)

NOTE: The unsaturated flow apparatus column data plotted here for a Yucca Mountain tuff retardation experiment show the breakthrough curves for selenium. The initial concentration, C_0, of selenium (as selenite) was 1.31 ppm in J-13 well water.

Figure 10.4-9. Selenium Breakthrough Curves

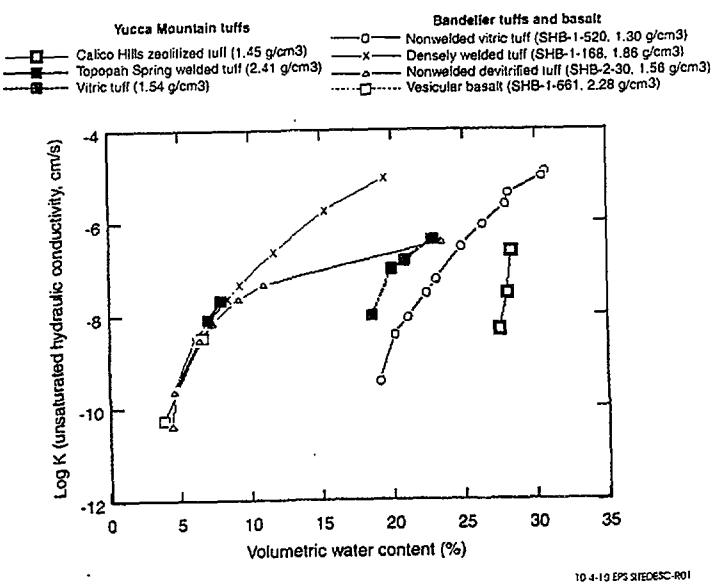

Source: CRWMS M&O (2000, Figure 22)

NOTE: These unsaturated flow apparatus column data for various Yucca Mountain and Bandelier tuffs and other soil samples show the unsaturated hydraulic conductivity, *K*, as a function of volumetric water content. The name and the density of each tuff are given in the legend.

Figure 10.4-10. Unsaturated Hydraulic Conductivity

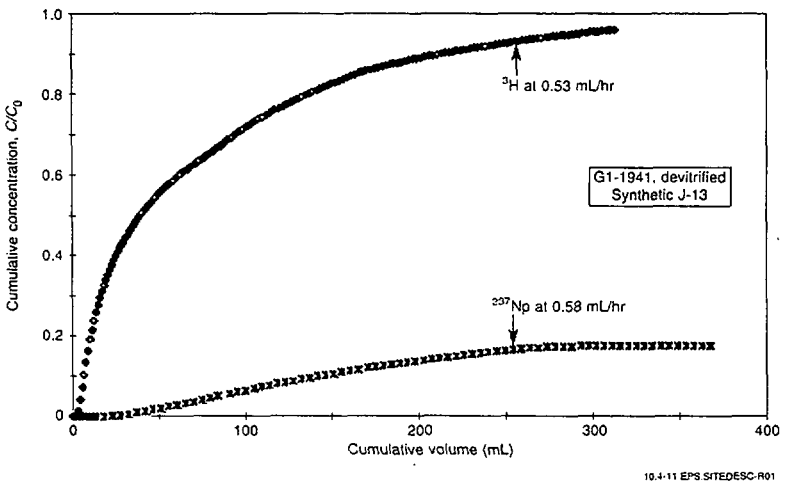

Source: CRWMS M&O (2000, Figure 23)

NOTE: This plot shows the elution curves for tritium and neptunium-237 in synthetic J-13 water through a fractured column of devitrified tuff sample G1-1941.

Figure 10.4-11. Neptunium in Fractured Tuff G1-1941

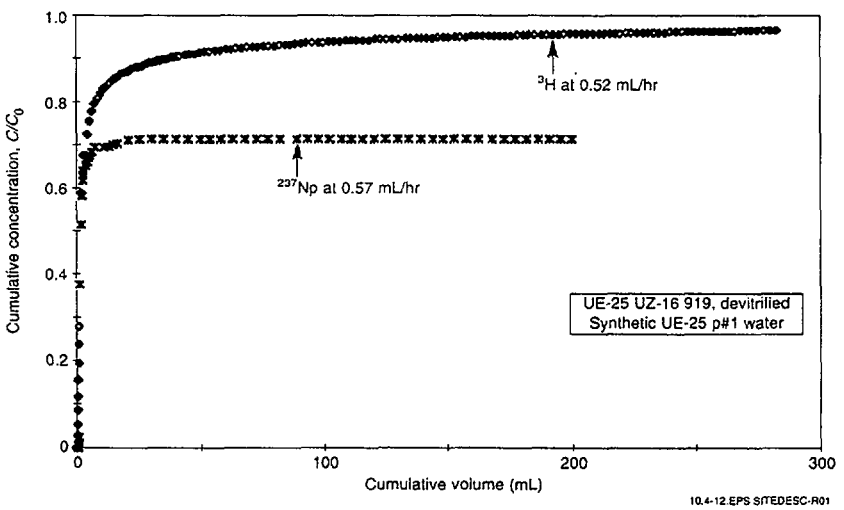

Source: CRWMS M&O (2000, Figure 24)

NOTE: This plot shows the elution curves for tritium and neptunium-237 in synthetic UE-25 p#1 water through a fractured column of devitrified tuff UE-25 UZ-16 919.

Figure 10.4-12. Neptunium in Fractured Tuff UZ-16 919

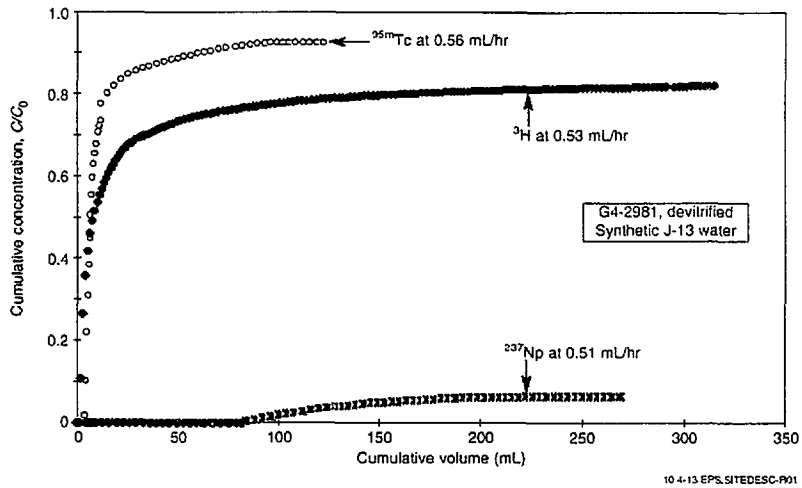

Source: CRWMS M&O (2000, Figure 25)

NOTE: The plot shows elution curves for tritium, neptunium-237, and technetium-95m in synthetic J-13 water through a fractured column of tuff G4-2981.

Figure 10.4-13. Neptunium and Technetium in Fractured Tuff G4-2981

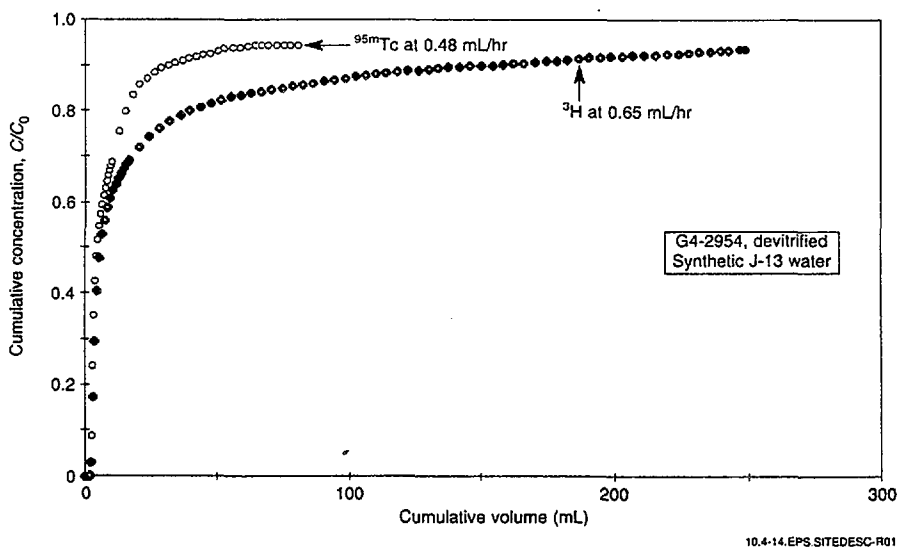

Source: CRWMS M&O (2000, Figure 26)

NOTE: The plot shows elution curves for technetium-95m and tritium in synthetic J-13 water through a fractured column of devitrified tuff G4-2954.

Figure 10.4-14. Technetium in Fractured Tuff G4-2954

INTENTIONALLY LEFT BLANK

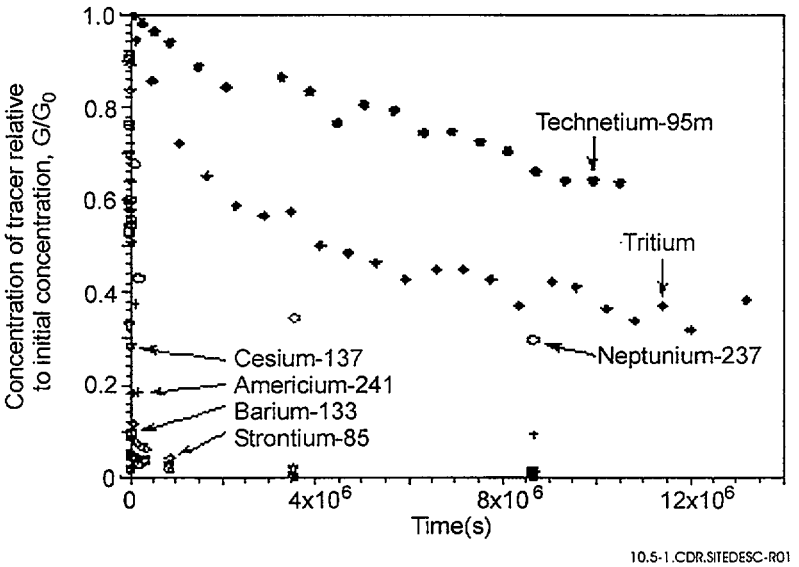

Source: CRWMS M&O (2000, Figure 27)

NOTE: These data for diffusion of tracers in J-13 water and in rock beakers made of tuff G4-737 show the concentration, C, of tracer (relative to the initial concentration, C_0) remaining in the beaker as a function of elapsed time.

Figure 10.5-1. Diffusion Data

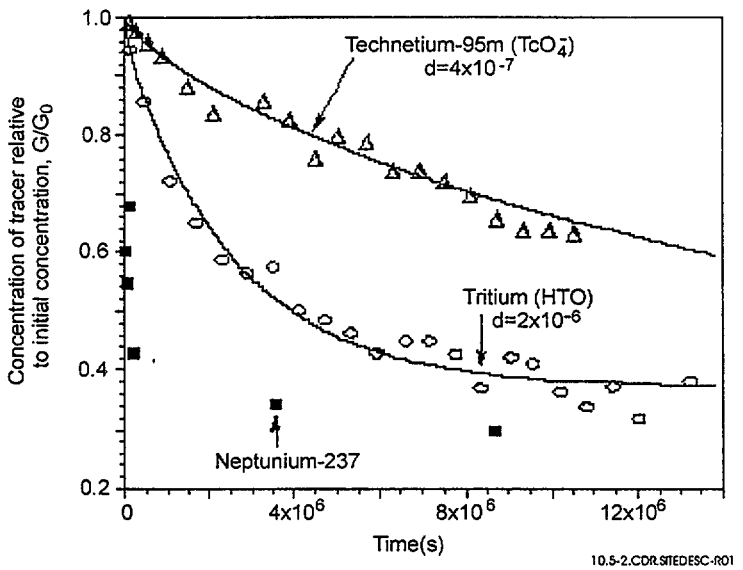

Source: CRWMS M&O (2000, Figure 28)

NOTES: The solid curves are fits to the diffusion data by the TRACRN code for the nonsorbing tracers tritium and technetium in the rock-beaker experiments with tuff G4-737. Units of d are in mL/g.

Figure 10.5-2. Diffusion Data Curve Fits

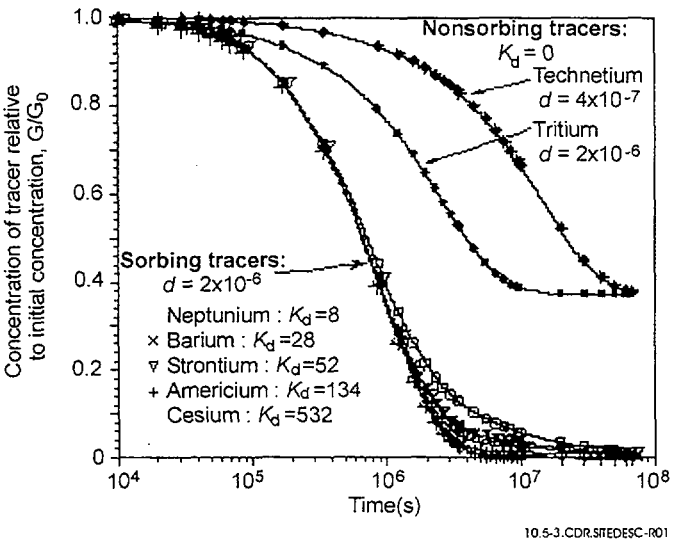

Source: CRWMS M&O (2000, Figure 29)

NOTES: These curves were calculated for tuff G4-737 using the diffusion coefficient, d, measured for tritiated water and the batch-sorption coefficients, K_d, measured for the sorbing radionuclides (Table 10.5-2). Diffusion curves for tritium and technetium are also shown. Units of d are in mL/g.

Figure 10.5-3. Calculated Diffusion Curves

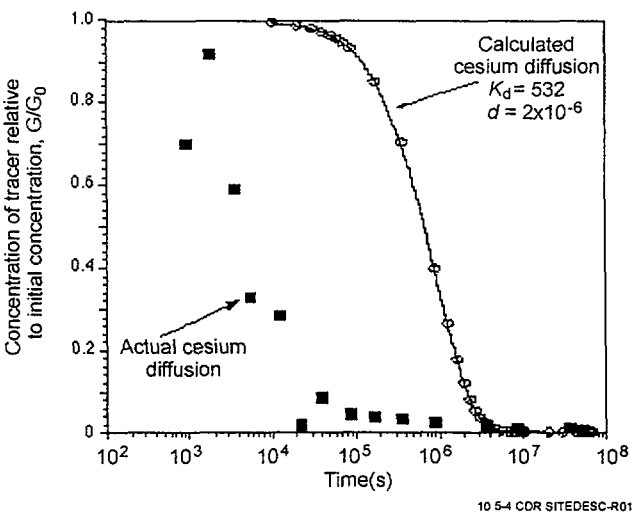

Source: CRWMS M&O (2000, Figure 30)

NOTES: The solid curve is the diffusion curve calculated for cesium using a K_d value and the diffusion coefficient for tritium (Figure 10.5-3); the squares are the actual diffusion data for cesium with tuff G4-737 (Figure 10.5-1). Units of d are in mL/g.

Figure 10.5-4. Comparison of Calculated and Actual Diffusion Data

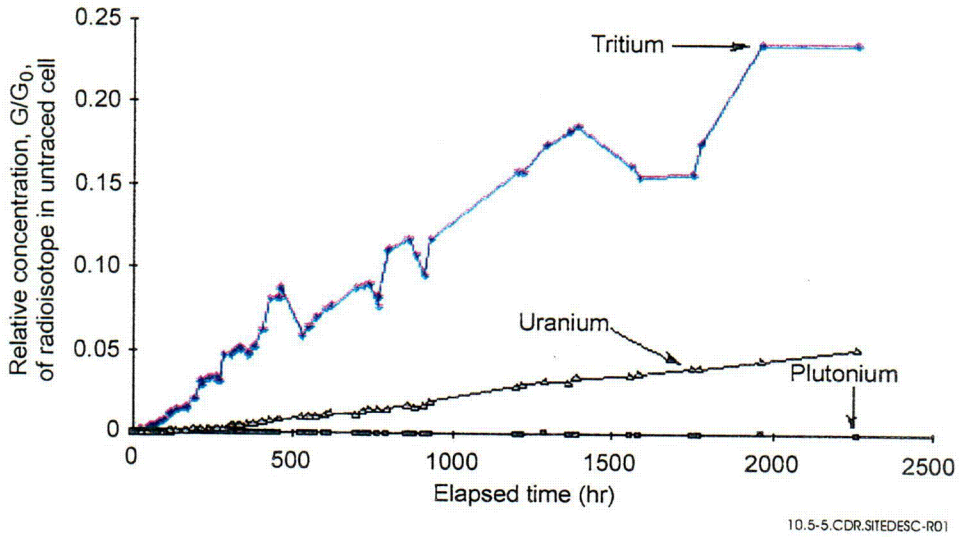

Source: CRWMS M&O (2000, Figure 31)

NOTES: The data show the concentration in synthetic UE-25 p#1 water of tritium, plutonium-239 (V), and natural uranium (VI) (relative to the concentration in the traced cell, C/C_0) diffusing through devitrified tuff G4-287 into the untraced cell as a function of time.

Figure 10.5-5. Tritium, Plutonium, and Uranium Diffusion through Devitrified Tuff

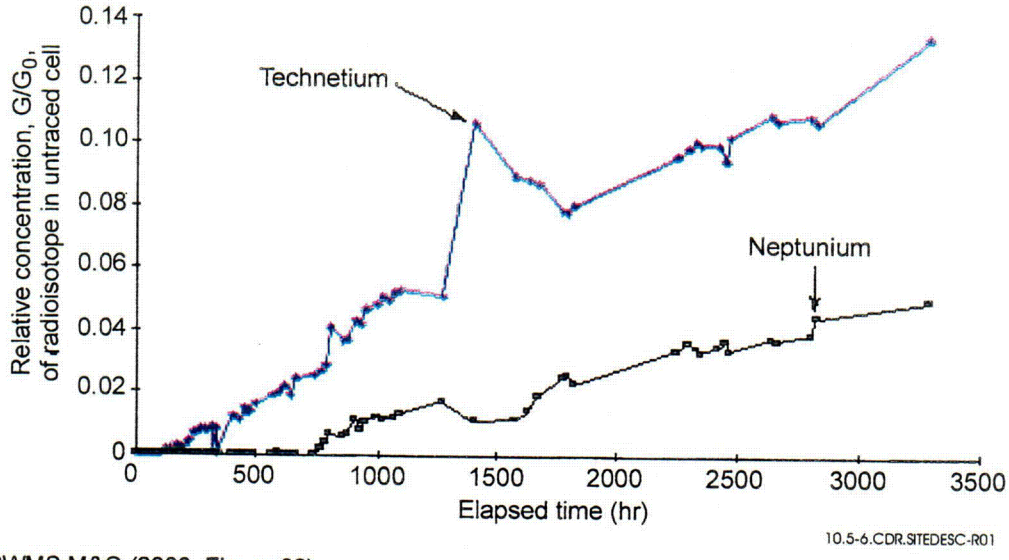

Source: CRWMS M&O (2000, Figure 32)

NOTES: The data show the concentration in synthetic UE-25 p#1 water of technetium-95m and neptunium-237 (relative to the concentration in the traced cell, C/C_0) diffusing through devitrified tuff G4-287 into the untraced cell as a function of time.

Figure 10.5-6. Technetium and Neptunium Diffusion through Devitrified Tuff

C23

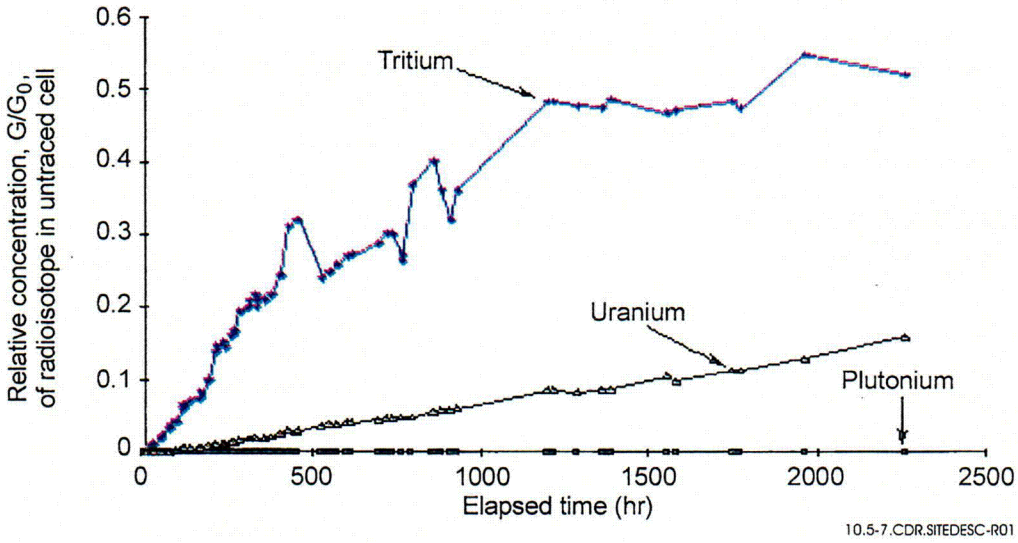

Source: CRWMS M&O (2000, Figure 33)

NOTES: The data show the concentration in synthetic UE-25 p#1 water of tritium, plutonium-239 (V), and natural uranium (VI) (relative to the concentration in the traced cell, C/C_0) diffusing through zeolitic tuff UE-25 1362 into the untraced cell as a function of time.

Figure 10.5-7. Tritium, Plutonium, and Uranium Diffusion through Zeolitic Tuff

C24

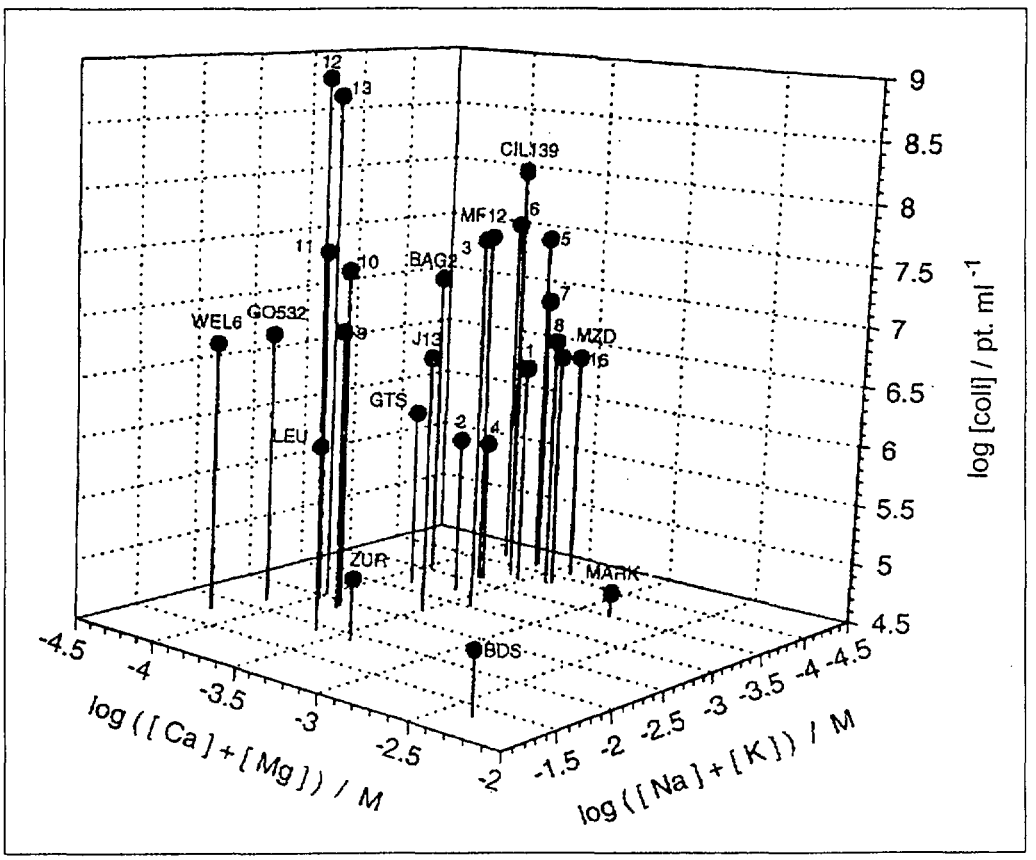

10.6-1.DOC.SITEDESC-R01

Source: CRWMS M&O (1997, Chapter VIIA, Figure 1)

NOTE: Concentrations of colloids are compared on the basis of alkali and alkaline-earth element concentration for colloid size greater than 100 nm.

Figure 10.6-1. Colloid Concentrations

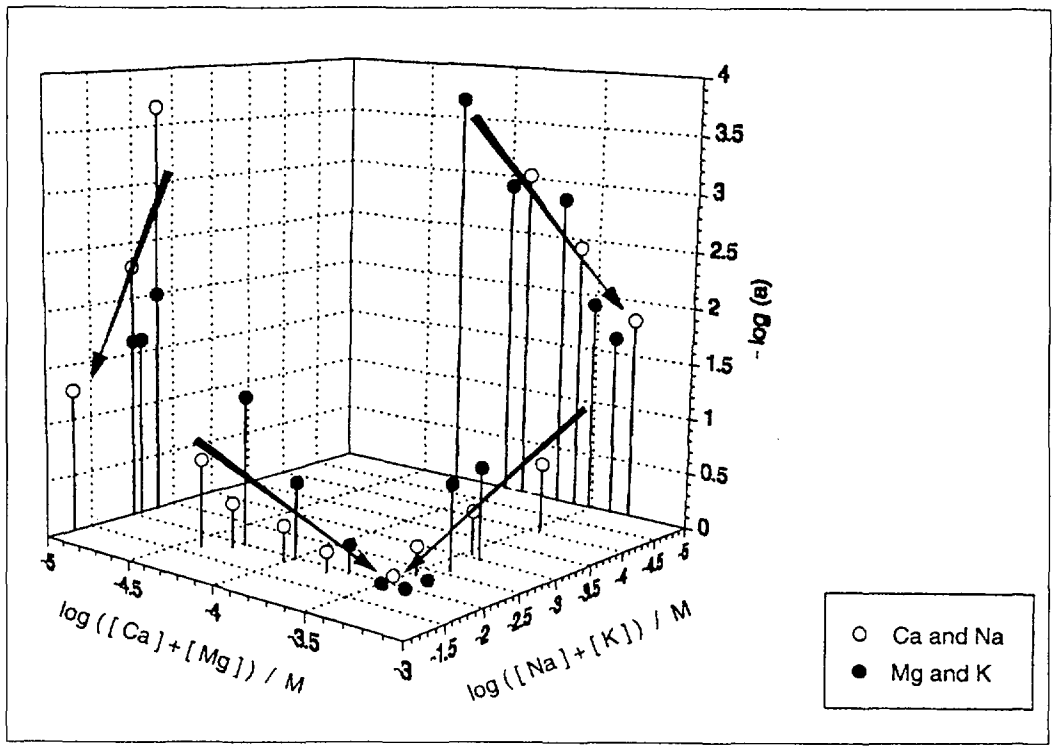

10.6-2.DOC.SITEDESC-R01

Source: CRWMS M&O (1997, Chapter VIIA, Figure 2)

NOTE: This plot shows the effect of calcium + magnesium and sodium + potassium on the colloid attachment factor at a pH of 8 for montmorillonite colloids of size greater than 100 nm with total organic carbon less than 5×10^{-5} M.

Figure 10.6-2. Colloid Attachment

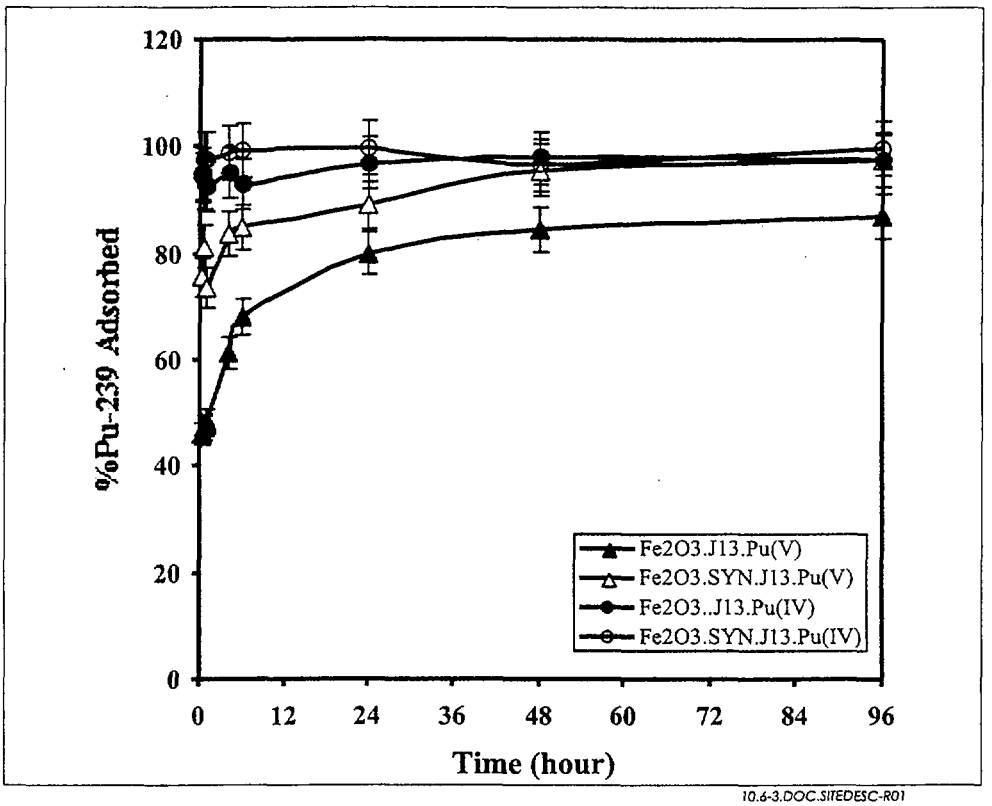

Source: CRWMS M&O (1997, Chapter VIID, Figure 1)

Figure 10.6-3. Sorption of Plutonium-239 onto Hematite Colloids as a Function of Time in Natural and Simulated Groundwater

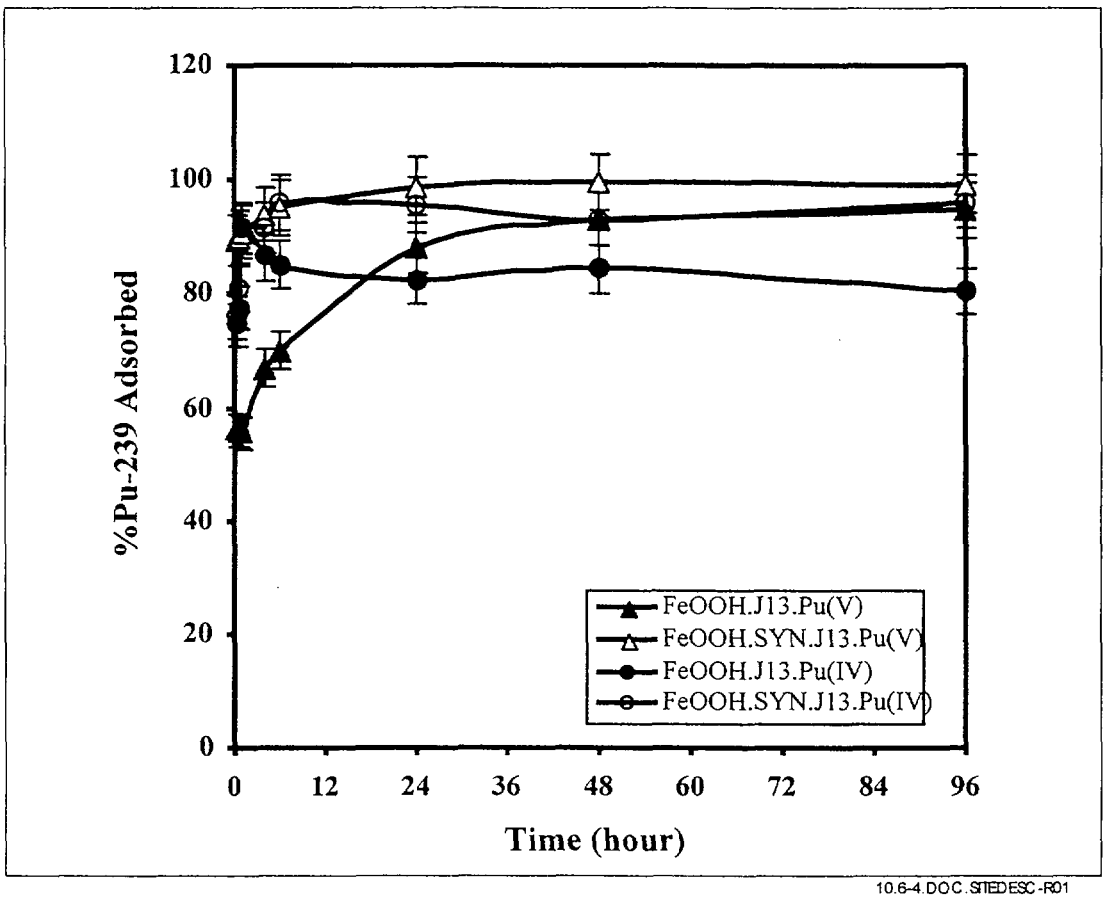

Source: CRWMS M&O (1997, Chapter VIID, Figure 1)

Figure 10.6-4. Sorption of Plutonium-239 onto Goethite Colloids as a Function of Time in Natural and Simulated Groundwater

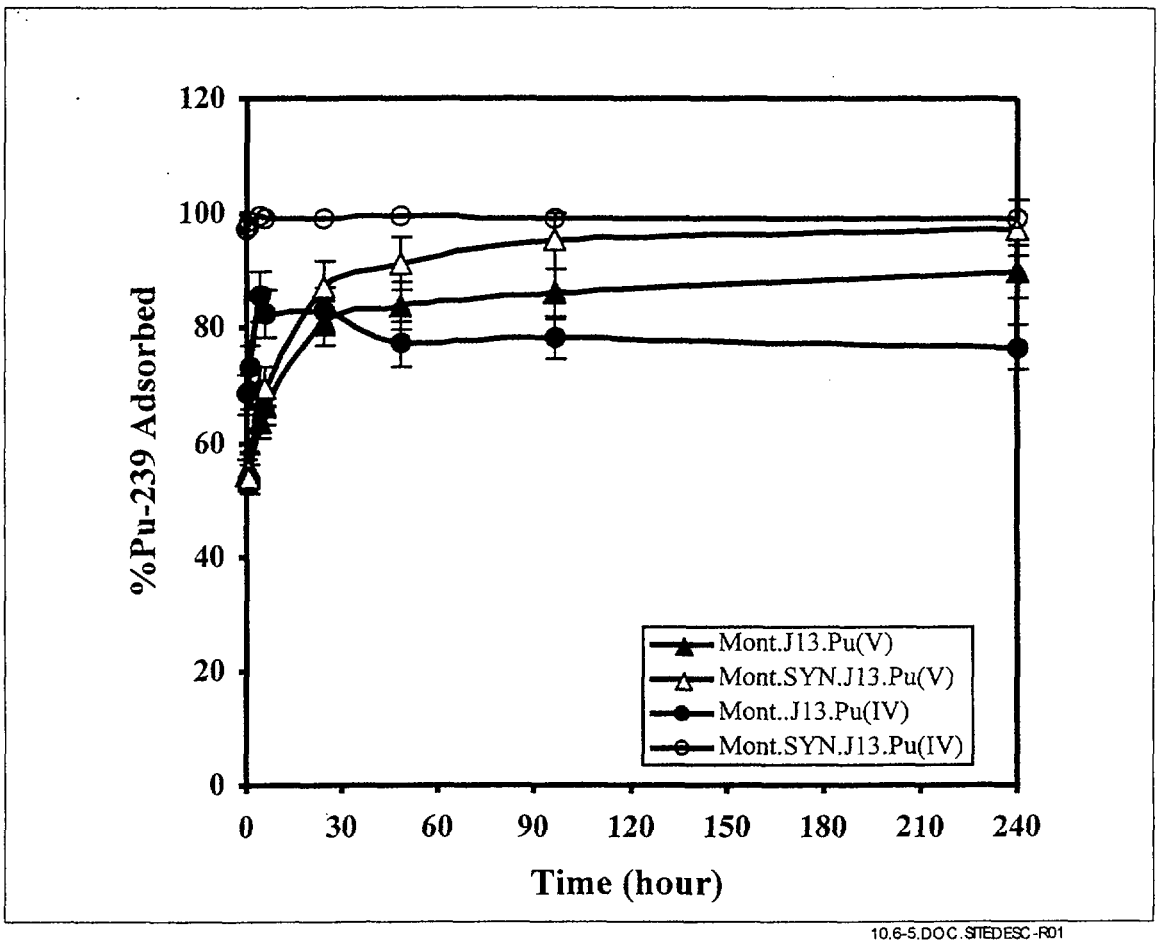

DTN: LA0004NL831352.001

Figure 10.6-5. Sorption of Plutonium-239 onto Montmorillonite Colloids as a Function of Time in Natural and Simulated Groundwater

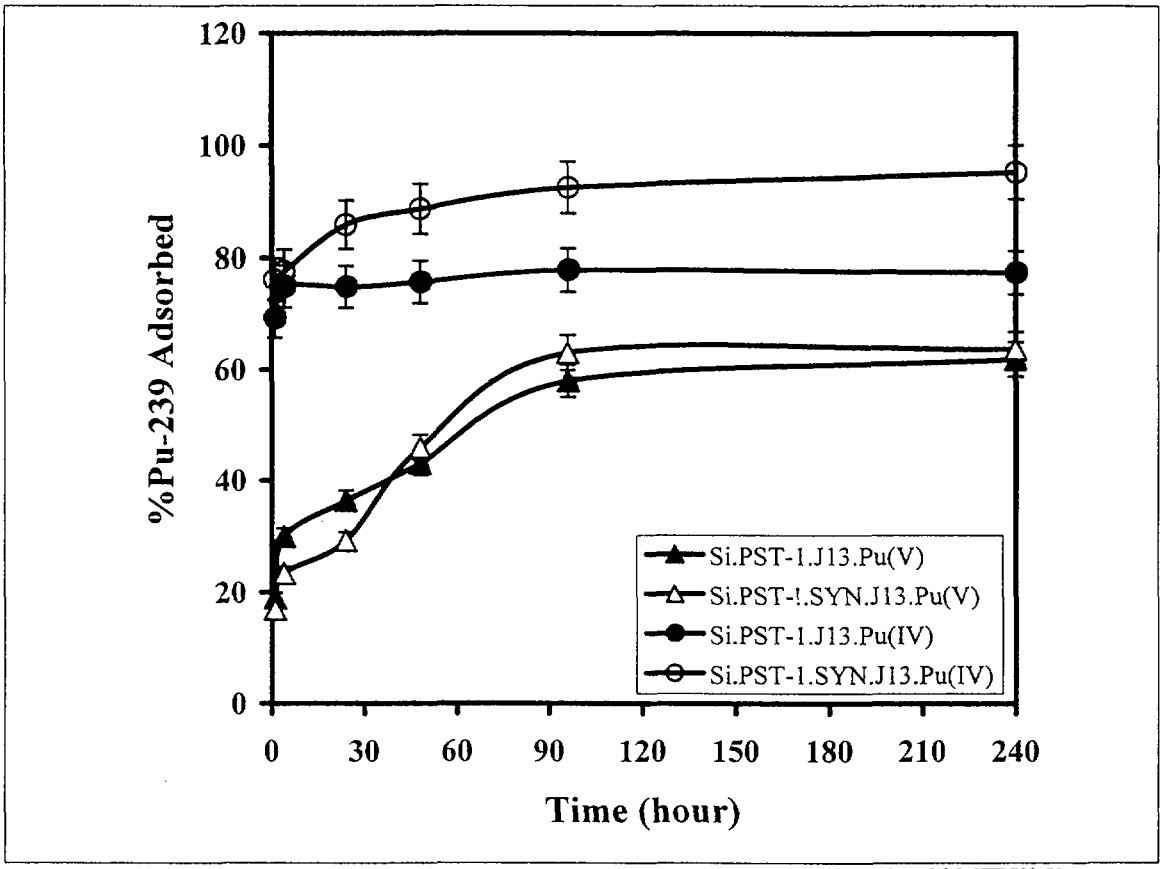

DTN: LA0004NL831352.001

Figure 10.6-6. Sorption of Plutonium-239 onto Silica-PST-1 Colloids as a Function of Time in Natural and Simulated Groundwater

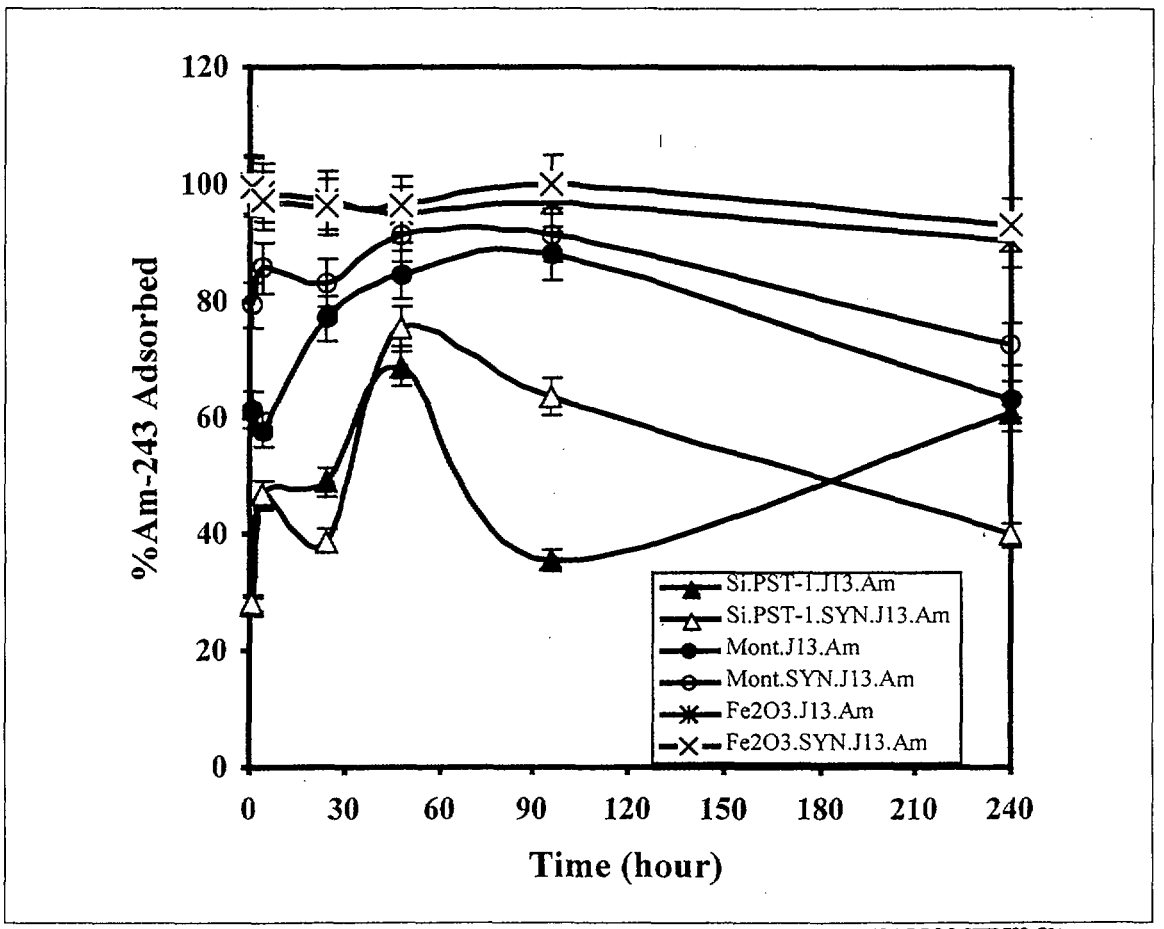

DTN: LA0003NL831352.001

Figure 10.6-7. Percentage of Americium-243 Adsorbed onto Colloids of Hematite, Montmorillonite, and Silica-PST-1 as a Function of Time in Natural and Simulated Groundwater

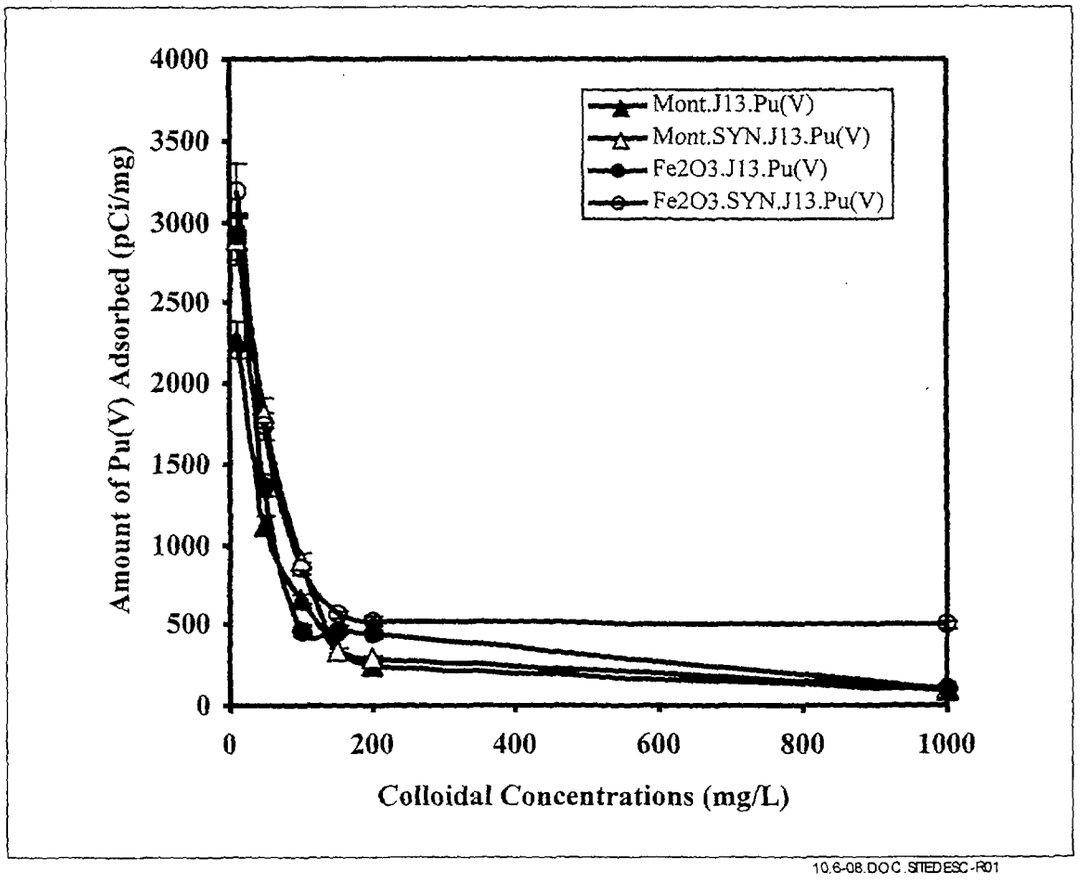

DTN: LA0004NL831352.003

Figure 10.6-8. Amount of Plutonium (V) Adsorbed onto Hematite and Montmorillonite as a Function of Colloidal Concentrations in Natural and Simulated Groundwater after 240 Hours

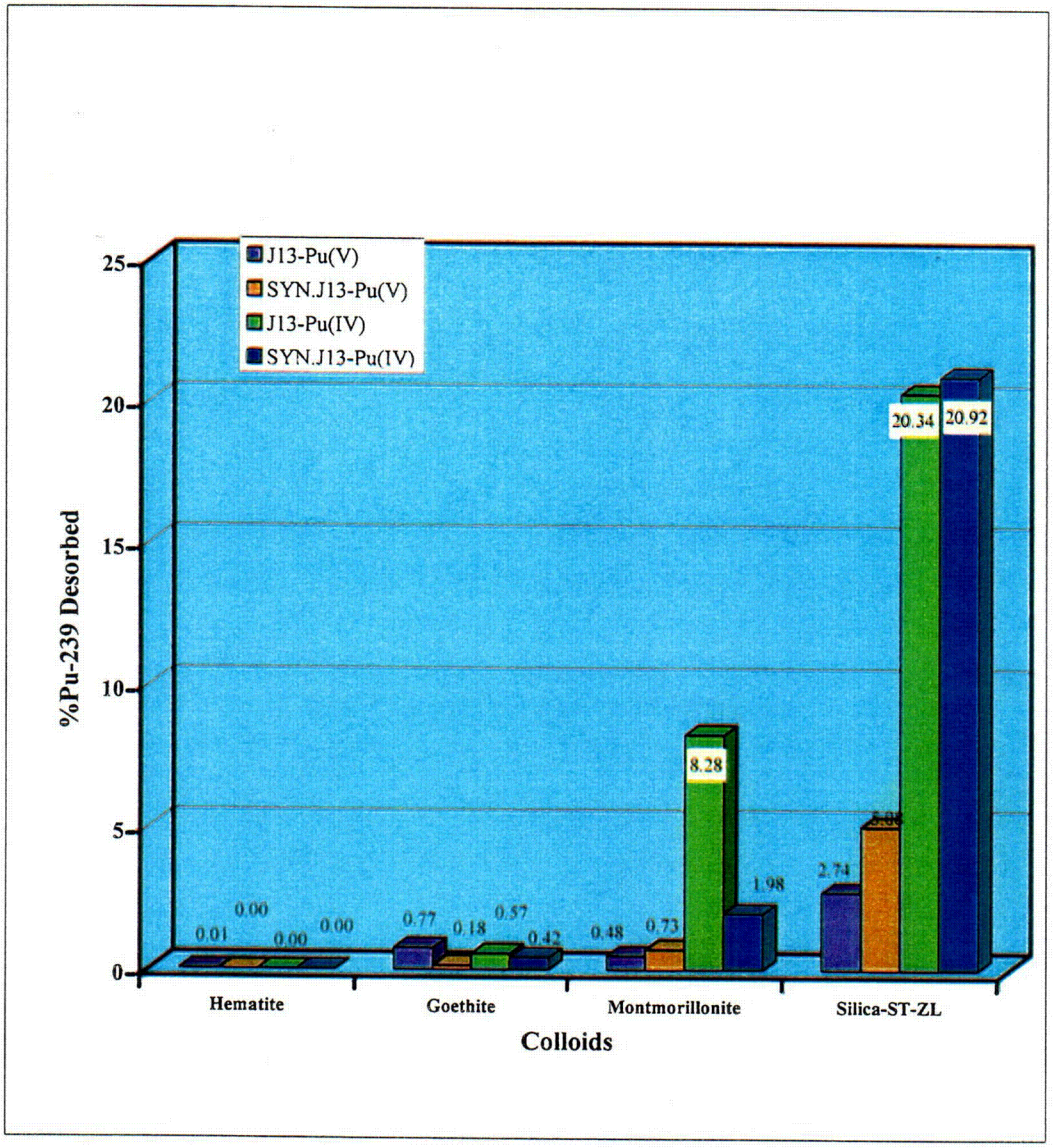

DTN: LA0005NL831352.001

Figure 10.6-9. Desorption of Plutonium-239 from Colloids of Hematite, Goethite, Montmorillonite, and Silica in Natural and Simulated Groundwater after 150 Days

C25

INTENTIONALLY LEFT BLANK